THE UNIVERSITY OF CALGARY

Analysis and Design of Passive Rotor Transverse Flux Machines with Permanent Magnets on the Stator

by

Bodo Eike Hasubek

A DISSERTATION SUBMITTED TO THE FACULTY OF GRADUATE STUDIES IN PARTIAL FULFILLMENT OF THE REQUIREMENTS FOR THE DEGREE OF DOCTOR OF PHILOSOPHY

DEPARTMENT OF ELECTRICAL AND COMPUTER ENGINEERING
CALGARY, ALBERTA
March, 2000

Abstract

In this dissertation novel magnetic circuit layouts of passive rotor transverse flux motors with a permanent magnet flux accumulator design on the stator are presented and investigated. The main advantage of these passive rotor designs is that the permanent magnets are fixed in place on the stator which reduces the mechanical stresses compared to the case of rotor mounted magnets. The fixed magnets allow higher rotational speeds. This design also is advantageous from the cooling perspective, because the magnets can dissipate their heat through the surrounding casing material. It also makes the magnets available for active fluid cooling in high power machines. Two novel passive rotor transverse flux motor designs are proposed and evaluated in this dissertation, that are referred to here as the *slanted rotor* design and the *reduced magnet material* design. The goal is to identify the passive rotor designs that have the least saturation problems, make economic use of the permanent magnet material and achieve high force densities. For the design that matches those criteria best, the *reduced magnet material* design, an analytical design methodology for the magnetic circuit is developed, that ensures a near optimal use of the magnet material by adjusting the operating point of the permanent magnets to their energy maximum. Using three-dimensional finite element analyses the preliminary optimum magnet use designs are then investigated to obtain relationships of the geometric design parameters providing the highest force densities. The results of the finite element and analytical analyses of the *reduced magnet material* design recommendations are derived reflecting the geometrical, magnet material and saturation constraints of this design. By combining the design recommendations with the theoretical efficient magnet use design methodology, it is possible to find magnetic circuit layouts that meet both the criteria of minimum magnet use and high force density.

Acknowledgments

I am very grateful for the interesting discussions with my supervisor Dr. E.P. Nowicki, who always encouraged me to pursue my ideas and supported me all the way. I am also very obliged to the Natural Science and Engineering Research Council (NSERC) of Canada that relieved the financial pressure on myself and my supervisor significantly by awarding me their scholarship. Talking about financial issues I would also like to thank my parents without whose support I would have accumulated large debts by now. And last but not least I would like to thank Jingbo, my wife, for her support in those dark moments in which nothing seemed to work as expected.

Dedication

To my wife and my parents.

Contents

List of Figures

List of Tables

List of Symbols

$\{V\}$	Vector
$[M]$	Matrix
$\hat{}$	Peak value
$\nabla\cdot$	Divergence operator
$\nabla\times$	Curl operator
∇	Gradient operator
∂	Partial derivative
d	Total derivative
A	Vector potential
A_e	Nodal vector potential
A_r	Current coverage from the ring winding
B	Magnetic induction or flux density
$\hat{B}_1$	Peak value of the air gap flux density in synchronous machines
B_{avrg}	Average value of the air gap flux density in induction machines
B_{max}	Maximum air gap flux density
B_n	Normal component of the flux density
$B_{n_{non}}$	Normal component of the flux density in non-permeable material
$B_{n_{perm}}$	Normal component of the flux density in permeable material
B_{pm}	Magnetic flux density in the permanent magnet
B_r	Remanent flux density in permanent magnets
B_δ	Flux density in the air gap
$B_{\delta_{pm}}$	Flux density in the air gap caused by the permanent magnet

$B_{\delta_{pm_t}}$	Flux density in the air gap caused by the permanent magnet, theoretical value
$B_{\delta_{pm_F}}$	Flux density in the air gap caused by the permanent magnet, FEA value
C_{eff}	Effective flux accumulation factor
C_m^*	Leakage adjusted mechanical flux accumulation factor
d	Rotor depth
d_m	Median rotor diameter
d_s	Stator iron depth
d_w	Winding depth
D	Electric flux density
E	Electrical field strength/intensity
f	Frequency
f_0	Reference frequency
f_s	Switching frequency
F	Force
F_{Ax}	Force density
h_r	Rotor height
h_s	Stator height
H	Magnetic field strength
H_c	Permanent magnet coercive force
H_{cB}	Permanent magnet coercive force where the external flux density becomes zero
H_{cJ}	Permanent magnet coercive force where the internal polarization becomes zero
H_m	Magnetization field strength/intensity
H_t	Tangential magnetic field strength
$H_{t_{non}}$	Tangential magnetic field strength in the non-permeable material
$H_{t_{perm}}$	Tangential magnetic field strength in the permeable material
H_s	Conductor (source) field strength/intensity
J	Current density
J_e	Eddy current density
J_s	Source current density
k	Leakage correction factor
k_c	Carter slot correction factor
k_{Fe}	Iron fill factor

k_h	Corrective factors for hysteresis losses
k_{ed}	Corrective factors for eddy current losses
k_{mag}	Corrective factors for overall magnetic losses
M_0	Remanent intrinsic magnetization
$\{n\}$	Normal vector
n_x, n_y, n_z	Components of the normal vector
N_A	Shape function for the vector potential
p	Number of machine pole pairs
r	Radius
r_m	Medium radius
$\{r\}$	Distance vector
R_a, R_i	Total reluctance at the outer/inner side of the machine model
R_{al}, R_{ar}	Total reluctance at the outer left/right side of the machine model
R_{il}, R_{ir}	Total reluctance at the inner left/right side of the machine model
R_{pm}	Reluctance of the permanent magnet
R_{pp}	Total pole-to-pole reluctance
R_{ppm}	Pole-to-pole reluctance at the medium machine radius
$R_{pp\sigma}$	Pole-to-pole leakage reluctance
R_{pra},R_{pri}	Outer/inner pole-to-rotor reluctance
$R_{t_{Fe}}$, R_t	Total circuit reluctance with and without iron reluctances
R_{xa}, R_{xi}	Cross reluctance at the outer/inner air gap
R_δ	Reluctance of the air gap
$R_{\delta a}$	Reluctance of the outer air gap
$R_{\delta i}$	Reluctance of the inner air gap
R_σ	Leakage reluctance
$R_{\sigma,xy}$	Leakage reluctance in the xy-plane
$R_{\sigma,yz}$	Leakage reluctance in the yz-plane
s	Coordinate direction for virtual work forces
t	Time
t_r	Rotor thickness
u_i	Induced voltage
V	Electric potential

V_c	Volume of conduction material
V_s	Volume of the air element next to the solid of interest
w	Number of winding turns
w_p	Rotor pole width
w_{pm}	Width of the permanent magnets on the stator
w_{pr}	Pole-to-rotor width
w_r	Width of the rotor iron
w_s	Width of the iron on the stator
ϵ	Permittivity
Φ	Magnetic flux
Φ_{pm}	Magnetic flux in the permanent magnet
Φ_δ	Magnetic flux in the air gap
Φ_σ	Magnetic leakage flux
Φ_m	Reduced magnetic scalar potential
Ψ_t	Total magnetic scalar potential
ω	Rotational frequency
Ω	Complete area of interest for the finite element analysis
Ω_0	Non-permeable, non-conducting parts of Ω
Ω_1	Permeable, non-conducting parts of Ω
Ω_2	Conduction parts of Ω
ρ	Electric charge density
σ	Conductivity
σ_e	Specific hysteresis losses
σ_h	Specific eddy current losses
σ_{loss}	Magnetic flux leakage loss factor
σ_{pm}	Magnetic flux leakage seen from the permanent magnet
σ_f	Magnetic flux leakage with respect to the air gap flux
τ_p	Machine pole pitch
τ_{p_i}	Inner machine pole pitch
τ_{p_m}	Medium machine pole pitch
τ_{p_o}	Outer machine pole pitch

Θ_{pm}	Equivalent permanent magnet m.m.f.
Θ_r	Ring winding m.m.f.
μ	Permeability
μ_0	Vacuum permeability $\left(4\pi \cdot 10^{-7} \frac{Vs}{Am}\right)$
$\mu_{r_{pm}}$	Relative permeability of the permanent magnet
$\mu_{r_{fe}}$	Relative permeability of the iron
ν	Reluctivity

Epigraph

Esse quam videri

Chapter 1

Introduction

It is not uncommon for a designer of electric machines to state that the principles of machine design have been established over 100 years ago and have not changed since and therefore only leave room for small improvements. In recent years this prejudice has given way due to dramatic advances in material science in the area of permanent magnet materials and the introduction of the new *transverse flux machine (TFM)* [1]-[3]. This type of electrical machine is also known as the variable reluctance permanent magnet (VRPM) machine [4]. The transverse flux machine, as it will be referred to here, has a magnetic flux path with sections where the flux is transverse to the rotation plane. There are three general concepts for transverse flux machines: Active rotor machines with permanent magnets on the rotor that were investigated in great detail by Beyer [5], passive rotor electrically excited reluctance motors without any magnets that were thoroughly analyzed by Degèle [6] and the so far uninvestigated passive rotor transverse flux machines with permanent magnets on the stator (PRTFMPM). In this dissertation the magnetic circuit layout of this last design, the passive rotor transverse flux motors with a permanent magnet flux accumulator design on the stator, is investigated. Two novel PRTFMPM designs are presented in this dissertation, the *slanted rotor design* and the *reduced magnet material* (RMM) design and evaluated using linear reluctance models and two-dimensional and three-dimensional finite element analysis.

The innovative design of the flux path for a TFM combined with the use of new magnet materials allows one to achieve force densities that are three to five times higher compared to conventional DC, synchronous and induction machines. In other words:

A transverse flux machine with the same power rating is one third to one fifth in size and weight compared to conventional machines, while still maintaining high efficiency. Using standard parameters for electrical machine comparison, such as power/weight ratio, torque/weight ratio and torque/volume, transverse flux machines are superior in all aspects. The achievable power to total machine weight ratios for active rotor transverse flux machines range from $0.5 - 2.0\,\frac{kW}{kg}$ compared to $0.25 - 0.8\,\frac{kW}{kg}$ for conventional machines [5]. The torque to weight ratio largely depends on the machine diameter and machine construction. For machine diameters between $25 - 50\,cm$ the torque/weight ratio can be expected to lie in the $10 - 30\,\frac{Nm}{kg}$ range, while for larger machines (diameter $50 - 250\,cm$) the torque/weight ratio increases to $30 - 50\,\frac{Nm}{kg}$[3]. The torque/volume capability of transverse flux motors reaches up $90\,\frac{kNm}{m^3}$for special high torque designs, but normally assumes values in the $20 - 40\,\frac{kNm}{m^3}$ range compared $5 - 10\,\frac{kNm}{m^3}$ for conventional machines [7]. There are several reasons for the higher performance of transverse flux machines compared to conventional machines. Most importantly they use a complicated three-dimensional flux path that leads to the decoupling of the space requirement of the flux carrying core iron path and the space occupied by the armature winding. It is therefore possible to maximize the m.m.f. without reducing the iron path. In conventional machines those two parameters are coupled in a trade-off manner. Transverse flux machines also have a short, more efficient core iron path compared to conventional machines, which allows one to reach higher air gap flux densities. Furthermore, transverse flux machines make favorable use of permanent magnet flux accumulator designs, since there are no permanent magnets that can provide air gap flux densities up to $1.5\,T$. The high torque/volume values can be attributed to the hollow cylinder shape structure of rotor and stator where both, the inside and the outside of the cylinder, can participate in the torque production. The torque producing area is therefore doubled for a given radius, reducing the volume to one half for the same torque output. On the downside, transverse flux machines have a large number of poles. This is caused by the small pole pitches used in transverse flux machines for best performance that typically range from $5\,mm$ to $20\,mm$. For a machine diameter of $40\,cm$ for example, that can lead to $50 - 150$ poles depending on the pole pitch. If at the same time a high machine rpm is desired, the converter design must be carefully considered. Depending on the machine's nominal rpm as well, the converter must be able to deliver the required power at switching frequencies

between $10\,kHz$ and $50\,kHz$, if some current wave form shaping is desired to eliminate torque pulsations. Furthermore high operating frequencies involve high specific iron losses. However, the overall losses are similar or lower than in conventional machines, because transverse flux machine use only a fraction of the core material of conventional machines. By careful selection of the core material the overall machine efficiency of transverse flux motors is generally higher than for conventional machines as exemplified below.

The small size and the low weight makes transverse flux motor a superior choice for mobile applications such as hub motors for electrical vehicles. Several implementations of variable speed active rotor transverse flux hub motors for electric vehicles (EV) can be found in the literature that confirm the high torque capability and high power to weight ratios achievable with those machines [8, 9], for example a gearless direct drive system for EV application that is realized using a hub motor with $300\,Nm$ torque capability [9]. One design is described in [10] that provides $280\,Nm$ of torque per phase and a similar design is presented in [11]. Avoiding the need for a gearbox reduces the overall weight of the drive system significantly. Other applications of active rotor transverse flux motors, such as ship drives [12] and train drives [5] show the successful implementation of this motor type in a wide range of drive applications. The ship drive investigated in [12] is also gearless and is designed to deliver $20\,MW$ at $200\,rpm$, with a $3\,MW$ test drive currently being built. The power to weight ratio is $0.5\,\frac{kW}{kg}$ for the transverse flux machine compared to $0.4\,\frac{kW}{kg}$ for a permanent magnet excited synchronous machine (PSM) and $0.25\,\frac{kW}{kg}$ for an induction machine of the same power and speed rating. At the same time the transverse flux machine reaches an efficiency of $\eta = 98.6\%$ compared $\eta = 98.2\%$ for the PSM and $\eta = 97.2\%$ for the induction machine. Those drives are applicable to passenger liners, ferries, coastal icebreakers and military vessels. The main advantages aside from the high torque/low weight ratio of the transverse flux machine include low noise emission, reduced operating cost and increased flexibility of operation. The direct drive system for trains proposed in [5] has a power to weight ratio of $1.9\,\frac{kW}{kg}$ compared to $0.78\,\frac{kW}{kg}$ of a high performance induction machine conventionally used in modern train drive systems. The high power/weight ratio reduces the machine weight of a $300\,kW$ machine from $390\,kg$ for the induction machine to only $160\,kg$ for the transverse flux machine. The weight of $390\,kg$ does not include the additional $150\,kg$ of

the gear box that is needed for the complete drive system with the induction machine. The light weight transverse flux machine allows for new train concepts with a distributed drive system, which is desirable for high speed trains. A distributed drive system also eliminates the need for a heavy weight drive head, which reduces the track construction cost significantly because of the lower stresses imposed on the driveway.

For small drive systems (less than $2\,kW$) axial flux brushless DC (AF-BLDC) machines have been investigated for the application of household appliances [7] and a solar race vehicle [13]. In [7] the AF-BLDC machine was found to have a superior torque/mass ratio compared to conventional radial flux machines, but requires a high switching frequency similar to transverse flux motors. No transverse flux motors of similar small size have been built yet. Therefore a comparison with the AF-BLDC machine is not possible, because the machine characteristics largely depend on the machine size.

To eliminate the influence of machine size and construction type from the machine comparison for a wide range of medium and high power machines, the passive rotor transverse flux motors are evaluated in terms of maximum achievable force density instead of power/weight or torque/weight ratios. This measurement describes the performance of the machine's magnetic circuit without making assumptions on the particular machine layout. It is left to the designer of a real machine to reduce the total machine weight by using light weight structural components such as glassfiber or aluminum. An alternate approach would be to chose a particular design that is always used in the comparison. This would constitute a limitation of the desired generality of the analysis and is therefore dismissed.

For variable speed applications it is also beneficial that transverse flux motors with field magnets either on the rotor or on the stator have a large operating frequency range due to their favorable behavior when operated under field weakening conditions [5]. It is shown in [5] that the overall efficiency of the drive system, that is the efficiency of the motor and the converter combined, even increases up $\eta = 95\%$ at 2.3 times nominal speed from $\eta = 89\%$ at nominal speed. This beneficial behavior is caused by the large inductance of the armature winding that is introduced through the large gaps in the iron path seen by the armature winding. The overall magnetic circuit gap includes not only the machine's air gaps, but also the magnet's gap between the rotor poles for the active rotor design or the stator poles for the passive rotor design. It is shown in [14] that there

is an inherent downside to this design characteristic as well. The large armature winding induction results in a low power factor of $\varphi = 0.4 - 0.5$. According to [14] this low power factor cannot be eliminated within the machine through design changes and must be taken as a price that must be paid for the high specific torque output. This finding is quite obvious considering the cause for the large inductance stated above, that says that the inductance is largely influenced by the design critical permanent magnet width (see Chapter 4, Section 4.2.2). The price for the low power factor is paid explicitely for the converter design that must have a higher VA rating, or preferably the converter compensates for the low power factor through a power factor correction design. Also, to date no open loop control scheme has been implemented for transverse flux machines that would allow for a control scheme similar to the widely used vector control of conventional AC machines [15]. Therefore closed loop control with a position encoder on the shaft is required for a variable speed drive using transverse flux machines.

Motivation

There are several advantages of the passive rotor design with permanent magnets on the stator compared to either the active rotor transverse flux motor or to Degèle's machine that make this novel design that is investigated in this dissertation for the first time very desirable. The magnets of the PRTFMPM are located on the fixed stator, while the active rotor machines magnets are located on the rotor. In the passive rotor TFM with permanent magnets on the stator the permanent magnets are better protected from mechanical shocks and stresses because they are not moving. Also, the magnets are directly connected to the machine's casing. The heat developed under operation can directly disperse through solid material and does not need to cross the highly heat insulating air gap. The magnets of active rotor machines can only be cooled by comparatively inefficient air convection cooling. For high performance machines the magnets as well as the winding are accessible for direct fluid cooling to avoid demagnetization due to overheating. The latter can be especially important for the modern heat sensitive permanent magnet materials such as NdFeB. Rotor deformation at high speeds limits the upper circumferential speed of active rotor transverse flux motors to $50 - 100\,\frac{m}{s}$ [5]. This is cause by the mechanical limitations of mounting brittle magnet material on the rotor. The passive rotor TFMs proposed here do not place any magnet material on the rotor,

which allows for a much stiffer rotor construction. The increased rotor stiffness allows circumferential speeds substantially larger than $100\,\frac{m}{s}$. Higher circumferential speeds are important in direct train drives for high speed trains for example.

Comparing the electrically excited reluctance transverse flux motor without permanent magnets to the passive rotor design with magnets on the stator, the former – conceptually similar to switched reluctance motors – is solely based on reluctance forces while the latter employs the superposition of the armature and the excitation fields for the force production. The important difference is that the forces created by the superposition of the aforementioned two fields retain their sign over one full pole pitch or $180°$ electrically, while electrically excited machines only produce unidirectional forces over one half pole pitch or $90°$ electrically, which requires a minimum of three mechanically coupled systems versus only two for transverse flux machines employing two fields.

The benefits of a passive rotor design with permanent magnets on the stator raises the decisive question as to whether those machines are magnetically, electrically and economically viable for the drive applications outlined above. The goal therefore is to identify the passive rotor designs that have the least saturation problems, make economic use of the permanent magnet material and achieve high force densities. The *slanted rotor design* consists of a U-shaped stator ring made of core iron and permanent magnets for the field excitation. Embedded in the stator's U-shape is the ring shaped armature winding and the slanted rotor. The slant in the rotor is required to provide a closed flux path for the excitation field. It is shown in this dissertation that the slanted rotor design provides similar performance as comparable active rotor designs. The disadvantage of this design is the high magnet material use. Also, it exhibits areas of excessive saturation at the pointed rotor edges that limit the maximum achievable force density. The *reduced magnet material* design on the other hand consists of two rings made of core iron and magnet material with the armature ring winding embedded in between. The rotor consists of two members that are mounted to the shaft with a one pole pitch offset to provide the closed excitation flux path. No slant is required in this configuration avoiding the saturation issues of the slanted rotor design. The reduced magnet material design uses less core iron material than comparable active rotor designs, which makes it perform even better than active rotor designs. The reduced magnet material design also makes economic use of the magnet material. In fact, a design procedure for the magnetic circuit is presented in this

dissertation, which ensures the near optimum use of the magnet material. This design procedure allows easy application of this novel machine design in industry for a wide variety of machine parameters. Through linear reluctance models and two-dimensional and three-dimensional finite element analysis, recommended constraints for the design parameters are determined in order to achieve high force densities in a practical design. These recommended constraints are applicable over a wide range of medium and high power machine designs.

Dissertation outline

In Chapter 2 the differences between transverse flux (TF) machines and conventional longitudinal flux (LF) machines are described in detail. It is explained why transverse flux machines achieve higher force densities than conventional machines. Different magnet circuit layouts for active rotor machines are reviewed and several possible passive rotor machine designs employing permanent magnets on the stator are proposed. A description of the working principles of the two novel motor designs that are investigated in the succeeding chapters, the *slanted rotor design* and the *reduced magnet material* design, is given as well. The chapter concludes with a short introduction to the relevant Maxwell equations and force calculation methods used by the finite element analysis programs for electromagnetic field problems.

In Chapter 3 the *slanted rotor design* is analyzed. A reluctance model analysis of the fields in the air gap caused by the exciting permanent magnets and by the armature winding is performed. Two-dimensional finite element analysis for the *slanted rotor design* is presented to verify the assumptions made about the field distribution in the reluctance model analysis. The results also show the benefits and limitations of a two-dimensional approach for the design of passive rotor transverse flux motors. The numerical solutions of the reluctance model field calculations are compared to the results of three-dimensional finite element calculations to exclude the possibility of modeling errors in the three-dimensional finite element model. The three-dimensional finite element analysis is conducted to determine the achievable force densities for the *slanted rotor design*. Also, it is evaluated how the local saturation at the pointed rotor edges affects the achievable force density.

Analyzing the magnetic circuit of the *reduced magnet material* using linear reluctance

models, a design approach that facilitates near optimum magnet material use for this design is presented in Chapter 4. This is achieved by ensuring that the magnets operate in or close to their maximum energy point transferring the maximum magnetic energy into the air gap for the force production. Analytical approaches such as Carter's slot factor and finite element solutions are employed to further investigate the geometries of the optimum magnet use designs to select the designs that also provide a high force density. Three-dimensional finite element calculations that include saturation are used to determine the maximum low-saturation flux accumulation factor for the field magnets and to determine the maximum armature winding m.m.f. to preserve low saturation levels. Finally, design recommendations are given for parameter relationships that should be adhered to for a material efficient low saturation design of a *reduced magnet material* transverse flux machine with permanent magnets on the stator.

The conclusions in Chapter 5 summarize the main achievements discussed in this dissertation and give recommendations for further research.

Chapter 2

Transverse Flux Machines and Finite Element Analysis

There are significant differences between conventional machines and transverse flux machines that need to be explained in order to understand why the transverse flux machines achieve three to five times higher force densities compared to conventional machines. Even among the transverse flux machines there are conceptual differences and common principles that need to be reviewed as well. In this context the two novel machine designs that are the focal point of this dissertation are introduced.

A major vehicle for the design and analysis of electric machines is the finite element analysis which permits the calculation of accurate field and force solutions. This tool is particularly useful in the optimization of the transverse flux machine (TFM) design. Therefore, the governing equations of electromagnetic fields and their application to the finite element analysis are discussed at the end of this chapter.

2.1 Transverse Flux Machines

The first paragraph of the information outlined above is presented in three sections: In Section 2.1.1 the principal differences and advantages of transverse flux motors over conventional machines are described, in Section 2.1.2 the transverse flux motor concepts and common principles are explained in detail and in Section 2.1.3 an overview of the novel passive rotor designs that are the object of this dissertation is given.

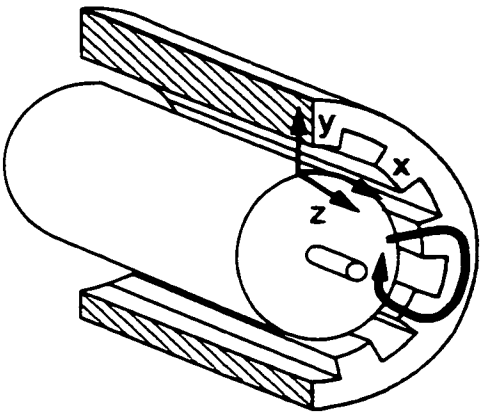

Figure 2.1: Two-dimensional flux plane of longitudinal flux machines

2.1.1 Conventional and Transverse Flux Machines

Looking at the flux path of conventional synchronous, induction and DC machines, most conventional machines can be classified as longitudinal flux (LF) machines, with very few exceptions such as axial flux machines [16]. All flux lines in LF machines follow a two dimensional pattern in planes perpendicular to the machine shaft. Thus, aside from fringe effects, the magnetic field for an LF machine can be represented in planar coordinates. Figure 2.1 shows the schematic of a non-salient synchronous machine. The rotation plane is the xy-plane. The thick circular arrow indicates that the flux plane of the stator and of the field winding extends only along or longitudinal to the rotation plane.

In Figure 2.2 a pie slice of a transverse flux machine is shown. The rotor mount connects the two rotor halves to the shaft. The rotor halves consist of core iron and filler material that is preferably magnetically and electrically inactive. The core iron in between the two rotor cylinders, the permanent magnets and the ring winding belong to the stator. The stator mount is not shown. The thick arrows show the flux path. While some parts of the flux path lie in the rotation (xy) plane as for longitudinal flux machines, other portions of the path are perpendicular to that plane, or in other words transverse to the xy-plane. Due to the two-dimensional flux path in longitudinal flux machines the space requirement for the winding and the flux carrying core iron path are related in a strict trade-off manner: An increase of the pole area (i.e. the flux carrying iron path) is only possible at the expense of slot width (i.e. the space for the

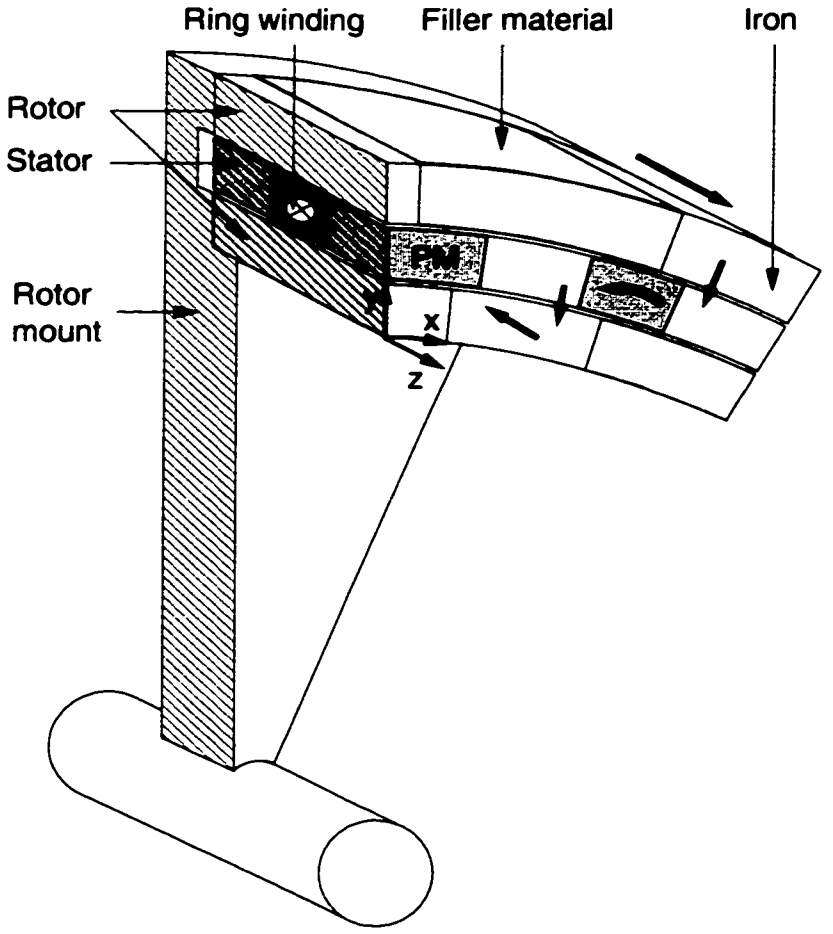

Figure 2.2: Three-dimensional TFM flux path shown for the passive rotor *reduced magnet material* design

Table 2.1: Typical armature and field current densities for LF machines for different cooling mechanisms

Machine Type	DC	Induction	Synchronous				
			Salient pole	Non-salient pole			
				indirect cooling		direct cooling	
				air	H_2	water	H_2
Armature $\frac{A}{mm^2}$	3.5-9	3-8	3-6.5	3-5	4-6	7-10	6-13
Field $\frac{A}{mm^2}$	1.5-8	n/a	1.5-4	3-5		13-18	6-13

winding). Thus, the maximum achievable force density, which is a common measure for the effective use of the materials in electrical machines, directly depends on the material properties of the iron and the thermally limited current density in the winding, leaving little room for geometrical optimizations. The force density F_{Ax} is defined as in (2.1), where F_{rotor} is the electromagnetic force on the rotor produced by the machine and A_{active} the electromagnetically active (or air gap) surface area of the rotor.

$$F_{Ax} \equiv \frac{F_{rotor}}{A_{active}} \tag{2.1}$$

Table 2.1 gives an overview of typical achievable current densities for armature and field windings [17]. As will be seen below those values have far less significance for transverse flux motors: It is generally possible to keep the current densities at low levels without impeding the machine's high performance. The large number of small winding turns and complicated geometry of the coils of longitudinal flux machine also yields low copper fill factors φ_{Cu} compared to the simple ring winding of transverse flux motors. Figure 2.3 shows a comparison of achievable fill factors for the low voltage range. The fill factor for transverse flux (TF) machines is significantly larger than comparable longitudinal flux (LF) machine values resulting in smaller cross sections for the same current carrying capability [5, 17].

The high force density of transverse flux motors compared to conventional machines

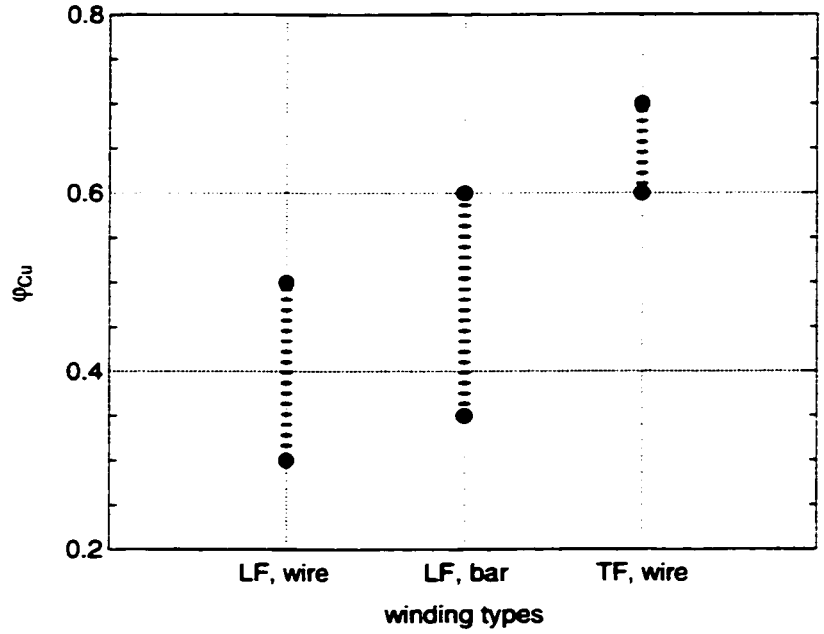

Figure 2.3: Comparison of copper fill factors φ_{Cu} of low voltage coils for longitudinal and transverse flux machines

can be largely attributed to the fact that the transverse flux design decouples the space requirements of the stator winding from the space requirement of the flux path for the field interaction, allowing new optimization methods that do not work for LF machines. In Chapter 4 it is observed that higher air gap flux densities contribute to the higher force densities as well. The independent design parameter variation of TF machines permits much smaller pole pitches which dramatically increases the achievable force density and an independent winding cross section to keep the air gap current coverage high while maintaining a low current density in the winding. Due to the high number of poles the cranking torque of transverse flux motors is high compared to conventional machines. This feature can save the need for a gear box for a given drive problem, which further reduces the overall weight of the drive system compared to a conventional system.

Figures 2.4 and 2.5 compare optimization methods to increase the achievable current coverage from the stator winding in the air gap for longitudinal and transversal flux machines. Note in these figures, that regions containing copper windings are indicated in dark grey, permanent magnets are light grey and iron regions are white. On the left side

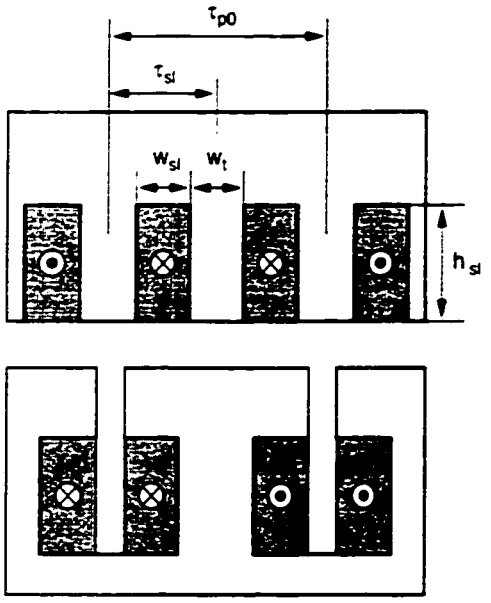

(A) Base case LF machine

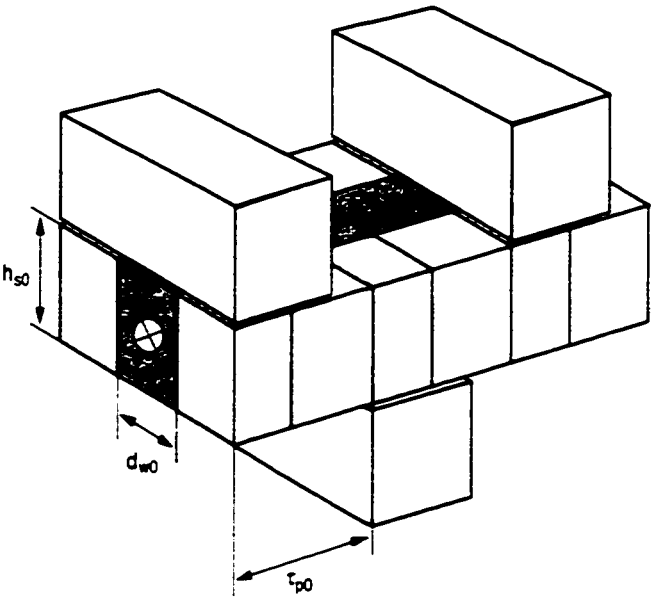

(A) Base case TF machine

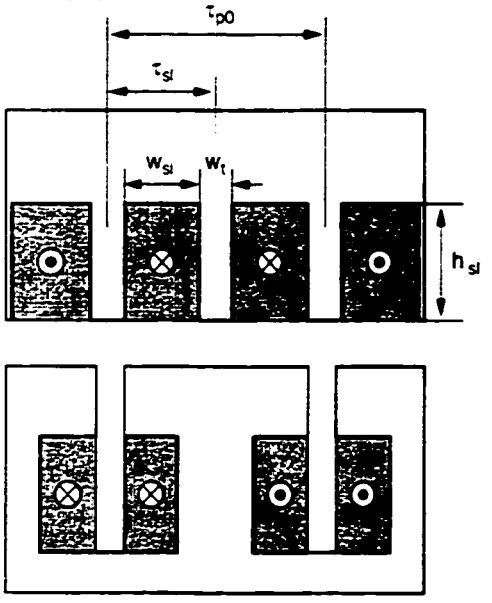

(B) Wider winding LF

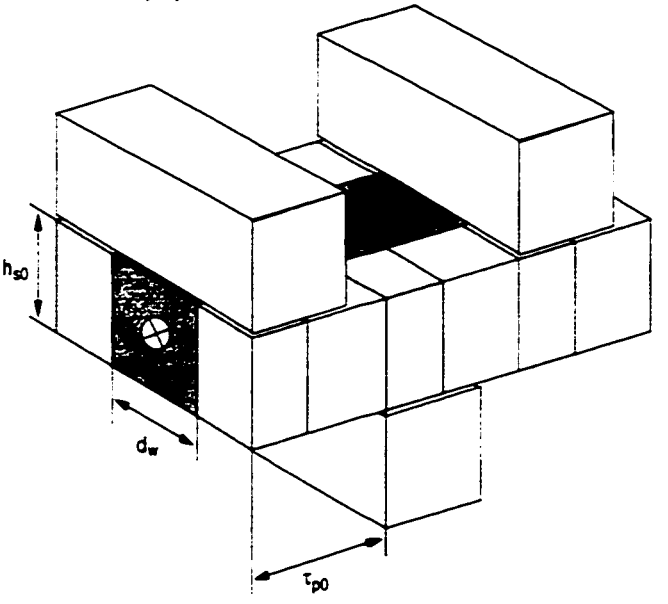

(B) Wider winding TF

Figure 2.4: Machine optimization 1: Base case and wider winding

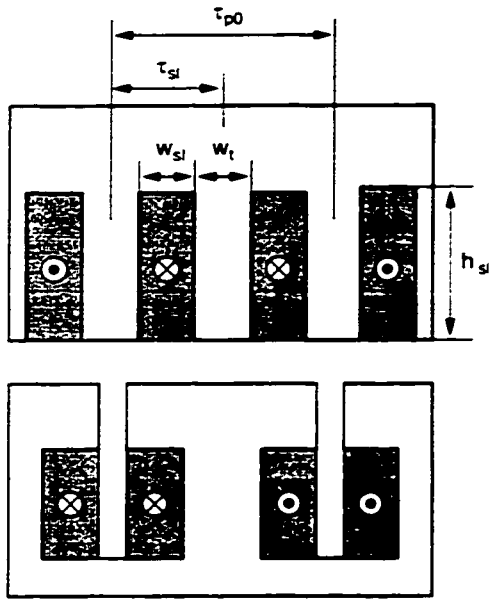

(C) Higher winding LF

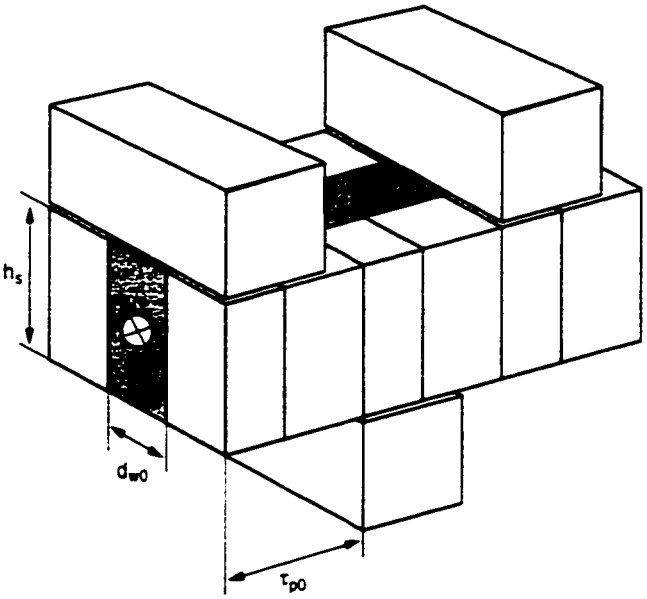

(C) Higher winding TF

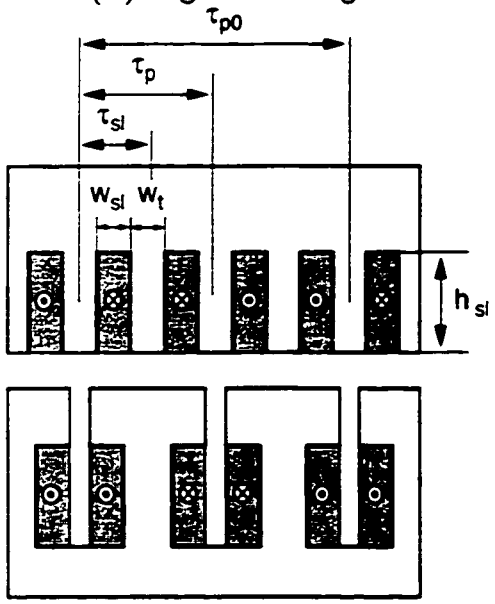

(D) Smaller pole pitch LF

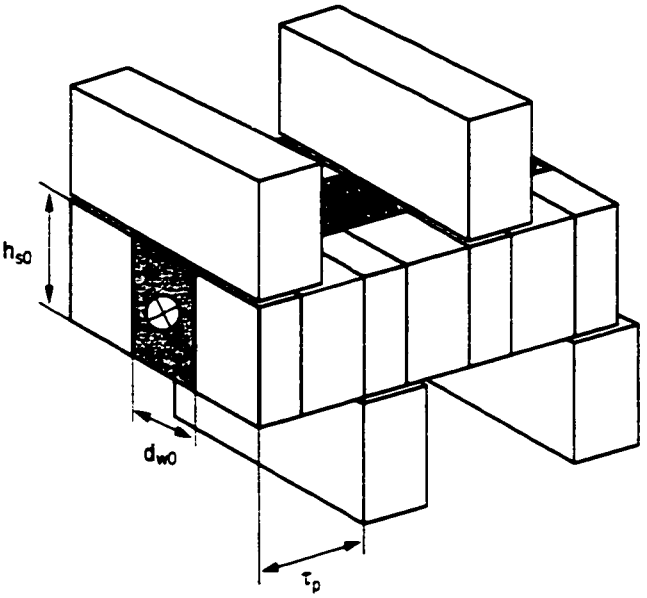

(D) Smaller pole pitch TF

Figure 2.5: Machine optimization 2: Higher winding and smaller pole pitch

of both figures a rolled out section of a salient pole synchronous machine is shown as an example for the longitudinal flux machines. On the right side a rolled out section of the passive rotor *reduced magnet material* design transverse flux motor (analyzed in detail in Chapter 4) is shown. Case (A) is the base case which is supposed to be optimized for higher armature current coverage in the air gap. In case (B) for the longitudinal (LF) machine the slot width w_{sl} is increased to accommodate more copper for the winding. Due to the geometric coupling to the tooth width w_t this leads to a reduced flux path and therefore early tooth saturation. The effect for the current coverage is counter-productive. The comparable design parameter for the transverse flux (TF) design is the winding depth d_w. Increasing d_w does not affect the stator pole width. The only side effect is a slightly increased rotor iron depth that has minimum impact on the machine's performance.

In case (C) the slot height h_{sl} is increased for the LF design or the stator height h_s is increased for the TF design to enlarge the cross-section. This is a feasible route to increase the force density in large machines often used in turbo generators in combination with direct coil cooling. With this approach turbo generators reach force densities between 150 and 200 $\frac{kN}{m^2}$ at pole pitches of $\tau_p = 120$-150 centimeters [5]. Obviously this is not a generally applicable method for any machine design. The main disadvantage is a largely increased machine diameter and large coil leakage across the winding slot due the slim, but high slots. For the TF machine an increase of the stator height h_s changes the flux accumulation layout of the machine, but since the stator height is a free design parameter of the machine it can be adjusted to achieve both, enough space for the winding and a favorable flux accumulation factor. Active rotor transverse flux motors do not have this dependency at all, because the winding is embedded in the magnet-free stator.

The last approach shown in case (D) is to reduce the pole pitch to increase the average current coverage in the air gap. For TF machines that does not produce the desired result because of the reduced winding cross-section. Therefore, standard LF machines usually have pole pitches of 6-12 cm or more [18, 19]. Transverse flux machines do not exhibit this dependency, because the space between the rotor poles only contains filler material and for the stator the permanent magnet height is reduced, but so is the covered area. Hence the current coverage increases for smaller pole pitches and so does the force density F_{Ax} reaching up to 200 $\frac{kN}{m^2}$ for pole pitches of $\tau_p = 5\,mm$. A comparison of achievable

Table 2.2: Typical achievable force densities for LF and TF machines

Motor type	Force Density $\left[\frac{kN}{m^2}\right]$
DC machine	15-25
Synchronous machine	40-60
Induction machine	20-30
Water cooled induction machine	65 (80 short term)
Transverse flux, active rotor	80-200
Transverse flux, passive rotor	80-200
Transverse flux, reluctance	20-40

force densities is given in Table 2.2 [3, 5, 18, 20]. The possible power rating of active rotor tranverse flux motors that have been built or investigated in concept studies ranges from the low kW (10kW) up to 20MW [5, 6].

Another important factor for the small machine size and weight of transverse flux motors is the ring shape of the rotor (or stator if it is a passive rotor machine) compared to the solid cylindric rotor of conventional machines: Referring to Figure 2.6 the active surface of the longitudinal flux machine is $A_{active_{LF}} = 2\pi\, r\, d$. For a cylinder thickness t_r that is small compared to the medium diameter $2r_m$ and assuming $r_m = r$ the active surface for the cylindrical shape of the transverse flux machine is $A_{active_{TF}} = 4\pi\, r_m\, d = 2 A_{active_{LF}}$. This fact, the doubling of the active area for the same diameter, inherently reduces the machine size to one half for transverse flux motors compared to a same power rating longitudinal flux machine.

2.1.2 Transverse flux machine concepts

As mentioned in the introduction transverse flux machines can be built in three generally different ways: The active rotor TFM, the passive rotor TFM with permanent magnets on the stator and the electrically excited TFM [5, 6, 21]-[26]. Figure 2.7 shows that the first two designs are both excited by permanent magnets, but differ in the location of the magnets. They employ two independent fields for the force production and their rotation follows the armature current wave form synchronously. Both machines therefore belong to the general category of synchronous machines. While different active rotor machine designs were investigated in [5], the novel passive rotor machines with permanent

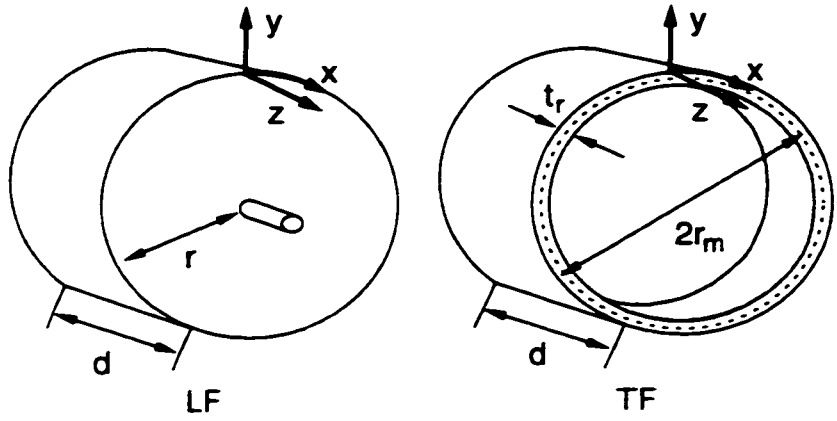

Figure 2.6: Active surface for LF and TF machines

magnets on the stator are the object of this dissertation. The third type, the electrically excited or reluctance transverse flux machine, was analyzed in terms of its construction, control and inverter technology in [6]. This machine is a translation of the switched reluctance motor into a transverse flux equivalent. The machine shares the robustness of the switched reluctance machine and its lower magnetic losses. It also uses the single switch converter technology, because for the unipolar currents used to run this type of machine an H-bridge is not needed. Unlike the classical switched reluctance machine the TF reluctance machine does not suffer from the low force densities and the high weight of the conventional reluctance machines: The TF reluctance machine reaches force densities that are two to three times higher than conventional reluctance machine's force densities bringing it well into the force density range of other conventional machines. A general problem of switched reluctance machines is their rotating torque pulsation due to the different number of rotor and stator poles. These pulsations occur, because at two different rotor positions there are different numbers of poles involved in the torque production. In the electrically excited transverse flux machine this problem does not exist, because at any given time all poles of one rotor strand are involved in the torque production simultaneously. A reluctance transverse flux machine needs at least three independent strands in order to be self-startable because of the sign change of the force produced by one strand after 90° electrical.

In the lower part of Figure 2.7 example designs are given for the different motor types. All transverse flux machines with permanent magnets need a built-in skew between rotor

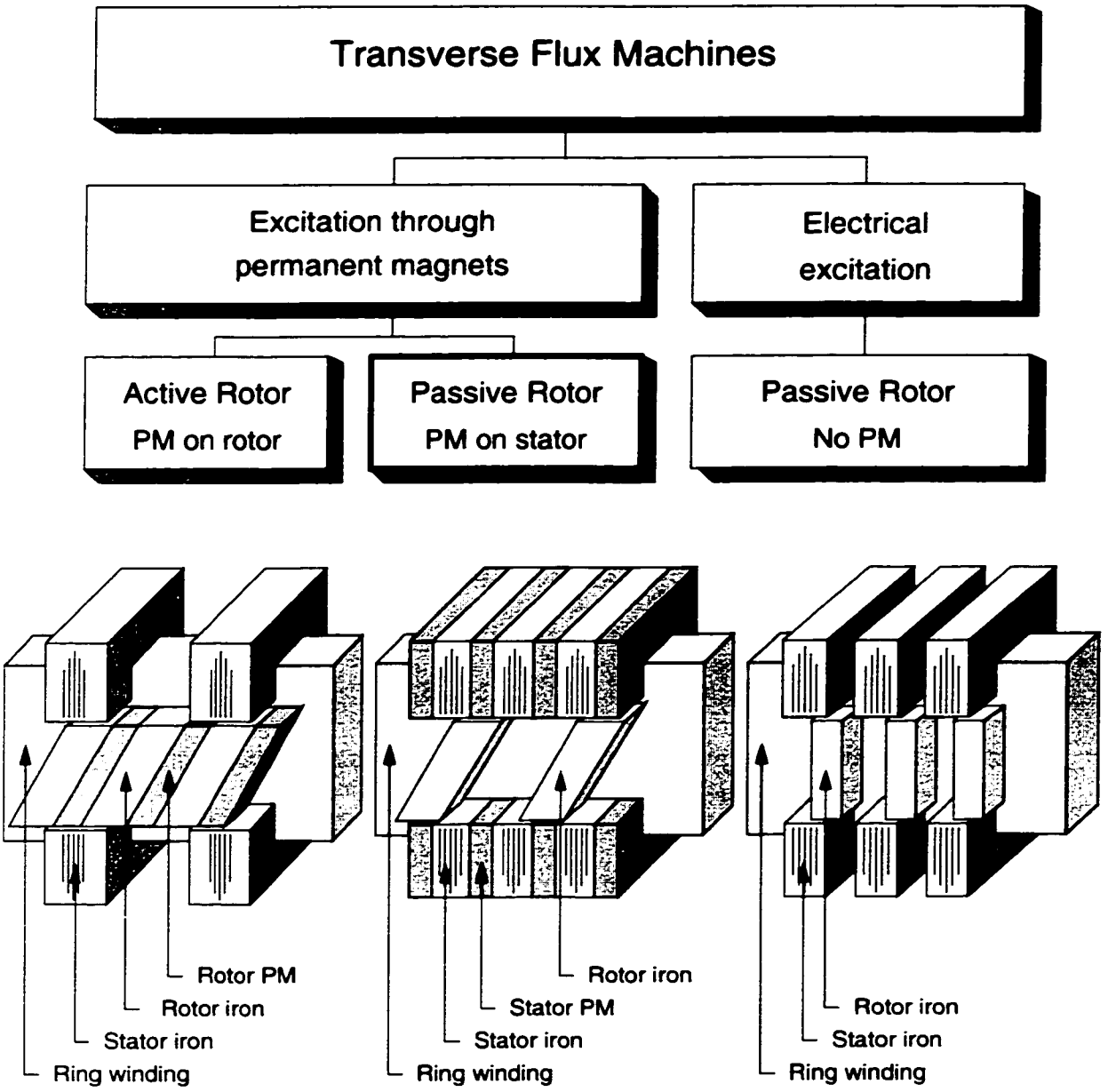

Figure 2.7: Categorization of the transverse flux motor concepts with design examples

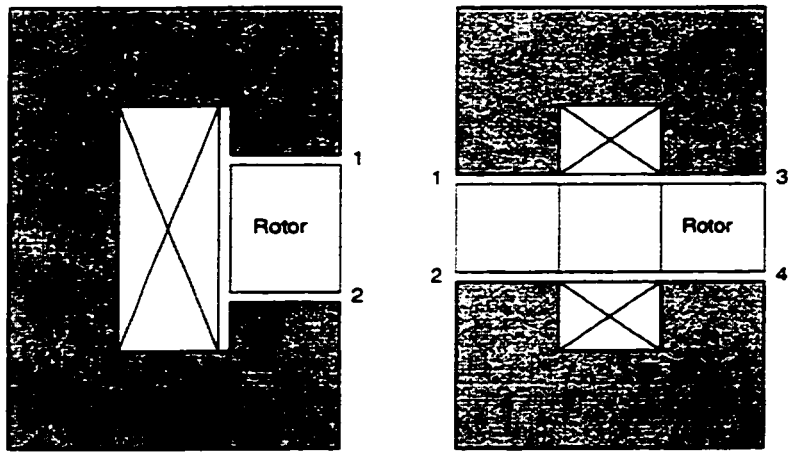

Figure 2.8: Single and double track machine design principles

and stator. Principally this skew can be implemented in the rotor or the stator. In fact, due to the location of the permanent magnets, active rotor machines usually exhibit the skew in the stator, while passive rotor TFMs are built more easily with the skew in the rotor. Figure 2.7 however shows the skew implemented for both cases as a slanted rotor, which makes the required skew most obvious.

Transverse flux motors can be built as single or double track machines. As shown in Figure 2.8 single track machines contain only one magnetically active rotor member which is enclosed by two air gaps. The double track machine consists of two active rotor members enclosed by a total of four air gaps. The advantage of a double track design is that the machine's skew can be implemented by offsetting the two rotor sides by one pole pitch. That way permanent magnets of opposing magnetization direction are mounted in the same angular rotor position providing a closed flux path for the excitation field that is supplied by two magnets. For a detailed description of the flux path for a passive rotor double track machine see Section 2.1.3. Single track machines inherently require more core iron material per active rotor area to close the flux path than double track machines. However, single track layouts can be built into very compact machines by combining two strands into a two-phase machine [28]-[30]. The combination of several independent strands into a multi-phase machine is the method of choice to allow the machines to be self-startable and to reduce torque ripple (see Section 4.3.4). This is achieved by constructing the machine in a way that all rotor segments are mechanically

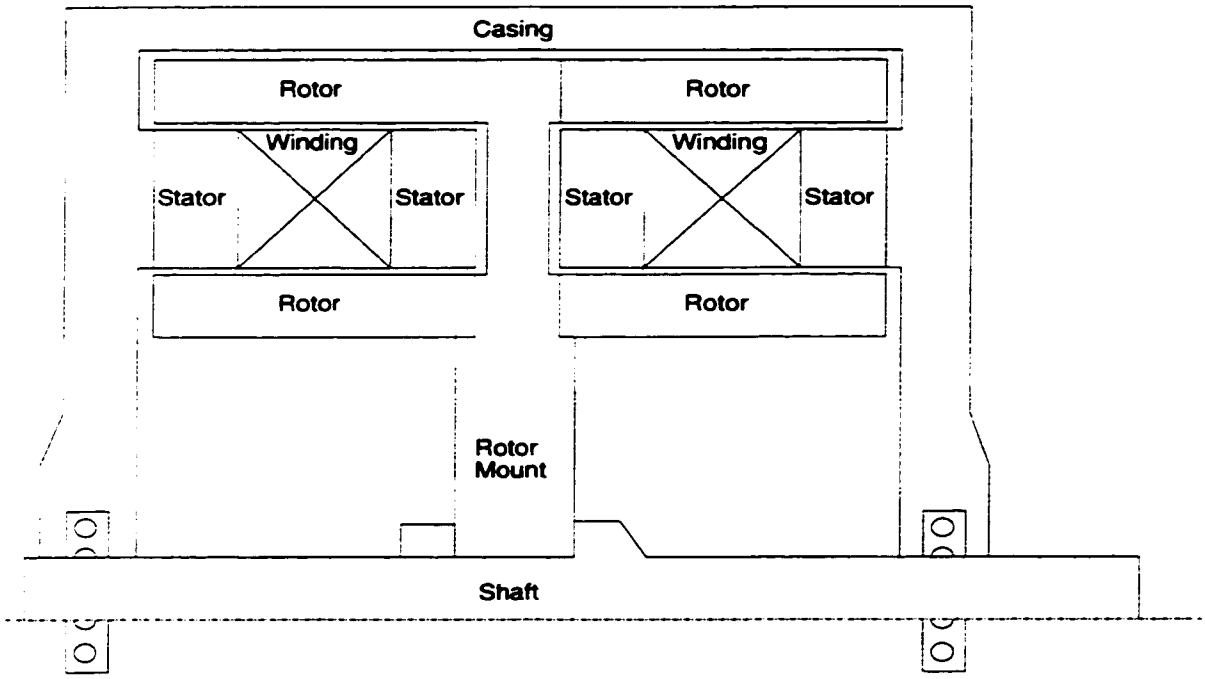

Figure 2.9: Cross section of a two phase *reduced magnet material* machine

connected to the same shaft. In order to achieve self-start capability the independent strands are mounted with a radial offset that is for example equivalent to 90° electrical for a two-phase design or equivalent 60° electrical for a three-phase design. A cross section of a two-phase machine is shown in Figure 2.9.

All transverse flux machines that employ permanent magnets to create the excitation field use the flux accumulation concept. The concept is illustrated in Figure 2.10: With A being the pole width, B its height and C its depth, the permanent magnet area A_{pm} is defined by $A_{pm} = B \cdot C$, while the pole area A_p is defined by $A_p = A \cdot C$. Since A is visibly smaller than B the flux through the pole is accumulated by the flux accumulation factor $C_m = \frac{B}{A}$, such that the flux density in the the pole area B_p is related to the flux density in the permanent magnet B_{pm} through Equation (2.2).

$$B_p = C_m B_{pm} \tag{2.2}$$

Note, that this simplified analysis does not account for any flux leakage.

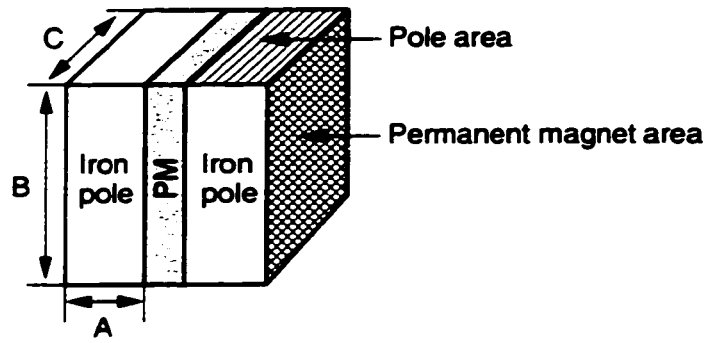

Figure 2.10: Flux accumulation principle for permanent magnets

Active and Passive Rotor Designs

The decoupling of the flux path and the winding requirement facilitates the possibility to build active rotor transverse flux motors in many different ways [5]. The magnets are built into the ring shaped rotor with low flux leakage which reduces the amount of required magnet material. The magnets are enclosed by core iron blocks that are subjected to high hysteresis losses at high operating frequencies generating significant amounts of heat. The location of this heat source on the rotating member of the machine can cause serious heat dissipation problems considering that today's highest performance NdFeB magnets have operating temperatures only up to 110-130°C. To overcome this problem it is desirable to shift the location of the magnets into the stator where they are easily accessible for active fluid cooling. Theoretically this approach is magnetically equivalent to an active rotor design. For the permanent magnet field in the air gap it is not important where it is generated, because it is channeled through the core material to be superimposed with the armature field in the air gap in the same manner. The correctness of this assumption can be seen by comparing the flux linkage with the ring winding of an active rotor machine to the one provided by a passive rotor machine: In both cases the flux linkage shows the same sinusoidal waveform if the rotor is moved over one pole pitch (see [5] and Section 4.2.5).

Changing the location of the permanent magnets implies a straightforward approach for converting an active rotor machine into a passive one, but it appears that none of the suggested magnetic circuit designs for active rotor machines lend themselves to a low magnet use conversion: Figure 2.11 shows a comparison of active (A) and passive

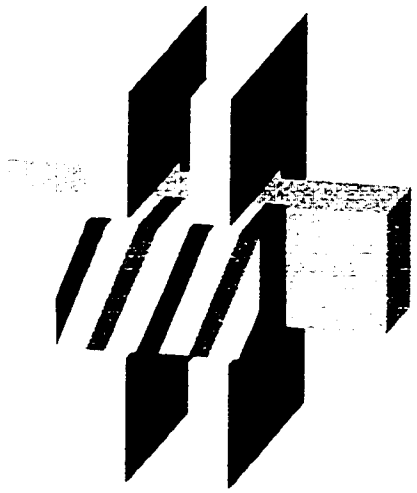

(A1) Skew in the rotor

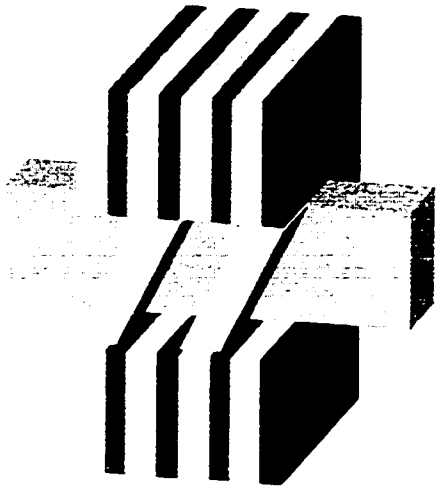

(P1) Skew in the rotor

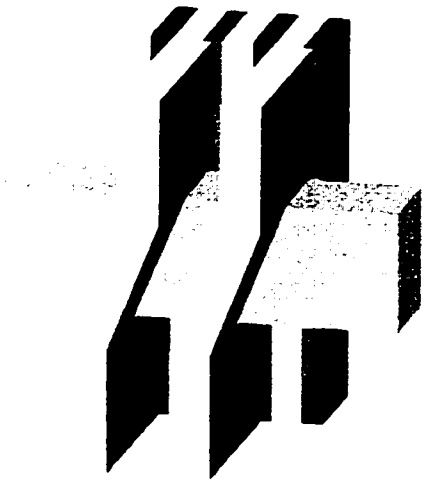

(A2) Skew in the stator

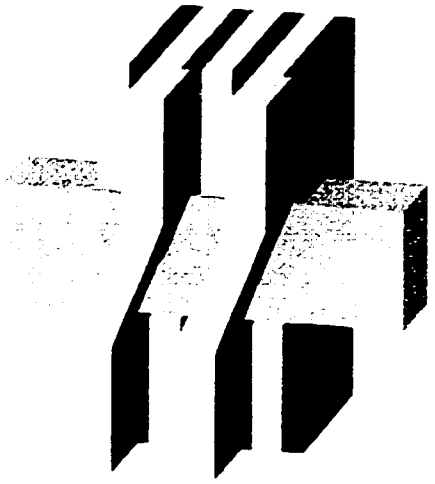

(P2) Skew changed to the rotor

Figure 2.11: Comparison of active and passive rotor designs with permanent magnets on the rotor or the stator 1: Single track machines

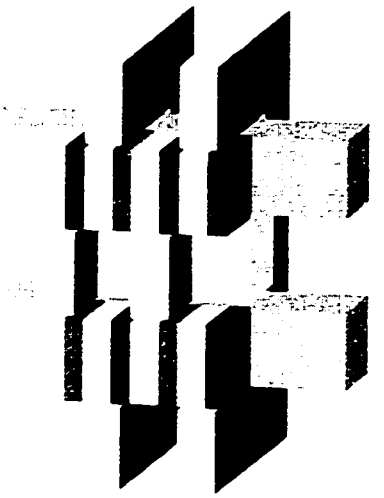

(A3) Vertical track stacking

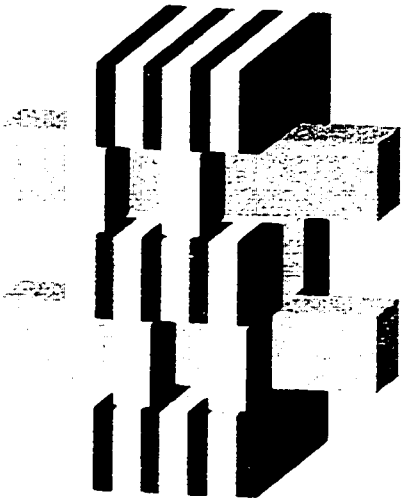

(P3) Vertical track stacking

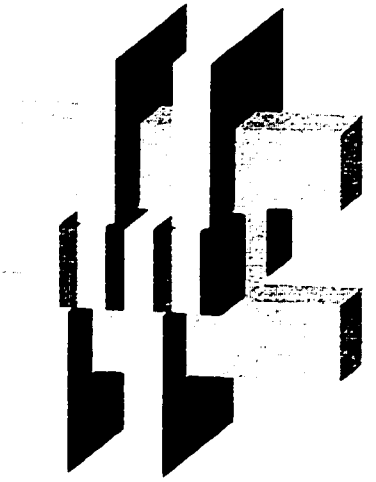

(A4) Horizontal track stacking

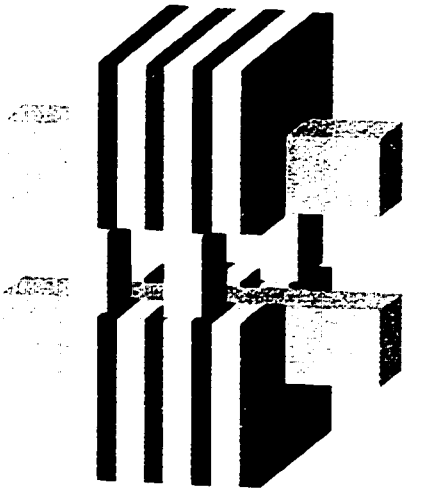

(P4) Horizontal track stacking

Figure 2.12: Comparison of active and passive rotor designs with permanent magnets on the rotor or the stator 2: Double track machines

rotor (P) designs for single track layouts (A1, P1, A2, P2) and 2.12 gives the same comparison for double track designs (A3, P3, A4, P4). While the amounts of iron (shown in light grey) are comparable for the active and the passive rotor designs, the required amounts of magnet material (shown in two darker shades of grey indicating the opposite magnetization directions) are significantly larger for the passive rotor designs derived from existing active rotor machines. This approach also generates a large flux accumulation area such that those designs can use inexpensive ceramic magnets which makes them viable solution non-the-less.

Another approach is to change the location of the ring winding. For single track designs this approach leads to a protruding ring winding enclosed by the moving rotor iron. This introduces the mechanical problem of mounting the ring winding properly and sometimes requires the construction of split rotor designs, which is generally undesirable. For double track machines however it was found that by sandwiching the ring winding between the two stator parts this approach results in a very compact and favorable design that uses the same amounts of permanent magnets as active rotor designs and even requires less core material than any known active rotor design.

2.1.3 Slanted Rotor and Reduced Magnet Material Design

The previously described double track design is one of the two novel passive rotor transverse flux motor designs that are investigated in this dissertation and that is referred to as the *reduced magnet material* design. The second design is a single track machine referred to as the *slanted rotor design*. Both designs are presented below. The slanted rotor design is analyzed in detail in Chapter 3 and the reduced magnet material design is evaluated in depth in Chapter 4.

The Slanted Rotor Design

The slanted passive rotor design investigated here employs inexpensive ceramic magnets on the stator. The stator consists of U-shaped core iron segments and U-shaped magnet layers that form the magnetically active ring of the machine. A pair of one core iron segment and one magnet layer defines one pole pitch τ_p. The permanent magnets provide the excitation field for the machine and change their magnetization direction from

one pole pitch to the next. Embedded at the bottom of the U-shaped stator ring is the armature winding that exhibits a ring shape with a rectangular cross-section and is therefore referred to as the *ring winding*. This term is used for other designs as well since this winding style is a typical characteristic of all transverse flux machines.

The skew needed in all transverse flux designs to work is introduced by the slanted rotor that is enclosed by the U-shaped stator. Figure 2.13 shows a perspective view of the proposed *slanted rotor design*. The stator mount is not shown and the rotor mount is partially cut away to reveal the slanted rotor segments. The rotor and stator segments hidden by the rotor mount are shown in lighter grey and dotted outlines. The rotor is drawn at the rotor position $x = 0.0\,\tau_p$. For all passive rotor transverse flux motors in this dissertation the rotor position $x = 0.0\,\tau_p$ is defined to be the position in which rotor pole and stator pole are directly opposing each other and are accurately centered. The rotor assumes the position $x = 0.5\,\tau_p$ when the stator permanent magnet and the rotor pole centrally oppose each other. The rotor position $x = 1.0\,\tau_p$ is mechanically identical to the position $x = 0.0\,\tau_p$, but the direction of the field of the permanent magnets is reversed. Consequently the rotor position $x = 2.0\,\tau_p$ is mechanically and magnetically identical to the position $x = 0.0\,\tau_p$. In terms of classical machine design one can interpret the position $x = 0.0\,\tau_p$, $x = 0.5\,\tau_p$, $x = 1.0\,\tau_p$ and $x = 2.0\,\tau_p$ as $0°$, $90°$, $180°$ and $360°$ electrical respectively.

The Reduced Magnet Material Design

In the proposed *reduced magnet material* design the stator comprises the front and rear stator halves and the ring winding in between. It is mounted to the casing of the machine. As for the stator of the slanted rotor design the front and rear halves of the stator consist of permanent magnet and core iron layers, where one magnet and one iron layer again define one pole pitch, τ_p. Instead of a U-shaped stator the *reduced magnet material* design has a ring shaped or hollow cylindrical stator with a rectangular cross-section. The magnetization direction of the permanent magnets changes from one pole pitch to the next. The upper and lower halves of the rotor consist of the magnetically active iron poles and electrically and magnetically inactive filler material between the rotor poles shaping the two halves into concentric rings. These rings are mounted to the motor shaft. Figure 2.14 shows the layout of the magnetic circuit of the *reduced*

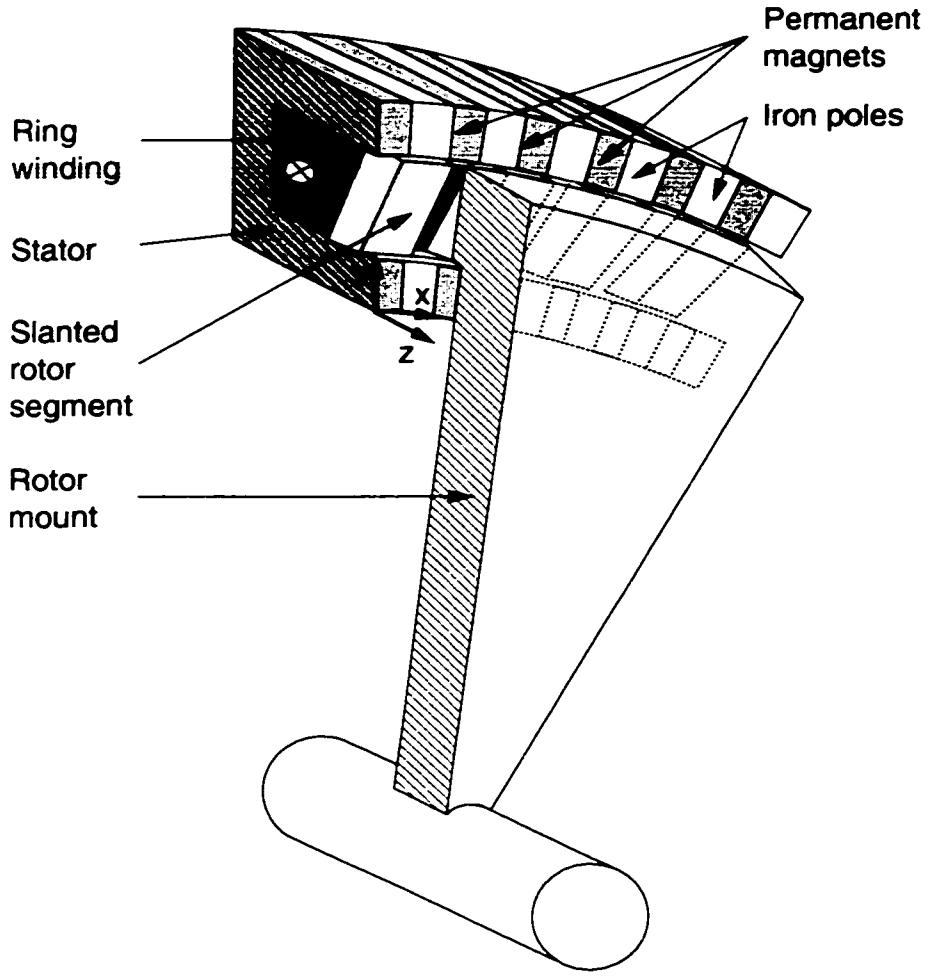

Figure 2.13: Perspective view of the slanted rotor transverse flux motor design shown in rotor position $x = 0.0\,\tau_p$

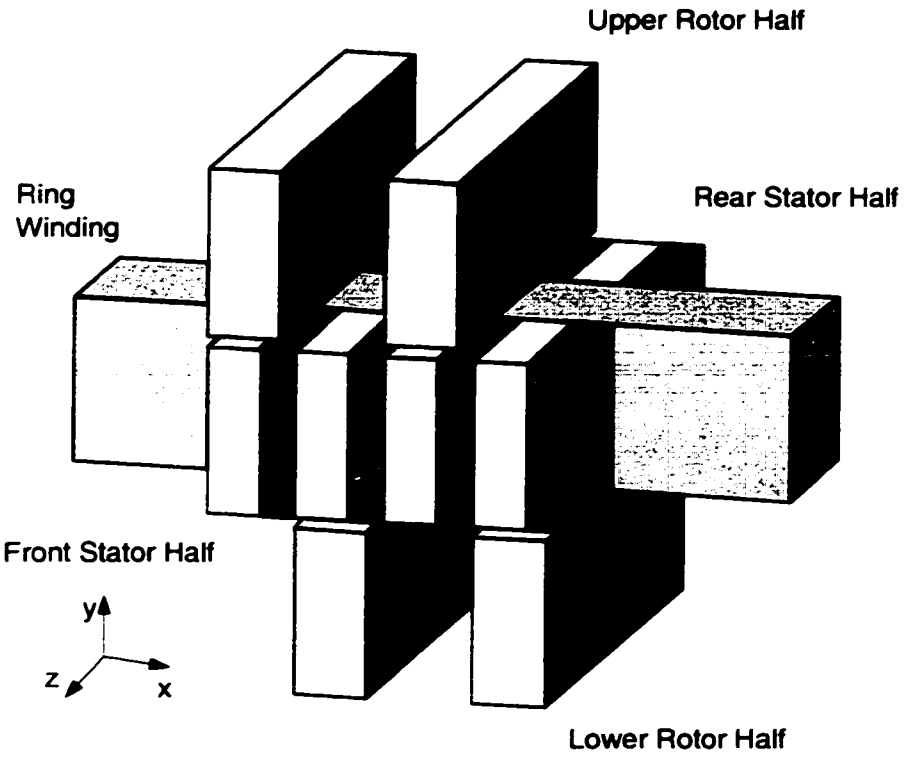

Figure 2.14: Overview of the *reduced magnet material* design

magnet material passive rotor transverse flux motor design in principle. Note, that the filler material on the rotor is not shown. For a perspective view of the reduced magnet material design refer to Figure 2.2.

The magnets at the same x position in the front and rear halves are magnetized in opposite directions to provide a closed flux path for the permanent magnet field at the $x = 0.0\,\tau_p$ rotor position: Starting at the top right rotor part, the flux crosses the air gap vertically, then goes horizontally thorough the permanent magnet that provides one half of the driving m.m.f. and is magnetized in the negative x-direction (triangular arrow) to change the direction again to the vertical passing through the lower air gap. Then the flux crosses over to the rear to follow a similar path there as at the front. Due to the opposite magnetization direction of the rear permanent magnet, which provides the other half of the driving m.m.f., the flux crosses in positive x-direction, closing its path

in the right upper rotor part. At the $x = 0.5\,\tau_p$ rotor position the permanent magnet flux closes locally. The flux only runs through one magnet and crosses the same air gap twice, once on the left half of the rotor pole and once – with the opposite sign – on the right side of the rotor pole. There is no closed flux loop around the ring winding in this position, leading to a zero induced voltage at $x = 0.5\,\tau_p$ (see Section 4.2.5).

The *reduced magnet material* design not only reduces the necessary amounts of magnet material to the same range as needed for active rotor machines, but also reduces the required iron significantly. While the stator of the passive design uses the same amounts of iron as the rotor of the active rotor machines, the material usage in the rotor of the passive rotor machine is only about 70-80% of that in the stator of the active rotor machine, giving it a considerable weight benefit. Notice that rotor and stator change roles going from active rotor to passive rotor motor designs. Figure 2.15 shows the cross section of the *reduced magnet material* passive rotor design at the top and a comparable active rotor design at the bottom. Both models have equivalent ring winding cross section areas to accommodate the same ring winding m.m.f. at the same current density, which ensures their electrical comparability. The passive design's stator parts and the active design's rotor parts must have the same size to achieve the same field flux density in the air gap, because these parts define the size of the permanent magnets. Evaluating the stator and rotor areas which are made of iron for both designs clearly shows the reduced iron usage. The third dimension in both cases is composed in the same way and therefore does not need to be taken into account for this comparison.

2.2 The Finite Element Method for Magnetic Field Calculations

The finite element method originated from mechanical and civil engineering for structural analysis in the 1950s and quickly gained momentum in that area. It took more than 20 years before this method was successfully adapted to and implemented for electromagnetic field problems. The general discretization procedure into finite elements and their solution can be found in [31] -[33] and will not be covered here. Magnetic fields pose the special problem that volume properties can considerably change within the simulated area. Therefore, the governing field equations are presented to provide insight into their

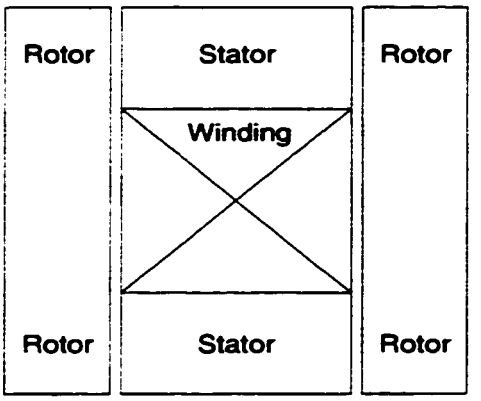

Passive Rotor Design

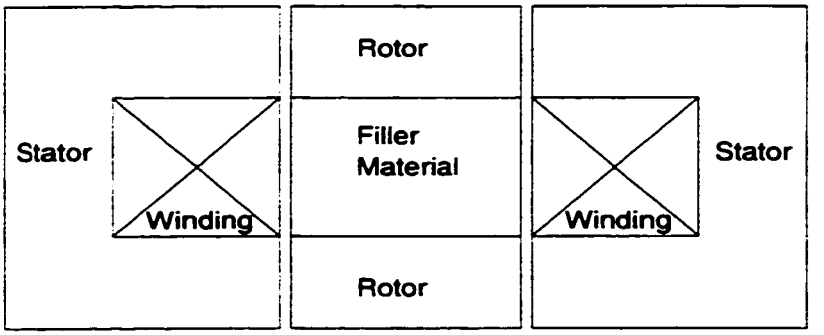

Active Rotor Design

Figure 2.15: Comparison of the core iron use in an active rotor design and the *reduced magnet material* passive rotor design

importance and proper application for the finite element simulation of electromagnetic fields [34]-[37].

2.2.1 Maxwell Equations and Material Regions

Electromagnetic field problems can be described by the Maxwell Equations (2.3)-(2.6) and the constitutive relations (2.7, 2.8) describing the material properties [38, 39]. Equation (2.3) gives the generalized Ampere's law or the first Maxwell equation describing the relationship between the magnetic field strength vector $\{H\}$, the total current density vector $\{J\}$ and the partial derivative of the electric flux density vector $\{D\}$, also known as the displacement current density. $\nabla\times$ represents the curl operator, $\nabla\cdot$ the divergence operator and ∇ applied to a scalar stands for the gradient operator. The total current density can be further split into the applied source current density vector $\{J_s\}$ and the induced eddy current vector $\{J_e\}$. In magnetostatic analysis $\{J_e\}$ is zero. Equation (2.4) is Maxwell's formulation of Faraday's induction law, where $\{E\}$ is the electric field intensity vector and $\{B\}$ is the flux density vector. Equation (2.5) states the requirement that all magnetic fields are point-source free and Equation (2.6) is the generalization of Coulomb's law extended for moving charges expressing the conservation of the electric charges, where ρ is the electric charge density.

$$\nabla \times \{H\} = \{J\} + \left\{\frac{\partial D}{\partial t}\right\} = \{J_s\} + \{J_e\} + \left\{\frac{\partial D}{\partial t}\right\} \tag{2.3}$$

$$\nabla \times \{E\} = -\left\{\frac{\partial B}{\partial t}\right\} \tag{2.4}$$

$$\nabla \cdot \{B\} = 0 \tag{2.5}$$

$$\nabla \cdot \{D\} = \rho \tag{2.6}$$

Equation (2.7) describes the magnetic constitutive relation for non-permanent magnetic materials such as iron, and Equation (2.8) or (2.9) for the case of permanent magnets, where $\{M_0\}$ is the remanent intrinsic magnetization vector, and $[\nu] = [\mu]^{-1}$ is the reluctivity matrix.

$$\{B\} = [\mu]\{H\} \tag{2.7}$$

$$\{B\} = [\mu]\{H\} + \mu_0\{M_0\} \tag{2.8}$$
$$\{H\} = [\nu]\{B\} - \mu_0[\nu]\{M_0\} \tag{2.9}$$

The magnetic permeability $[\mu]$ is generally a function of $\{H\}$ and is given as BH-curves. It may also be a function of the temperature, but this feature is rarely implemented in finite element analysis programs, because it requires a coupled electromagnetic-thermal analysis. If permeability is a function of the magnetic field strength, it is described as in (2.10) allowing for anisotropic materials. The matrix only contains values on its main diagonal, because the material's permeabilities in the different coordinate directions are not coupled. If the material in a design is not aligned to the Cartesian coordinates, transformation matrices are used to rotate the property matrix into the correct position. The transformation matrices are given through a set of angular coordinates during the model definition phase. For isotropic materials Equation (2.10) reduces to a scalar function of the magnetic field strength and for linear materials the functional dependency is eliminated.

$$[\mu] = \mu_0 \begin{bmatrix} \mu_{rx}(H) & 0 & 0 \\ 0 & \mu_{ry}(H) & 0 \\ 0 & 0 & \mu_{rz}(H) \end{bmatrix} \tag{2.10}$$

The constitutive relations for the electric field are given in Equations (2.11) and (2.12), where $[\sigma]$ is the electrical conductivity matrix that has the format given in (2.13) and $[\epsilon]$ is the permittivity matrix that takes on the format given in (2.14).

$$\{J\} = [\sigma]\{E\} \tag{2.11}$$

$$\{D\} = [\epsilon]\{E\} \tag{2.12}$$

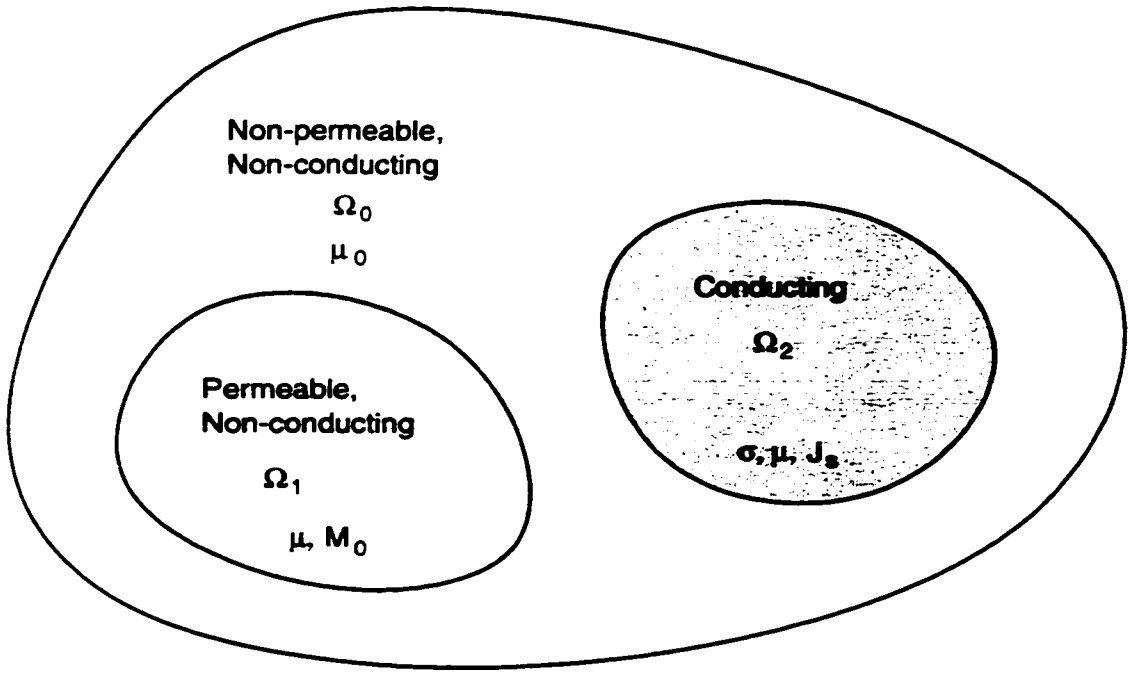

Figure 2.16: Visualization of the material regions Ω_0-Ω_2 for the finite element analysis of electromagnetic fields

$$[\sigma] = \begin{bmatrix} \sigma_{xx} & 0 & 0 \\ 0 & \sigma_{yy} & 0 \\ 0 & 0 & \sigma_{zz} \end{bmatrix} \tag{2.13}$$

$$[\epsilon] = \begin{bmatrix} \epsilon_{xx} & 0 & 0 \\ 0 & \epsilon_{yy} & 0 \\ 0 & 0 & \epsilon_{zz} \end{bmatrix} \tag{2.14}$$

Figure 2.16 shows the three types of regions Ω_0-Ω_2 that are treated differently in the finite element analysis of electromagnetic fields: Non-permeable regions, Ω_0, usually containing air are characterized by μ_0, permeable and non-conduction regions, Ω_1, that are used for the permanent magnets and core iron are described by the parameters μ and M_0 and conducting regions Ω_2 for the winding are defined by its values of σ, μ and J_s. Usually permeable and conduction regions are enclosed by air regions for simulation purposes as indicated in the figure.

2.2.2 2D Magneto-Static Analysis

For 2D finite element analyses, the vector potential as defined in (2.15) is the approach of choice because for two dimensional fields the vector reduces to only the A_z value provided that the field extends in the xy-plane.

$$\{B\} \equiv \nabla \times \{A\} \tag{2.15}$$

According to [39], applying the vector potential definition (2.15) to (2.4) yields the equation for the electric field intensity vector shown in (2.16), where ∇V is the gradient of the electric scalar potential. The time dependant term is zero for the magnetostatic analysis, but non-zero if a pseudo-stationary solution is required.

$$\{E\} = -\left\{\frac{\partial A}{\partial t}\right\} - \nabla V = -\nabla V \tag{2.16}$$

Note that the vector potential automatically satisfies the source free requirement (2.5), because divergence of the curl of any vector $\nabla \cdot (\nabla \times \{A\})$ is always zero. For magnetostatic analysis there are no displacement currents which reduces Maxwell's version of Ampere's law to the expression in Equation (2.17) and eliminates the extended Coulomb law (2.6) as well as Faraday's law (2.4) from the analysis. Note, that for pseudo-stationary solutions the latter can not be eliminated. The complete set of the Maxwell equations for magnetostatic fields therefore only consists of the two Equations (2.17) and (2.18).

$$\nabla \times \{H\} = \{J\} \tag{2.17}$$

$$\nabla \cdot \{B\} = 0 \tag{2.18}$$

Note that for the pseudo-stationary case, (2.18) would remain as in (2.5). The magnetic and electrical constitutive relations in (2.7, 2.8) and (2.11, 2.12) remain unchanged.

By using the vector potential $\{A\}$ instead of the flux density $\{B\}$ to describe the field a non-uniqueness is introduced which can be observed if one considers the vector potential $\{A'\} = \{A\} + \nabla\Phi$, where Φ can be any scalar field. Applying the curl to $\{A'\}$ one finds that $\nabla \times \{A'\} = \nabla \times \{A\}$, because $\nabla \times (\nabla\Phi) = 0$. This non-uniqueness

has to be eliminated through gauging. For magnetostatic problems the Coulomb gauge $\nabla \cdot \{A\} = 0$ is used [40]. The magnetostatic field analysis introduces the additional constraint that the current density must be divergence- or source-free (2.19) in the conducting regions, because the charge density does not change over time for a static current [40].

$$\nabla \cdot \{J\} + \frac{\partial \rho}{\partial t} = \nabla \cdot \{J\} = 0 \tag{2.19}$$

For conducting regions Ω_2 the vector potential solution is found by solving Ampere's law (2.17) in terms of the vector potential and the constitutive equations and satisfying the source free condition for the current density. Both equations are given in (2.20) for the pseudo-stationary case and in (2.21) for the static case, where $\nu_e = \frac{1}{3}\text{tr}\,[\nu] = \frac{1}{3}(\nu_{xx} + \nu_{yy} + \nu_{zz})$ is the trace of the reluctivity matrix.

$$\left.\begin{array}{c} \nabla \times [\nu]\ \nabla \times \{A\} - \nabla \nu_e \nabla \cdot \{A\} + [\sigma] \left\{\frac{\partial A}{\partial t}\right\} + [\sigma]\ \nabla V = \{0\} \\ \nabla \cdot \left(-[\sigma] \left\{\frac{\partial A}{\partial t}\right\} - [\sigma]\ \nabla V\right) = \{0\} \end{array}\right\} \text{ in } \Omega_2 \tag{2.20}$$

Note that by choosing the Coulomb gauge, the divergence of the vector potential is zero.

$$\left.\begin{array}{c} \nabla \times [\nu]\ \nabla \times \{A\} + [\sigma]\ \nabla V = \{0\} \\ \nabla \cdot (-[\sigma]\ \nabla V) = \{0\} \end{array}\right\} \text{ in } \Omega_2 \tag{2.21}$$

For non-conducting regions only Ampere's law must be satisfied with Equation (2.22) [39].

$$\nabla \times [\nu]\ \nabla \times \{A\} - \nabla \nu_e \nabla \cdot \{A\} = \nabla \times [\nu]\ \nabla \times \{A\} = \nabla \times \mu_0\ [\nu]\ \{M_0\} \text{ in } \Omega_0, \Omega_1 \tag{2.22}$$

The vector potential for the magnetostatic two dimensional finite element analysis only requires the solution for one vector potential component which leads to fast and accurate solutions. The equations for the two-dimensional, magnetostatic case can be deducted by calculating (2.21) and (2.22) for the magnetic vector potential containing only a z-component $\{A\} = \left\{\begin{array}{ccc} 0 & 0 & A_z \end{array}\right\}^T$ and the intrinsic magnetization only having

an x- and y-component $\{M_0\} = \left\{ \begin{array}{ccc} M_x & M_y & 0 \end{array} \right\}^T$. Furthermore all partial derivatives in z-direction are zero, because all 2D calculations are strictly homogeneous in z-direction. For conducting areas Ω_2 the derivation is given in (2.23)-(2.29) for constant reluctivity ν_{xx} and ν_{yy}. In the case of non-linear reluctivity ($\nu_{xx} = f(A_z)$ and $\nu_{yy} = f(A_z)$) the second curl operator would introduce extra addends by applying the product rule for derivatives.

$$\nabla \times [\nu] \nabla \times \{A\} = \nabla \times [\nu] \nabla \times \left\{ \begin{array}{c} 0 \\ 0 \\ A_z \end{array} \right\} \tag{2.23}$$

$$= \nabla \times [\nu] \begin{vmatrix} e_x & e_y & e_z \\ \frac{\partial}{\partial x} & \frac{\partial}{\partial y} & \frac{\partial}{\partial z} \\ 0 & 0 & A_z \end{vmatrix} \tag{2.24}$$

$$= \nabla \times \left[\begin{array}{ccc} \nu_{xx} & 0 & 0 \\ 0 & \nu_{yy} & 0 \\ 0 & 0 & \nu_{zz} \end{array} \right] \left\{ \begin{array}{c} \frac{\partial A_z}{\partial y} \\ -\frac{\partial A_z}{\partial x} \\ 0 \end{array} \right\} \tag{2.25}$$

$$= \nabla \times \left\{ \begin{array}{c} \nu_{xx} \frac{\partial A_z}{\partial y} \\ -\nu_{yy} \frac{\partial A_z}{\partial x} \\ 0 \end{array} \right\} \tag{2.26}$$

$$= \begin{vmatrix} e_x & e_y & e_z \\ \frac{\partial}{\partial x} & \frac{\partial}{\partial y} & \frac{\partial}{\partial z} \\ \nu_{xx} \frac{\partial A_z}{\partial y} & -\nu_{yy} \frac{\partial A_z}{\partial x} & 0 \end{vmatrix} \tag{2.27}$$

$$= \left\{ \begin{array}{c} 0 \\ 0 \\ -\nu_{yy} \frac{\partial^2 A_z}{\partial x^2} - \nu_{xx} \frac{\partial^2 A_z}{\partial y^2} \end{array} \right\} \tag{2.28}$$

$$= \left\{ \begin{array}{c} 0 \\ 0 \\ -J_z \end{array} \right\} \tag{2.29}$$

The equation lines (2.28) and (2.29) can be written as a single scalar equation of Poisson type shown in Equation (2.30), where J_z is the z-component of the current

density.

$$\nu_{yy}\frac{\partial^2 A_z}{\partial x^2} + \nu_{xx}\frac{\partial^2 A_z}{\partial y^2} = J_z \tag{2.30}$$

A similar derivation for the intrinsic magnetization delivers the scalar differential Equation (2.31) for permanent magnet materials.

$$\nu_{yy}\frac{\partial^2 A_z}{\partial x^2} + \nu_{xx}\frac{\partial^2 A_z}{\partial y^2} = \mu_0\left(\nu_{yy}\frac{\partial M_y}{\partial x} - \nu_{xx}\frac{\partial M_x}{\partial y}\right) \tag{2.31}$$

In non-permanent-magnetic material without intrinsic magnetization such as iron core material Equation (2.31) further reduces to the Laplace type equation given in (2.32).

$$\nu_{yy}\frac{\partial^2 A_z}{\partial x^2} + \nu_{xx}\frac{\partial^2 A_z}{\partial y^2} = 0 \tag{2.32}$$

The finite element solution employs a variational approach minimizing the stored field energy W_m. For the 2D linear magnetostatic case described above the energy stored at any point in the field is calculated by Equation (2.33). For non-linear reluctivity the coenergy $W_c = \int \{B\}\ \mathrm{d}\ \{H\}$ has to be taken into account as well giving a total energy $W_t = 2W_m - W_c$ [41].

$$W_m = \frac{1}{2}\{B\}\{H\} = \frac{1}{2\mu}(\{B\})^2 \tag{2.33}$$

The variational formulation for the linear 2D case for conducting material then can be found by integrating over the complete simulation area (volume for 3D) as given in Equation (2.34) [17].

$$F(A_z) = \int\left(\nu\left[\left(\frac{\partial A_z}{\partial x}\right)^2 + \left(\frac{\partial A_z}{\partial y}\right)^2\right] - 2A_z J_z\right)\mathrm{d}A \tag{2.34}$$

Forming the coefficient matrices $[K]$ and the load matrices $[J_i]$ for the finite element discretization leads to the solution for the discrete nodal vector potentials $\{A_e\}$ [39]. From that solution the magnetic flux density vector is found using (2.35), where $[N_A]$ are the shape functions.

$$\{B\} = \nabla \times [N_A]^T \{A_e\} \tag{2.35}$$

The whole area of interest Ω can be solved using one potential. Material differences are handled internally, which makes the vector potential versatile and easy to use. However, for a three-dimensional field problem the system must be solved completely for all three potentials A_x, A_y and A_z. That makes this method computationally very expensive, especially because of the largely increased number of elements in three dimensional FEA problems. Therefore, the scalar potential approach is often used for three-dimensional field problems as described in the next section.

2.2.3 3D Magneto-Static Analysis

The scalar potential approach has the advantage that the solution only requires the determination of a scalar field solution for 3D problems. The governing equations are the same as in the vector potential case for the magnetostatic fields. But instead of introducing a vector potential for $\{B\}$, for use with the scalar potential, the magnetic field strength vector $\{H\}$ is split into a magnetization field strength $\{H_m\}$ and a conductor (source) field intensity $\{H_s\}$ as given in (2.36) [42, 43].

$$\{H\} = \{H_m\} + \{H_s\} \tag{2.36}$$

$\{H_s\}$ can be directly evaluated using the Biot-Savart formulation on the current carrying volumes V_c as given in (2.37).

$$\{H_s\} = \frac{1}{4\pi} \int_{V_c} \frac{\{J_s\} \times \{r\}}{|\{r\}|^3} \, \mathrm{d}V_c \tag{2.37}$$

To find the magnetization field strength vector $\{H_m\}$ the reduced scalar potential Φ_m is introduced as shown in (2.38)

$$\{H_m\} \equiv -\nabla \Phi_m \tag{2.38}$$

With the constitutive Equation (2.8) the source-free Equation (2.5) for $\{B\}$ can be written in terms of the reduced scalar potential and the Biot-Savart equation as in (2.39).

$$\nabla \cdot [\mu] \nabla \Phi_m - \nabla \cdot [\mu] \left(\frac{1}{4\pi} \int_{V_c} \frac{\{J_s\} \times \{r\}}{|\{r\}|^3} \, \mathrm{d}V_c \right) - \nabla \cdot \mu_0 \{M_0\} = \{0\} \tag{2.39}$$

Equation (2.39) suggests that this approach would deliver a field solution for the complete region of interest Ω, for permeable and non-permeable regions. Experiments however have shown that this method suffers from high inaccuracy in permeable regions [32, 42, 43]. The explanation for this observation is that $\{H_s\}$ is calculated directly from the integral in (2.37) while Φ_m is only calculated at discrete finite element points. This causes unwanted field cancellations and leads to the inaccuracies. Therefore, the reduced scalar potential cannot be used in high-permeability materials. To circumvent this problem the realistic assumption is made, that highly permeable materials do not contain current source elements meaning that $\{H_s\}$ is zero in those areas so that (2.36) becomes $\{H\} = \{H_m\}$. For those regions the total scalar potential Ψ_t is introduced in Equation (2.40) [39, 42, 44].

$$\{H\} \equiv -\nabla \Psi_t \tag{2.40}$$

Again writing the source-free condition using the constitutive equation yields the solving equation for Ψ_t shown in (2.41).

$$\nabla \cdot [\mu] \nabla \{\Psi_t\} - \mu_0 \{M_0\} = \{0\} \tag{2.41}$$

In order to calculate the fields from the current density within the highly permeable material as well, the reduced potential is evaluated for the permeable/non-permeable interface elements and propagated into the permeable material through the $\{B\}$ and $\{H\}$ continuity conditions given in (2.42), where the index 't' stands for tangential, 'n' for normal, 'non' for the non-permeable and 'perm' for the highly permeable material.

$$H_{t_{non}} = H_{t_{perm}} \qquad B_{n_{non}} = B_{n_{perm}} \tag{2.42}$$

These results are crucial for the practical use of finite element software packages that use the scalar potential approach such as the Vector Field Opera 3D package[1] [42]. From the above equations and insights one can derive three important guidelines for the practical use of finite element software packages using the scalar potential approach to insure accurate solution: (a) All regions containing a winding must use the reduced scalar potential, (b) All highly permeable regions (core iron) must use the total scalar potential

[1]This package is used for the three-dimensional finite element analysis in this dissertation.

and (c) Magnets should use total potential since they are current density free.

2.2.4 Force Calculation Methods

There are two methods to determine the force exerted on a solid in the simulation space; (1) the virtual work approach often used for mechanical problems adapted for electromagnetic fields, and (2) the Maxwell stress tensor approach. Both calculate the total force experienced by the solid: The total force may be caused by reluctance forces and/or forces caused by the interaction of two fields since only the resulting fields are used for the calculations, which makes no assumption about their origin.

Force Calculation using the Virtual Work Approach

Calculating the forces using the virtual work approach requires determining the derivative of the magnetic field energy versus the virtual displacement using Equation (2.43) for the air elements surrounding the solid body of interest [39]. F_s is the force in the direction of the selected coordinate s, which can be the x-, y- or z-coordinate direction for Cartesian coordinates. V_s then is the volume of the air element neighboring the solid of interest.

$$F_s = \int_{V_s} \{B\}^T \left\{ \frac{\partial H}{\partial s} \right\} \mathrm{d}V_s + \int_{V_s} \frac{\partial}{\partial s} \left(\int \{B\}^T \{\mathrm{d}H\} \right) \mathrm{d}V_s \qquad (2.43)$$

This method has several drawbacks: Firstly, it requires that there be an air space surrounding the entire area of interest. That may not always be possible if the ferromagnetic part interfaces with a permanent magnet for example. Secondly, experiments show (see Chapter 3) that the air elements surrounding the region of interest must be all of uniform thickness and irregular finite element mesh geometries must be avoided in order to yield accurate results. Therefore, this method is generally not recommended for accurate calculations unless the requirements above are met meticulously.

Force Calculation using the Maxwell Stress Tensor Approach

The Maxwell stress tensor allows one to evaluate the stresses exerted on ferromagnetic surfaces. The magnetic flux density is evaluated directly on the air side of the surface elements without the requirement of a uniform surrounding air layer. In fact, a method

exists [41] for calculating the Maxwell stress tensor even within core iron materials by assuming an infinitely small air gap within the material and evaluating only the magnetic field strength vector $\{H\}$, that way eliminating the effects of the irons high relative permeability.

In Equations (2.44)-(2.46) the Maxwell stress tensor is integrated over the surface to calculate the forces for the three coordinate directions, where A_s is the surface of interest, $\{n\}$ a vector normal to that surface and B_x, B_y, B_z and n_x, n_y, n_z the components of $\{B\}$ and $\{n\}$ respectively.

$$F_x = \int_{A_s} \left(\frac{1}{\mu} B_x \left(\{B\} \cdot \{n\} \right) - \frac{1}{2\mu} \left| \{B\} \right|^2 n_x \right) \, \mathrm{d}A_s \tag{2.44}$$

$$F_y = \int_{A_s} \left(\frac{1}{\mu} B_y \left(\{B\} \cdot \{n\} \right) - \frac{1}{2\mu} \left| \{B\} \right|^2 n_y \right) \, \mathrm{d}A_s \tag{2.45}$$

$$F_z = \int_{A_s} \left(\frac{1}{\mu} B_z \left(\{B\} \cdot \{n\} \right) - \frac{1}{2\mu} \left| \{B\} \right|^2 n_z \right) \, \mathrm{d}A_s \tag{2.46}$$

This method produces more accurate results than the virtual work method in most cases because of the larger independence on the finite element discretization. For calculations neglecting saturation and cases where the solid of interest has pointed edges or corners, it is advisable to avoid the almost singular fields at those points by displacing the integration surface slightly away from the iron surface. The Maxwell stress tensor is generally preferred for force calculations on highly permeable materials because of its straightforward application.

Chapter 3

Slanted Rotor Transverse Flux Motor Design

The proposed *slanted rotor design* is chosen as a typical representative of single track passive rotor transverse flux motors. This design lends itself to a two- and three-dimensional finite element analysis because of the stator's uniformity in the third dimension which is important for the two-dimensional analysis. To insure that the finite element modeling results are not flawed by modeling errors, reluctance models are derived for the permanent magnet and the ring winding field for the linear, saturation-free case. The two-dimensional finite element analysis allows one to verify the assumptions of the locations of the concentrated reluctances by comparing them with the flux line solutions from the finite element analysis. The three-dimensional finite element analysis solutions are compared to the quantitative field solutions from the linear reluctance model. The three-dimensional finite element analysis is also used to calculate the force densities and evaluate saturation effects on the *slanted rotor design*.

3.1 Analytical Study based on Linear Reluctance Models

To model a complicated three-dimensional magnetic structure such as the one from the *slanted rotor design*, it is necessary to have a sufficient knowledge of the flux distribution

within the system. While it is fairly straightforward to model simple geometries in terms of concentrated linear reluctances, the geometry here poses a more challenging problem because of various cross-couplings between the rotor and the stator. To cope with this problem, after identifying the major flux paths within the geometries for different rotor positions of the motor and assigning concentrated reluctances to them, the reluctances are separately approximated using reluctance equations for simple geometries that reflect the physical geometry. From this geometrical reluctance model the equivalent circuit is derived allowing the use of linear network analysis techniques to determine the flux components in each reluctance.

The flux distributions caused by the ring winding and by the permanent magnets are investigated separately. For both sources the $x = 0.0\,\tau_p$ and the $x = 0.5\,\tau_p$ positions are analyzed. For the permanent magnets these are the positions of the maximum (at $x = 0.0\,\tau_p$ or $x = 1.0\,\tau_p$) and the minimum (at $x = 0.5\,\tau_p$) permanent magnet flux through the stator, which can be used to determine the no-load field e.m.f. of the machine at nominal speed (see Section 4.2.5). In the stator field cases the two positions can be used to determine the static inductances of the ring winding when the rotor moves over one pole pitch.

All models are concerned with the same $2\,\tau_p$ sections as the finite element models. The symmetry from the finite element models is retained by connecting the left and right side to each other in the reluctance model.

To visualize the geometries more clearly for the identification of the main flux paths, the graphs in Figures 3.1, 3.4, 3.6 and 3.8 are not drawn as circular sections but rather as rectangles. Nevertheless, for the calculations the exact different dimensions for the inner and the outer air gap radii are used as they appear in the real circular geometry.

3.1.1 Ring Winding Fields

The main flux paths generated by the ring winding are identified through the reluctances in Figure 3.1 for the $x = 0.0\,\tau_p$ rotor position and in Figure 3.4 for the $x = 0.5\,\tau_p$ rotor position. In the third dimension the ring winding flux closes through the permanent magnets between the stator poles. The permanent magnet gap causes a reluctance $R_{ppm}||R_{pp\sigma}$, which describes the pole-to-pole reluctance R_{ppm} in parallel with the pole-to-pole leakage reluctance $R_{pp\sigma}$. Additional pole-to-rotor leakage occurs at the left and

the right side of the rotor as indicated by R_{pral}, R_{prar}, R_{pril} and R_{prir}. To visualize the symmetry at the left and the right side of the model, R_{pp}, $R_{pp\sigma}$, R_{prar} and R_{pril} are drawn at each of the symmetry boundaries in full, but are cut in half by the dotted symmetry boundary line. Thus, each side only accounts for one half of the total respective reluctance for the calculation.

Position $x = 0.0\,\tau_p$

Each iron stator pole encloses the ring winding. In the reluctance model this is reflected by a m.m.f. source Θ_r connected to each stator pole. As mentioned above, the inner and the outer air gap reluctances are different due to the circular geometry, but both consist of a main reluctance of the fully covered pole areas ($R_{\delta af}$, $R_{\delta if}$ respectively) and two leakage reluctances ($R_{\delta a\sigma}$, $R_{\delta i\sigma}$ respectively).

Figure 3.2 shows the equivalent circuit derived directly from Figure 3.1. To reduce the order of the system for the analysis, reluctances that are magnetically parallel in Figure 3.1 are combined into single reluctances according to Equations (3.1)-(3.5).

$$R_{\delta a} = \frac{1}{2} R_{\delta a\sigma} || R_{\delta af} \tag{3.1}$$

$$R_{\delta i} = \frac{1}{2} R_{\delta i\sigma} || R_{\delta if} \tag{3.2}$$

$$R_{pra} = R_{pral} || R_{rpar} \tag{3.3}$$

$$R_{pri} = R_{pril} || R_{rpir} \tag{3.4}$$

$$R_{pp} = \frac{1}{2} \left(R_{ppm} || R_{pp\sigma} \right) \tag{3.5}$$

Applying the equivalent of Kirchhoff's Voltage law to the mesh fluxes Φ_1, Φ_2, Φ_3 and Φ_4 in Figure 3.2, which is permissible because of the assumption of linearity, the four mesh flux Equations (3.6)-(3.9) are deducted.

$$(R_{pp} + R_{\delta a} + R_{pra}) \cdot \Phi_1 - R_{pra} \cdot \Phi_2 + R_{\delta a} \cdot \Phi_3 = 0 \tag{3.6}$$

$$-R_{pra} \cdot \Phi_1 + (R_{\delta i} + R_{pra}) \cdot \Phi_2 + R_{\delta i} \cdot \Phi_4 = \Theta_r \tag{3.7}$$

$$R_{\delta a} \cdot \Phi_1 + (R_{\delta a} + R_{pri}) \cdot \Phi_3 - R_{pri} \cdot \Phi_4 = \Theta_r \tag{3.8}$$

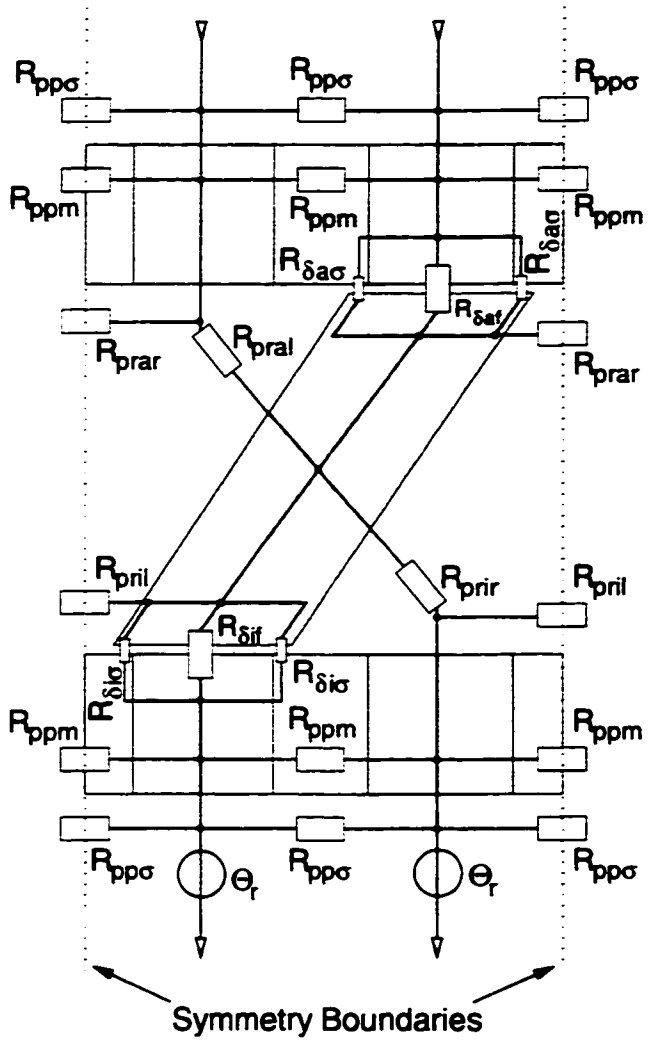

Figure 3.1: Linear reluctance model for the ring winding field at rotor position $x = 0.0\,\tau_p$ showing the concentrated reluctances and the model symmetry of the *slanted rotor design*

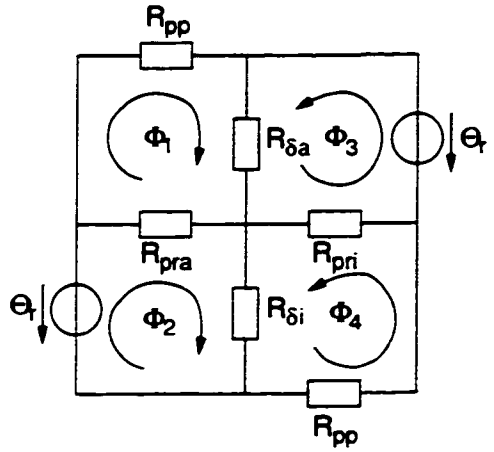

Figure 3.2: Equivalent circuit of the linear reluctance model for the ring winding field at position $x = 0.0\,\tau_p$

$$R_{\delta i} \cdot \Phi_2 - R_{pri} \cdot \Phi_3 + (R_{pp} + R_{\delta i} + R_{pri}) \cdot \Phi_4 \;=\; 0 \tag{3.9}$$

Solving the equation system (3.6)-(3.9), the four fluxes of interest $\Phi_{\delta a} = \Phi_1 + \Phi_3$, $\Phi_{\delta i} = \Phi_2 + \Phi_4$, $\Phi_{pra} = \Phi_2 - \Phi_1$ and $\Phi_{pri} = \Phi_3 - \Phi_4$ can be expressed as,

$$\Phi_{\delta a} = \frac{(2\cdot(R_{pra}\,R_{pri}+R_{pra}\,R_{\delta i})+R_{pp}\,(R_{pra}+R_{\delta i}))\cdot\Theta_r}{2R_{pra}\,(R_{pri}\,(R_{\delta i}+R_{\delta a})+R_{\delta i}\,R_{\delta a})+R_{pri}\,(R_{pp}\,(R_{\delta i}+R_{pra})+2\,R_{\delta i}\,R_{\delta a})+R_{pp}\,(R_{\delta a}\,(R_{\delta i}+R_{pra}))}$$

$$\Phi_{\delta i} = \frac{(2\cdot(R_{pri}\cdot R_{pra}-R_{pri}\cdot R_{\delta a})+R_{pp}\cdot(R_{pri}+R_{\delta a}))\cdot\Theta_r}{2R_{pra}\,(R_{pri}\,(R_{\delta i}+R_{\delta a})+R_{\delta i}\,R_{\delta a})+R_{pri}\,(R_{pp}\,(R_{\delta i}+R_{pra})+2R_{\delta i}\,R_{\delta a})+R_{pp}\,(R_{\delta a}\,(R_{\delta i}+R_{pra}))}$$

$$\Phi_{pra} = \frac{(2\cdot R_{\delta a}\,(R_{\delta i}+R_{pri})+R_{pp}\,(R_{pri}+R_{\delta a}))\cdot\Theta_r}{2R_{pra}\,(R_{pri}\,(R_{\delta i}+R_{\delta a})+R_{\delta i}\,R_{\delta a})+R_{pri}\,(R_{pp}\,(R_{\delta i}+R_{pra})+2R_{\delta i}\,R_{\delta a})+R_{pp}\,(R_{\delta a}\,(R_{\delta i}+R_{pra}))}$$

$$\Phi_{pri} = \frac{(2\cdot R_{\delta i}\cdot(R_{\delta a}+R_{pra})+R_{pp}\cdot(R_{pra}+R_{\delta i}))\cdot\Theta_r}{2R_{pra}\,(R_{pri}\,(R_{\delta i}+R_{\delta a})+R_{\delta i}\,R_{\delta a})+R_{pri}\,(R_{pp}\,(R_{\delta i}+R_{pra})+2R_{\delta i}\,R_{\delta a})+R_{pp}\,(R_{\delta a}\,(R_{\delta i}+R_{pra}))}$$

The different reluctances are derived from the geometries using the general magnetic reluctance formula (Equation 3.10), where l is the length of the flux path and A is the area penetrated by the flux. In the areas where iron surfaces are directly opposing one another, the straight distance between the iron surfaces is used for l. If the areas through which the flux crosses are not directly opposite to each other, it is assumed that the flux follows a circular arc. Circular arcs are the modeling approach of choice here because of their versatility even in complicated structures such as the ones investigated

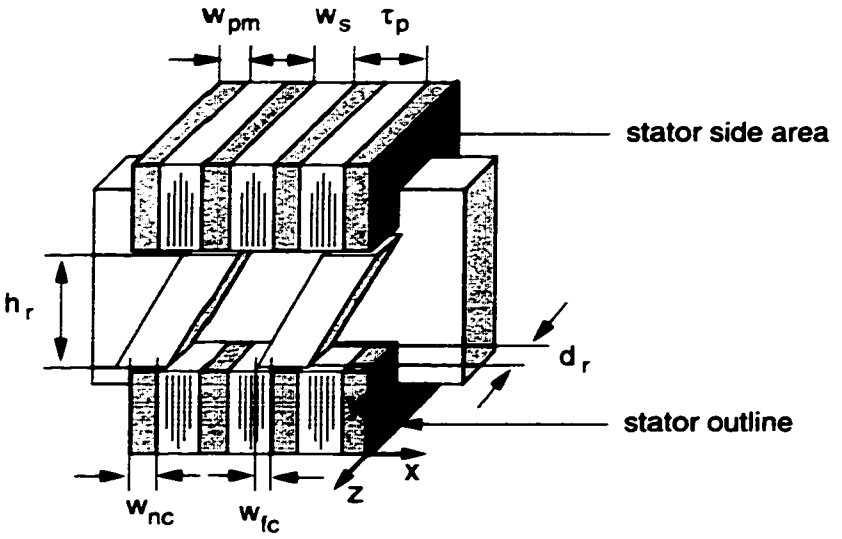

Figure 3.3: Geometrical parameters for the *slanted rotor design*

here. The length of the arc depends on the enclosed angle, which can be 90°, 180°, the slanting angle 56.3° or 180° − 56.3°, depending on the geometry of the reluctance that is calculated. The arc's radius is one half of length of that side of the flux penetrated area, that coincides with the radial direction of the arc.

$$R = \frac{l}{\mu_0 \cdot \mu_r \cdot A} \tag{3.10}$$

The pole-to-pole reluctance R_{pp} and the air gap reluctances $R_{\delta af}$ and $R_{\delta if}$ fall into the first category with the flux penetrated areas directly opposing each other (Equations (3.11)-(3.13)). For R_{pp}, w_{pm} is the width of the permanent magnet as a fraction of τ_p, τ_{p_m} is the medium pole pitch and A_{p_s} is the stator side area of each pole. $R_{\delta af}$ and $R_{\delta if}$ depend on the air gap δ, the width of the overlapping iron parts, w_{fc}, as a fraction of τ_p, the depth of the rotor iron in z-direction d_r (see Figure 3.3 for the coordinate directions and parameters) and the outer/inner pole pitch τ_{p_a}/τ_{p_i}. Note, that τ_{p_a} and τ_{p_i} are linear quantities: The angular pole pitch is chosen to be 5°, but the linear pole pitches at the inner air gap radius (index i), the median radius (index m), which is the length from the machine center to the middle of the rotor, and the outer air gap radius (index a) vary.

$$R_{ppm} = \frac{w_{pm} \cdot \tau_{p_m}}{\mu_0 \cdot \mu_{r_{pm}} \cdot \frac{1}{2} A_{p_s}} \tag{3.11}$$

$$R_{\delta af} = \frac{\delta}{\mu_0 \cdot w_{fc} \cdot \tau_{p_a} \cdot d_r} \tag{3.12}$$

$$R_{\delta if} = \frac{\delta}{\mu_0 \cdot w_{fc} \cdot \tau_{p_i} \cdot d_r} \tag{3.13}$$

All other reluctances fall into the second category where the flux path length follows an arc. For the pole-to-pole leakage reluctance $R_{pp\sigma}$ (Equation (3.14)), π indicates that the flux path follows a half circle, while l_s is the complete outline length of the stator iron. Note, that common factors were intentionally retained to point out how $R_{pp\sigma}$ is derived.

$$R_{pp\sigma} = \frac{\frac{1}{2} \cdot w_{pm} \cdot \pi \cdot \tau_{p_m}}{\frac{1}{2} \cdot \mu_0 \cdot l_s \cdot \tau_{p_m}} \tag{3.14}$$

For the parts of the air gap that are not enclosed by iron on both sides the reluctances are given by Equations (3.15) and (3.16), where w_{nc} describes the non-covered fraction of τ_p and $\frac{\pi}{2}$ indicates the 90° angle enclosed by the two surfaces.

$$R_{\delta a\sigma} = \frac{\frac{1}{2} \cdot w_{nc} \cdot \tau_{p_a} \cdot \frac{\pi}{2}}{\mu_0 \cdot w_{nc} \cdot \tau_{p_a} \cdot d_r} \tag{3.15}$$

$$R_{\delta i\sigma} = \frac{\frac{1}{2} \cdot w_{nc} \cdot \tau_{p_i} \cdot \frac{\pi}{2}}{\mu_0 \cdot w_{nc} \cdot \tau_{p_i} \cdot d_r} \tag{3.16}$$

The pole-to-rotor leakages are given in Equations (3.17) - (3.20), where h_r is the height of the rotor. The length of the arc is determined by the ratio of rotor height to medium pole pitch τ_{p_m}. Note, that $\arctan\left(\frac{h_r}{\tau_{p_m}}\right)$ evaluates to the aforementioned slanting angle of 56.3° if calculated in degrees rather than radians as required in Equations (3.17) - (3.20).

$$R_{pral} = \frac{\frac{1}{2} \cdot w_{pr} \cdot \tau_{p_a} \cdot \arctan(\frac{h_r}{\tau_{p_m}})}{\mu_0 \cdot w_{pr} \cdot \tau_{p_a} \cdot d_r} \tag{3.17}$$

$$R_{prar} = \frac{\frac{1}{2} \cdot w_{pr} \cdot \tau_{p_a} \cdot \left(\pi - \arctan(\frac{h_r}{\tau_{pm}})\right)}{\mu_0 \cdot w_{pr} \cdot \tau_{p_a} \cdot d_r} \quad (3.18)$$

$$R_{pril} = \frac{\frac{1}{2} \cdot w_{pr} \cdot \tau_{p_i} \cdot \left(\pi - \arctan(\frac{h_r}{\tau_{pm}})\right)}{\mu_0 \cdot w_{pr} \cdot \tau_{p_i} \cdot d_r} \quad (3.19)$$

$$R_{prir} = \frac{\frac{1}{2} \cdot w_{pr} \cdot \tau_{p_i} \cdot \arctan(\frac{h_r}{\tau_{pm}})}{\mu_0 \cdot w_{pr} \cdot \tau_{p_i} \cdot d_r} \quad (3.20)$$

The numerical results based on the above equations are compared with the finite element analysis results in Section 3.4.

Position $x = 0.5\,\tau_p$

In the $x = 0.5\,\tau_p$ position similar symmetries exist, but the symmetry planes cut through the middle of the pole iron instead of through the permanent magnets. Figure 3.4 contains three m.m.f. sources Θ_r, but the sources on the left and right side are the same, duplicated only for symmetry reasons since each pole is fed by a single Θ_r. Compared to the $x = 0.0\,\tau_p$ position the new reluctances R_{xi} and R_{xa} are introduced to refine the results in the rotor surrounding areas. The equivalent circuit for the $x = 0.5\,\tau_p$ position is shown in Figure 3.5. For simplification of the equations the reluctances are combined here as given in Equations (3.21)-(3.24).

$$R_{al} = R_{\delta a} \,||\, R_{\delta a\sigma} \,||\, R_{pral} \quad (3.21)$$

$$R_{ar} = R_{\delta a} \,||\, R_{\delta a\sigma} \,||\, R_{prar} \,||\, R_{xa} \quad (3.22)$$

$$R_{il} = R_{\delta i} \,||\, R_{\delta i\sigma} \,||\, R_{pril} \,||\, R_{xi} \quad (3.23)$$

$$R_{ir} = R_{\delta i} \,||\, R_{\delta i\sigma} \,||\, R_{prir} \quad (3.24)$$

Kirchhoff's Voltage law applied to the mesh fluxes Φ_1, Φ_2, Φ_3 and Φ_4 in Figure 3.5 delivers the four mesh flux Equations (3.25)-(3.28).

$$2 \cdot R_{pp} \cdot \Phi_1 - R_{pp} \cdot \Phi_2 - R_{pp} \cdot \Phi_4 = 0 \quad (3.25)$$

$$-R_{pp} \cdot \Phi_1 + (R_{al} + R_{ar} + R_{pp}) \cdot \Phi_2 - R_{ar} \cdot \Phi_3 = 0 \quad (3.26)$$

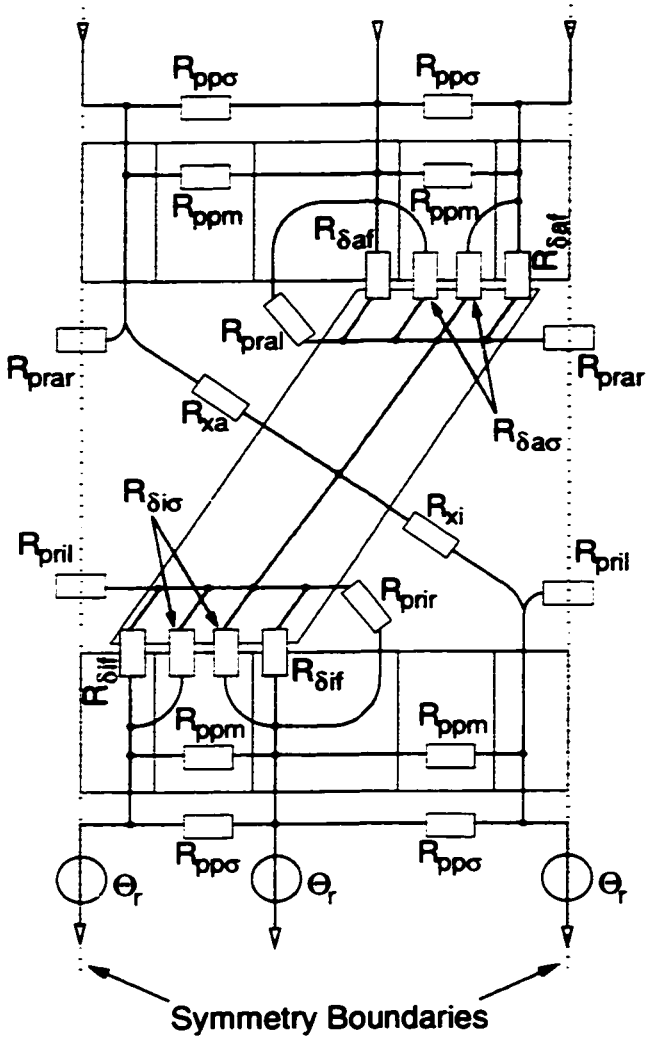

Figure 3.4: Linear reluctance model for the ring winding field at rotor position $x = 0.5\,\tau_p$ showing the concentrated reluctances and the model symmetry of the *slanted rotor design*

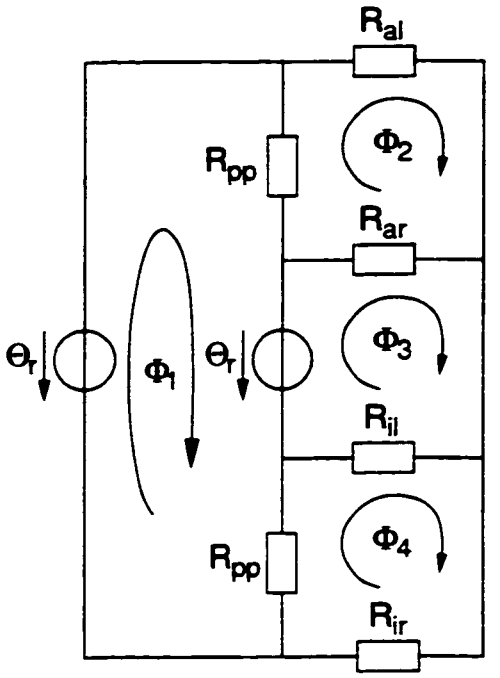

Figure 3.5: Equivalent circuit of the linear reluctance model for the ring winding field at position $x = 0.5\,\tau_p$

$$-R_{ar} \cdot \Phi_2 + (R_{ar} + R_{il}) \cdot \Phi_3 - R_{il} \cdot \Phi_4 = \Theta_r \quad (3.27)$$

$$-R_{pp} \cdot \Phi 1 - R_{il} \cdot \Phi_3 + (R_{ir} + R_{il} + R_{pp}) \cdot \Phi_4 = 0 \quad (3.28)$$

The pole-to-pole reluctances are the same here as for the $x = 0.0\,\tau_p$ case (Equations (3.11) and (3.14)). As for the air gap reluctances they follow the same equations as for the $x = 0.0\,\tau_p$ case (Equations (3.12)-(3.13) and (3.15)-(3.16)), but have different values for w_{fc} and w_{nc}. Furthermore, the pole-to-rotor leakages follow the equations given for the $x = 0.0\,\tau_p$ position ((3.17)-(3.20), but have their parameter values adjusted to reflect the different geometries of the $x = 0.5\,\tau_p$ position. The cross-leakages R_{xa} and R_{xi} are given in Equations (3.29)-(3.30), where w_x is the width of the cross-leakage area.

$$R_{xa} = \frac{\frac{1}{2} \cdot w_x \cdot \tau_{p_a} \cdot \arctan(\frac{h_r}{\tau_{p_a}})}{\mu_0 \cdot w_x \cdot \tau_{p_a} \cdot d_r} \quad (3.29)$$

$$R_{xi} = \frac{\frac{1}{2} \cdot w_x \cdot \tau_{p_i} \cdot \left(\pi - \arctan(\frac{h_r}{\tau_{p_a}})\right)}{\mu_0 \cdot w_x \cdot \tau_{p_i} \cdot d_r} \quad (3.30)$$

3.1.2 Permanent Magnet Fields

The permanent magnets create the magnetic fields which one would refer to in conventional machines as the field winding or excitation field. The field coupling between the stator and the permanent magnet field changes from a positive (or negative) maximum at the rotor position $x = 0.0\,\tau_p$ to a zero value for the $x = 0.5\,\tau_p$ position back to a negative (or positive) maximum at the $x = 1.0\,\tau_p$ rotor position (see Section 4.2.5). The basic layout of the main flux components (Figures 3.6 and 3.8) is similar to the ring winding setup. The major difference here is that the m.m.f. source Θ_{pm} is located in the stator inter-iron regions filled with the permanent magnet material. Through the inner reluctance of the permanent magnet R_{ppm}, the m.m.f. source feeds the air gaps, but is subject to the main losses introduced by $R_{pp\sigma}$. Simplifying the model by evaluating the symmetry of the permanent magnet setup leads to an equivalent circuit with two flux loops instead of four as in the ring winding case.

Position $x = 0.0\,\tau_p$

Most of the reluctances outlined in Figure 3.6 have the location and the same value as in the ring winding case, because the geometry is not changed. However, the reluctances R_{ppm} and $R_{pp\sigma}$ have half the value of their counter parts in the ring winding cases, because they only exist once in the reluctance models for the magnet's field instead of twice as in the ring winding cases. That way they account for the complete stator side area A_{p_s} instead of only half the area as in Equation (3.11). This change stems from the new location of the m.m.f. source. The location change also requires to redefine the complete pole-to-pole reluctance as seen from the m.m.f source R_{pp} as shown in Equation (3.31).

$$R_{pp} = R_{ppm} \tag{3.31}$$

By using the symmetry of the system the equivalent circuit shown in Figure 3.7 is derived. Note, that the equivalent circuit has been simplified by replacing the two parallel m.m.f. sources Θ_{pm} by one equivalent source which is accounted for by the factor $\frac{1}{2}$ in front of R_{pp}. The two leakages reluctances $R_{pp\sigma}$ are connected in parallel as well resulting in half of the reluctance. R_a and R_i are the replacement reluctances given in Equations (3.32) and (3.33).

$$R_a = R_{\delta a} \,||\, R_{pral} \,||\, R_{prar} \tag{3.32}$$

$$R_i = R_{\delta i} \,||\, R_{pril} \,||\, R_{prir} \tag{3.33}$$

Kirchhoff's voltage law applied to the two mesh fluxes Φ_1 and Φ_2 in Figure 3.7 gives the equations (3.34) and (3.35).

$$\left(\frac{1}{2}\cdot R_{pp} + R_a + R_i\right)\cdot\Phi_1 - (R_a + R_i)\cdot\Phi_2 = \Theta_{pm} \tag{3.34}$$

$$-(R_a + R_i)\cdot\Phi_1 + \left(\frac{1}{2}\cdot R_{pp\sigma} + R_a + R_i\right)\cdot\Phi_2 = 0 \tag{3.35}$$

Solving Equations (3.34) and (3.35) delivers the main flux $\Phi = \Phi_1 - \Phi_2$ through R_a

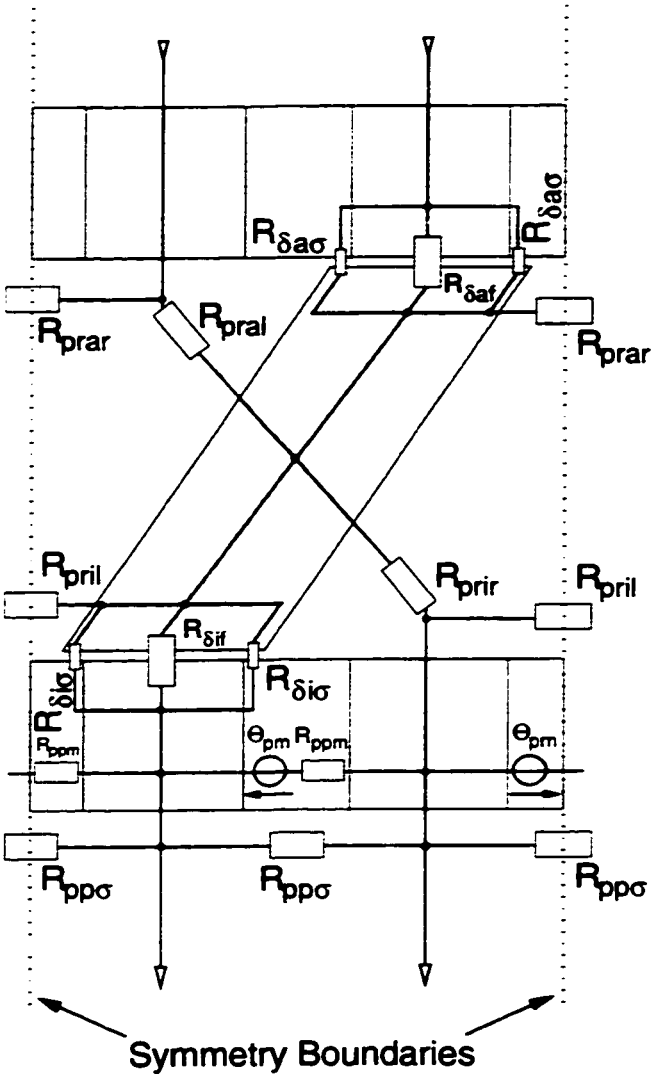

Figure 3.6: Linear reluctance model for the permanent magnet field at rotor position $x = 0.0\,\tau_p$ showing the concentrated reluctances and the model symmetry of the *slanted rotor design*

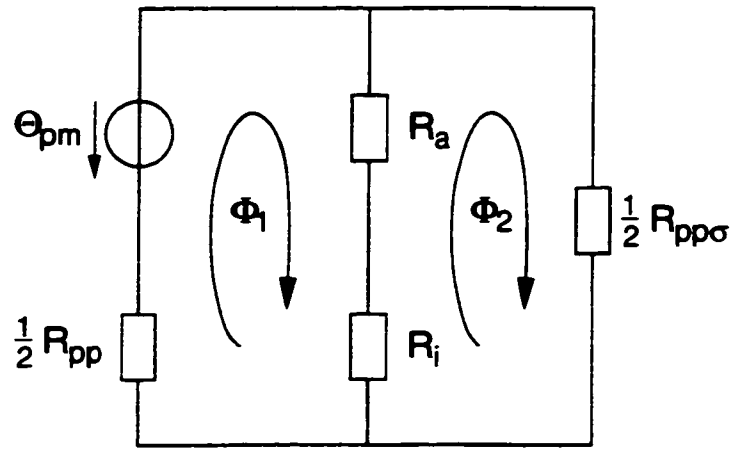

Figure 3.7: Equivalent circuit of the linear reluctance model for the permanent magnet fields for position $x = 0.0\,\tau_p$

and R_i given in Equation (3.36).

$$\Phi = \frac{R_{pp\sigma}}{R_{pp} \cdot (R_a + R_i + R_{pp\sigma}) + R_{pp\sigma} \cdot (R_a + R_i)} \cdot \Theta_{pm} \tag{3.36}$$

Position $x = 0.5\,\tau_p$

The layout of the different reluctances for the $x = 0.5\,\tau_p$ case is depicted in Figure 3.8. The fluxes in the air gaps are modeled separately for the inner and the outer air gaps, because the net flux through the back of the stator iron in the $x = 0.5\,\tau_p$ position is zero (see Section 3.4). It is found that a model based on the assumption that a net flux passes through the back of the stator iron does not match the numerical results of the finite element analysis.

The two separate equivalent circuits for the inner and the outer gap areas are shown in Figure 3.9. While the structure of both circuits is the same, the composition and the value of the reluctances R_{al}/R_{ar} and R_{il}/R_{ir} are different as formulated in Equations (3.37)-(3.40).

$$R_{al} = R_{\delta a} \,||\, R_{\delta a\sigma} \,||\, R_{pral} \,||\, R_{xa} \tag{3.37}$$

$$R_{ar} = R_{\delta a} \,||\, R_{\delta a\sigma} \,||\, R_{prar} \tag{3.38}$$

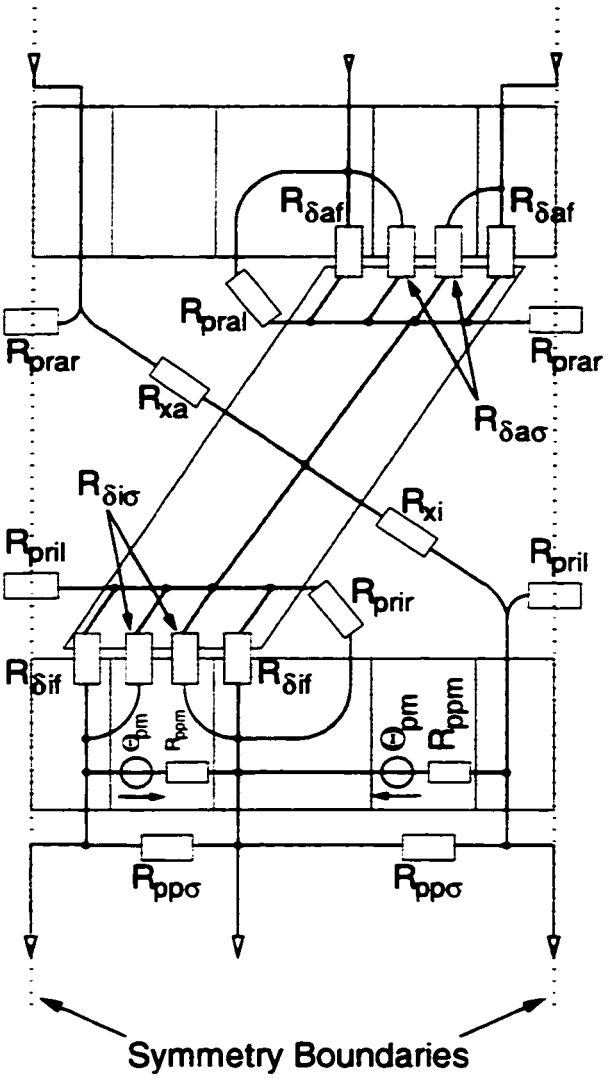

Figure 3.8: Linear reluctance model for the permanent magnet field at rotor position $x = 0.5\,\tau_p$ showing the concentrated reluctances and the model symmetry of the *slanted rotor design*

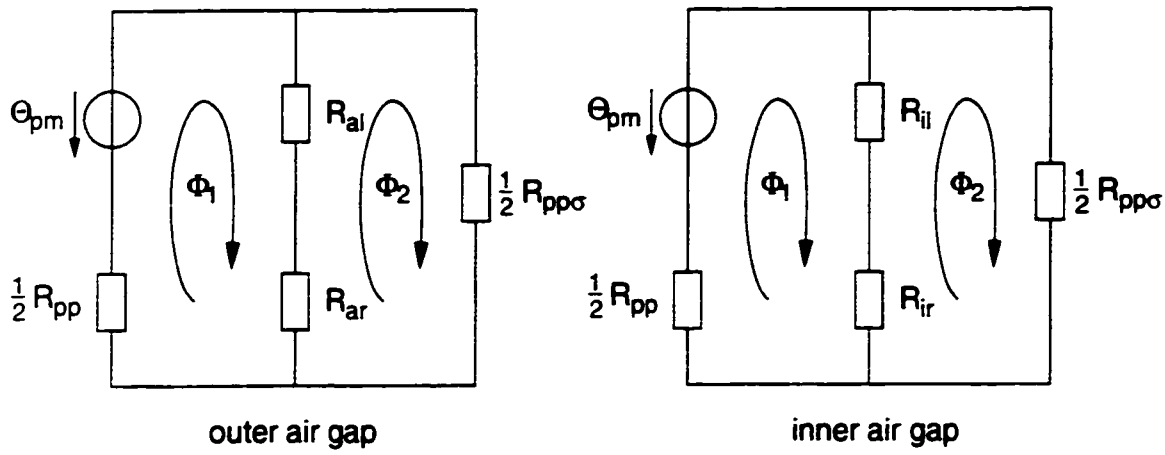

Figure 3.9: Equivalent circuits of the linear reluctance model for the permanent magnet fields for position $x = 0.5\,\tau_p$

$$R_{il} = R_{\delta i} \,||\, R_{\delta i\sigma} \,||\, R_{pril} \tag{3.39}$$

$$R_{ir} = R_{\delta i} \,||\, R_{\delta i\sigma} \,||\, R_{prir} \,||\, R_{xi} \tag{3.40}$$

For both equivalent circuits shown in Figure 3.9 Kirchhoff's voltage law yields a two variable equation system similar to the equations (3.34) and (3.35). Solving those equations allows to find the solutions for the flux through the inner and the outer air gaps.

The numerical results of the equations for all four cases (two fields times two positions) are compared with the finite elements solutions in Section 3.4.

3.2 The 2D Finite Element Model

The *slanted rotor design* may be simulated using two dimensional finite element analysis because of its uniformity in the third dimension: The stator is composed of iron and magnet layers that have the same magnetization direction all around. The simulation plane cuts through the middle of the slanted rotor in the z-direction (see Figure 3.3 for the coordinate directions). The results derived from this design are valuable for other designs as well since the general principle of flux superposition in the air gap is the same for all transverse flux machines despite the large visual and mechanical differences of

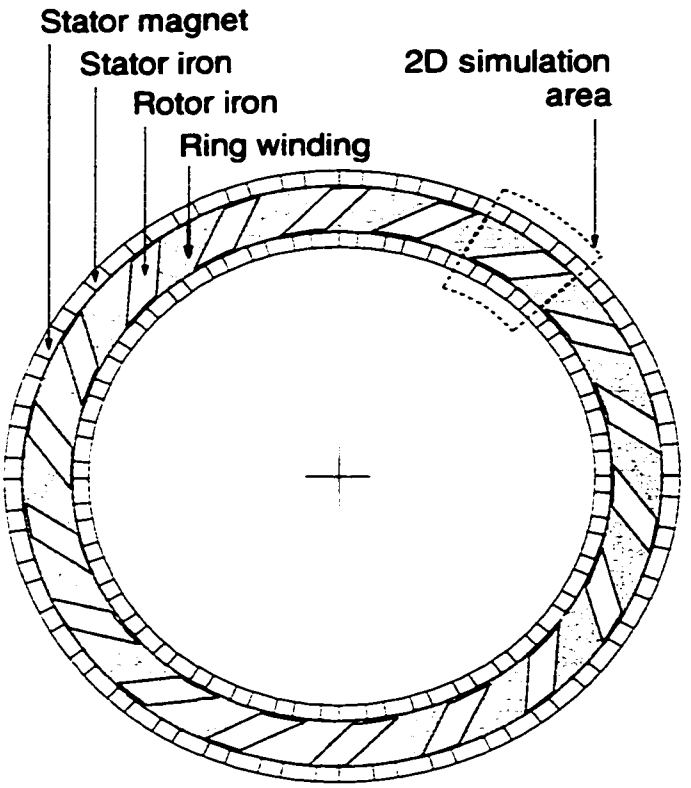

Figure 3.10: Cross section of the passive rotor machine with *slanted rotor design* showing the two-dimensional simulation area

possible designs. In the following it is shown how the three-dimensional flux path can be reduced to a two dimensional finite element model. The consequences of this approach are examined.

3.2.1 General Setup

In Figure 3.10 the complete ring of one phase of the *slanted rotor design* looking from the rotor side is shown. Note, not indicated in the figure is the rigid non-magnetic filler material between the iron segments. The rotor and the stator mount are not shown either. Marked by a dashed outline, Figure 3.10 shows the ring segment comprising two pole pitches of the machine that define the width of the two-dimensional simulation area. The same area is emphasized by a dashed line in the three-dimensional view of the ring structure shown in Figure 3.11. The ring structure in Figure 3.11 is rolled out into a

linear stretch showing a total of four pole pitches. The stator iron halves on the left and right are not shown, therefore the stator contains all four magnets, but only three iron segments.

The two dimensional finite element model shown in Figure 3.12 is based directly on the rectangular section indicated in Figure 3.11. Figure 3.12 depicts the geometry of the model as well as the permanent magnets used for the field production. In the stator sections at the top and the bottom of the model, each pole iron segment is followed by a permanent magnet defining one pole pitch. The magnetization direction of the permanent magnet changes from one pole pitch to the next as indicated by the black triangles within the magnets.

The ring winding, which can not be modeled directly in a two-dimensional model, is represented by thin permanent magnet layers in the air gap creating an equivalent ring winding field. Equation 3.41 relates the residual induction B_r, the coercive force H_c of the magnet and the magnet thickness t_m to the equivalent magneto-motive force of the ring winding $\Theta_{r_{eq}}$. The factor 2 reflects the two magnet layers in the top and the bottom air gap, and $\mu_{r_{pm}}$ is the relative permeability of the permanent magnet.

$$\Theta_{r_{eq}} = \frac{B_r}{\mu_0 \cdot \mu_{r_{pm}}} \cdot 2\,t_m = H_c \cdot 2\,t_m \tag{3.41}$$

Each permanent magnet layer in the air gap is defined to be half as thick as the air gap in this model. That way the rotor segment can be completely surrounded by a uniform air layer of $0.5\,mm$ for an air gap of $\delta = 1.0\,mm$. As explained below this restriction is introduced to compare the forces on the rotor segment calculated by the Maxwell stress tensor and by a virtual work approach (see also 2.2.4). The dependence of the force calculation on the geometry of the finite element mesh when using the virtual work approach creates additional overhead and modeling problems. Modern finite element programs employ sophisticated meshing algorithms to automatically create the finite element mesh, but often do not allow to control the element shape precisely, especially if complicated geometries as the one of the *slanted rotor design* are meshed. Therefore, it is difficult to ensure that a uniform element layer around the area of interest is created by the meshing algorithm. The dependence of the method on the existence of an air layer surrounding the object of interest, cannot be guaranteed in some real world problems, which prohibits the use of the virtual work method for those cases, but does not pose a

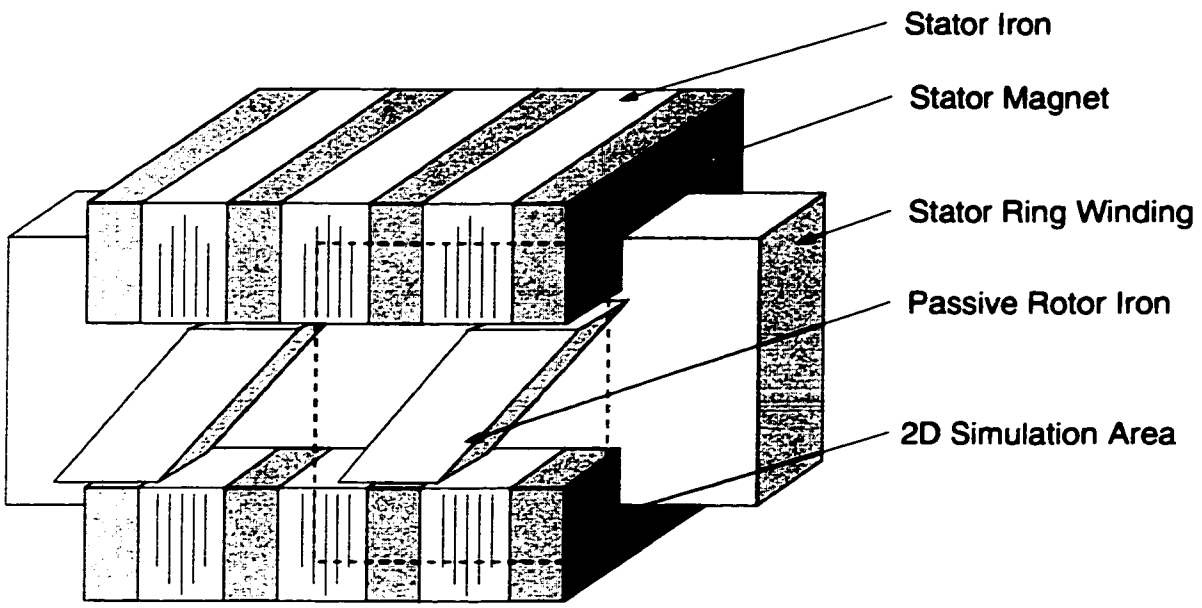

Figure 3.11: Three-dimensional section of the *slanted rotor design* showing the two-dimensional simulation area

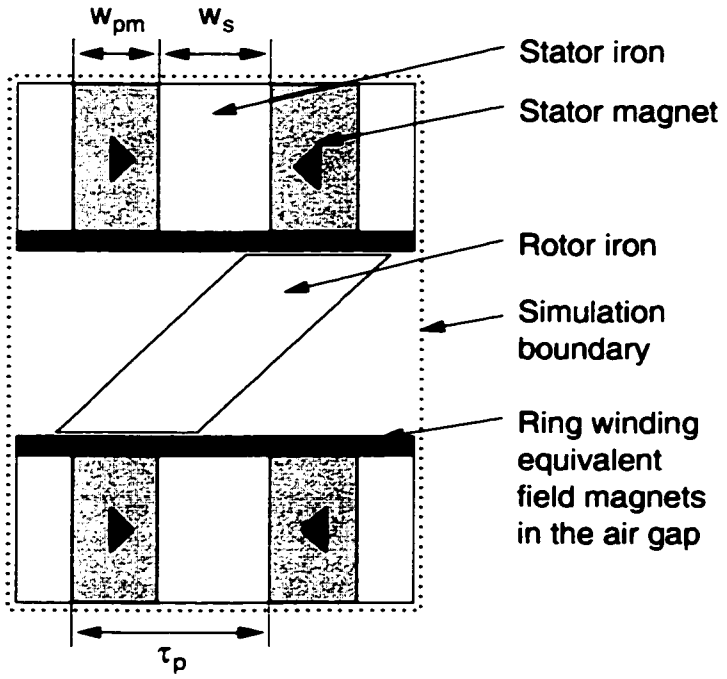

Figure 3.12: Two-dimensional finite element simulation model with arrows indicating the direction of the residual magnetization of the permanent magnets

problem here.

To allow for the use of both, the virtual work and the Maxwell stress tensor approach, additional geometrical areas of $0.5\,mm$ thickness containing air are introduced around the rotor segment. Taking this measure, it can be ensured that a uniform meshing takes place around the rotor, because the meshing is largely influenced by the geometry of the area that is meshed, in a way that rectangular or trapezoidal geometries lead to uniform meshes. Preliminary 2D simulations with unit (infinite) length in the z-direction using a finite element model without a uniform air layer around the rotor segment of interest show that the virtual work calculations exhibit large errors in such models (often 100-500%) compared to models with a uniform air layer enclosing the rotor segment. Further investigations verify, that if all limitations of the virtual work calculation are taken into account precisely, virtual work forces and forces calculated by the Maxwell stress tensor match closely with a maximum difference between 5 and 10%. Furthermore it is found that the results of the Maxwell stress tensor are largely unaffected by the element shapes around the area of interest. This makes the Maxwell stress tensor the superior choice for force calculations in finite element programs for electromagnetic fields and forces.

The boundary conditions reflect common procedures for similar problems [33, 45] and completely surround the model: Referring to Figure 3.12, from the left to the right side of the model there is a periodic boundary condition and the top and the bottom are connected to each other through even symmetry. The periodic boundary condition is inherent to the machine design since the flux pattern repeats after two pole pitches, but the symmetry at the top and the bottom copes with the non-simulated third dimension, virtually connecting the top and the bottom to each other for the simulation.

By default all 2D finite element simulations assume a unit length of the model perpendicular to the simulation plane. For the model here that means that the rotor and the stator iron are $1\,m$ long in the z-direction. No leakage can be simulated at the front and the rear of the rotor and the stator due to the two dimensional simulation.

The iron is assumed to have a realistic relative permeability of $\mu_{r_{Fe}} = 10000$ and does not exhibit saturation effects. To ensure results within the limits of linearity the m.m.f. of the ring winding is limited to $\Theta_{max} = 2200A$-turns per phase and the flux density provided by the stator magnets is kept at $1\,T$. Even upon partially additive superposition of the two fields the core iron remains in low saturation with flux densities between 1.6

and $1.8\,T$ [46]. The three-dimensional saturation simulation in Section 3.5.2 however shows that these assumptions are optimistic because of local saturation effects.

All two-dimensional finite element calculations are performed with the ANSYS program package made by SAS [38, 39].

3.2.2 Flux Line Patterns

Flux line patterns can serve several purposes: In conjunction with a finite element analysis they are an important tool to verify the finite element model. Symmetries can be easily determined and compared with the modeling [47]. With regard to the flux line densities it can be determined whether the flux follows the intended flux paths. For linear reluctance modeling, knowing the flux line distribution within the model allows a proper placement of the reluctances.

Figure 3.13 displays the flux lines caused by the stator magnets for the two rotor positions $x = 0.0\,\tau_p$ and $x = 0.5\,\tau_p$. The base machine model used in the simulations has an air gap of $1\,mm$ and a pole pitch of $\tau_p = 20\,mm$. The permanent magnet's width on the stator measures $w_{pm} = 0.4\,\tau_p = 8\,mm$, the stator iron width $w_{fe} = 0.6\,\tau_p = 12\,mm$ and the rotor width $w_r = 0.6\,\tau_p = 12\,mm$. The anticipated symmetry of the field distribution can be seen clearly in all cases.

The flux patterns caused by the permanent magnets in the two rotor positions differ fundamentally from each other: For the position $x = 0.0\,\tau_p$, starting at the top middle of the figure, the flux lines follow the magnetization direction of the permanent magnets horizontally and change the direction in the stator iron becoming vertical. Then the flux crosses the upper air gap and follows the slanted rotor to cross the lower air gap entering an adjacent stator iron. The flux lines close horizontally through the permanent magnet at the bottom or, as described in the first step, at the top of the figure. In practice the flux lines would close through the stator magnets anywhere along the stator in the third (not simulated) dimension. For the $x = 0.5\,\tau_p$ position on the other hand, the flux closes locally and separately at the top and the bottom part of the stator: Passing horizontally through the permanent magnets, the flux then vertically follows the stator iron, crosses the air gap on one half of the rotor iron, then follows mostly horizontally through the rotor iron to close its path through the air gap on the other half of the rotor and the stator iron. This information confirms the assumption made in Section 3.1.2 for

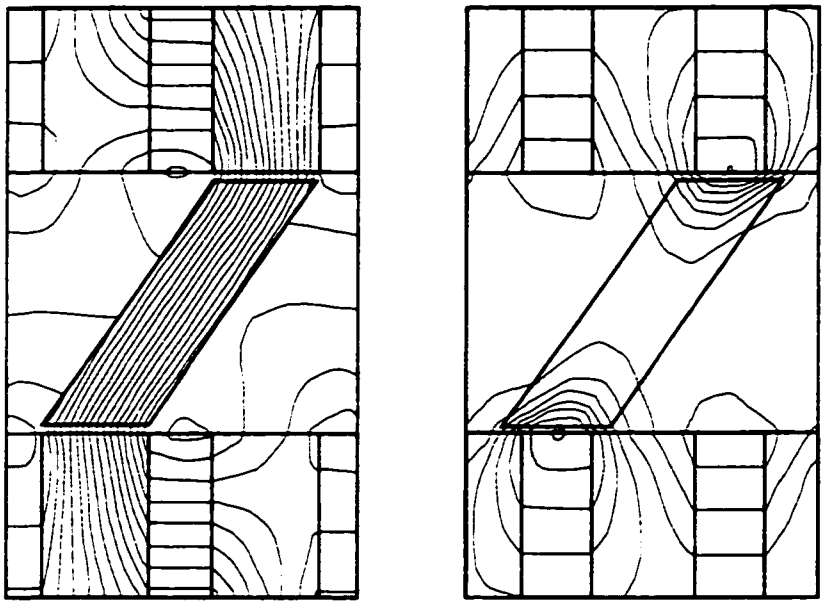

Figure 3.13: Flux lines caused by the stator magnets (field winding equivalent) for position $x = 0.0\,\tau_p$ (left) and $x = 0.5\,\tau_p$ (right)

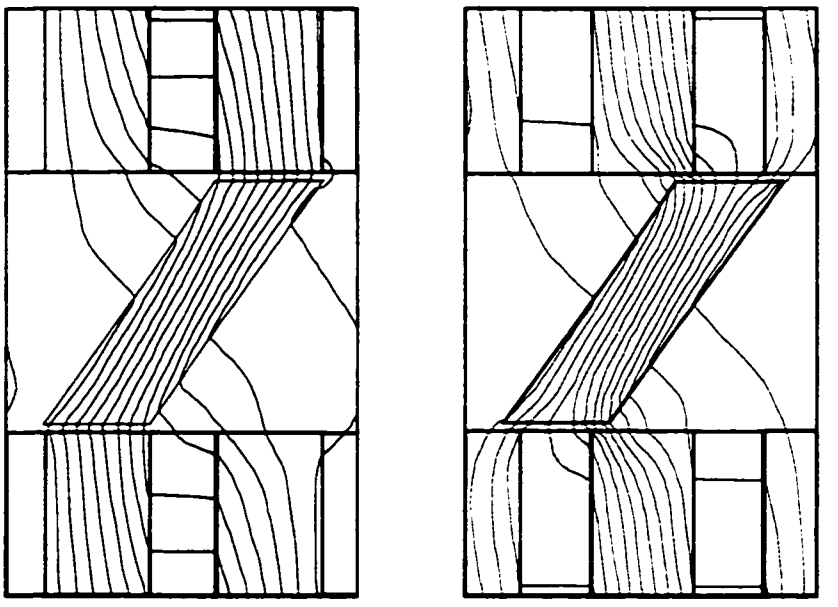

Figure 3.14: Flux lines caused by the ring winding (armature winding equivalent) for position $x = 0.0\,\tau_p$ (left) and $x = 0.5\,\tau_p$ (right)

the linear reluctance modeling.

Referring to Figure 3.14 the differences in the flux pattern caused by the stator ring winding are far less dramatic and directly reflect the requirement for the minimum energy storage in the magnet fields by following the paths with the least total reluctance: In both rotor positions the flux is channeled vertically through the stator iron, crosses the first air gap, follows the slanted rotor, crosses the second air gap and then eventually closes through the grey shaded gap introduced by the permanent magnets at the bottom and the top of the figures. The only difference comparing the two positions is that for $x = 0.0\,\tau_p$ all flux lines have to cross the permanent magnet gap, while in the $x = 0.5\,\tau_p$ position the flux partly closes directly due to the overlapping rotor and iron parts in the middle of the figure.

3.2.3 Influence of the Stator Iron Width on the Force Densities

The investigation of different geometries reveals the geometric dependencies of the force density in order to determine favorable machine layouts [48]. As an example to show that useful qualitative results can be obtained using the 2D finite element analysis approach despite the significant modeling assumptions, the influence of the stator iron width w_s on the force density F_{Ax} is demonstrated. However, the analysis' quantitative results differ significantly from the 3D finite element and reluctance model based solutions. With prior knowledge of the expected results the 2D model can be adjusted to deliver correct results, but that would defy the main purpose of a finite element analysis approach which is to calculate more accurate results by modeling the physical realities without prior knowledge of the exact solution.

To investigate the influence of the stator iron width on the force density only, it is necessary to keep all other parameters fixed. For the geometrical parameters that fact is immediately apparent, because a change there would constitute a visible change of the flux path. However, for a constant pole pitch τ_p, by changing the stator iron width w_s, the field permanent magnet width w_{pm} changes as well because of the relationship given in Equation (3.42).

$$\tau_p = w_s + w_{pm} \tag{3.42}$$

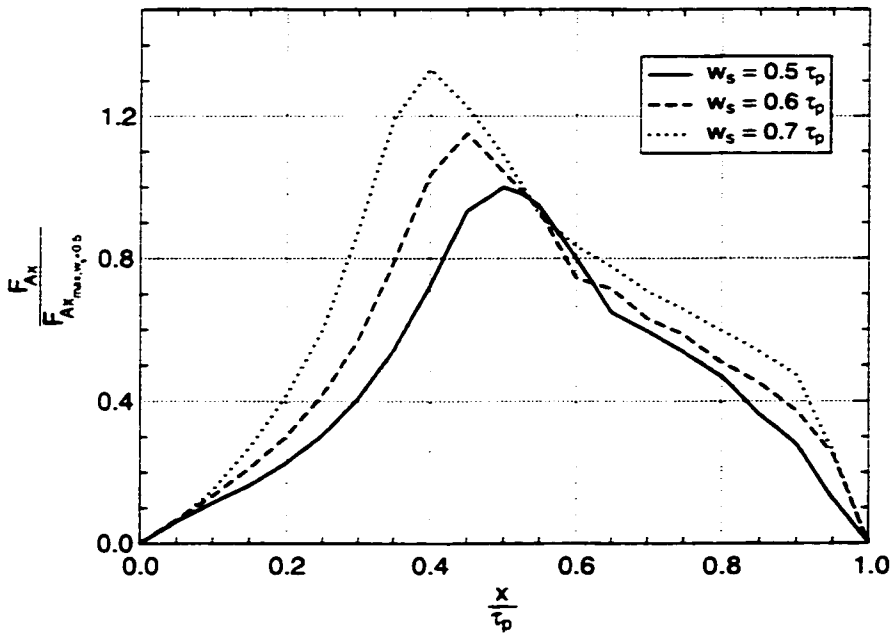

Figure 3.15: Force variation for a rotor movement over one pole pitch of the *slanted rotor design* for stator iron widths between $0.5\,\tau_p$ and $0.7\,\tau_p$

Following Equation (3.41), where $t_s = w_{pm}$ in this case, a change of w_{pm} is inherently equivalent to a change of the field m.m.f. Θ_{pm}. To overcome this problem, Θ_{pm} is fixed and the magnet's coercive force is adjusted to accommodate the width change. Without this adjustment one would effectively measure the influence of the changing field m.m.f. combined with a geometry change rather than the impact of the geometry change alone.

The force variations for a rotor movement over one pole pitch (which can be translated into torque variations for a given radius) are investigated by stepping through 21 rotor positions for each new geometrical or ring winding field case. While the geometrical changes, such as changes in rotor and stator iron width, show their influence on the force variation over one pole pitch, changes of the ring winding m.m.f. deliver the forces for different torque load points. The normalized force density as a function of the rotor position shown in Figure 3.15 follow from the Maxwell stress tensor calculations performed within the finite element analysis program by dividing all values by the force at rotor position $x = 0.5\,\tau_p$ for the case with the stator iron width $w_s = 0.5\,\tau_p$. Comparing

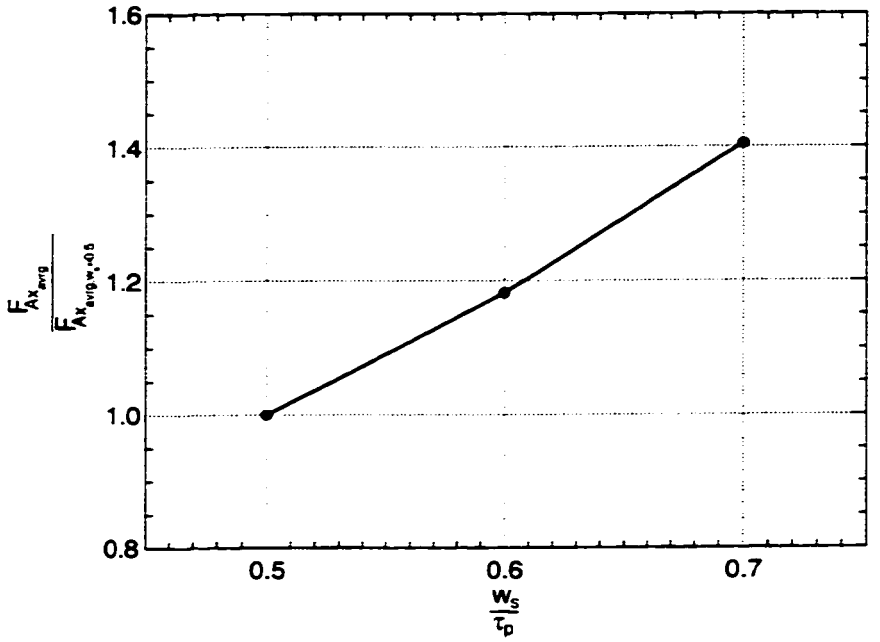

Figure 3.16: Influence of the stator iron width of the *slanted rotor design* on the force density shown as normalized average values

the three curves for the different stator iron widths one can observe that the curves' maxima increase significantly with increased iron width. This increase is caused by a better flux path for the ring winding m.m.f.

The average force densities $F_{Ax_{avrg}}$ are calculated using a discrete integration, where the points are connected through straight lines. The integration formula is given in Equation (3.43) where n is the number of discrete force density solutions, which has a value of $n = 21$ for the curves in Figure 3.15.

$$F_{Ax_{avrg}} = \frac{1}{n-1} \sum_{i=0}^{n-1} \frac{F_{Ax}(x_i) + F_{Ax}(x_{i+1})}{2} \Delta x \tag{3.43}$$

Figure 3.16 displays the average force density normalized to the $w_s = 0.5\,\tau_p$ value. The force density shows a progressive increase for larger iron widths in the range of interest between $w_s = 0.5\,\tau_p$ and $w_s = 0.7\,\tau_p$. The maximum value is reached at $w_s = 1.0\,\tau_p$ for a solid iron stator, but does not have practical relevance here because of the complete absence of permanent magnets in that case. In Chapter 4 the progressive change will be

captured in a theoretical approach by the Carter slot factor k_c [5, 17]. For a real physical machine the assumption of a free choice of the permanent magnet coercive force H_c or remanent induction B_r is not given. It is therefore not advisable to solely maximize the iron widths w_s because of the relationship given in Equation (3.42) and the fact that the material properties limit the maximum available remanent induction. This relationship is investigated in detail for the reduced magnet material design in Section 4.2.2.

3.3 The 3D Finite Element Model

Three-dimensional finite element models are much more involved than the two-dimensional models, not only in terms of the computational complexity, but also in terms of the model definition phase. The benefit of this overhead is that no assumptions about the real geometrical distribution of the major components stator, rotor and ring winding need to be made, yielding quantitatively accurate results without making model adjustments to meet prior results as required in the 2D case. Three-dimensional finite element analysis therefore provides an excellent design tool for industrial applications.

3.3.1 General Setup

The cross section of the ring structure for the slanted passive rotor machine is repeated from Section 3.2.1 in Figure 3.17 to visualize the differing simulation area for the three-dimensional finite element analysis. Figure 3.17 shows that the simulation volume is defined by a pie slice comprising two pole pitches of the machine instead of a ring segment, implying a circular periodicity instead of the translational periodicity in the linear 2D model. This requires that a decision be made on the actual machine dimensions instead of on the magnetic circuit dimensions only as in the 2D case. The physical dimensions of the ring setup that follow typical design parameters for active rotor machines are shown in Table 3.1 [5]. Note, to be comparable with the 2D model, the medium pole pitch is chosen as $20\,mm$ here as well, although a smaller pole pitch would yield higher force densities as shown in Chapter 4 for the *reduced magnet material* design.

The slanted rotor is enclosed at the inside and outside radii by the U-shaped stator of permanent magnet and iron layers as in the 2D case. Viewed in the axial direction the cross-section of the stator iron parts and permanent magnets are ring segments, which

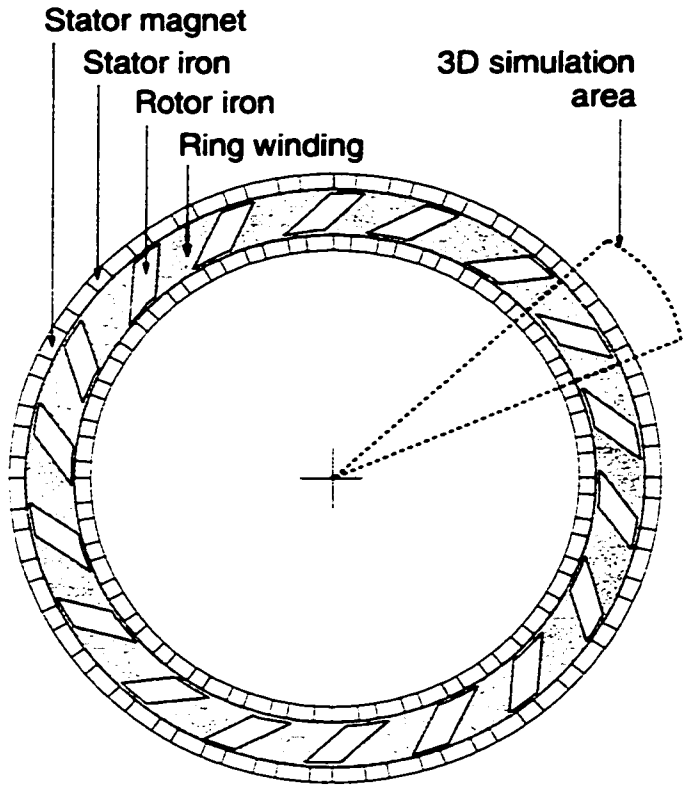

Figure 3.17: Cross section of the passive rotor machine with *slanted rotor design* showing the three-dimensional simulation area

Table 3.1: Physical dimensions of the three-dimensional finite element model of the *slanted rotor design*

Property	Value	Unit
Inner rotor radius	214	mm
Outer rotor radius	254	mm
Air gap width	1	mm
Pole pitch (medium)	20	mm
Pole pitch angle	5	°
Active rotor iron depth	20	mm
Rotor slant angle	56.3	°
Ring winding cross-section	1120	mm^2

means that the stator and rotor parts defining the outer radius geometries are slightly wider than their inner counter parts. As introduced in the reluctance model analysis in Section 3.1, this geometry is responsible for the higher stator field flux densities in the inner air gap. This behavior can be observed in the simulation results in Section 3.4 as well. Since each slanted rotor iron segment occupies two pole pitches, equaling a 10° circular section, there is a total of 36 rotor iron elements and 72 stator poles along the circumference. The 5° pole pitch angle is not only convenient for analysis purposes, but is also reasonable for a practical design to accommodate an average pole pitch of $20\,mm$ for the chosen radius.

The permanent magnet magnetization direction is perpendicular to a ray that cuts through the middle of the magnet from the center of the machine. For example, if the magnet extends from 1.5° to 3.5° (which happens to be the magnet position for the rotor position $x = 0.5\,\tau_p$) then the magnetization direction is perpendicular to the 2.5° ray from the machine center to the motor ring structure. The local coordinate system of the magnetic material is adjusted to account for this effect. The ring winding fills the U-shape between the stator back and the rotor completely except a $5\,mm$ gap at the rotor side which is needed for mechanical reasons to be able to mount the rotor elements in a real machine. The simulation assumes a solid copper ring with an evenly distributed current over its cross section. In the simulation this is achieved by selecting a current density of $1.785 \cdot 10^6 \frac{A}{m^2}$, providing for the stator m.m.f. of $\Theta_r = 2000\,A$-turns. The assumption of equal current distribution for the simulation has no negative effect on the calculated fields, since only magnetostatic calculations are performed that do not exhibit skin effects. In a real system however, the assumption of an equal current distribution is not valid per se, but requires significant constructive measures, especially if several winding strands connected in parallel are required as it is often the case for TFMs [5, 6]. The current distribution can be kept even and skin effect problems are reduced to a minimum, if the winding is constructed of stranded wire using the special Roebel layout [17]. Another practical effect is the 30%-40% higher space requirements or a 30%-40% lesser maximum allowable current density for a given ring winding geometry with a copper fill factor of $\varphi_{Cu} = 0.6\text{-}0.7$ compared to a solid copper ring. This must be considered in the geometrical layout of the stator by providing enough space for the winding to reach the targeted A-turns value for a given maximum current density. Active cooling on

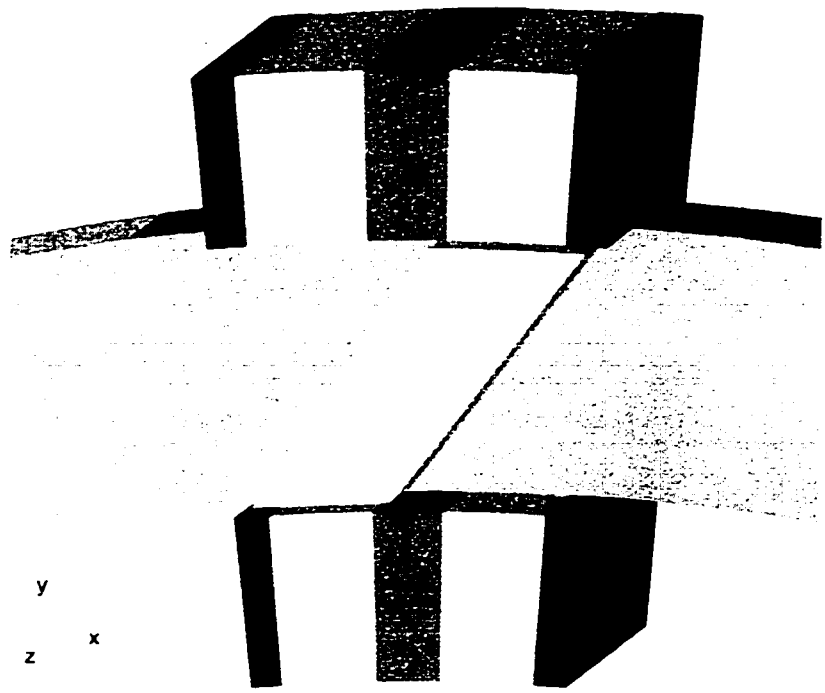

Figure 3.18: Perspective view of the three-dimensional finite element model of the *slanted rotor design*

the other hand can reduce the winding size by allowing higher current densities without thermal breakdown of the winding.

The geometry of the $2\tau_p$ section in rotor position $x = 0.0\,\tau_p$ (stator and rotor poles opposing each other) created with Vector Fields' Opera 3D FEA package is shown in Figure 3.18. The light grey parts are the iron elements, while the dark grey parts depict the magnets. The mechanical support structure for the rotor iron elements is not shown and does not affect the magnetic properties of the machine if made of electrically and magnetically inactive filler material. For computational reasons the circular modeling using Opera 3D requires that the ring winding be defined as a full 360° circle. In Figure 3.18 the ring winding is only shown partially in a medium grey.

The electrical and magnetic properties for the linear simulations are listed in Table 3.2. The permanent magnets possess a typical linearized relative permeability of modern magnet materials of $\mu_{r_{pm}} = 1.06$. The coercive force of $H_c = 400\,000\,\frac{A}{m}$ is a typical

Table 3.2: Electrical and magnet properties for the linear case of the three-dimensional finite element model of the *slanted rotor design*

Part	Material Property
Stator Iron	$\mu_{r_{fe}} = 10\,000\,000$
Rotor Iron	$\mu_{r_{fe}} = 10\,000\,000$
Permanent Magnets	$\mu_{r_{pm}} = 1.06,\ H_c = 400\,000\,\frac{A}{m}$
Stator m.m.f.	$\Theta_r = 2000\,A$

value for a high grade ceramic or a plastic bound rare earth magnet material [49]-[51]. The iron is assumed to be of infinite permeability which is approximated by a very large value in the simulation ($\mu_{r_{fe}} = 10\,000\,000$). There are no saturation and lamination effects in the iron unless stated otherwise (see Section 3.5.2).

3.3.2 Boundary Conditions

For the simulation of traditional longitudinal flux machines it is often possible to enclose most of the structure with a 'flux parallel' boundary condition ($\frac{d\{B\}}{d\{n\}} = 0$, where $\{n\}$ is the normal vector on the outside surface) along the outer surface of the stator iron without large error. For TFM designs this is not possible, because there is no closed iron path all around the machine with negligible leakage to the outside. To cope with this problem for the simulation the structure is padded with air elements at the front, the rear and in the circular direction (Figure 3.19). By choosing the air padding in the front and the rear at least as wide as the area of interest, the calculation error can be kept minimal according to [52, 53]. Since the area of interest (marked in white in the picture) is $8\,cm$ thick the front and rear air padding is set to be $10\,cm$ wide (base area shaded in light grey). In the radial direction the padding is $5.5\,cm$ wide (base area shaded in dark grey). Investigations performed with larger air padding show that extending the padding areas further only increases the calculation time without changing the results.

At the outside boundaries of the padded areas the $\frac{d\{B\}}{d\{n\}} = 0$ boundary condition is applied. An equivalent solution approach could be a far field element type, but the software package used does not supply this element type and claims that this does not have a significant influence on the results. This claim is true and valid for the motor designs investigated here where most of the flux is channeled through highly permeable

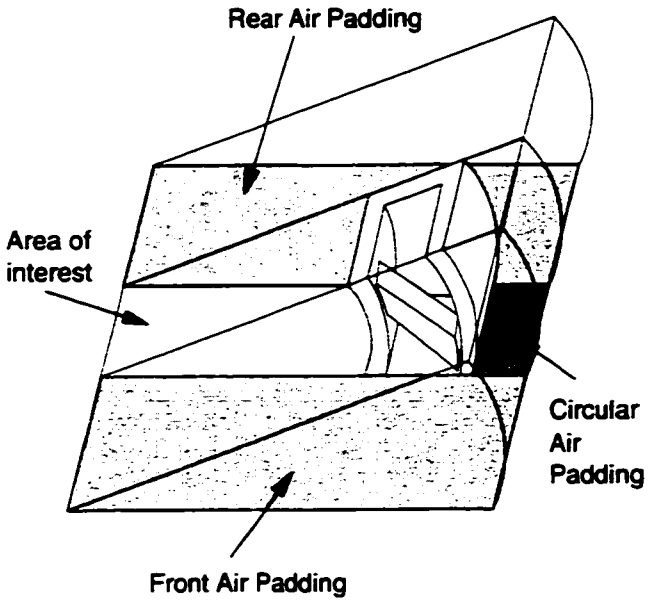

Figure 3.19: Air padding for three-dimensional finite element analysis of the *slanted rotor design*

iron. However, it may be questionable for systems operating at high frequencies. The top and the bottom of the pie slice are connected through even radial periodicity which reflects the real field periodicity of the machine: The top and the bottom nodes are coupled and assume the same field values during the calculation.

3.4 Field Comparison of 3D FEA and reluctance model Field Calculations

Figure 3.20 shows three-dimensional views of the flux density in the inner and the outer air gaps produced by the ring winding m.m.f. and by the permanent magnets. All figures show the flux density component 'BY' in the y-coordinate direction. The y-component is chosen because it allows to show one the sign of the field. Compared to the absolute value of the flux density vector, where the sign information is lost, the y-component gives a much better understanding of the flux path in the air gap. The difference between 'BY' and the vector value under the poles is less than 1%. It can be observed that the main flux is closely confined to the areas of directly opposing rotor and stator iron elements.

For the $x = 0.0\,\tau_p$ rotor position this leads to one block shaped maximum in the inner and the outer air gap for both the ring winding m.m.f. and the permanent magnet field. For the $x = 0.5\,\tau_p$ rotor position one can see two peaks in each air gap. For the ring winding m.m.f. the peaks are separated by a depression where the permanent magnet is located on the stator, while the permanent magnet field changes its sign leading to a positive and a negative peak value.

For a better numerical comparison with the reluctance model results, these curve shapes are analyzed in detail in the 2D plots shown in Figures 3.21 to 3.28. The curves shown in the 2D graphs follow a line that is located in the middle of the air gap in the y-direction and centered with respect to the rotor iron in the z-direction. Each graph depicts a rotational section (general direction of x) of $2\,\tau_p$. Due to the geometry and the chosen $2\,\tau_p$ sections the areas of high flux densities for the outer gap are always located at the right side of the graphs, while the inner is always at the left side. The staircase-like curves are the reluctance model results from the linear reluctance models introduced in Section 3.1, while the more continuous curves are calculated using Vector Fields' Opera 3D according to the model described in Section 3.3.

In Figures 3.21 and 3.22 the rotor is at the $x = 0.0\,\tau_p$ position and the flux densities shown are caused solely by the ring winding at the given m.m.f. of $2000\,A$-turns. Reluctance model and finite element calculation results match very well. In the main overlap area of the rotor and stator iron (the areas with the highest flux density) the reluctance model slightly over-estimates the flux density compared to the finite element analysis, but the error at the center of the peak is less that 3%. The steps at the left and the right side of the maximum flux density area are the parts of the rotor iron that are not covered by the stator iron since the width of the stator iron is only $0.6\,\tau_p$ while that of the rotor iron is $0.8\,\tau_p$. The other areas match quite well too, but are not significantly involved in the production of torque. As a consequence, the larger percentage errors there do not have a significant influence on the torque production. As mentioned in Section 3.1, due to the continuity of the flux through the rotor and the smaller gap area at the inner air gap, the inner flux density maximum is higher than the outer flux density maximum. The difference in the maxima is about 10%. This implies that the machine should be designed for a maximum flux density in the inner air gap. The effect is reduced if the machine radius is increased compared to the rotor height.

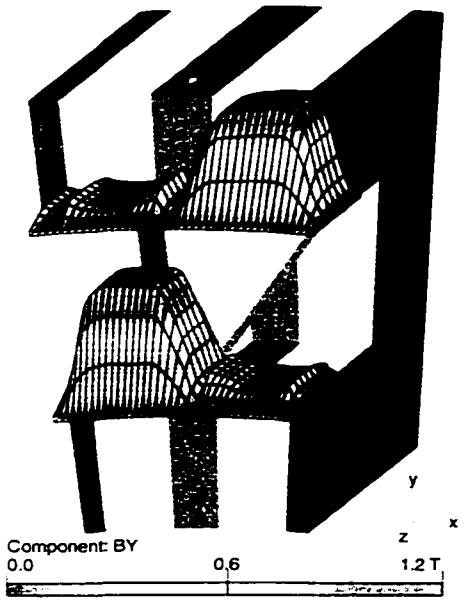

Ring winding field, $x = 0.0\,\tau_p$

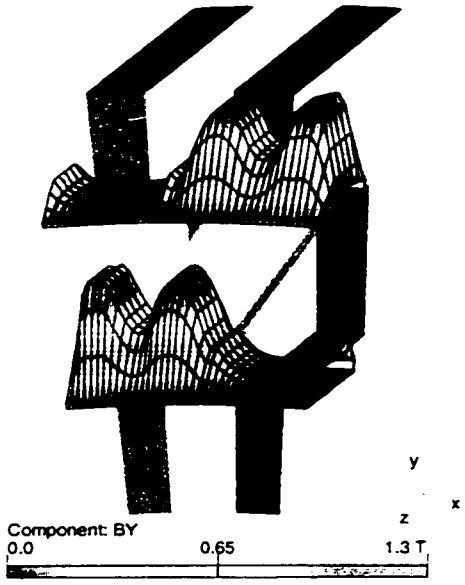

Ring winding field, $x = 0.5\,\tau_p$

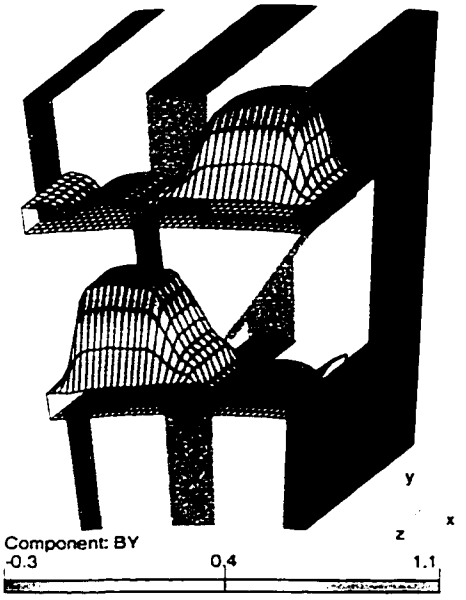

Permanent magnet field, $x = 0.0\,\tau_p$

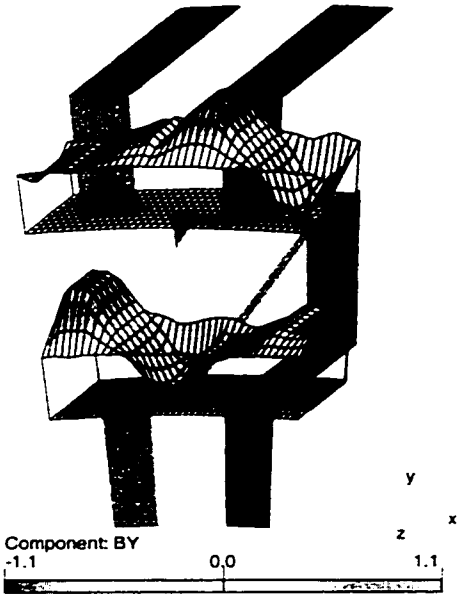

Permanent magnet field, $x = 0.5\,\tau_p$

Figure 3.20: Three-dimensional views of the inner and outer air gap ring winding and permanent magnet fields at rotor positions $x = 0.0\,\tau_p$ and $x = 0.5\,\tau_p$ of the *slanted rotor design*

Figures 3.23 and 3.24 show the flux densities in the outer and the inner air gap caused by the ring winding with the rotor at the $x = 0.5\,\tau_p$ position. The reluctance model again over-estimates the flux densities slightly. A more apparent feature is the difference in the local maximum flux density values of the areas where the rotor iron is fully covered by the stator iron on the opposite side of the air gap, which are the two main peak areas. This asymmetry cannot be explained by the reluctance model which provides two plateaus of the same height. Assuming that the total flux through each air gap is the same for symmetry reasons, the lesser peak can be explained by the slanted geometry of the rotor which leads to a less focused flux density (and therefore lower peak value) in the areas where rotor and stator iron directly oppose each other: Comparing the curve shapes by doubling the covered width (i.e. $0.4\,\tau_p$ versus $0.2\,\tau_p$) it can be seen that the curve integrals are almost the same, which is equivalent to a constant flux in both fully covered areas.

Figures 3.25 and 3.26 show the results for the permanent magnet excitation for the rotor position $x = 0.0\,\tau_p$ in the outer and the inner air gaps. The reluctance model's results are in excellent agreement with the finite element solutions, only underestimating the center of the peak by less than 2%. Furthermore this solution gives a very accurate flux equivalent solution, which is obtained by integration over the fully covered area: While the reluctance model solution delivers an integral value of $0.585\,\frac{Wb}{m}$, the finite element solution yields an integral value of $0.581\,\frac{Wb}{m}$, corresponding to an error of less than 1%. The parts of the rotor that are not covered by the stator iron also exhibit a very close match in terms of flux equivalence. Notice that again the two curves have different maximum values in the outer and the inner air gap, indicating that the net flux closes through the stator iron as in the ring winding field case. However, it will be seen below, that this is not the case for the rotor position $x = 0.5\,\tau_p$.

In Figures 3.27 and 3.28 the permanent magnet fields are displayed in the outer and the inner air gaps for the rotor position $x = 0.5\,\tau_p$. The reluctance model solutions over-estimate the finite element maxima by between 6 and 15% in the iron covered parts. It can be observed that due to the changing excitation direction from the permanent magnets, the flux density in the air gaps changes its sign over one pole pitch, unlike the ring winding field in the air gap that only changes direction if the polarity of the feeding current is changed, but is unaffected by the rotor movement. The sign change is

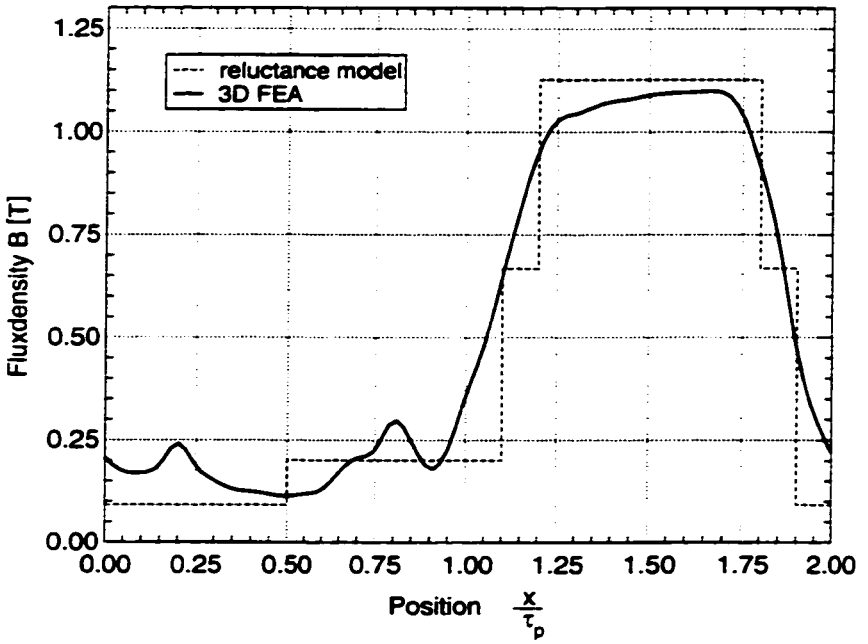

Figure 3.21: Flux density in the outer air gap for the ring winding field at $x = 0.0\,\tau_p$

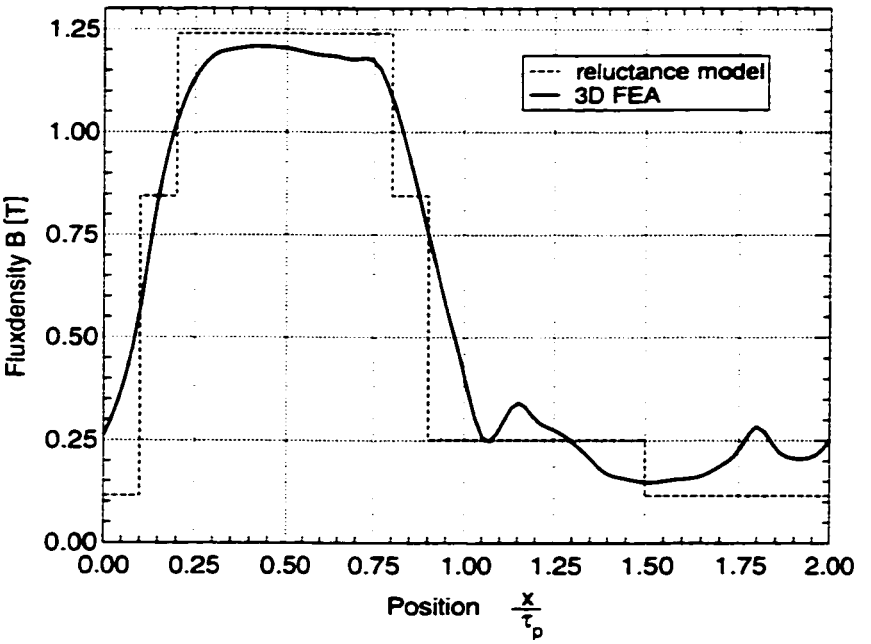

Figure 3.22: Flux density in the inner air gap for the ring winding field at $x = 0.0\,\tau_p$

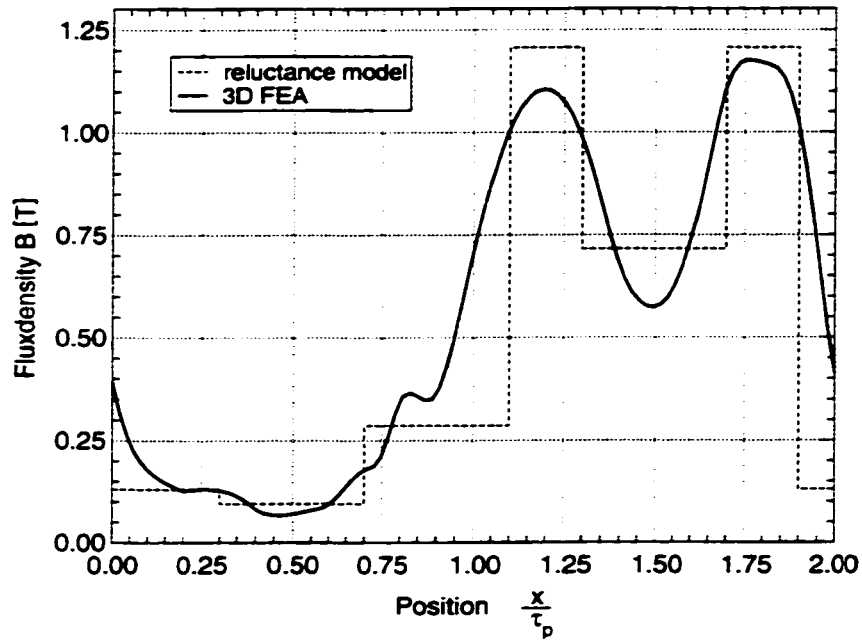

Figure 3.23: Flux density in the outer air gap for the ring winding field at $x = 0.5\,\tau_p$

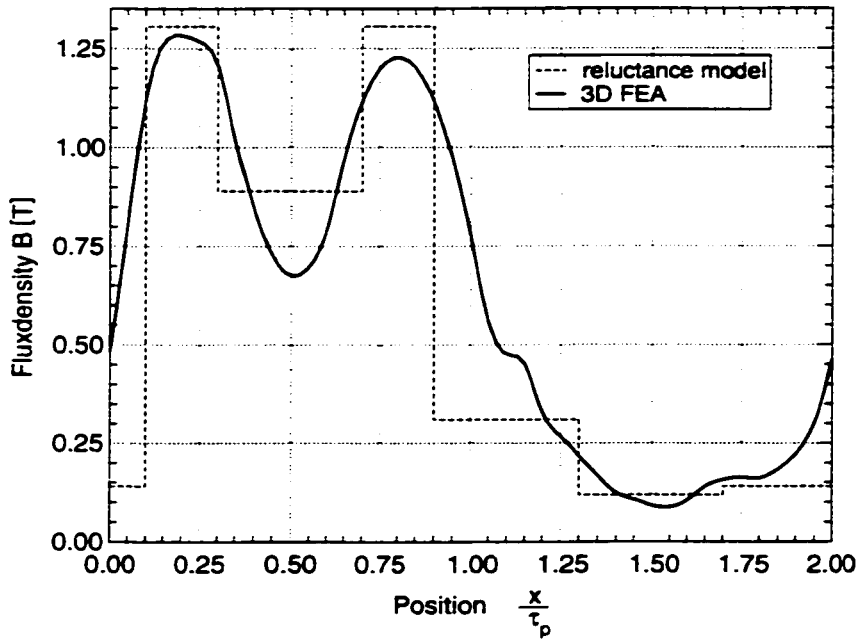

Figure 3.24: Flux density in the inner air gap for the ring winding field at $x = 0.5\,\tau_p$

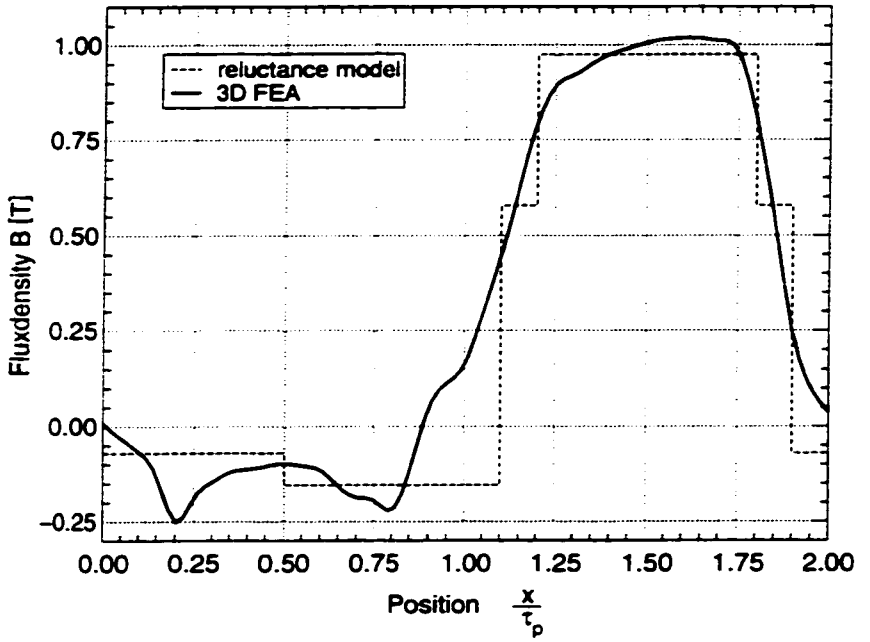

Figure 3.25: Flux density in the outer air gap for the PM field at $x = 0.0\,\tau_p$

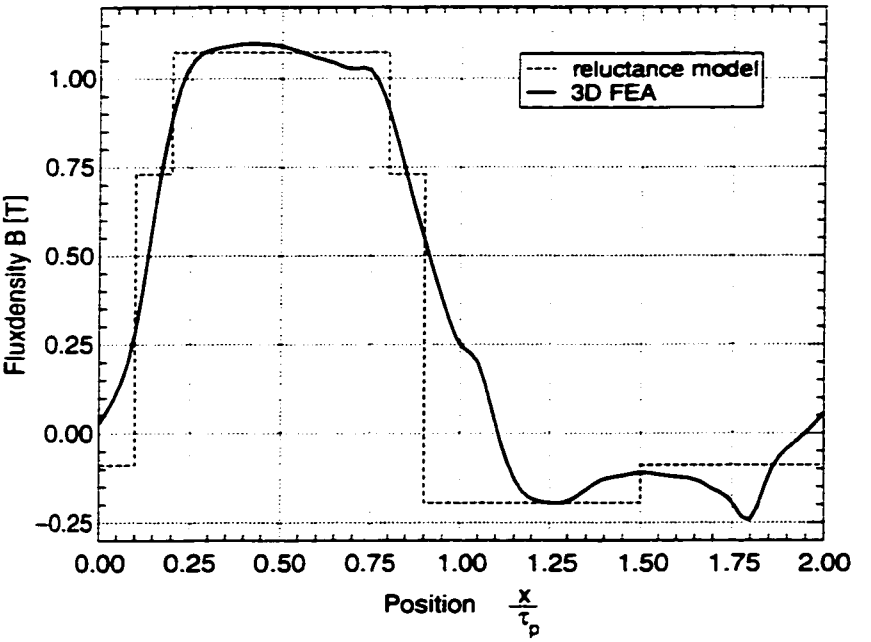

Figure 3.26: Flux density in the inner air gap for the PM field at $x = 0.0\,\tau_p$

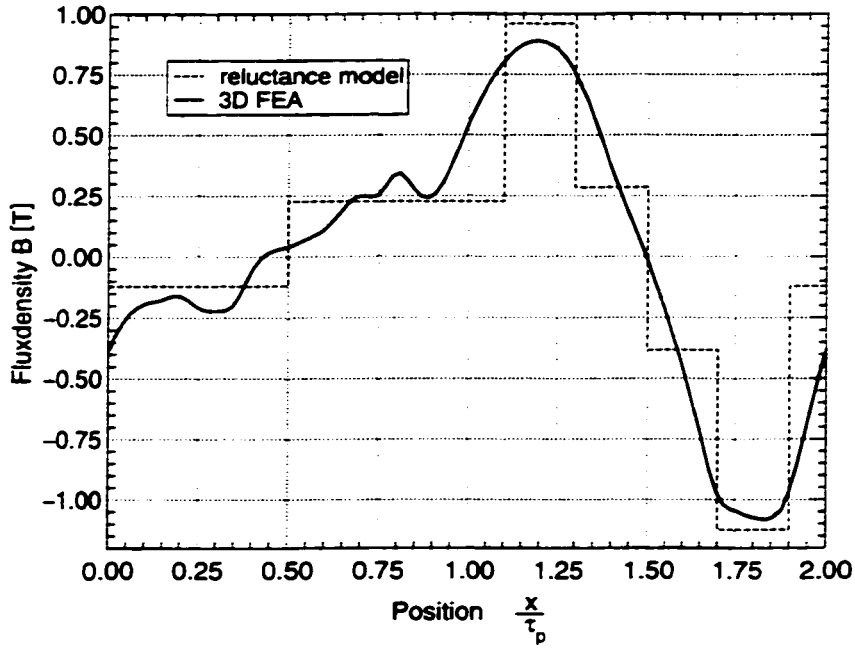

Figure 3.27: Flux density in the outer air gap for the PM field at $x = 0.5\,\tau_p$

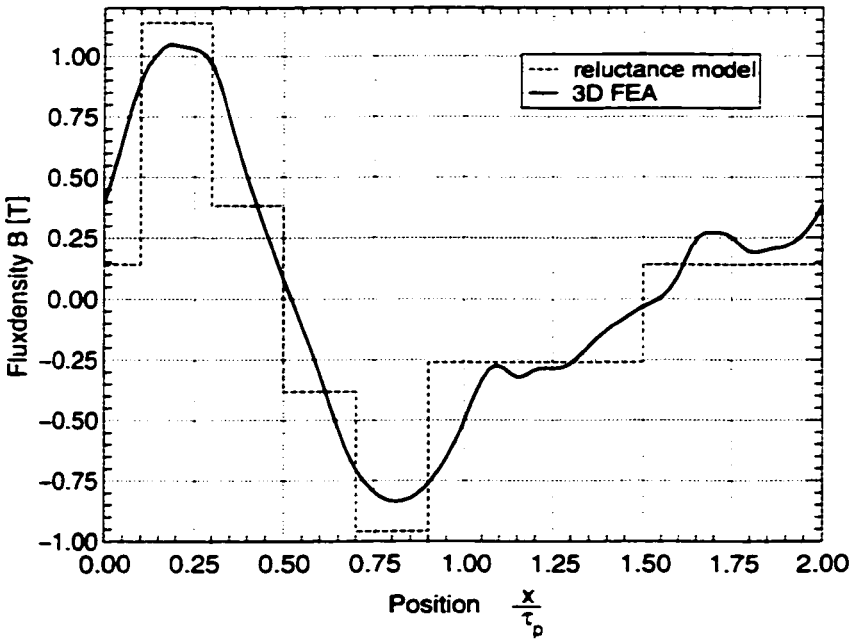

Figure 3.28: Flux density in the inner air gap for the PM field at $x = 0.5\,\tau_p$

most obvious in the $x = 0.5\,\tau_p$ cases, where a positive and a negative peak are observed. The most noticeable difference compared to the ring winding field for the $x = 0.5\,\tau_p$ position is that the maximum value of the peak of the outer air gap is almost equal to the maximum peak value of the inner air gap. This behavior can only be explained if there is no net flux through the rear of the stator iron from the permanent magnets, because a continuous flux would have to lead to a higher flux density in the inner air gap due to the smaller inner pole area. Consequently, there is no flux linkage with the ring winding in the $x = 0.5\,\tau_p$ position (see also Section 4.2.5). Evaluating the results from the finite element analysis reveals that this conclusion is indeed true as can be seen in Figure 3.29, which depicts the flux density in the rear of the stator iron: While the permanent magnet flux in the rear of the stator iron is not zero, the integral value over $2\,\tau_p$ is zero and therfore no net flux goes through the rear part of the stator.

In conclusion the reluctance model field results match the finite element solutions very closely. It can be observed though that the reluctance model results for the $x = 0.0\,\tau_p$ positions are generally better than the reluctance model results for the $x = 0.5\,\tau_p$ positions. This is not unexpected considering that the areas with a nearly homogeneous air gap field are only one third in width compared to the $x = 0.0\,\tau_p$ position. Therefore, the system exhibits larger deviations from the idealized linear reluctance model in the $x = 0.5\,\tau_p$ position compared to $x = 0.0\,\tau_p$, which is better captured by the finite element analysis.

To improve the accuracy of the reluctance model results one would have to include the pole-to-rotor leakage in the third dimension, model the air gap areas with a larger number of reluctances and take the leakage inside the U-shaped stator iron into account. The latter would directly reduce the flux that actually crosses the air gap: In the equivalent circuits it would be in parallel with the m.m.f. source Θ_r reducing the main flux. For our purposes the accuracy of the above presented reluctance modeling is high enough to verify the validity of the results of the finite element analysis. After excluding modeling errors in the finite element model through the comparison with the reluctance model results, it can be safely assumed that the finite element analysis provides the more accurate results, because it employs a much larger number of variables for the field approximation than those used in the reluctance model approach.

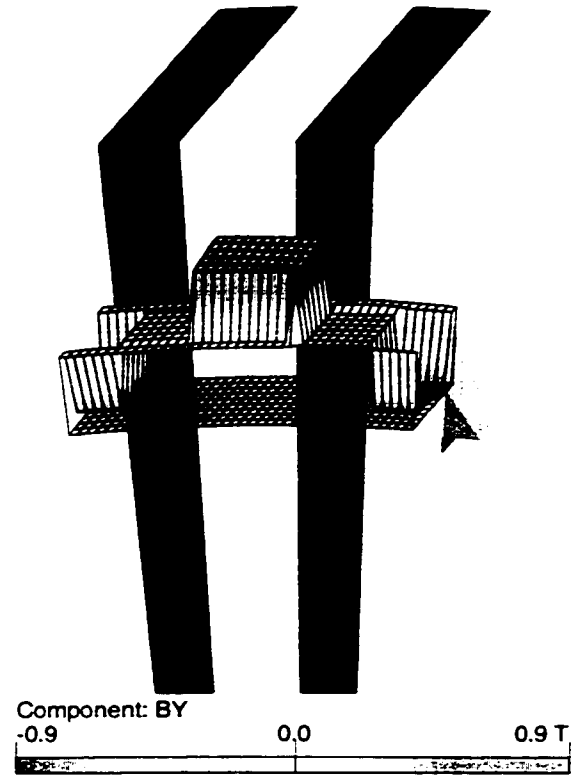

Figure 3.29: Three-dimensional view of the *slanted rotor design* showing a zero net flux through the stator iron at rotor position $x = 0.5\,\tau_p$

3.5 Torques and Saturation of the Slanted Rotor Design

Saturation is a highly non-linear phenomenon that cannot be captured by linear one-step approximations. The saturation finite element analysis of a magnetic circuit solves this problem by taking an iterative approach using the Newton approximation or the linear update method to minimize the total field energy. In Section 3.5.1 the torque without saturation is compared with the 2D solutions before the effects of saturation on the *slanted rotor design* are evaluated in Section 3.5.2.

3.5.1 Linear Torques

The torques are calculated from the 3D field solutions using the Maxwell stress tensor method introduced in Equations (2.44)-(2.46). The 3D FEA results follow the curve shape known from the 2D simulations as shown in Figure 3.30. The torque given in the figure along the y-axis is the torque produced by one rotor iron element. In this machine there are 36 rotor elements, which means the torque produced by the machine is 36 times the given value. Note, that a practical machine must have at least two ring structures to be self-startable, doubling the total torque of the machine. The average torque shown as a dashed line has a value of $T_a = 33.18\,Nm$. From the average torque T_a the force density F_A is found according to Equation (3.44), where r_m is the medium machine radius and A_{active} is the active pole area of one rotor segment.

$$F_A = \frac{T_a}{r_m \cdot A_{active}} = \frac{T_a}{4 \cdot r_m \cdot \tau_{p_m} \cdot d_r} \tag{3.44}$$

Figure 3.30 compares the results from the 3D calculation with the results from the 2D finite element model. While the curve shapes are very similar, the values of the 2D solution are only about two thirds of the 3D ones. Considering that the 2D model does not incorporate leakages as much as the 3D model does, this result seems to be unexpected. Further investigations reveal that this result is caused by a larger pole-to-pole reluctance in the 2D model due to the unmodeled stator parts in the third dimension. Therefore, both, the stator and the rotor field are significantly smaller in the 2D case, which leads to lower force densities. The force density calculated from the 3D model is

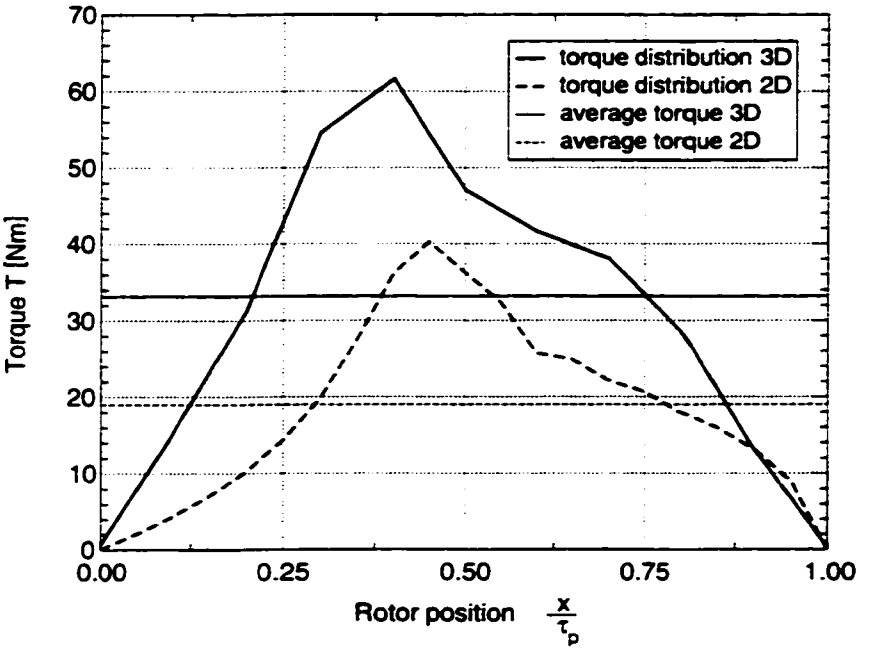

Figure 3.30: Comparison of the torques calculated by two- and three-dimensional finite element models over one pole pitch and as averages

$F_{A_{3D}} \cong 90\,\frac{kN}{m^2}$ while the 2D model yields $F_{A_{2D}} \cong 52\,\frac{kN}{m^2}$. This result shows once again, that a two-dimensional finite element solution for the passive rotor transverse flux motor with slanted rotor requires special adjustments and prior knowledge of the results to yield valid quantitative results.

3.5.2 Saturation Effects

In the calculations considered so far no saturation effects have been taken into account. As long as all the iron parts are only magnetized within their linear section, the error is negligible, but in a complicated structure such as the *slanted rotor design* there is no guarantee that all iron parts stay within their linear limits even if the air gap flux density would suggest that. Therefore, the influence of saturation on the design is explored in this section. Also, the location of 'hot spots' is investigated so that they may be avoided in a final design. 'Hot spots' represent areas within the rotor or stator iron that assume very large flux density values in the linear finite element analysis, but suffer from heavy

saturation in the non-linear saturation finite element analysis.

For the non-linear calculations the saturation curve for solid Waasner Korno W-10 material [54] in Figure 3.31 is used. The curve shown is characteristic for a highly permeable iron considered to be linear up to $1.6\,T$. For all magnetostatic finite element field solutions the saturation curve does not show any hysteresis, but is an initial magnetization curve of the material. These mean values of the initial magnetization curve are the best choice, because the iterative solution does not follow a time line, i.e. the simulation can not determine the previous state of the material, which makes it impossible to determine a location on a split hysteresis curve. Therefore, only single valued curves as the one given in Figure 3.31 are allowed for the simulations with Vector Fields' Opera 3D software. A multi-valued curve would render the system unsolvable because of the missing time-line and the unknown initial material state.

For the comparison of the torques in the unsaturated case and the saturated case the torque for the position $x = 0.5\,\tau_p$ is calculated with $\Theta_r = 500\text{-}2000\,A$-turns. In the $x = 0.5\,\tau_p$ position the reluctance torques are zero because of the mechanical symmetry, and the superimposed fields are at their maximum torque position, making this position a suitable choice for the torque comparison. While the torque is largely unaffected by saturation up to $\Theta_r = 1000\,A$-turns as indicated in Figure 3.32, saturation effects reduce the produced torque by about one third for $\Theta_r = 2000\,A$-turns (see also 4.3.4 where the force density distribution over one pole pitch and the averages are shown for the *reduced magnet material* design).

Figure 3.33 shows the combined ring and permanent magnet fields for the rotor position $x = 0.5\,\tau_p$ with and without saturation. Using the simplified version of the Maxwell stress tensor shown Equation (3.45) for fields that leave the iron surface perpendicularly in the air gap, the loss of torque can be directly attributed to the reduced air gap field.

$$\sigma = \frac{1}{2 \cdot \mu_0} B_n^2 \tag{3.45}$$

Equation (3.46) calculates the relative change of the air gap flux density and shows that this change is equivalent to the relative torque change as implied by Equation (3.45).

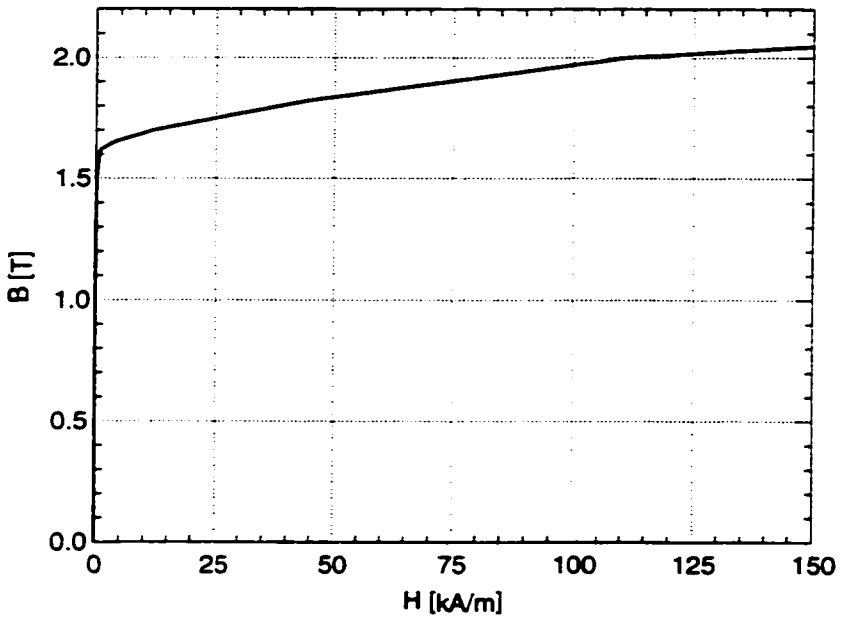

Figure 3.31: Saturation curve for the highly permeable core iron material "Waasner Korno W-10" used for the saturation finite element analysis of the *slanted rotor design*

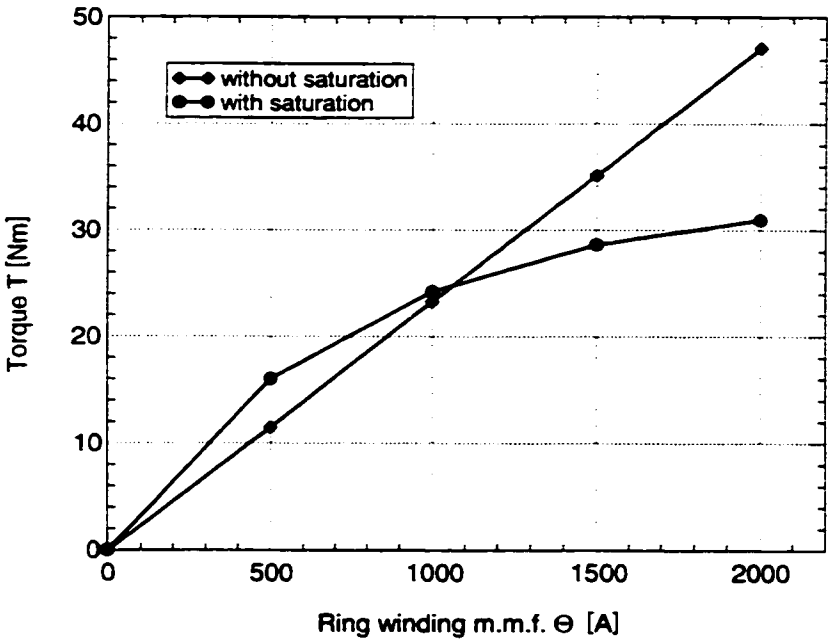

Figure 3.32: Comparison of the torques for the linear and the saturation case at rotor position $x = 0.5\,\tau_p$ for the ring winding m.m.f. changing from $\Theta_r = 0A$-turns to $\Theta_r = 2000A$-turns

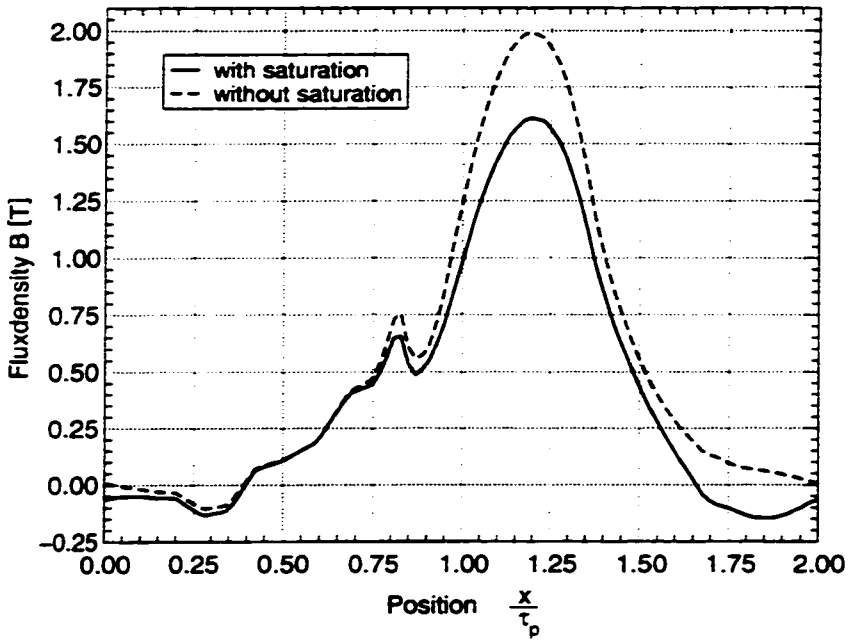

Figure 3.33: Flux density in the inner air gap at $x = 0.5\,\tau_p$ with and without saturation for $\Theta_r = 2000\,A$ and permanent magnet excitation

$$\left(\frac{\hat{B}_{i.inf}}{\hat{B}_{i,sat}}\right)^2 = \left(\frac{1.99\,T}{1.61\,T}\right)^2 = 1.53 \cong \frac{47.1\,Nm}{31.0\,Nm} = \frac{F_{0.5.inf}}{F_{0.5,sat}}\bigg|_{\Theta_r=2000\,A\text{-turns}} \tag{3.46}$$

Further investigation of the field solutions shows that a weak point of the design is the sharp edge of the slanted rotor: Figure 3.34 shows flux density in the rotor iron at the inner air gap (see inset of Figure 3.34) from the linear (unsaturated) and the saturation analysis for a stator field of $\Theta_r = 2000\,A$ and permanent magnet excitation. It shows clearly that the lower sharp edge on the left is one of the 'hot spots' introduced earlier. In order to guarantee the linear increase of the torque shown in Figure 3.32 the flux density must take on values over $5\,T$ in the simulation without saturation. This is not achievable with saturation present, where the maximum of the flux density remains at about $2.2\,T$ in the curve with saturation. Therefore, a better slanted design would be the one shown in the bottom right corner (P2) in Figure 2.11: It does not have any thin edges where extreme flux densities would occur. Similar findings are made by [5] for the active rotor

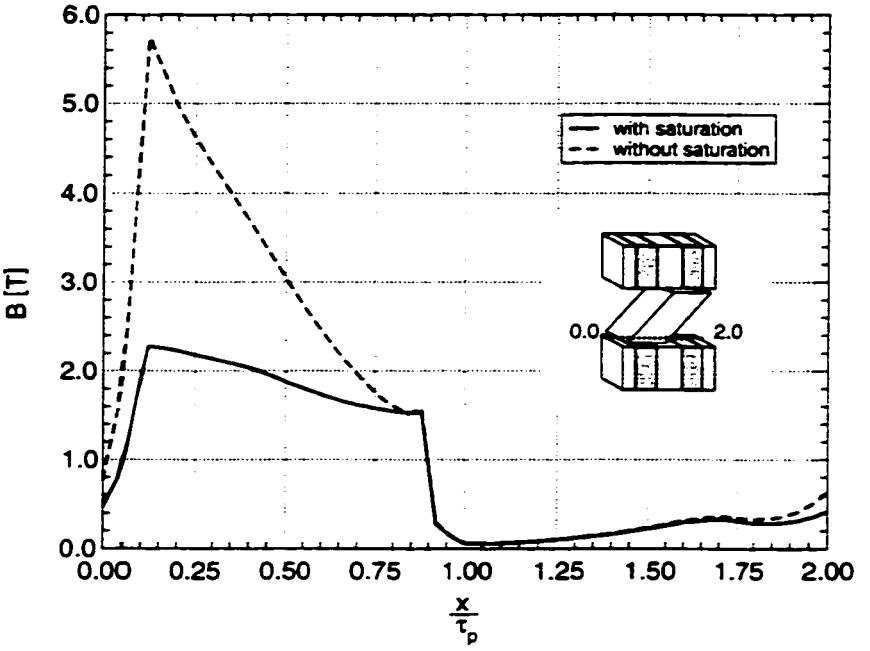

Figure 3.34: Flux density in middle of the rotor core iron close to the inner air gap at rotor position $x = 0.5\,\tau_p$ for a stator field of $\Theta_r = 2000\,A$-turns

machine shown in the top left corner (A1) of Figure 2.11, but [5] only attributes the less than expected performance vaguely to saturation effects.

3.6 Design Recommendations for the Slanted Rotor Design

To construct a good slanted rotor transverse flux motor with permanent magnets on the stator, or in more general terms to be able to build a good single track passive rotor machine, the following recommendations are given:

- A wider stator iron width provides a better flux path leading to higher achievable force densities. However, the stator iron width and the permanent magnet's m.m.f. are coupled in a trade-off manner.
- Reduce the amounts of magnet material. This is an especially challenging task for

single track machines. One idea for further research is given in the conclusions in Chapter 5.

- An improved slanted rotor design should avoid pointed geometries such as sharp, thin edges to avoid magnetic 'hot spots'.

Chapter 4

Reduced Magnet Material Transverse Flux Motor Design

The *slanted rotor design* investigated in Chapter 3 allows one to determine favorable layouts and to verify the accuracy of the finite element analysis software used for the simulations. The *slanted rotor design* uses significant amounts of magnet material, which does not affect the machine cost excessively because the ceramic magnets used in that design are inexpensive. To further reduce the machine's weight and size it is advantageous to use high power permanent magnet materials to create the excitation field in the air gap. Modern rare earth permanent magnet materials made of Neodymium-Iron-Boron (NdFeB) or Samarium-Cobalt (SmCo) alloys have residual inductions of up to $B_{r_{re}} = 1.28\,T$ compared to ceramic magnets at about $B_{r_{cer}} = 0.4\text{-}0.5\,T$. By operating the rare earth magnets at or close to their energy maximum point the required amounts of this costly magnet material can be controlled effectively.

4.1 Analysis and Machine Design

The interest during the design stage of the *reduced magnet material* passive rotor transverse flux motor is focused on finding a suitable solution for the machine design parameters, namely, air gap δ, pole pitch τ_p, permanent magnet width w_{pm}, stator iron width w_s, the stator height h_s, the stator pole depth d_s, the rotor pole width w_p, the rotor height h_r and the ring winding depth d_w. In Figure 4.1 the location of those parameters

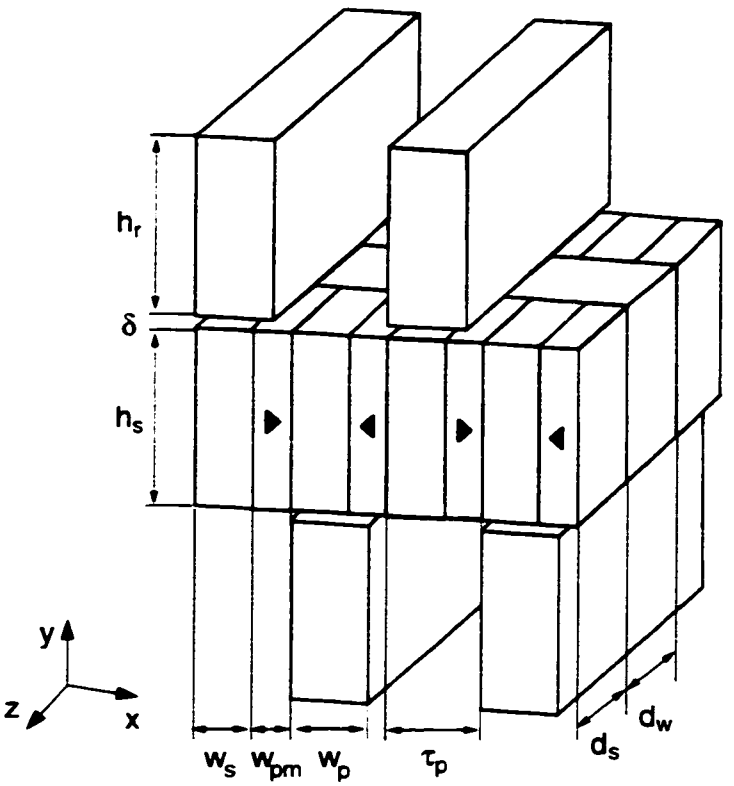

Figure 4.1: Three-dimensional view of the *reduced magnet material* design showing the location of the geometry parameters

within the geometry is illustrated. While principally all parameters can be chosen within a wide range, the goals of a good design are to make optimum use of the permanent magnet material and to achieve the maximum possible force density. The permanent magnet material should operate at its energy maximum point $E_{max} = (BH)_{max}$ for optimum material use. Since modern magnet materials are almost perfectly linear, the energy maximum is achieved at a magnet flux density that is half its remanent induction, $B_{pm} = \frac{1}{2}B_r$.

Figure 4.2 shows the temperature corrected curve for $80°C$ and the energy maximum area for the type 190/250h NdFeB material made by the Magnetfabrik Schramberg, Germany, which is used in the simulations [49]. The energy maximum constraint is the main concern of the theoretical layout approach [55]. The analysis and design steps allow one to determine the flux in the air gap as well as the achievable force density for a non-

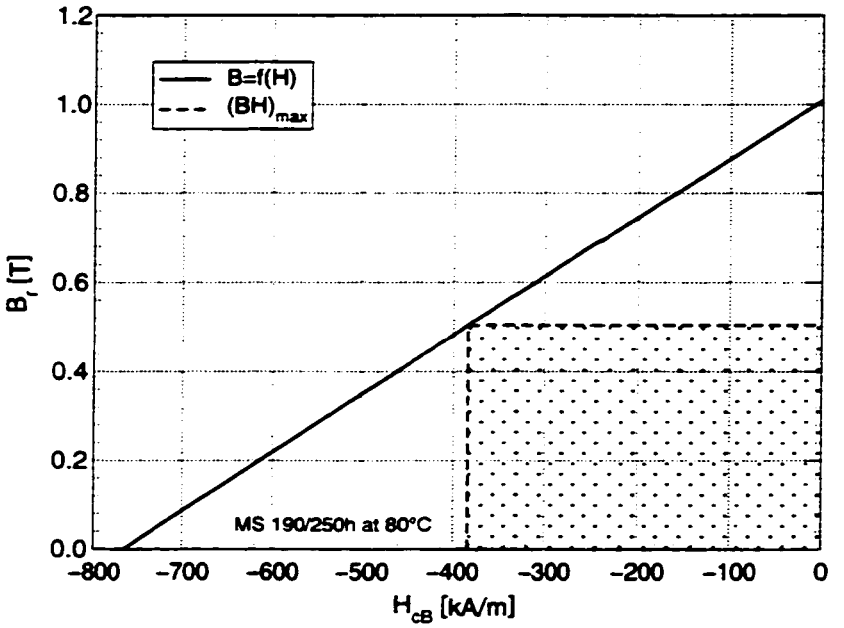

Figure 4.2: BH-characteristic for NdFeB material 190/250h at 80°C illustrating the magnets energy maximum point

saturated model, while always ensuring the *optimum magnet use* through the theoretical model. The magnet flux density in the theoretical analysis is always $B_{pm} = \frac{1}{2}B_r$ due to the design process and is matched closely in the finite element model solutions. Therefore, the layout procedure to be introduced in the following is referred to here as the *optimum magnet use layout* and often addressed as an *optimum* solution although it is derived from a condition matching rather than from an optimization process.

4.1.1 Analysis

The basis for the motor design is the analysis of the rotor position $x = 0.5\,\tau_p$, because it represents the point at which the forces caused by the field superposition are at a maximum, while the machine symmetry leads to the absence of reluctance forces. As a vehicle for the design a reluctance model following the same principles as in the slanted design's field analysis is derived for this position. Fewer reluctances are needed to achieve high accuracy for the field calculations because of the less complicated geometry compared to

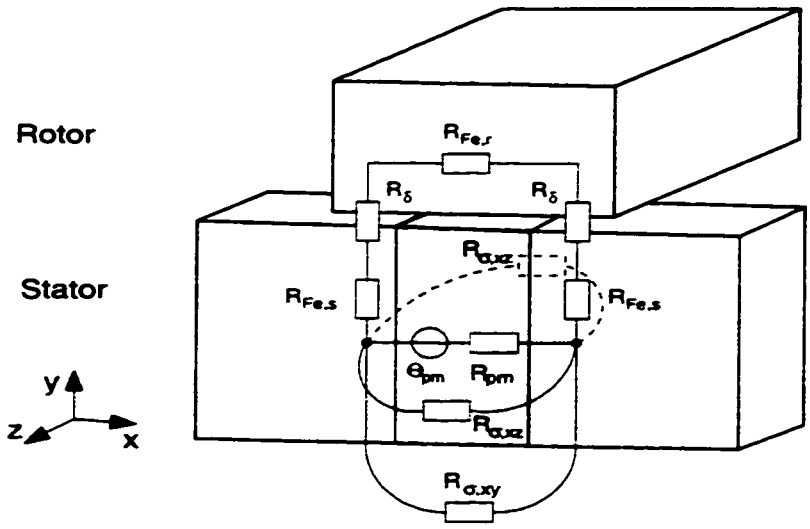

Figure 4.3: Concentrated reluctances of the *reduced magnet material* design at rotor position $x = 0.5\tau_p$ including iron reluctances

the *slanted rotor design*. Figure 4.3 shows the location of the concentrated reluctance elements at rotor position $x = 0.5\,\tau_p$. The main circuit reluctances are the two air gap reluctances R_δ and the permanent magnet's reluctance R_{pm}. In addition there are three leakage reluctances, one representing the leakage in the xy-plane ($R_{\sigma,xy}$) and two more reluctances in the xz-plane ($R_{\sigma,xz}$) accounting for the leakages at the front and the rear of the stator. The iron reluctances $R_{Fe,s}$ on the stator and $R_{Fe,r}$ on the rotor are also shown in Figure 4.3.

Figure 4.4 shows the simplification steps followed by the analysis: The leftmost equivalent circuit contains all reluctances including the iron reluctances, the middle one neglects the iron reluctances and the one on the right expresses the circuit in terms of leakages and is otherwise equivalent to the circuit in the middle . The total equivalent circuit reluctance including iron reluctances given in Equation (4.1) is derived from the leftmost circuit in Figure 4.4.

$$R_{t_{Fe}} = R_{pm} + \left[R_{\sigma,xy} \left\| \frac{1}{2} R_{\sigma,xz} \right\| (2R_\delta + 2R_{Fe,s} + R_{Fe,r})\right] \tag{4.1}$$

The linear iron reluctances that are determined by the medium iron path lengths $l_{Fe,s}$ and half the cross-section of the stator pole in the xz-plane, $A_{s,xz}$, for the stator and for

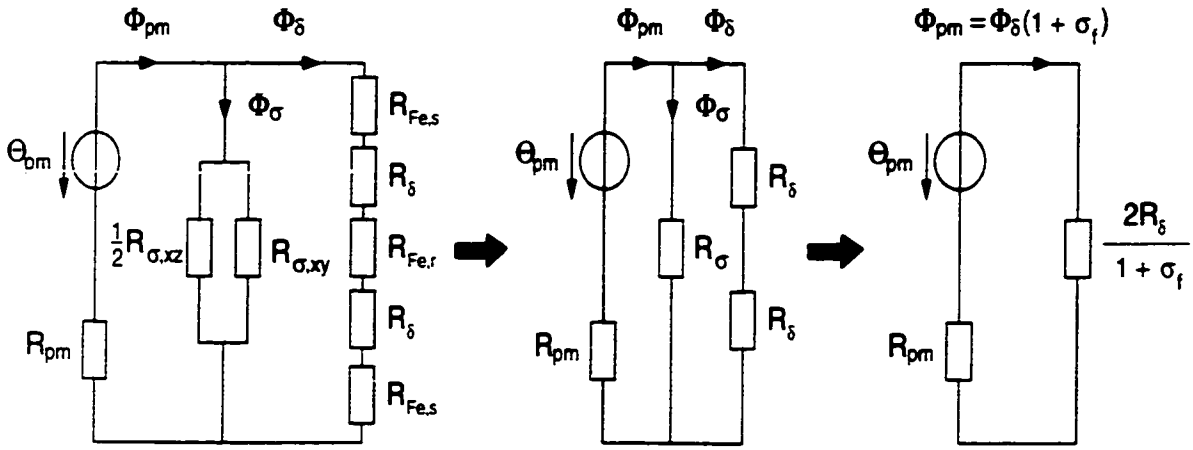

Figure 4.4: Simplification stages of the reluctance equivalent circuit for the *reduced magnet material* design at rotor position $x = 0.5\,\tau_p$ for design purposes

the rotor by $l_{Fe,r}$ and the cross-section of the rotor part directly over the stator in the yz-plane, $A_{r,yz}$, are given in Equations (4.2) and (4.3).

$$R_{Fe,s} = \frac{l_{Fe,s}}{\mu_0 \cdot \mu_{r_{Fe}} \cdot A_{s,xz}} = \frac{2l_{Fe,s}}{\mu_0 \cdot \mu_{r_{Fe}} \cdot \frac{1}{2} w_s \cdot d_s} \tag{4.2}$$

$$R_{Fe,r} = \frac{l_{Fe,r}}{\mu_0 \cdot \mu_{r_{Fe}} \cdot A_{r,yz}} = \frac{2l_{Fe,r}}{\mu_0 \cdot \mu_{r_{Fe}} \cdot h_r \cdot d_s} \tag{4.3}$$

Typically the relative permeability of the iron is $\mu_{r_{Fe}} \geq 10000$ as long as saturation is avoided, which puts the values of the iron reluctances into the pars pro mille range compared to the other reluctances. Therefore, the influence of the iron reluctances is neglected for the design analysis.

Looking at the fluxes Φ_δ, Φ_{pm} and Φ_σ in the equivalent circuit given in Figure 4.4 one can define two leakage factors: The leakage flux with respect to the air gap flux, σ_f, and the air gap flux with respect to the permanent magnet flux, σ_{pm}. While σ_f is a measure of the relation of the useful flux to the leakage, σ_{pm} expresses how much of the permanent magnet's flux actually reaches the air gap for force production. The definitions for both leakages are given in Equations (4.4) and (4.5).

$$\sigma_f = \frac{\Phi_\sigma}{\Phi_\delta} = \frac{R_\delta}{R_\sigma} \tag{4.4}$$

$$\sigma_{pm} = \frac{\Phi_\delta}{\Phi_{pm}} \tag{4.5}$$

In the analysis σ_f is represented in terms of the reluctances, because the reluctances can be derived from the geometry. In the finite element analysis on the other hand, the leakage is more easily evaluated in terms of σ_{pm}, because the local flux concentrations in the magnet and in the air gap allow one to accurately measure Φ_{pm} and Φ_δ respectively. In contrast, Φ_σ occurs in all areas of the machine that are not part of either the air gap or the magnets and is therfore more difficult to extract from the finite element solution. Since both leakage factors describe the same phenomenon, the factors are related to each other through Equation (4.6).

$$\sigma_{pm} = \frac{1}{1+\sigma_f} \tag{4.6}$$

From the geometry of the motor one can find the concentrated reluctances according to the general reluctance formula (3.10) from Section 3.1.1 by properly adapting the equation's parameters: For the air gap reluctance R_δ of one side (Figure 4.3) the gap length l is the air gap δ and the covered area A is defined by half the rotor's pole width in the x-direction, w_p, and the stator's depth in the z-direction, d_s, as given in Equation (4.7).

$$R_\delta = \frac{\delta}{\mu_0 \cdot \frac{1}{2} w_p \cdot d_s} \tag{4.7}$$

For the permanent magnet reluctance R_{pm} the gap length l is the permanent magnet's width w_{pm} and the area A is the product of the stator height h_s and the stator depth d_s, which leads to Equation (4.8).

$$R_{pm} = \frac{w_{pm}}{\mu_0 \cdot \mu_{r_{pm}} \cdot h_s \cdot d_s} \tag{4.8}$$

The case is more complicated for the leakage reluctances. The affected area A, which is the area penetrated by the leakage flux, is defined by one half of the pole pitch τ_p and by the stator's depth d_s for the xy-plane leakage or the stator's height h_s for the xz-plane leakage. This is a reasonable approach considering that the leakage covers the stator in x-direction from the middle of one stator iron pole to the next no matter how

wide the magnet is, because in the middle of the stator, due to the stator's symmetry, the leakage must be zero before the leakage flux of the next pole pitch with an opposite magnetization direction can develop. For the leakage gap length l_l it is assumed that the flux lines follow a semi-circle as shown in Figure 4.5. The radius can be determined by two different approaches. The first one is shown on the left side of Figure 4.5. In that approach a fixed leakage gap length is assumed, which is $l_l = \frac{1}{2}\tau_p \cdot \pi$ for any magnet width [5]. For a medium magnet width this solution yields satisfactory results. Nevertheless, by choosing a smaller permanent magnet width, as indicated in the lower cases in Figure 4.5, it becomes obvious that the first approach underestimates the leakage by assuming a too large leakage gap length. For a larger permanent magnet width the leakage is overestimated. The second approach, shown on the right side of Figure 4.5, determines the leakage gap length as a multiple of the permanent magnet width w_{pm} such that $l_l = k \cdot w_{pm} \cdot \pi$. The factor k is introduced as a variable correction factor that must be about 25-35% larger than one half reflecting the fact that the average radius must be larger than half the magnet's width as will be shown after the derivation of the leakage reluctances.

The leakage reluctances for the xy- and the xz-plane, R_{σ,xy_f} and R_{σ,xz_f} for the fixed width approach and R_{σ,xy_v} and R_{σ,xz_v} for the variable width approach, are derived as given in Equations (4.9)-(4.12).

$$R_{\sigma,xy_f} = \frac{\frac{1}{2}\tau_p \cdot \pi}{\mu_0 \cdot \tau_p \cdot d_s} = \frac{1}{2\mu_0 \cdot d_s} \tag{4.9}$$

$$R_{\sigma,xz_f} = \frac{\frac{1}{2}\tau_p \cdot \pi}{\mu_0 \cdot \tau_p \cdot h_s} = \frac{1}{2\mu_0 \cdot h_s} \tag{4.10}$$

$$R_{\sigma,xy_v} = \frac{k \cdot w_{pm} \cdot \pi}{\mu_0 \cdot \tau_p \cdot d_s} \tag{4.11}$$

$$R_{\sigma,xz_v} = \frac{k \cdot w_{pm} \cdot \pi}{\mu_0 \cdot \tau_p \cdot h_s} \tag{4.12}$$

By connecting the leakages in parallel the total leakage reluctance for the fixed width case are derived from (4.9) and (4.10) as in Equation (4.13) and for the variable width version from (4.11) and (4.12) as in Equation (4.14).

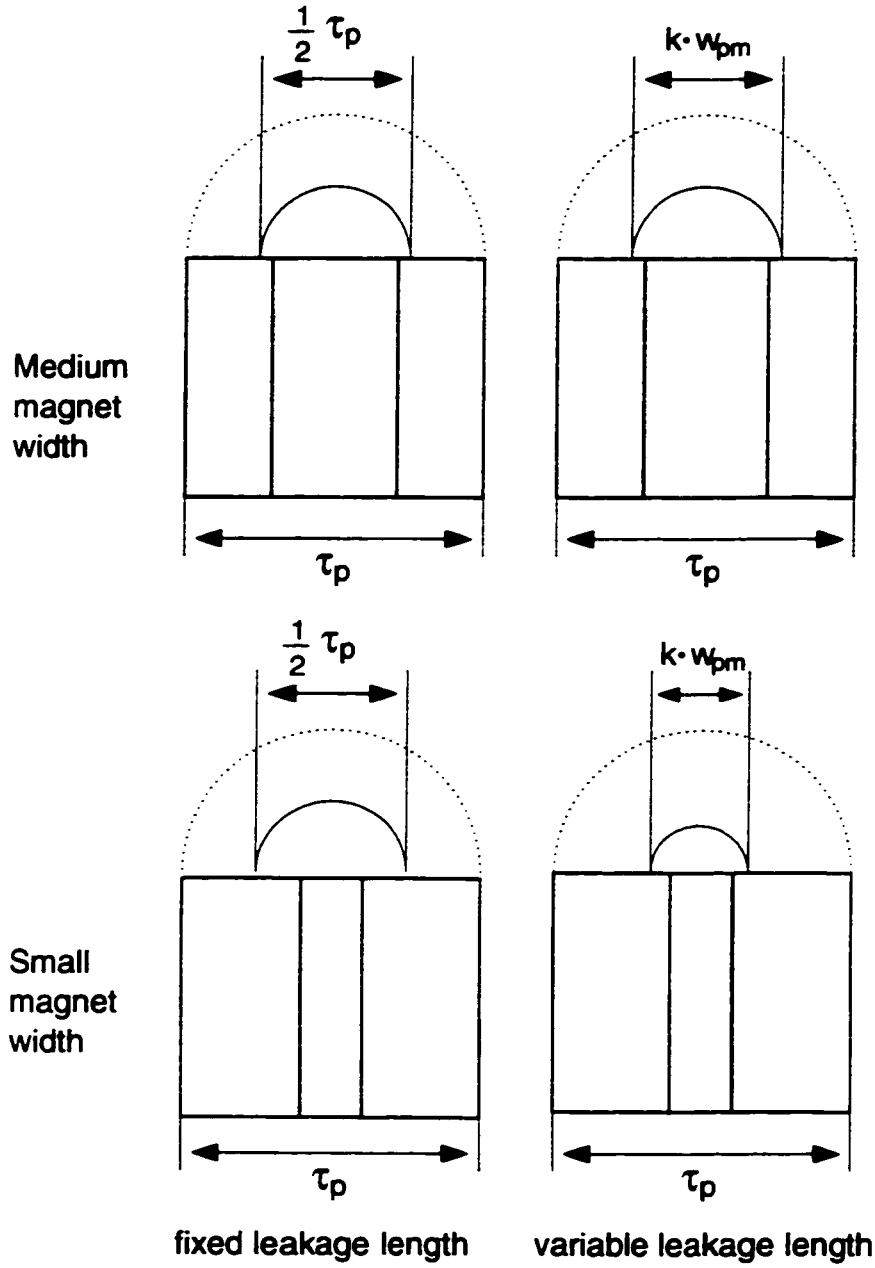

Figure 4.5: Fixed and variable leakage gap length approaches for the *reduced magnet material* design

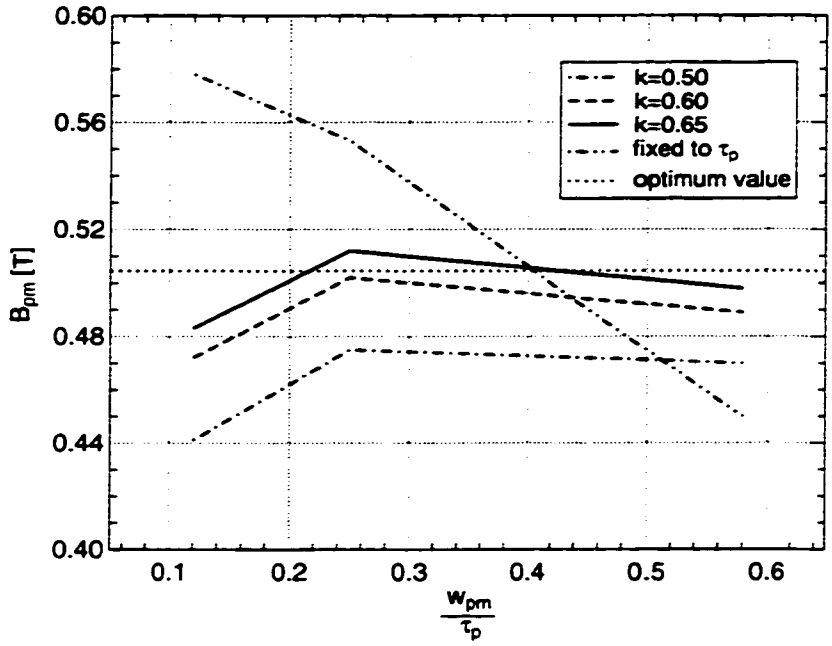

Figure 4.6: Comparison of different leakage gap compensation factors k for the *reduced magnet material* design

$$R_{\sigma_f} = R_{\sigma,xy_f} \left\| \frac{1}{2} R_{\sigma,xz_f} = \frac{\pi}{2\mu_0 \cdot (2h_s + d_s)} \right. \tag{4.13}$$

$$R_{\sigma_v} = R_{\sigma,xy_v} \left\| \frac{1}{2} R_{\sigma,xz_v} = \frac{\pi \cdot k \cdot w_{pm}}{\mu_0 \cdot \tau_p \cdot (2h_s + d_s)} \right. \tag{4.14}$$

For the total reluctance without the iron reluctances as seen from the source Θ_{pm} Equation (4.1) simplifies to Equation (4.15) following the equivalent circuit.

$$R_t = R_{pm} + (2R_\delta \,||\, R_\sigma) = R_{pm} + \frac{2R_\delta}{1 + \sigma_f} = R_{pm} + 2R_\delta\,\sigma_{pm} \tag{4.15}$$

The introduction of a correction factor is a common method to accurately meet a design objective. The aim is to define a correction factor that improves the results over a wide range of other parameter changes or to establish different characteristics for certain parameter ranges. In this reluctance case it is shown that a fixed correction factor can be used for a wide range of permanent magnet widths. Three finite element analysis series

for $k = 0.5$, 0.6 and 0.65 are performed for a wide range of $\frac{w_{pm}}{\tau_p}$ ratios with the rotor at the position $x = 0.5\,\tau_p$ to investigate the impact of the correction factor k. The *optimum* value for the material used in the calculations (Figure 4.2) is $B_{pm} = \frac{1}{2}B_r = 0.5045$. According to Figure 4.6, that displays the results of the finite element analyses, the value $k = 0.65$ delivers a curve deviating the least from the *optimum* flux density value for a wide range of $\frac{w_{pm}}{\tau_p}$ ratios. It can be seen that a value smaller than $k = 0.65$ generally overestimates the leakage, which means that the design in reality has less leakage than assumed. Therefore, the leakage reluctance R_σ is larger than assumed compared to the permanent magnet's reluctance R_{pm}. That way the total permanent magnet flux Φ_{pm} is smaller than it is designed for, resulting in a lower than *optimum* magnet flux density B_{pm}. This is generally undesirable, not only because of the uneconomic magnet use, but also because of a reduced air gap flux density and possible demagnetization of the magnets (see Section 4.3.4). For comparison the results for the case with a leakage length l_l fixed to the pole pitch τ_p are shown in Figure 4.6 as well. The simulation results confirm the theoretical considerations that a variable width allows a better match to the *optimum* flux density in the permanent magnet B_{pm}. As a result, the variable leakage length approach is used in the following finite element evaluations for its higher accuracy. The derivations of the machine design equations for both leakage models are given in the next section for comparison.

4.1.2 Machine Design Equations

First the actual machine design procedure requires that the abstract quantities such as leakage or air gap reluctance be converted into meaningful design parameters, then the following two step design approach is taken:

1. Find the permanent magnet width w_{pm} for an *optimum magnet use design* without any leakage.

2. Adjust the magnets height h_s to account for the leakage while retaining the *optimum magnet use*.

By following this strategy the machine design takes the leakage into account and makes *optimum* use of the permanent magnet material by operating it at $B_{pm} = \frac{1}{2}B_r$. It also

allows an estimation of the air gap flux density and the expected force density. From the derivations of the reluctances in the previous section one can see that the design phase does not take saturation into account. Therefore, the results are only applicable as long as the magnetic circuit stays out of saturation. A reasonable estimation of the air gap flux density provides a solid way to anticipate and avoid saturation effects. Over-designing the field permanent magnets increases the weight and the losses of the machine with little benefit for the force density in the physical machine. The exact implications of over-designing the magnets, saturation and different geometries are investigated in detail using 3D finite element solutions in Sections 4.2 and 4.3.

To determine the flux accumulation effect of the permanent magnet field in the air gap, the rotor pole width w_p can be related to the permanent magnet (or stator) height h_s through the mechanical flux accumulation factor C_m. By using the quotient of the permanent magnet's area $A_{pm} = h_s \cdot d_{pm}$ to the pole gap area $A_p = w_p \cdot d_p$, the geometry factors are linked as given in Equation (4.16).

$$C_m = \frac{A_{pm}}{\frac{1}{2}A_p} = \frac{2\,h_s \cdot d_{pm}}{w_p \cdot d_p} = \frac{2\,h_s}{w_p} \tag{4.16}$$

Note that although the permanent magnet depth d_{pm} and the pole depth d_p are often slightly different in a physical design to be able to mount magnets and core iron parts properly, it is assumed here that $d_s = d_{pm} = d_p$. Taking leakage into account the effective flux accumulation factor C_{eff} can be defined following the equivalent circuit as in Equation (4.17).

$$C_{eff} = C_m \frac{1}{1+\sigma_f} = C_m \sigma_{pm} \tag{4.17}$$

For the no-leakage case in the design Step 1 the mechanical and the effective flux accumulation factor are equal since for no leakage $\sigma_{pm} = 1$.

The permanent magnet flux Φ_{pm} as defined by the geometry is given in Equation (4.18). Through σ_{pm} the equation also establishes the relationship between the flux density in the permanent magnet B_{pm} and the flux density in the air gap caused by the magnets $B_{\delta_{pm}}$.

$$\Phi_{pm} = \frac{\Theta_{pm}}{R_c} = B_{pm}\,A_{pm} = \frac{1}{2}A_p\,\frac{B_{\delta_{pm}}}{\sigma_{pm}} \tag{4.18}$$

Using Equations (4.16), (4.17) and (4.18) and the *optimum magnet use condition* $B_{pm} = \frac{1}{2}B_r$ one can derive the flux densities in the air gap (Equation (4.19)) and in the permanent magnet (Equation (4.20)) as a function of the mechanical parameters and the effective flux accumulation factor C_{eff}.

$$B_{\delta_{pm}} = \frac{B_r\, C_{eff}}{1 + \frac{2\delta}{w_{pm}}\mu_{r_{pm}} C_{eff}} \tag{4.19}$$

$$B_{pm} = \frac{B_r}{1 + \frac{2\delta}{w_{pm}}\mu_{r_{pm}} C_{eff}} \tag{4.20}$$

Substituting the reluctances R_δ (Equation (4.7)) and R_{σ_f} (Equation (4.13)) or R_{σ_v} (Equation (4.14)) into Equation (4.4), the field leakage factors σ_{f_f} and σ_{f_v} are derived as functions of the mechanical measurements for the fixed leakage length in Equation (4.21) and the variable leakage length in Equation (4.22).

$$\sigma_{f_f} = \frac{8\,\delta\,(2\,h_s + d_s)}{\pi\, w_p\, d_s} \tag{4.21}$$

$$\sigma_{f_v} = \frac{4\,\delta\,\tau_p\,(2\,h_s + d_s)}{\pi\, w_p\, k\, w_{pm}\, d_s} \tag{4.22}$$

Using Equations (4.16), (4.17), (4.20) and (4.21) or (4.22) one can find a leakage adjusted mechanical flux accumulation factor C_m^* based on the initial permanent magnet width found in Step 1 of the design procedure and the mechanical parameters introduced in Section 4.1. For the fixed leakage length case $C_{m_f}^*$ is expressed by Equation (4.23) and $C_{m_v}^*$ by Equation (4.24) for the variable leakage length reluctances.

$$C_{m_f}^* = \frac{w_{pm}\, d_s\,(\pi\, w_p + 8\,\delta)}{2\,\delta\, w_p\,(\pi\,\mu_{r_{pm}}\, d_s - 4\, w_{pm})} \tag{4.23}$$

$$C_{m_v}^* = \frac{d_s\,(\pi\, w_p\, k\, w_{pm} + 8\,\delta\,\tau_p)}{2\,\delta\, w_p\,(k\,\pi\,\mu_{r_{pm}}\, d_s - 2\,\tau_p)} \tag{4.24}$$

To verify that both equations from a theoretical point of view lead to an *optimum magnet use solution* one can substitute Equations (4.21) and (4.23) or (4.22) and (4.24) into 4.17. Either result for C_{eff} then is substituted into (4.20) which in both cases resolves to the optimum magnet use condition $B_{pm} = \frac{1}{2}B_r$. The analytical approach

therefore is conclusive in itself, but it should be noted, that the ability to match the optimum magnet flux density value in a physical machine or in a finite element analysis largely depends on the quality of the leakage model itself. For that reason the adjustable correction factor k was introduced.

Another interesting aspect of this design approach that follows from the equations above is that the initially chosen flux accumulation factor in the no-leakage case equals the actual effective flux accumulation factor C_{eff} after the leakage is included. This is advantageous, because with the knowledge of the residual flux density of the permanent magnet B_r it allows to directly design for a specific air gap flux density according to Equation (4.25).

$$B_{\delta_{pm}} = \frac{1}{2} B_r C_{eff} \tag{4.25}$$

The design procedure can be summarized by the following step-by-step approach:

1. Choose an initial set of parameters for δ, τ_p, w_p, C_{eff} and d_s. In Section 4.2 will be determined, which values represent good choices.

2. Choose a permanent magnet material to find the associated relative permeability $\mu_{r_{pm}}$ of the magnets.

3. Calculate the width of the permanent magnet using $w_{pm} = 2\,\mu_{r_{pm}}\,C_{eff}\,\delta$[1].

4. Calculate the mechanical flux accumulations factor C_m^* using Equation (4.23) or (4.24).

5. Calculate the magnet height $h_s = \frac{1}{2} C_m^* {w_p}^2$.

6. Evaluate $B_{\delta_{pm}}$ and B_{pm} according to (4.19) and (4.20) respectively.

7. Compare with finite element analysis results and adjust parameters if necessary.

Following this procedure, parameter tables such as the one shown in Table 4.1 are derived and verified with 3D finite element analyses. These tables make an excellent

[1]This equation follows from Equation (4.16) and from condition $B_{pm} = \frac{1}{2} B_r$. For the leakage-free case considered in this step the latter condition is equivalent to the formulation that $2R_\delta = R_{pm}$. Writing R_δ and R_{pm} according to equations 4.7 and 4.8 and substituting 4.16 delivers the expression given for w_{pm}.

[2]This equation equivalent to Equation (4.16), but including leakage.

Table 4.1: Exemplary design parameters for $w_{pm} = 10\,mm$, $\tau_p = 12.5\,mm$, $d_s = 20\,mm$, $\delta = 0.5,\ 0.75$ and $1.0\,mm$ and $C_{eff} = 1.5,\ 2.0,\ ...,\ 3.5$

Air gap δ [mm]	rel. perm. PM $\mu_{r_{pm}}$	Flux acc. factor C_{eff}	PM width w_{pm} [mm]	Pole pitch τ_p [mm]	Rotor pole width w_r [mm]	Stator depth d_s [mm]	Flux acc. factor C_m [mm]	PM/ stator height h_s [mm]	Air gap flux density $B_{\delta_{pm}}$ [T]
0.50	1.048	1.5	1.57	12.5	10	20	2.94	14.72	0.76
0.50	1.048	2.0	2.10	12.5	10	20	3.65	18.25	1.01
0.50	1.048	2.5	2.63	12.5	10	20	4.36	21.78	1.26
0.50	1.048	3.0	3.14	12.5	10	20	5.06	25.31	1.51
0.50	1.048	3.5	3.68	12.5	10	20	5.77	28.84	1.77
0.75	1.048	1.5	2.36	12.5	10	20	2.94	14.72	0.76
0.75	1.048	2.0	3.14	12.5	10	20	3.65	18.25	1.01
0.75	1.048	2.5	3.95	12.5	10	20	4.36	21.78	1.26
0.75	1.048	3.0	4.72	12.5	10	20	5.06	25.31	1.51
0.75	1.048	3.5	5.50	12.5	10	20	5.77	28.84	1.77
1.00	1.048	1.5	3.14	12.5	10	20	2.94	14.72	0.76
1.00	1.048	2.0	4.19	12.5	10	20	3.65	18.25	1.01
1.00	1.048	2.5	5.24	12.5	10	20	4.36	21.78	1.26
1.00	1.048	3.0	6.30	12.5	10	20	5.06	25.31	1.51
1.00	1.048	3.5	7.34	12.5	10	20	5.77	28.84	1.77

preliminary selection tool to narrow down the choice of parameters by excluding extreme geometries, such as very high but narrow, bar-like magnets that yield very high leakage flux values. An extensive set of tables is given in Appendix A.

4.1.3 Finite Element Analysis and Results

In Table 4.1 one can see that all designs differ in their mechanical parameters from one-another. It is an impossible task to define all the (several hundred) models investigated here through the graphical user interface provided by the Vector Fields Opera 3D software used for the analyses. Therefore, a parameterized model need to be programmed that only depends on the design parameters shown in Figure 4.1. Although Vector Fields makes the claim, that fully parameterized models can be programmed within their Opera 3D software package, close inspection of the program's facilities reveal that the software can only do limited partial parameterization, that does not meet the requirements of the problem at hand. For example, single points can be shifted or scaled once, but consecutive shift/scale operations are not possible, because the selection scheme used by the program operates with fixed coordinates.

Java Classes for the Input File Generation

Opera 3D offers the possibility of saving and loading geometry definitions created with the graphical user interface in human readable text format. By analyzing the file format it is possible to create or change models by manipulating those input files directly. A set of Java classes developed into a Java package encapsulate the commands needed for the model creation [56]-[58]. The Java program first collects all the model information in proprietary data structures and translates them after all structures are defined into two Opera 3D input files: One with the actual model geometries and one with the meshing commands and the database creation commands, material definitions and periodicity conditions. Two files are needed, because the model data input file, while sharing the same commands with the command input files cannot execute all of them. The benefit of collecting the data first is that the strict input order in the Opera 3D model geometry files can be discarded, allowing much more flexible model definitions. It is possible to generate Opera 3D command files that loop through different model cases, but it was decided to

define each model independently to avoid memory overflows or other undesirable side effects.

Most of the classes map directly onto primitive commands for the Opera 3D input files, but some classes implement a higher level of functionality. The best example for the latter case is the class *Areas*: Opera 3D requires one to define each area separately through a set of points. Limiting the area shapes to rectangles and trapezoids, which is sufficient for the models investigated here, it is possible to develop an algorithm that automatically creates rectangular and trapezoidal areas for all given points, which reduces the area creation within the Java model definition to only one command instead of several hundred point definitions that are now generated automatically.

All the functionality of the model creation classes is solely accessible through the method interface of the class *OP3Gen*. It provides the interface for all inner classes and other functionality necessary to create the machine model. Figure 4.7 shows the class hierarchy of the model generator. The classes with a light grey background are inner classes, while entries with a darker grey background are Java interfaces. Principally the classes *Point*, *Area* and *SolverData* could be inner classes as well, but for better documentation they were extracted, because their types are needed in the model definition and post-processing classes *RMMi* and *RMMiPost*. The class *RMMi* implements the parameterized motor model with the support of the general *OP3Gen* methods and reads the model parameters from an input file that is created with a text editor. *RMMiPost* creates a parameter file for the post processing, i.e. the extraction of the results and their storage after the simulation solution is computed, by evaluating the same input file as the one used by *RMMi*. That is not only convenient, but also avoids human error in the post-processing. The evaluation of the model's parameters such as $B_{\delta_{pm}}$ and B_{pm} is carried out with an Opera 3D post-processor command file that reads the parameter file created by *RMMiPost*. The command file is documented in Appendix B. For the documentation of the input file formats used see Appendix C.

Figure 4.8 depicts an example model generated by the *RMMi* class and executed in Opera 3D. The ring winding is not shown. Note that this model differs slightly from the model schematic given in Figure 2.14: In the model shown in Figure 4.8 the rotor iron has an extra $2\,mm$ edge in the winding window. This edge is introduced to the simulation model to have a more realistic model around the sensitive air gap region: To reduce eddy

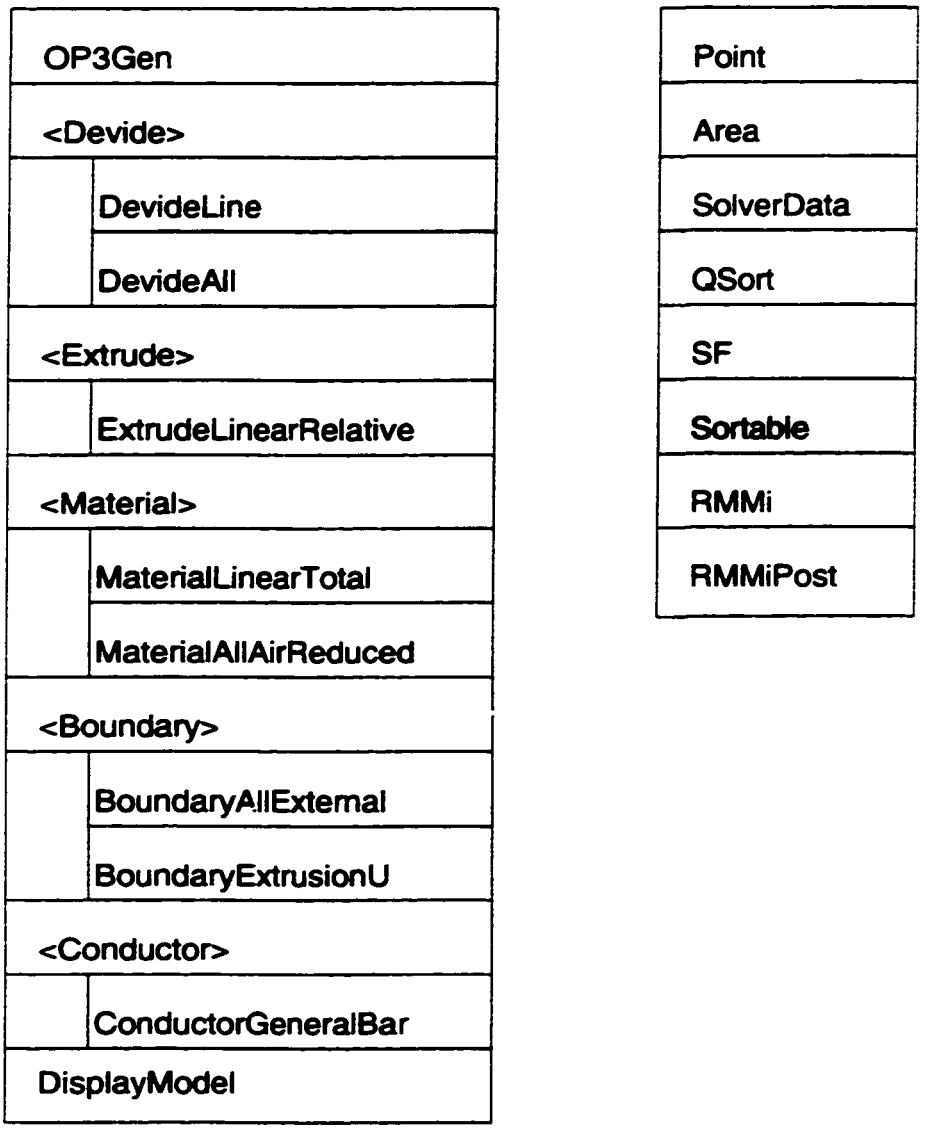

Figure 4.7: Java Class Hierarchy for the Vector Fields Opera 3D model generator

currents the rotor iron is constructed from wound core material which is cut into several pieces. The minimum inner edge radius of the wound cores is typically 1.5-$2.5\,mm$, which therefore is the minimum distance for cutting the wound core, leaving the modeled edge at the inside. See Section 4.3.1 for lamination details. Also note that the discretization around the iron edges in x-direction is increased for higher accuracy at those edges that can have almost singular field values in linear analyses without saturation.

Analogous to the 2D finite element model of the *slanted rotor design*, the *reduced magnet material* model has a linear even periodicity in the x-direction. The padding with an air layer on all other sides to simulate all possible leakages follows the approach for the 3D finite element model of the *slanted rotor design*. The magnet material is modeled with linear, but anisotropic characteristics, because the characteristic of the permanent magnet material is almost perfectly linear. The magnet's magnetization vector points in the positive or the negative x-direction, and the non-magnetic properties of the magnet are applied in the y- and the z-direction. In all three directions the magnets have a relative permeability of $\mu_{r_{pm}} = 1.048$. The current density in the winding window is automatically derived to match the current-turns value given in the input file for changing winding cross sections.

Results

The design equations introduced in the step-by-step approach in Section 4.1.2 perform very well for all of the 270 cases (see Appendix A) that do not exhibit extreme geometries. For example, in a case of an extremely high stator in the x-direction that is very slim in the z-direction by a ratio of more than 15:1, the design deviates from the *optimum* solution by $+17\%$. This design also produces 90% of leakage loss, which makes it an undesirable design under any circumstance. Therefore, this large deviation from the optimum value in this example does not provide any grounds for changes to the theoretical model. All other results lie in a very small error margin of $\pm 5\%$ for the flux density in the permanent magnet B_{pm}.

Figure 4.9 shows an example from the values given in Appendix A for the flux density in the permanent magnet B_{pm} for an air gap of $\delta = 0.75\,mm$ and a rotor pole width of $w_p = 0.85\,\tau_p$ over the effective flux accumulation factor C_{eff} for pole pitches of $\tau_p = 8.82.\ 11.76$ and $14.71\,mm$. The figure also shows the extreme case with the

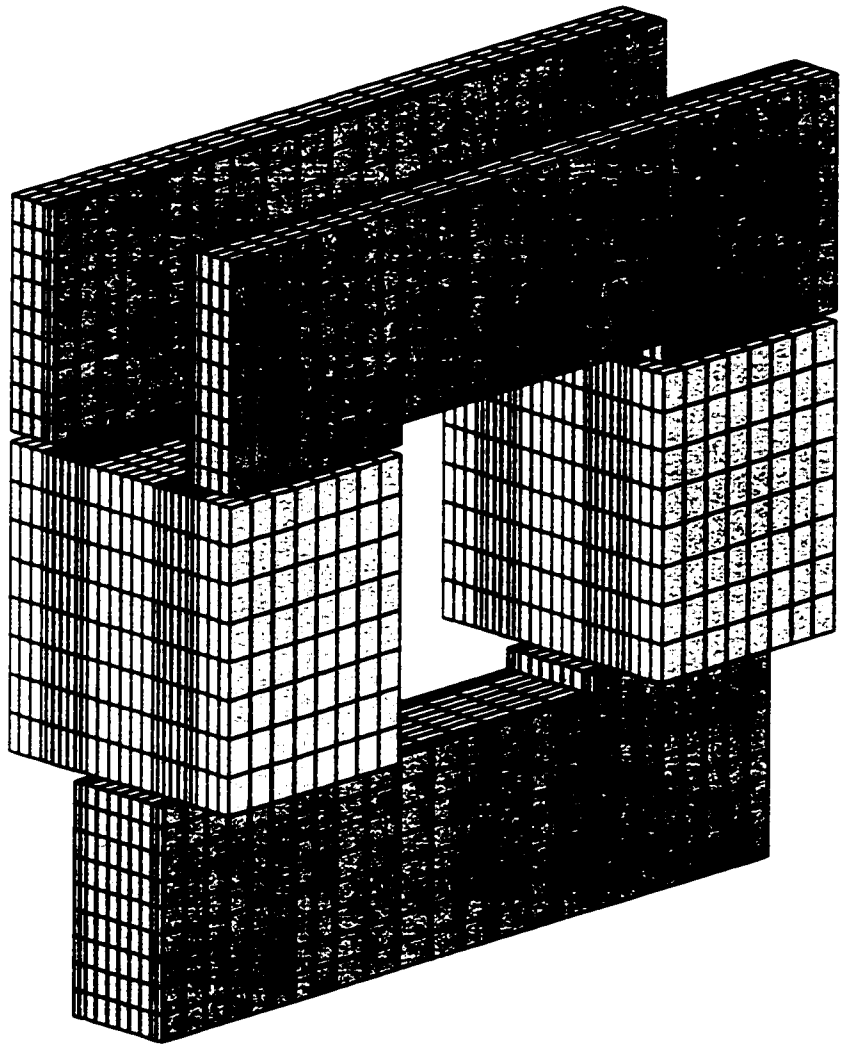

Figure 4.8: Generated *reduced magnet material* model with finite element discretization

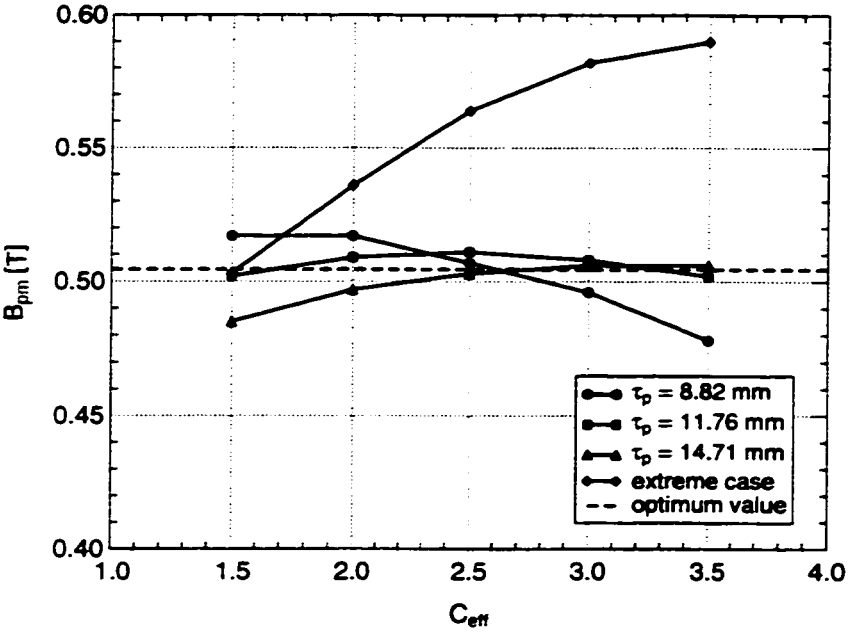

Figure 4.9: Comparison of the finite element analysis B_{pm} to the optimum value

magnet width to height ratio between 8.1:1 at $C_{eff} = 1.5$ and 15.7:1 at $C_{eff} = 3.5$.

The air gap flux density B_δ from the finite element analysis matches the values predicted by Equation (4.25) closely. While the maximum error in one case out of the 270 calculated cases reaches 19.2%, the error for cases that avoid geometrical extremes is in the same $\pm 5\%$ range as for the permanent magnet flux density B_{pm}. In most cases the error is even less than that as shown in Figure 4.10.

4.2 Design Parameters and Limitations

Although it is possible with the approach given in Section 4.1 to find a minimum magnet use solution for a given set of parameters, it is the choice of the materials and parameters themselves that determine the success or failure of an actual machine design. With theoretical considerations and the help of finite element calculations the question of how to find a good set of parameters for a machine design is answered in the following.

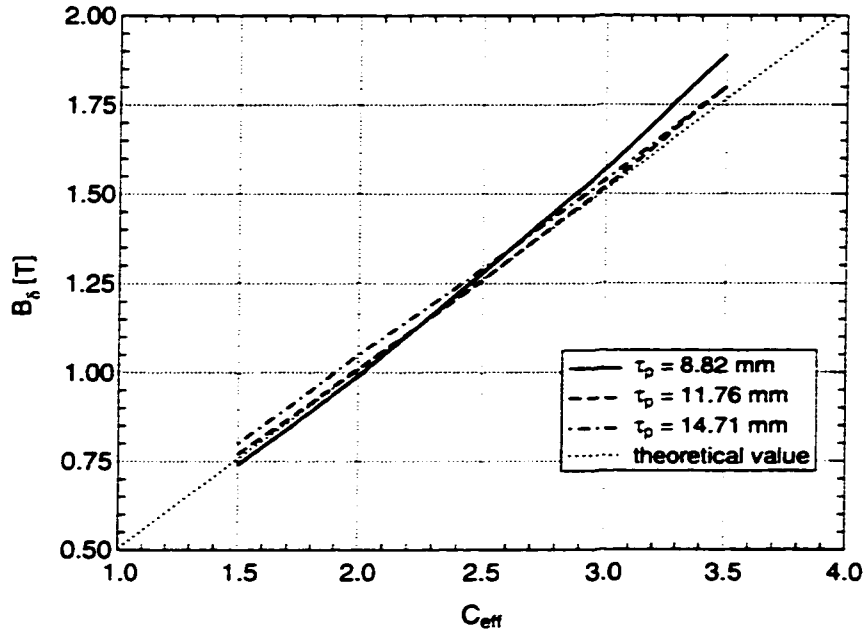

Figure 4.10: Comparison of the finite element analysis B_δ to the design value

4.2.1 Magnet Materials

The choice of the magnet material dictates the feasibility of a certain motor layout. Especially when large air gaps are required for mechanical reasons, it is advantageous to use high performance rare earth magnets to achieve the desired flux density in the air gap B_δ (see Section 4.3.3). The mechanical properties of the permanent magnet material set another design limit: Both SmCo and NdFeB magnets are mechanically very hard and brittle. The use of diamond cutting tools is needed and it is generally preferred to use water jet cutting techniques. The consequence for the machine design is that the minimum manufacturable magnet width is about $w_{pm} = 2\text{-}3\,mm$. This inherently excludes very small pole pitches of less than $\tau_p = 5\,mm$. The Curie temperature of SmCo magnets usually ranges between 720-825°C, allowing safe operation temperatures up to 350°C, but SmCo is also the most expensive material and reaches maximum residual inductances between 0.88 and 1.01 T at room temperature. NdFeB magnets on the other hand have a much lower Curie temperature of 310-350°C, allowing safe operation between 110-220°C, but reach residual inductances of $B_r = 1.01\text{-}1.28\,T$ at

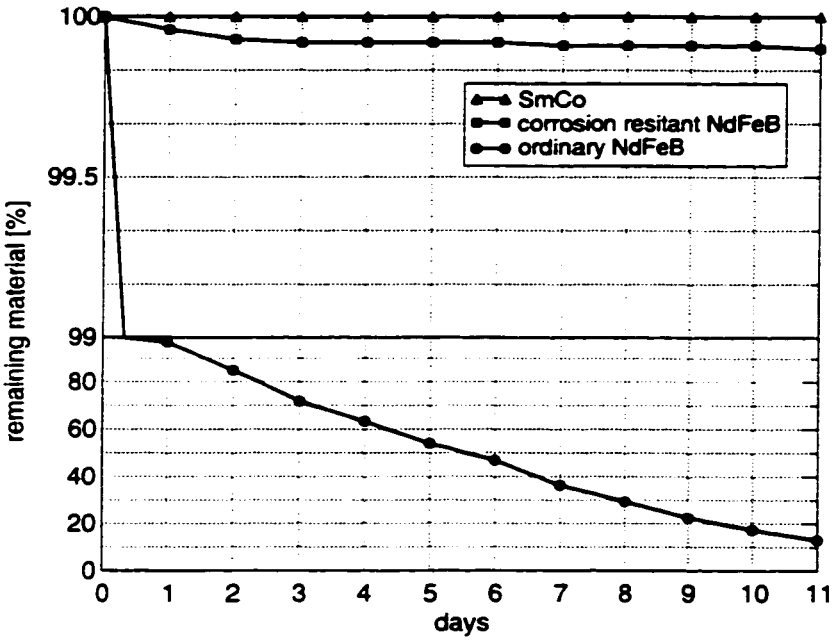

Figure 4.11: Corrosion resistance characteristics of corrosion resistant and highly corrosion degradable NdFeB magnet materials

room temperature, where the alloys with the highest B_r have the lowest safe operation temperature. In all cases the magnetization decreases non-linearly with increasing temperature. Linear temperature correction therefore is usually only valid within a 20-100°C temperature range.

The permanent magnet material used in the analysis is the highly corrosion resistant NdFeB magnet material of the type 190/250h (Magnetfabrik Schramberg) [49]. The material characteristics are adjusted for a typical machine temperature of 80°C. For the temperature correction the median remanent induction of the permanent magnet at 20°C $B_{r,20°C} = 1.06\,T$ is subjected to the temperature correction coefficient $T_{c,B} = -0.085\frac{\%}{K}$, giving the corrected value for the operation temperature (80°C) as $B_{r,80°C} = 1.009\,T$. Similarly, with a coercive force of $H_{cB,20°C} = 820000\,\frac{A}{m}$ and the temperature correction factor for the coercive force $T_{c,H_B} = -0.11\frac{\%}{K}$, the corrected value for $T = 80°C$ results in $H_{cB,80°C} = 765880\,\frac{A}{m}$. Provided that the material is magnetically strictly linear the relative permeability of the magnets is $\mu_{r_{pm}} = \frac{B_{r,80°C}}{\mu_0 H_{c,80°C}} = 1.048$.

While the type 190/250h magnet is not the highest performance material, it is a new

development of the Magnetfabrik Schramberg, Germany, which has the benefit of being highly resistant to corrosion. Figure 4.11 [49] illustrates the importance of that property at a temperature of $130°C$, a pressure of $3\,bar$ and a steam saturated environment. Ordinary NdFeB magnets thoroughly corrode in this environment so that after 11 days only 13% of the magnet material is left. Clearly that means that this material requires an air and water tight coating for any application. It is doubtful that ordinary NdFeB material could be used successfully longterm in such a machine design because of the material's exposure to mechanical stresses, harsh environments and temperature changes in its intended transportation application. Corrosion resistant NdFeB and SmCo magnets on the other hand exhibit only negligible surface corrosion with a magnet material loss less than 0.1% over 11 days. They do not need a protective coating, which makes them the materials of choice for transverse flux motor applications.

4.2.2 Magnet Width

The initial design phase as outlined in Section 4.1.2 is solely concerned with the *optimum* use of the magnet material and does not take the implications of different flux path architectures for the ring winding field into account. In Section 3.2.3 it was already found that the force density increases when the stator iron width increases, which was attributed to the better flux path for the ring winding field. Therefore, one could assume that the wider the stator iron is, the better is the overall design. On the other hand, the permanent magnet width is tied to the overall performance of the machine, because the ampere-turns equivalent of the permanent magnet Θ_{pm} depends on the magnet's width w_{pm} and the coercive force H_c as given in Equation (4.26).

$$\Theta_{pm} = H_c\, w_{pm} \tag{4.26}$$

Moreover the permanent magnet width is connected to the stator iron width through the Equation (4.27).

$$w_{pm} = \tau_p - w_s \tag{4.27}$$

Therefore, for a fixed pole pitch τ_p this is a trade-off situation. A solution needs to be found that offers the best compromise between the field performance from the

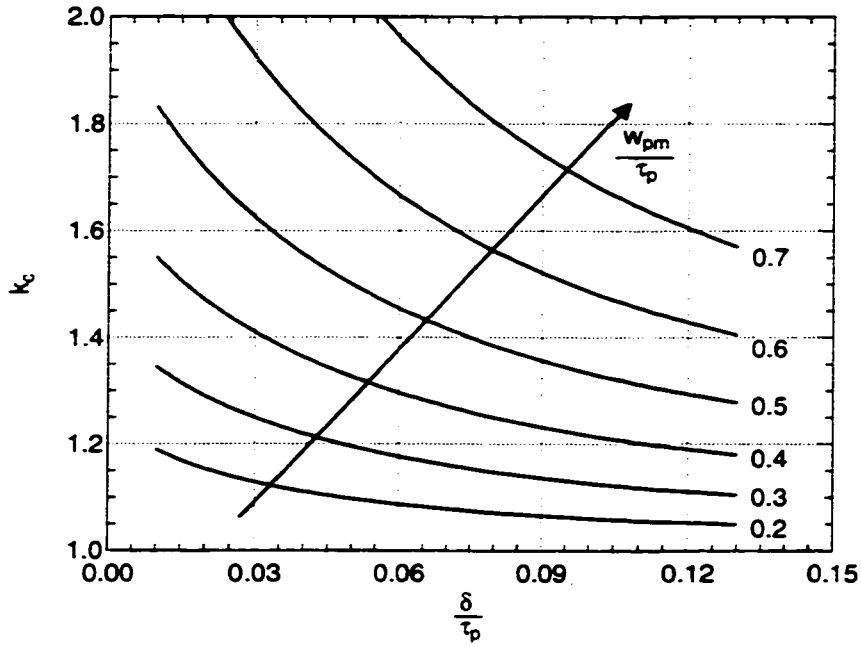

Figure 4.12: Carter's slot factor adapted for passive rotor TFMs

permanent magnet and the flux path of the stator field. To estimate the impact of the stator pole width on the quality of the flux path, Carter's slot factor k_c from classical machine design [17] can be adapted to the passive rotor transverse flux motor (Equation (4.28)) in which case the pole gap is equivalent to the permanent magnet width w_{pm} [5]. The impact of the pole gap can be expressed as a fictitious increase of the air gap width δ^* (Equation (4.29)) compared to the mechanical air gap δ.

$$k_c = \frac{\frac{w_{pm}}{\tau_p} + 5\,\frac{\delta}{\tau_p}}{\frac{w_{pm}}{\tau_p}\left(1 - \frac{w_{pm}}{\tau_p}\right) + 5\,\frac{\delta}{\tau_p}} \tag{4.28}$$

$$\delta^* = k_c\,\delta \tag{4.29}$$

Consequently, the larger k_c is, the worse is the flux path for the ring winding field because of the fictitiously increased air gap δ^*. Figure 4.12 illustrates k_c for different magnet width to pole pitch ratios $\frac{w_{pm}}{\tau_p}$ over the air gap to pole pitch ratio $\frac{\delta}{\tau_p}$. The analysis of different parameter layouts reveals that k_c for passive rotor transverse flux motor designs can be expected to lie in the $k_c = 1.2$-1.6 range. By keeping all geometrical and

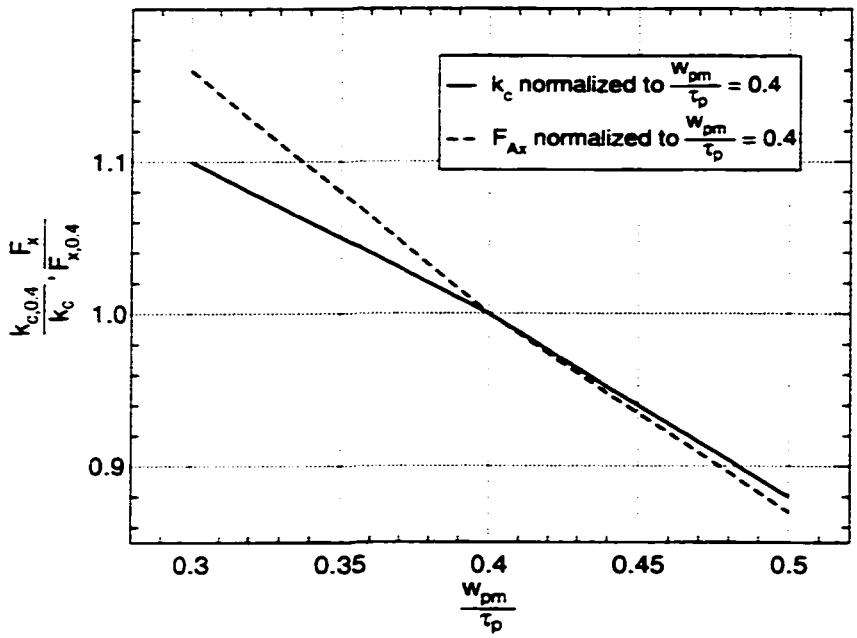

Figure 4.13: Carter factor and force maximum from 2D finite element analysis with constant parameters

electrical parameters of the design fixed, except for the width of the permanent magnet w_{pm} and the stator iron width w_s as described in Section 3.2.3, one can observe that the normalized results for the force maximum from the 2D finite element show a very close relation to the normalized inverse of the Carter factor $\frac{1}{k_c}$. Figure 4.13 implies that F_x is inversely reciprocal to k_c ($F_x \propto \frac{1}{k_c}$). The adapted Carter factor therefore is indeed a suitable correction factor for the produced driving force F_x to calculate a more realistic theoretical force density in the design phase. However, if one assumes that all designs use the same magnet material or, in technical terms, one fixes the permanent magnet's coercive force H_c, instead of fixing the equivalent permanent magnet m.m.f., the picture changes significantly. Figure 4.14 shows the force density normalized to the force density at a magnet width of $w_{pm} = 0.4\,\tau_p$ for the *reduced magnet material* design. It can be seen that the m.m.f. loss for a magnet width of $w_{pm} = 0.3\,\tau_p$ cannot be compensated for by the better flux path of the ring winding m.m.f., which leads to a drastic decline in the force density. On the other hand the decline of the force density due to the worsening ring winding m.m.f. path is slowed down for a permanent magnet width of $w_{pm} = 0.5\,\tau_p$

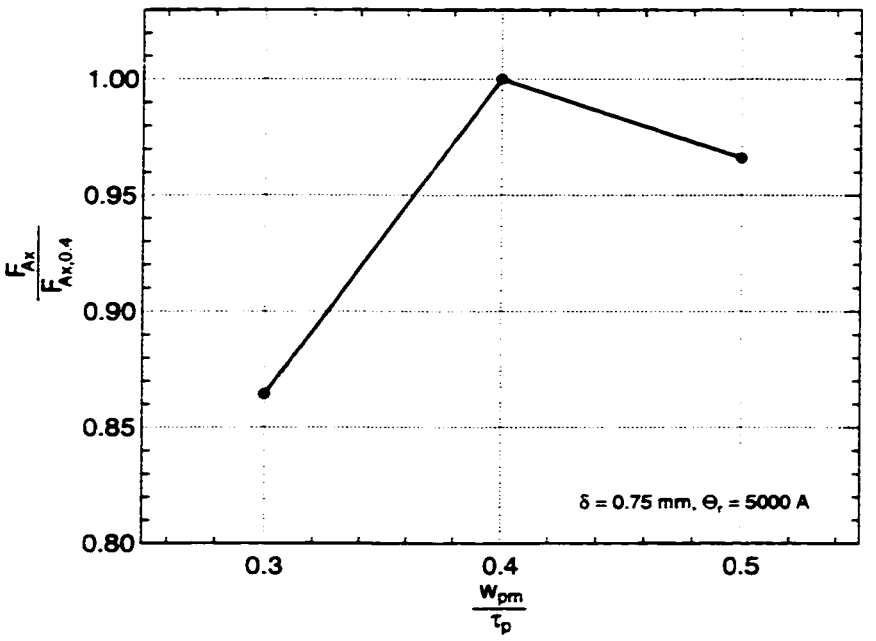

Figure 4.14: Normalized force density for changing magnet width with constant permanent magnet m.m.f.

because of the largely increased permanent magnet m.m.f. It can therefore be concluded, that a permanent magnet width of $w_{pm} = 0.4\text{-}0.5\,\tau_p$ is the best overall solution for a given magnet material.

4.2.3 Rotor Pole Width

In a similar way that the stator iron width influences the flux path of the ring winding field, the rotor pole width w_p can be expected to have an influence on the force densities as well. From a flux path point of view only, one could assume that the wider the rotor is compared to the pole pitch, the higher is the force density. There is however a natural limit to that assumption, when the rotor pole width w_p is equal to the pole pitch τ_p: Extending the width over this limit creates new unwanted alternative flux paths through the neighboring pole pitch's magnets with an opposite magnetization direction, reducing the propelling force density. At the lower end of possible rotor pole widths the limit is set by the permanent magnet width: To produce a high force density in the

$x = 0.5\tau_p$ position there must be a considerable overlap of rotor and stator iron. With a useful magnet width of up to $w_{pm} = 0.5\tau_p$, the minimum rotor pole width for further investigations can be set to $w_p = 0.7\tau_p$.

To give a conclusive answer to the question of the most suitable rotor pole width range, it is necessary to investigate the force density shape for different rotor positions over one pole pitch. Figure 4.15 shows the force density shapes for a motor with parameters in the middle of the investigated parameter range to avoid the influence of extreme geometries on the results ($\delta = 0.75\,mm$, $\tau_p = 11.72\,mm$, $C_{eff} = 2.5$ and $d_s = 20\,mm$). The shapes for different rotor pole width to pole pitch ratios ($\frac{w_p}{\tau_p}$) are shown normalized to the maximum value. It can be seen that the curve for the rotor pole width $w_p = 1.0\tau_p$ does not fully enclose all other cases as one could expect from the preliminary considerations. This finding implies that the adverse effect of misguided portions of the flux already occurs for rotor pole widths smaller than one pole pitch. On the other hand the effect of lower force densities for small rotor pole widths can be seen clearly in the $\frac{w_p}{\tau_p} = 0.7$ case. That means that the rotor pole width for the highest force density lies somewhere in between.

For a numerical evaluation of these results Figure 4.16 shows the force density averages over one pole pitch for different $\frac{w_p}{\tau_p}$ ratios. The figure confirms the observations made for Figure 4.15. It can be seen that the maximum occurs at $\frac{w_p}{\tau_p} = 0.775$ with a fast decrease towards smaller ratios and a slow decrease towards larger ratios. A good choice for a rotor pole width therefore should lie in a range of $\frac{w_p}{\tau_p} = 0.75$-$0.88$. To better cope with saturation effects it appears to be advisable to select a value leaning towards the middle or upper ranges of those values.

4.2.4 Stator Pole Depth

The stator depth largely influences the size of the homogenous field region under the pole. For that same reason conventional electrical machines developed from ring shape structures into drum type machines, it would be best to make the pole depth as long as possible. Due to the cylindrical nature of the rotor and stator of the passive rotor transverse flux motor, the rotor/stator length in the axial direction is limited for mechanical reasons. At the first glance this may appear to be a disadvantage of transverse flux machines compared to conventional machines, but unlike conventional electrically excited

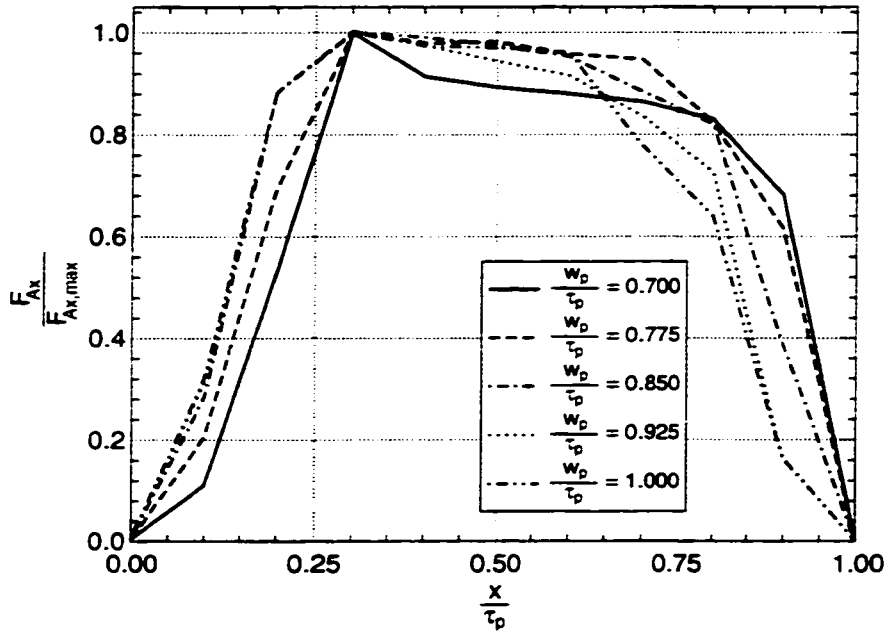

Figure 4.15: Normalized force densities over rotor position for different $\frac{w_p}{\tau_p}$ ratios

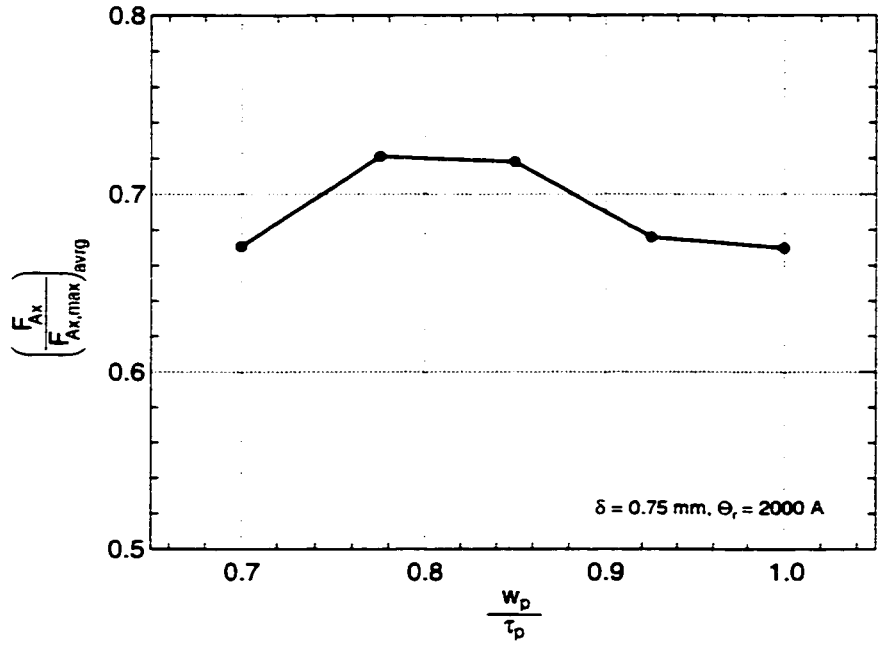

Figure 4.16: Average force densities for different $\frac{w_p}{\tau_p}$ ratios for an air gap of $\delta = 0.75\,mm$ and a ring winding m.m.f. of $2000\,A$-turns

machines, the excitation field for the transverse flux machine is created by permanent magnets, without involving any electrical loss and therefore not influencing the overall machine losses. The trade-off however is the need for a slightly higher amount of magnet material compared to a larger rotor depth resulting in a slight increase in machine cost and weight. It is therefore important to investigate the influence of the stator depth d_s to find mechanically feasible and magnetically viable solutions. The other major influencing factors on the homogeneity of the field under the pole are the air gap size and the rotor pole width. Consequently, the leakage flux as seen from the permanent magnet $\sigma_{pm} = \frac{\Phi_\delta}{\Phi_{pm}}$ as a measure for the actual flux passing through the air gap, is investigated in terms of the three parameters w_p, d_s and δ. Figures 4.17 - 4.19 show the influence of the rotor pole width w_p on the leakage for different air gaps. Note that according to its definition, a larger value of σ_{pm} means that more flux generated by the permanent magnet passes through the air gap. As expected, the leakage loss $\sigma_{loss} = 1 - \sigma_{pm}$ for a small stator depth of $d_s = 10\,mm$ is significantly larger than that for $d_s = 20\,mm$. Furthermore the leakage loss increases for larger air gaps. It is also found that for larger rotor pole widths w_p the rate of increase of σ_{pm} decreases, suggesting that a larger w_p is less sensitive to different stator depths d_s. Figure 4.20 investigates the sensitivity of the leakage σ_{pm} towards different air gaps. It shows that for small air gaps a smaller pole depth has far less impact on the leakage than for larger air gaps. That means that the choice for a reasonable stator depth should be connected to the air gap size. To reach leakage losses of 40% or less, a stator depth of $d_s = 20\text{-}30\,\delta$ must be chosen. Principally, the larger d_s is, the lower is the leakage. However, a larger stator depth d_s also translates into a larger rotor height h_r because of the geometrical properties of cut wound iron cores and the fact that the flux path should not be reduced in the rotor section that crosses over to the other stator half in the z-direction in the model. That means that the space requirement in radial direction increases, resulting in a larger machine diameter. Of course, the power rating of the machine would also increase.

Another important influencing factor on the permanent magnet leakage σ_{pm} is the stator (magnet) height to stator (magnet) width ratio. Figure 4.21 suggest that for reasonable leakage losses of $\sigma_{pm} > 0.6$, the stator height to width ratio should not exceed $\frac{h_s}{d_s} = 1.5$, but if the size of the ring winding requires it, ratios up to $\frac{h_s}{d_s} = 2.0$ are acceptable without excessive losses.

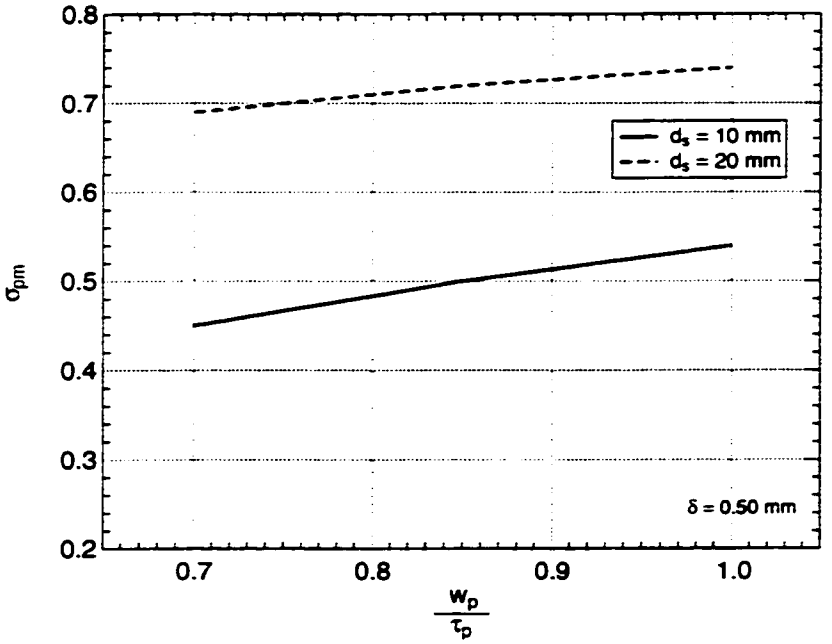

Figure 4.17: Leakage σ_{pm} over pole width/pole pitch ratio for $\delta = 0.5\,mm$

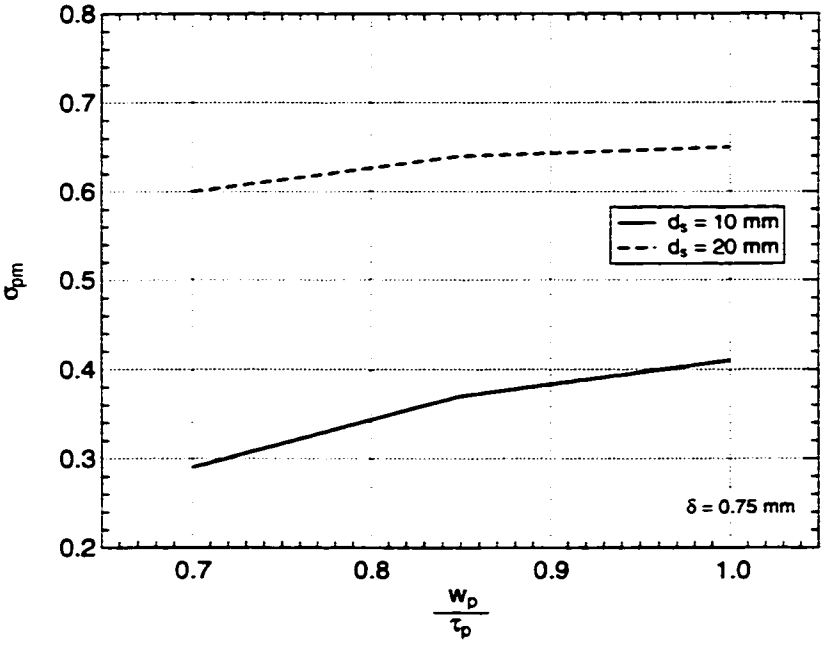

Figure 4.18: Leakage σ_{pm} over pole width to pole pitch ratio $\frac{w_p}{\tau_p}$ for $\delta = 0.75\,mm$

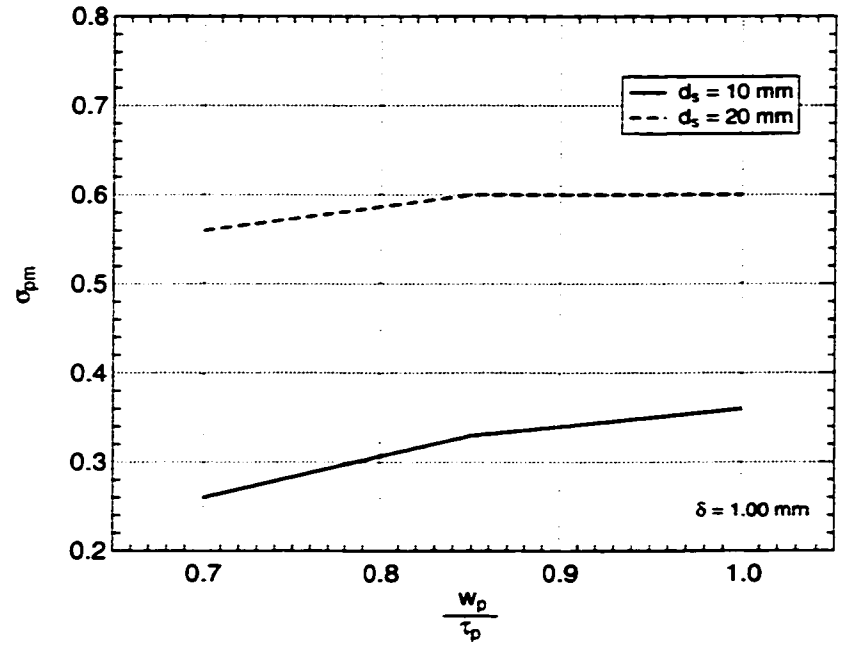

Figure 4.19: Leakage σ_{pm} over pole width to pole pitch ratio $\frac{w_p}{\tau_p}$ for $\delta = 1.0\,mm$

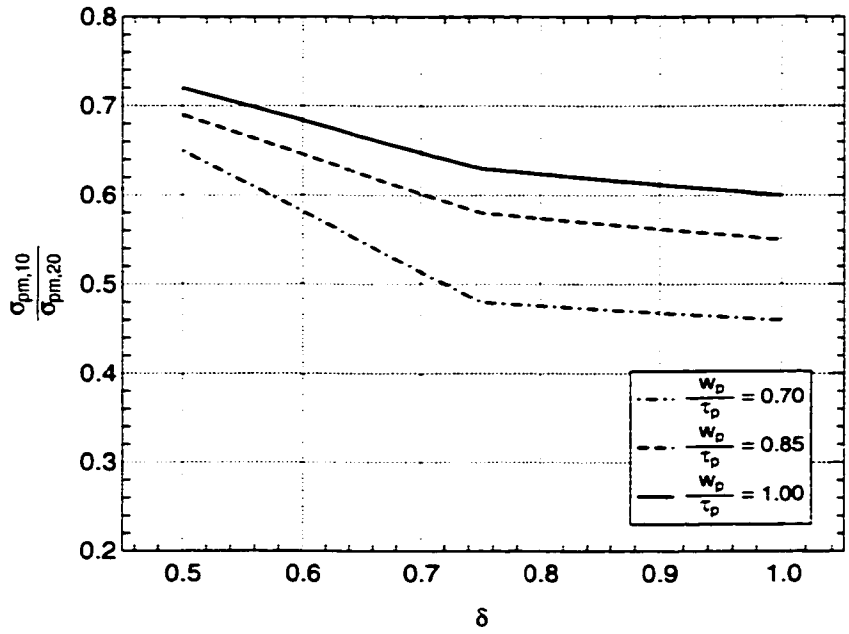

Figure 4.20: Leakage ratio $\frac{\sigma_{pm,10}}{\sigma_{pm,20}}$ over air gap δ for different pole width to pole pitch ratios $\frac{w_p}{\tau_p}$

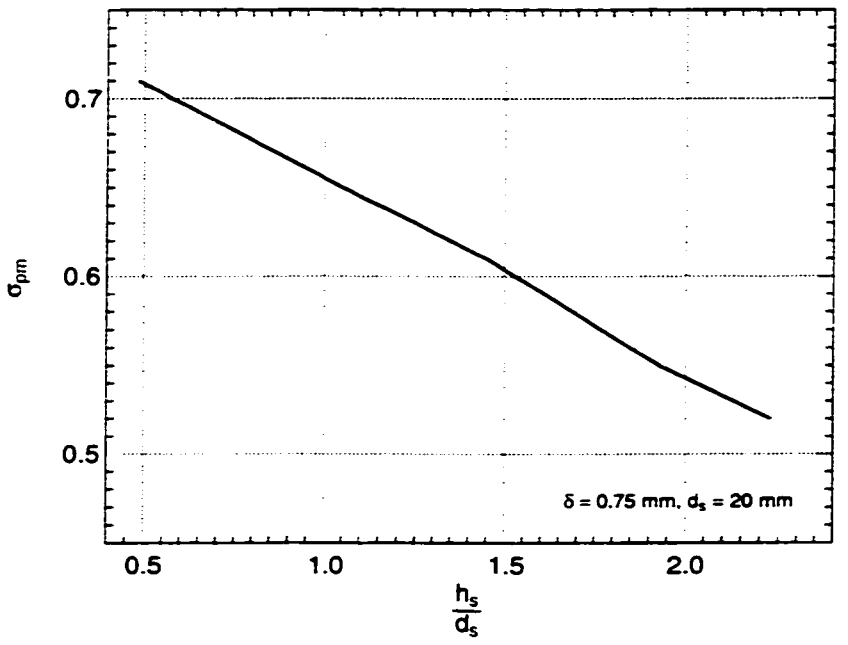

Figure 4.21: Leakage for different magnet height to magnet depth ratios $\frac{h_s}{d_s}$

4.2.5 Pole Pitch and Operating Frequency

In Sections 4.2.3 and 4.2.4 the influence of the design parameters is often investigated through values that are normalized to the pole pitch. The reason for that approach is that the pole pitch itself has a major influence on the achievable force density. Using Equation (4.45) and incorporating the Carter factor k_c allows Equation (4.30) to calculate the expected force densities in the $x = 0.5\tau_p$ rotor position.

$$F_{Ax,x=0.5} = \frac{B_{\delta_{pm}} \cdot A_r}{k_c} = \frac{1}{k_c} \frac{B_{\delta_{pm}} \Theta_r}{\tau_p} \tag{4.30}$$

Equation (4.30) is evaluated in Figure 4.22 for different air gaps over the pole pitch τ_p. For larger pole pitches the influence of the air gap size on the achievable force density is small, while for smaller pole pitches the force density exhibits a wide spread for the different air gaps. Overall the force density progressively increases for smaller pole pitches. The same trend is confirmed by the finite element simulation results in comparison to the theoretical values shown in Figure 4.23. Figure 4.23 also shows that

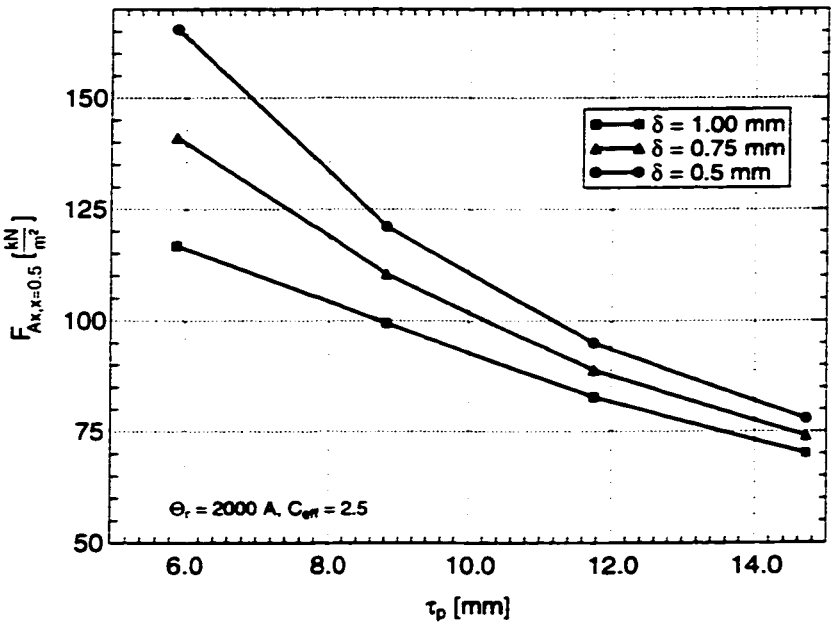

Figure 4.22: Theoretical force density for rotor position $x = 0.5\tau_p$ and $\delta = 0.5,\ 0.75,\ 1.00\,mm$

for small air gaps the force density is overestimated by the theoretical approach more than for larger air gaps, which can be attributed to the fringing flux leakage around the air gap that are not modeled in the reluctance model. This effect is stronger for small air gaps. One can also measure that for a small air gap ($\delta = 0.5\,mm$) at small pole pitches the discrepancies between theoretical and finite element analysis results grow larger, in absolute as well as in relative numbers. This indicates that there is a magnetic circuit limit for the smallest pole pitch, where the magnetic cross coupling between the poles prevents the further increase of the flux density.

However, as introduced in section 4.2.1, there are also manufacturing limits for the smallest possible pole pitch that affect the design earlier than the magnetic cross-couplings as the following considerations show: It is difficult to produce rare earth magnets thinner than 2-3 mm. For good flux collection factors C_{eff} the magnet's relative width $w_{pm_{rel}}$ is usually about $w_{pm_{rel}} = 0.4\text{-}0.5\,\tau_p$. That means that the minimum manufacturable pole pitch is $\tau_p = 5\text{-}7.5\,mm$. On the other hand, the magnetic cross-coupling effects at a pole pitch of $\tau_p = 5.88\,mm$ are small and more significant influence can

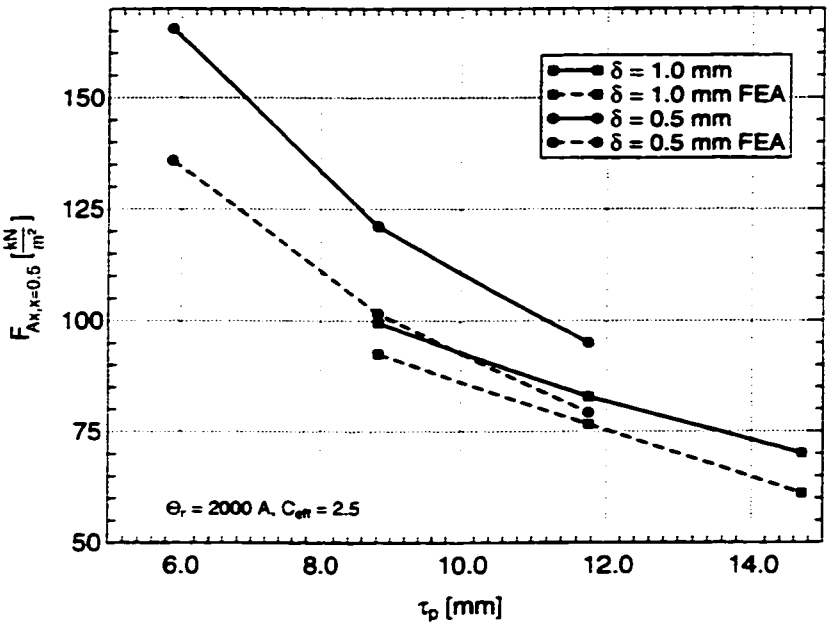

Figure 4.23: Comparison of theoretical force density and finite element simulation force density

be expected only for pole pitches below $\tau_p = 5\,mm$. Thus, the lower pole pitch limit is a mechanical one rather than a magnetic one. Furthermore very thin magnets can be subject of demagnetization by the ring winding m.m.f. and should be avoided (see Section 4.3.4).

In combination with the machine diameter d_m the pole pitch also determines the operating frequency (i.e. switching frequency) f_s and the open-circuit peak voltage of the machine $\widehat{u}_i$ according to Equations (4.31) and (4.32) respectively, where ω is the rotational speed of the machine, p the number of pole pairs, n the number of turns of the ring winding and $\widehat{\Phi}_{pm_r}$ the maximum flux linkage from the permanent magnet with the ring winding.

$$f_s = \frac{\omega\, p}{2\pi} = \frac{\omega\, d_m}{4\tau_p} \tag{4.31}$$

$$\widehat{u}_i = \omega\, p\, n\, \widehat{\Phi}_{pm_r} \tag{4.32}$$

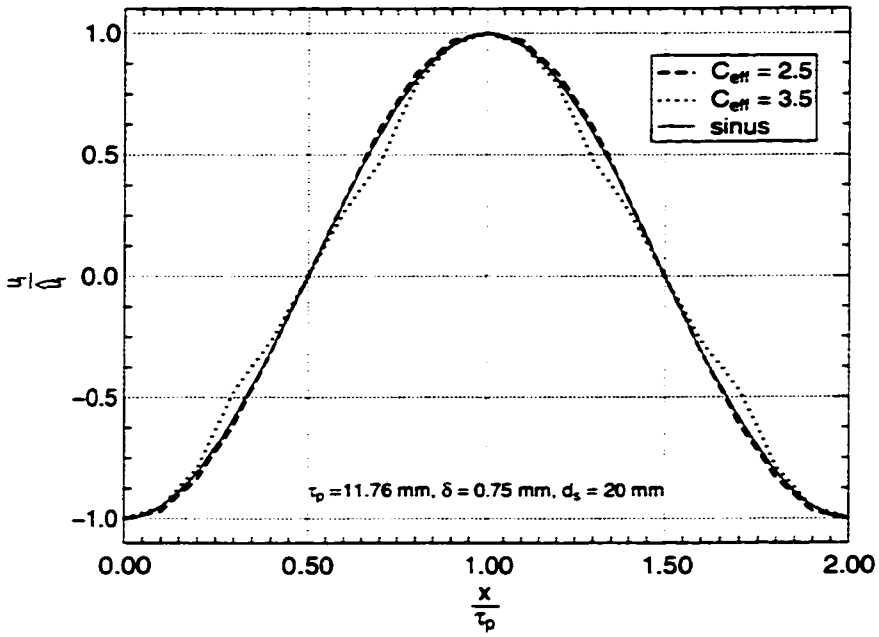

Figure 4.24: No-load induced voltage with saturation from the finite element analysis compared to a sinusoidal wave form

The switching frequency determines the converter technology to be used and influences possible rotation speed variation due to torque variations (see Section 4.3.4). The open-circuit peak voltage can be adjusted by choosing the number of winding turns for a given rotational speed ω and the number of pole pairs determined from the geometry as $p = \frac{\pi d_m}{2\tau_p}$. The normalized no-load voltage calculated with 3D saturation finite element analysis is shown in Figure 4.24 for two different effective flux accumulation factors. For $C_{eff} = 2.5$ the voltage has an almost perfect sinusoidal waveform and for $C_{eff} = 3.5$ it shows some minor deviations due to the pole saturation at the rotor positions $x = 0.3\,\tau_p$ and $x = 0.7\,\tau_p$. For design calculation purposes the induced voltage therefore can be described as a sinusoidal voltage (4.33), where $\omega_s = 2\pi\, f_s$.

$$u_i = \widehat{u}_i\, sin(\omega_s t) = \omega\, p\, n\, \widehat{\Phi}_{pm_r}\, sin(\omega_s t) \tag{4.33}$$

A numerical example allows one to gain some insight on the layout of the winding: Assuming a machine with a diameter $d_m = 374.3\,mm$ and a pole pitch $\tau_p = 11.76\,mm$, leads to a pole pair number of $p = 50$. From the saturation finite element analysis

for $C_{eff} = 2.5$ in the rotor position $x = 0.0\,\tau_p$, one finds a flux linkage of $\widehat{\Phi}_{pm_r} = 202.28 \cdot 10^{-6}\,Wb$. For a nominal rotational speed of $\omega = 2\pi\,50\,\frac{1}{s}$ a peak voltage for one winding turn of $\widehat{u}_{i_1} = 3.18\,V$ is induced. The operating frequency is $f_s = 2500\,Hz$. Considering a desired operation peak voltage of 150-300 V for mobile applications the winding has 50 to 100 turns and for a low saturation operation must supply an m.m.f. of up to $\Theta_r = 5000\,A$-turns. The winding must be made of stranded wire to reduce the skin effect because of the high operating frequency f_s. Furthermore it may be constructed of parallel winding branches to reduce the current load on each individual branch. However, to ensure an equal current distribution, the separate branches must be carefully interwoven exhibiting a Roebel characteristic [5, 17]. This method insures that all branches have the same length and that voltages induced from one branch into another cancel each other. Overall the ring winding is easily manufacturable and very efficient compared to a typical bed-stead winding used in conventional machines particularly because of its shorter copper length that stems from the absence of winding ends.

4.3 Losses and Saturation

The accurate finite element calculation of losses would require a non-linear time-line analysis, which is not only computationally very expensive, but would have to allow for multi-valued material characteristics for the saturation curve as well, which for example cannot be done by the Vector Fields Opera 3D package used here. Therefore, the best approach is to estimate the losses by categorizing them into electrical and magnetic losses. The latter can be further divided into hysteresis and eddy current losses. With this approach reasonable loss estimates based on analytical models can be made that can be incorporated into finite element post-processing calculations as well. In Section 3.5.2 it is mentioned that saturation finite element analysis problems are solved through iteration. It is illustrated in Section 4.3.1 that the iterative solution method can have problems of its own if used with laminated, strongly anisotropic materials.

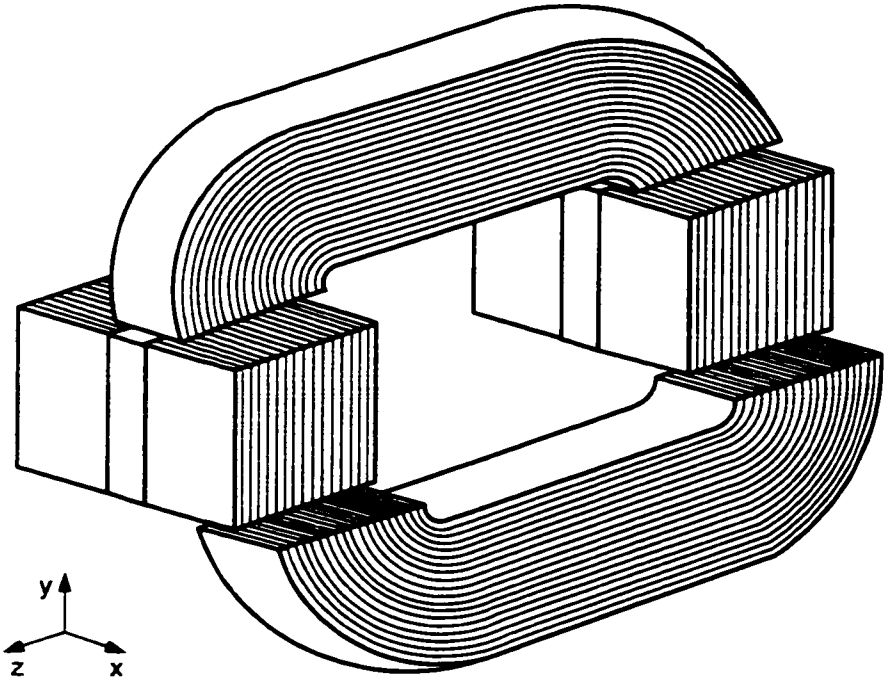

Figure 4.25: Lamination of rotor and stator for the *reduced magnet material* design

4.3.1 Rotor and Stator Lamination

Lamination is the classical solution to curb eddy current losses in the iron parts of rotating machines by electrically isolating each thin plate from the next [59]. The same approach is taken for active rotor transverse flux motors [5, 6]. Figure 4.25 shows the wound laminate core that is cut into the stator and the rotor core iron for the passive rotor *reduced magnet material* design. Considering the field and the motion vectors it is found that for best results the lamination is done perpendicular to the rotation plane (xy-plane in the figure) in z-direction. For the stator iron this approach does not impose any difficulties, but in the rotor a simple lamination in the z-direction prevents the main flux from flowing properly, as the flux direction changes in the rotor from the y- to the z-direction. A solution to that problem is to cut wound iron cores that themselves change the preferential flux direction as can be seen in Figure 4.25.

Losses

Electrical losses make up a significant part of the overall losses and are calculated from the ohmic losses and the winding parameters (4.34) [17], where k_r adjusts for increased losses due to skin effects at higher frequencies.

$$P_{l_{el}} = k_r \, R_0 \, I^2 \tag{4.34}$$

With the resistance $R_0 = \frac{\rho_{Cu} \, l_w}{A_w}$, the winding length $l_w = 2p \, \tau_p \, w$, the specific resistance of copper ρ_{Cu} and the winding cross-section $A_w = h_s \, d_w$ the electrical losses can be expressed for each ring winding using the geometry parameters introduced in Section 4.1 as shown in Equations (4.35) [5, 17]. For multiple phase motors that expression must be multiplied with the number of phases.

$$P_{l_{el}} = k_r \, \frac{\rho_{Cu} \, l_w}{A_w} \left(\frac{\Theta_r}{w} \right)^2 = k_r \, \frac{\rho_{Cu} \, 2p \, \tau_{p_m}}{h_s \, d_w \, w} \Theta_r^2 \tag{4.35}$$

Magnetic losses largely depend on the amounts and the quality of the materials used as well as the the peak flux density $\hat{B}$ and operating frequency f_s to which the material is exposed to. From classical machine design it is known, that with the specific hysteresis losses p_h and the specific eddy current losses p_{ed}, given in Equation (4.37) and Equation (4.36) respectively, the overall magnetic losses P_{mag} can be derived incorporating the weight of the iron m_{Fe} as shown in Equation (4.38) [17].

$$p_h = \sigma_h k_h \frac{f_s}{f_0} \left(\frac{\hat{B}}{\widehat{B_0}} \right)^2 \tag{4.36}$$

$$p_{ed} = \sigma_{ed} k_{ed} \left(\frac{f_s}{f_0} \right)^2 \left(\frac{\hat{B}}{\widehat{B_0}} \right)^2 \tag{4.37}$$

$$P_{l_{mag}} = m_{Fe} k_{mag} \left[\sigma_h \frac{f_s}{f_0} + \sigma_{ed} \left(\frac{f_s}{f_0} \right)^2 \right] \left(\frac{\hat{B}}{\widehat{B_0}} \right)^2 \tag{4.38}$$

These equations assume that standardized measurements of the materials of choice are available for a reference frequency f_0, which is usually $60\,Hz$ in North America and $50\,Hz$ in Europe, and a reference peak flux density $\widehat{B_0}$, which is usually $1\,T$. Then σ_h

Table 4.2: Specific losses of grain-oriented and cold-rolled (high-frequency) iron material in preferential direction $\widehat{B_0} = 1\,T$ and $f_0 = 50\,Hz$

Material	Thickness $d\ [mm]$	Hysteresis Losses $\sigma_h\ \left[\frac{W}{kg}\right]$	Eddy Current Losses $\sigma_{ed}\ \left[\frac{W}{kg}\right]$
grain-oriented	0.10	0.59	0.012
	0.05	0.65	0.003
cold-rolled	0.20	0.91	0.040
	0.10	0.94	0.009

and σ_{ed} are the specific losses for those reference values. The corrective factors k_h, k_{ed} and k_{mag} reflect the fact that measurements on real machines show higher losses than those predicted using the pure formulas, which occur due to the manufacturing process and the curve shape of the magnetization change [17]. According to [17] for conventional machines k_{mag} ranges from 1.5 to 2.5. [5] measured values for active rotor transverse flux motors in the 1.5-1.8 range. Because of their principal vicinity similar values can be expected for passive rotor machines.

Table 4.2 shows the specific losses for grain-oriented and cold-rolled materials [60]. Grain-oriented materials have one preferential direction in which they achieve the least losses, while in the other directions their losses are significantly higher. Since the flux changes its direction from the y- to the x-direction in the stator, cold rolled material is a better choice for the stator despite its higher hysteresis loss value shown in Table 4.2. For the rotor the direction change is facilitated by the rolled material itself. Therefore, the flux always follows the preferential direction which makes it suitable for a grain-oriented material. Figure 4.26 shows the specific magnetic losses for grain-oriented material according to Equation (4.38). Although the specific losses are relatively high for high operating frequencies the total iron mass of the active parts of transverse flux machines is only a fraction of the amounts in conventional machines leading to good overall magnetic loss values.

Lamination not only limits the eddy current losses, but it also reduces the amount of solid iron contained in a given geometry. The effects in the preferential flux plane are solely caused by the lesser amount of material and a continuous flux path in the iron is still provided. Perpendicular to that plane the isolating glue between the iron layers

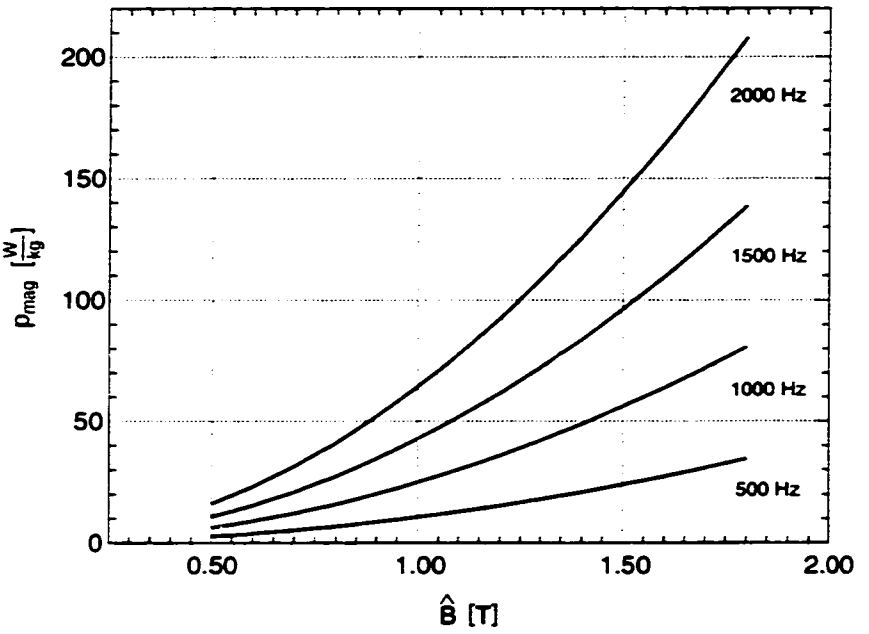

Figure 4.26: Magnetic losses for operating frequencies from 500 Hz to 2000 Hz for grain-oriented material

introduces significant air gaps within the material. For example, for an iron fill factor of $k_{Fe} = 0.92$, which can be reached using $d = 0.1\,mm$ sheets, that means that a $10\,mm$ pole contains a $0.8\,mm$ air gap perpendicular to the preferential flux direction. The effects of the reduced iron contents are incorporated into the finite element analysis by analyzing the field continuity at the iron/air interfaces and deriving an average permeability in tangential (preferential) and perpendicular flux direction [52]: In the preferential direction the tangential magnetic field strength H_t is continuous at the interface, which is described in Equation (4.39).

$$H_t = \frac{B_{air}}{\mu_0} = \frac{B_{iron}}{\mu_{iron}} \tag{4.39}$$

The average tangential flux density is defined by Equation (4.40). The average permeability in tangential (preferential) direction then follows in Equation (4.41).

$$B_t = k_{Fe}B_{iron} + (1 - k_{Fe})B_{air} \tag{4.40}$$

$$\mu_t = \frac{B_t}{H_t} = k_{Fe}\mu_{iron} + (1 - k_{Fe})\mu_0 \tag{4.41}$$

Following a similar approach for the normal direction, where the normal flux density B_n is continuous across the air/iron interface (Equation (4.42)). Defining the normal magnetic field strength H_n as in Equation (4.43) one finds the average permeability for the laminated material in the normal direction according to Equation (4.44).

$$B_n = \mu_0 H_{air} = \mu_{iron} H_{iron} \tag{4.42}$$

$$H_n = k_{Fe}H_{iron} + (1 - k_{Fe})H_{air} \tag{4.43}$$

$$\mu_n = \frac{\mu_0 \mu_{iron}}{(1 - k_{Fe})\mu_{iron} + k_{Fe}\mu_0} \tag{4.44}$$

Figure 4.27 shows the material characteristics for Waasner "Korno W-10" grain-oriented material as solid material [54] and laminated with an iron fill factor of $k_{Fe} = 0.92$ calculated through application of (4.41) and (4.44). As expected the impact in the perpendicular direction is much stronger than in the tangential direction. These curves can be directly used in an anisotropic material definition for the laminated material with saturation. Several finite element analyses using these anisotropic materials properties show that strongly anisotropic materials can cause severe convergence problems for the simulations. It can be observed that by using the Newton approximation of the relaxation factor for the next iteration, the solution shows a controlled, but sustained oscillation that does not disappear even after 100 iterations. By choosing a linear update approximation instead, a stable solution can be found, but only after over 50 iterations. For isotropic materials the solution for the same case converges already after 8 iterations. In an attempt to eliminate the 6-7 times increase in the calculation time, the effects on the magnetic flux density for the anisotropic versus the isotropic case are investigated. It is found that for the model analyzed here the z-component in the stator iron has a value in the $0.01\,T$ range compared to 1-2 T in the x- and y-direction. The z-component changes by 20-50% to 0.012-$0.015\,T$ for the isotropic solution. No effect could be measured for

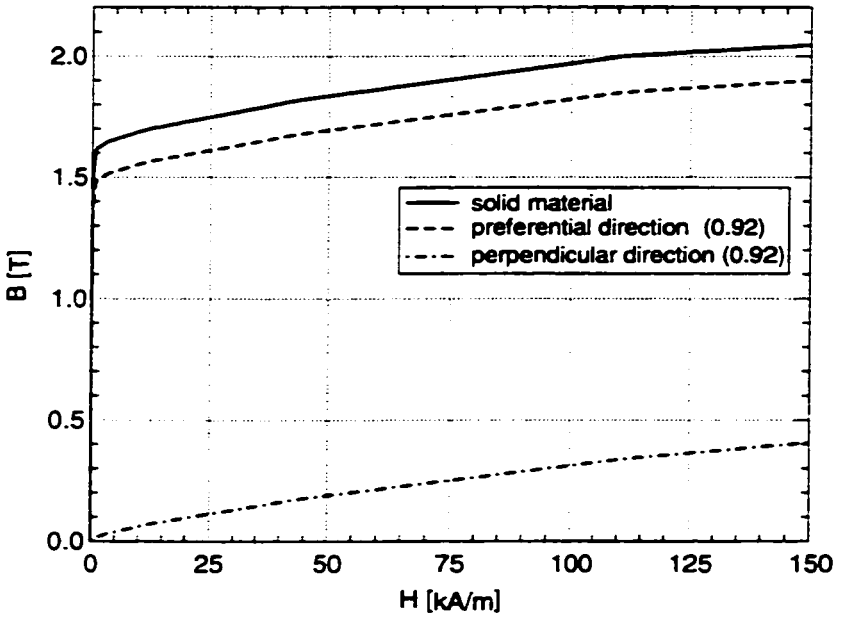

Figure 4.27: BH-characteristic for Waasner "Korno W-10" iron as solid material and laminated with an iron fill factor of 0.92

the x- and y-components, which is not surprising, considering that the flux density in the z-direction is in the pars pro mille range compared to the main flux direction.

The rotor lamination on the other hand follows the main flux direction. The permeability seen by the magnetic field in this case is the tangential permeability. Therefore, for both, the rotor and the stator, isotropic permeability in preferential direction, as shown by the middle line in Figure 4.27, is used for the simulations.

4.3.2 Saturation and the Optimum Magnet use Layout

The *optimum* magnet use layout procedure does not consider saturation effects in the iron. Therefore, it can be expected that the solution with saturation does not match the optimum permanent magnet flux density value exactly. However, one can attempt to compensate for the undesirable effects. To illustrate those effects, Figure 4.28 compares the finite element simulation results for flux density inside the permanent magnet B_{pm} with and without saturation. The figure shows that, because the overall reluctance increase due to the saturation is not captured, the flux density in the permanent magnet

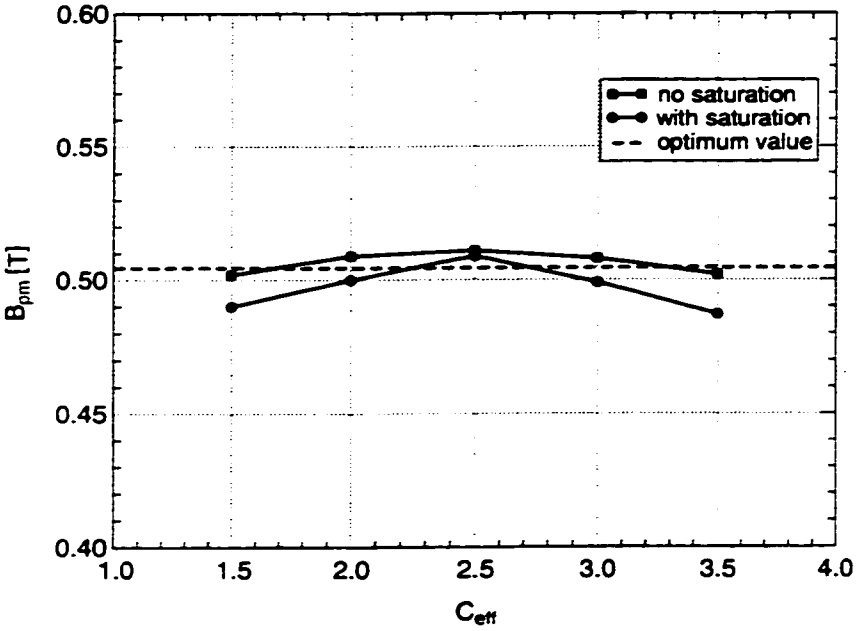

Figure 4.28: Permanent magnet flux density for the same magnetic circuit with and without saturation for changing effective flux accumulation factor

generally decreases. The effect is larger for low and high effective flux accumulation factors C_{eff}, while the effect is smaller for $C_{eff} = 2.5$.

In Section 4.3.3 it is shown that high flux accumulation factors are most desirable for an efficient design and in Section 4.3.4 the benefits of a higher magnet induction for the protection of the magnet are described. Accordingly the magnet's flux density should be increased to levels slightly above the *optimum* value for large flux accumulation factors. Physically that is achieved by either increasing the magnet width w_{pm} or by decreasing the magnet height h_{pm} (h_s). In both cases the flux density in the magnet increases. A straight forward way to incorporate this knowledge into the design phase is to adjust the leakage gap compensation factor k. Following the findings about the influence of k shown in Figure 4.6, a compensation factor between $k = 0.7$ and $k = 0.75$ can compensate for saturation effects. The exact solution can only be verified for each specific case with a saturation finite element analysis.

4.3.3 Flux Accumulation Factor

The flux accumulation factor directly determines the air gap flux density under the pole where the driving force density F_{Ax} is created through the interaction of the magnet field in the air gap $B_{\delta_{pm}}$ and the ring winding current coverage A_r according to the general equation (4.45).

$$F_{Ax} = B_{\delta_{pm}} \cdot A_r = B_{\delta_{pm}} \frac{\Theta_r}{\tau_p} \tag{4.45}$$

Since the air gap flux density $B_{\delta_{pm}}$ is provided by loss-less permanent magnets, but the ring winding current coverage involves electrical losses, it is immediately apparent that a design should maximize $B_{\delta_{pm}}$ in order to reduce the current required to reach a given force density. Figure 4.29 shows the force densities of finite element saturation calculations for constant current-turns $\Theta_r = 2000\,A$-turns in the $x = 0.5\tau_p$ rotor position for the same magnetic circuit layout used in Section 4.2.3. It can be seen in Figure 4.29 that effective flux accumulation factors over $C_{eff} = 3.5$ do not further increase the achievable force density F_{Ax}. For comparison the flux density created by the permanent magnet in the air gap $B_{\delta_{pm}}$ is given in the lower scale. It shows that the maximum force density is linked directly to the saturation characteristics of the iron. Therefore, in more general terms, any design that attempts to raise the air gap flux density provided by the permanent magnets into regions of high saturation of the iron will not increase the achievable force density, but only the machine's weight.

Another important aspect of increasing the exciting flux is the influence of saturation at the rotor position of maximum flux linkage $x = 0.0\,\tau_p$. Figure 4.30 compares the air gap flux density over the geometries for the rotor positions $x = 0.0\,\tau_p$ and $x = 0.5\,\tau_p$ and flux accumulation factors of $C_{eff} = 2.5$ and $C_{eff} = 3.5$. The model surfaces are shaded according to the flux density to which they are exposed. Note that a larger flux accumulation factor leads to a larger magnet width and a clearly visible larger stator height.

It can be observed that for $C_{eff} = 2.5$ the theoretical value of the flux density $B_{theo} = 2.5 \cdot \frac{1}{2} B_r = 1.26\,T$ is very well matched in the rotor position $x = 0.5\,\tau_p$ it was designed for. Moreover the same holds true for the rotor position $x = 0.0\,\tau_p$. It is found that this stands for all cases that do not exhibit saturation or extreme geometries. The

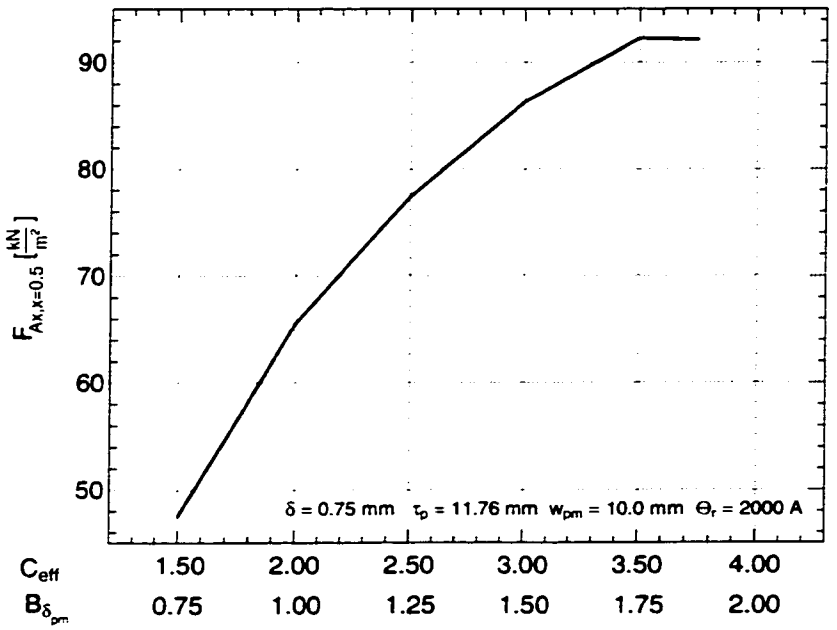

Figure 4.29: Saturation characteristic of the core iron limiting the maximum flux accumulation factor C_{eff}

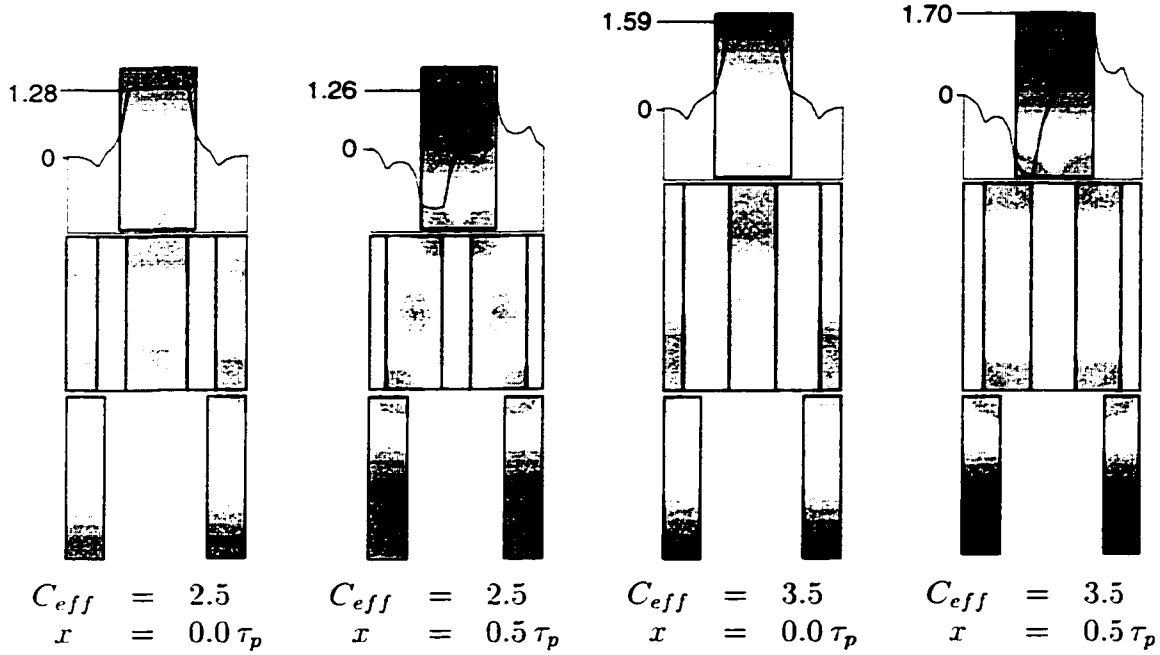

Figure 4.30: Comparison of the maximum flux densities for $C_{eff} = 2.5$ and $C_{eff} = 3.5$ for the rotor positions $x = 0.0\,\tau_p$ and $x = 0.5\,\tau_p$

Table 4.3: Comparison of maximum air gap flux densities of the *reduced magnet material* TFM to conventional machines

Machine type	Parameter	Value $[T]$
DC	B_{max}	0.5-1.1
SM salient	$\widehat{B}_1$	0.8-1.05
SM non-salient	$\widehat{B}_1$	0.75-1.05
Induction	B_{avrg}	0.4-0.65
RMM TFM	B_{max}	1.2-1.5

reason for that behavior is that the air gap reluctances for those positions are very similar as one can see by comparing the stator pole areas that are directly opposed by the rotor core iron. For the case with the high flux accumulation factor $C_{eff} = 3.5$, the target value for the air gap flux density $B_{theo} = 1.77\,T$ is not reached because of saturation. The flux density is even further reduced at the rotor position $x = 0.0\,\tau_p$. This is caused by the significantly longer, saturation exhibiting, iron path, since the flux crosses through the whole rotor iron instead of closing locally as it is the case in the $x = 0.5\,\tau_p$ rotor position.

Comparing the maximum excitation air gap flux densities of conventional machines [17] with the *reduced magnet material* transverse flux machine it shows that the high achievable force densities of the latter can be partially attributed to the better magnetic circuit leading to higher achievable air gap flux densities (see Table 4.3). Some caution has to be taken in the comparison however: While the maximum value of the transverse flux machine compares directly with the maximum value of DC machines and the peak value of the fundamental wave $\widehat{B}_1$ in synchronous machines (SM), it cannot be compared directly with the average value B_{avrg} that is used for the design of induction machines. Calculating the average flux density over one pole pitch for the transverse flux machine, it is found that this value ranges between 0.8 and $1.1\,T$ compared to 0.4-$0.65\,T$ in induction machines.

4.3.4 Ring Winding M.M.F.

After fixing the flux density under the pole provided by the permanent magnets $B_{\delta_{pm}}$ to its maximum low saturation value using an effective flux accumulation factor of $C_{eff} = 2.5$-

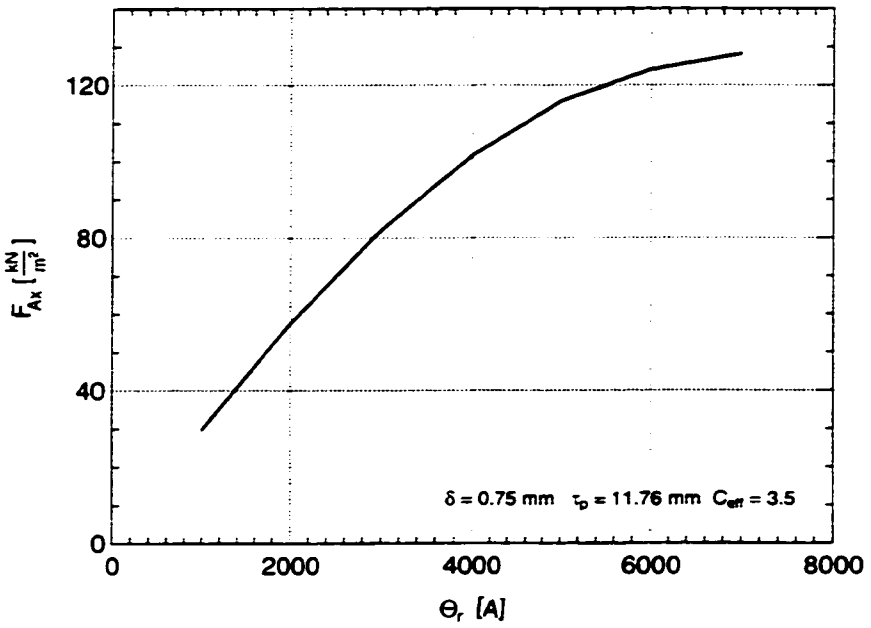

Figure 4.31: Average force densities over ring winding m.m.f. with saturation

3.5, the second influence factor on the achievable force density is the ring winding m.m.f. Since the magnet's and the ring winding's fields mostly oppose each other for the force production, fixing $B_{\delta_{pm}}$ at a high value does not limit the maximum useful ring winding m.m.f. Θ_r. Figure 4.31 shows the average force density over one pole pitch when the ring winding m.m.f. is varied between $\Theta_r = 1000\,A$-turns and $\Theta_r = 7000\,A$-turns for a model with an effective flux accumulation factor of $C_{eff} = 3.5$. Increasing Θ_r beyond $6000\,A$-turns only marginally increases the force density from $F_{Ax} = 124\,\frac{kN}{m^2}$ to $F_{Ax} = 128\,\frac{kN}{m^2}$, because the iron is mostly in saturation at that point. Comparing the force density curve with the torque curve from the *slanted rotor design* in Section 3.5.2, Figure 3.32 it can be observed that for the slanted design, saturation effects set in at $\Theta_r = 1500$-$2000\,A$-turns compared to a one air gap pair equivalent of $\Theta_{r,one\,side} = 3000\,A$-turns for the *reduced magnet material* design. Note that the *reduced magnet material* design's ring winding feeds four air gaps, requiring double the m.m.f. to produce the same air gap flux as a two air gap design. That confirms the importance to avoid the 'hot spots' in a transverse flux motor design observed in Section 3.5.2.

The force density of the *reduced magnet material* motor as a function of the relative

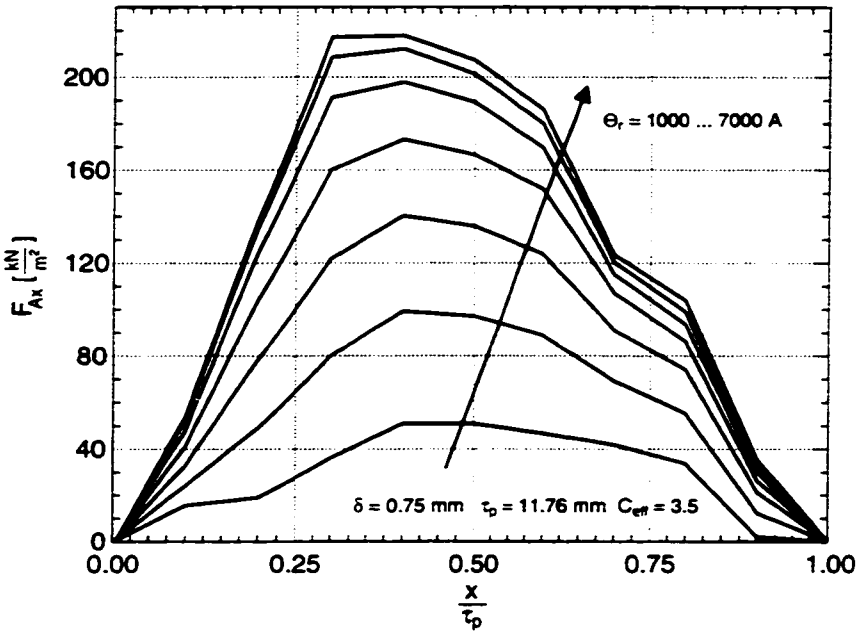

Figure 4.32: Force density distribution for different ring winding m.m.f. over rotor position with saturation

rotor position is shown in Figure 4.32 for different ring winding m.m.f. Θ_r. The curve shape changes from an almost sinusoidal wave form at $\Theta_r = 2000\,A$-turns to a much more pointed shape at $\Theta_r = 7000\,A$-turns. Assuming a two phase motor fed by a rectangular current wave form, this shape change translates into an increase of force ripple for increased Θ_r (Figure 4.33). The ripple reaches up to 25% at $\Theta_r = 5000\,A$-turns. This could theoretically lead to speed pulsations, because the rotor mass of transverse flux motor is small compared to conventional machines (about one fifth to one tenth). However, the operating frequency of the transverse flux machine is about 25 to 50 times larger than that of a conventional machine as pointed out in Section 4.2.5. Therefore, the speed variations even for a two phase motor are very small. There are two prominent counter measures that can be used to further reduce the force density ripple to eliminate any speed pulsations:

1. Especially for larger machines, building the machine as a three or four phase machine significantly reduces the force ripple. Figure 4.34 shows the relative force density ripple for a rectangular current wave form at $\Theta_r = 5000\,A$-turns. For the

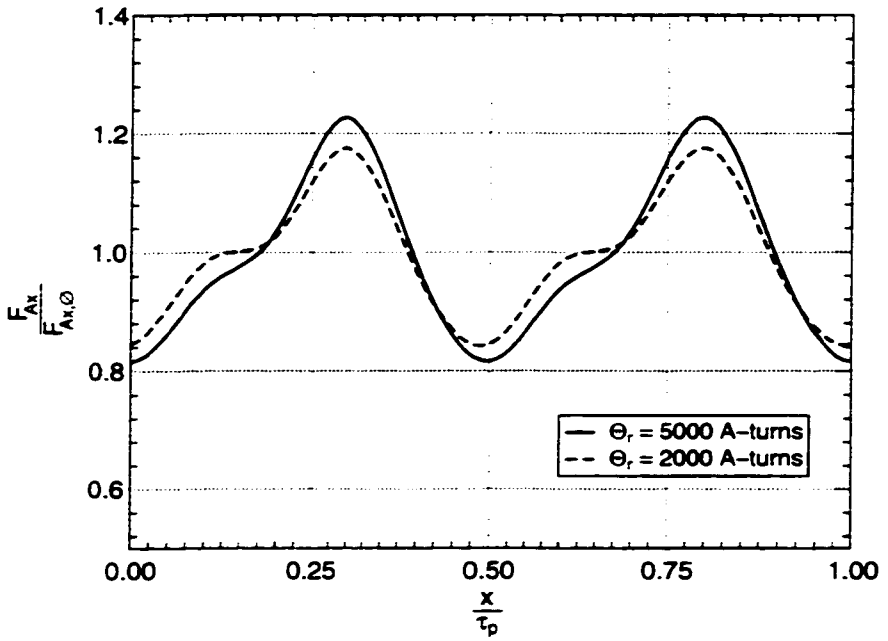

Figure 4.33: Force ripple increase from $\Theta_r = 2000\,A - turns$ to $\Theta_r = 5000\,A - turns$ for a two phase motor

four phase case the ripple is only ±5%.

2. Instead of using a rectangular current wave form, the current can be controlled to counter the magnetically caused ripple by increasing or decreasing the ring winding current accordingly. This method can be used very effectively on transverse flux motors [5].

4.3.5 Permanent Magnets under high Ring Winding M.M.F.

For a lasting motor design it is mandatory to avoid demagnetization of the permanent magnets caused by the ring winding m.m.f. Assuming the worst case, a loss-less connection between the ring winding m.m.f., Θ_r, and the equivalent permanent magnet m.m.f., Θ_{pm}, one can derive a rule of the thumb for safe magnet operation for which the ring winding m.m.f. must be smaller than the equivalent magnet m.m.f. (Equation (4.46)).

$$\Theta_r < \Theta_{pm} \tag{4.46}$$

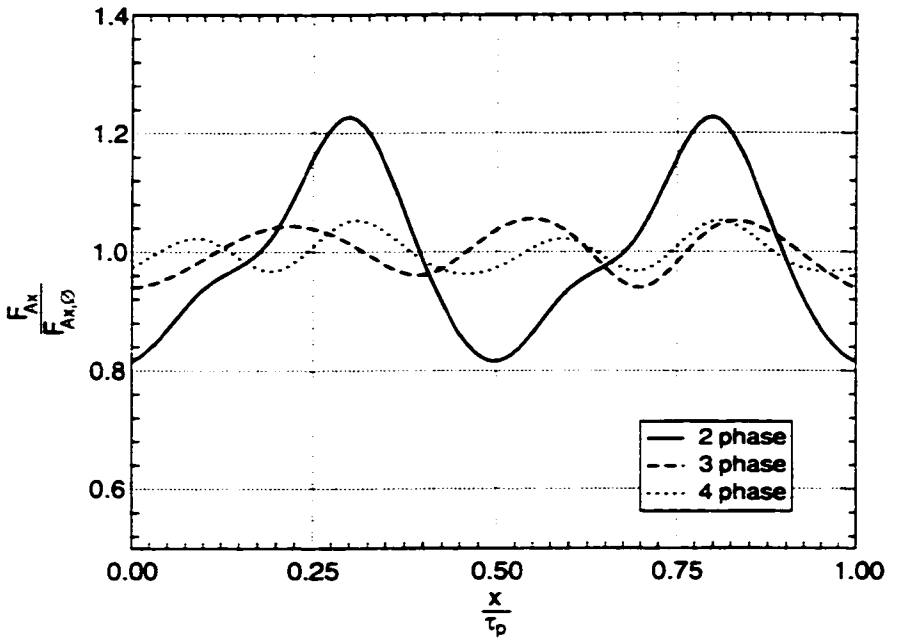

Figure 4.34: Force ripple decrease for higher phase machines at $\Theta_r = 5000\,A - turns$

For the machine design analyzed in Section 4.3.4 the relative permanent magnet width is $w_{pm_{rel}} = 0.47\tau_p$. With a pole pitch of $\tau_p = 11.76\,mm$ that results in a permanent magnet width of $w_{pm} = 5.5\,mm$. With $H_{cB,80°C} = 765880\,\frac{A}{m}$ from Section 4.2.1 and Equation (3.41), the equivalent permanent magnet m.m.f. is $\Theta_{pm} = 4212\,A$-turns per side. At $\Theta_r = 6000\,A$-turns, which is equivalent to $\Theta_{r,one\,side} = 3000\,A$-turns, the values for Θ_r and Θ_{pm} meet the requirement of Equation (4.46). As long as the magnet is wider than $w_{pm} = 4\,mm$ or it is made of a higher H_c valued material, it can be assumed that all *reduced magnet material* designs meet this condition.

With the magnetization direction of the permanent magnets and the current direction of the ring winding chosen for the finite element analysis the most destructive superposition of permanent magnet and ring winding fields occur at the rotor position $x = 0.0\,\tau_p$. Reverting the ring winding current, the same results can be obtained at the rotor position $x = 1.0\,\tau_p$. Figure 4.35 shows the flux density plot in the middle of the permanent magnet at a ring winding m.m.f. of $\Theta_r = 6000\,A$-turns. The minimum flux density value at the center of the plot is $B = 0.31\,T$. This value is only reduced by less than 40% compared to its design value with external field absent and well above the zero flux

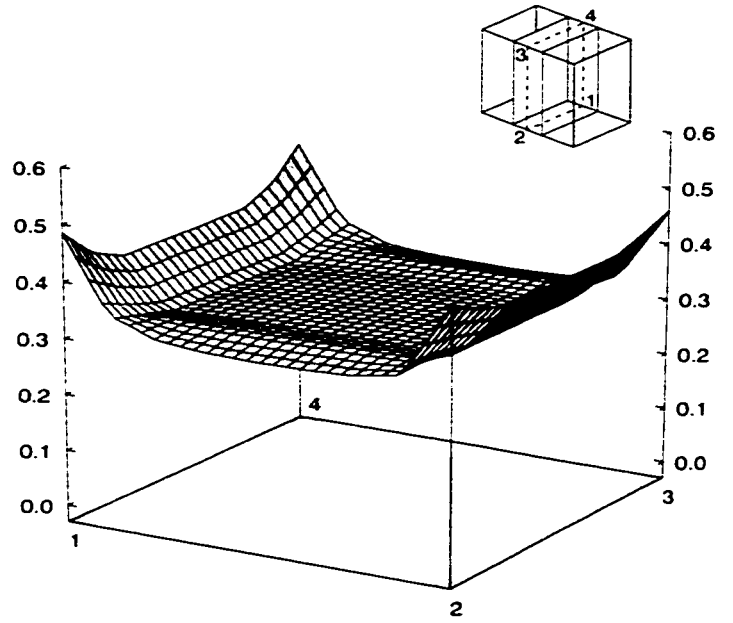

Figure 4.35: Flux density in x-direction in the middle of the magnet ($\Theta_r = 6000\,A$-turns, $C_{eff} = 3.5$)

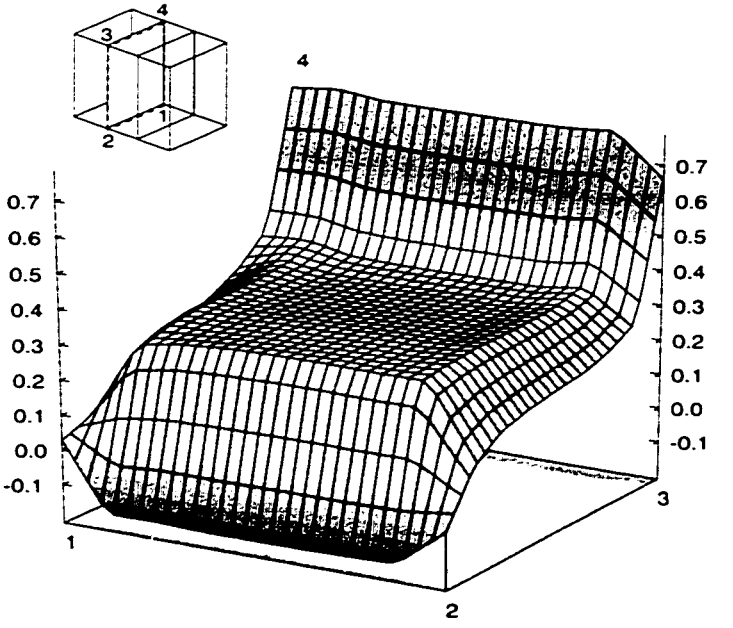

Figure 4.36: Flux density in x-direction at the side of the magnet ($\Theta_r = 6000\,A$-turns, $C_{eff} = 3.5$)

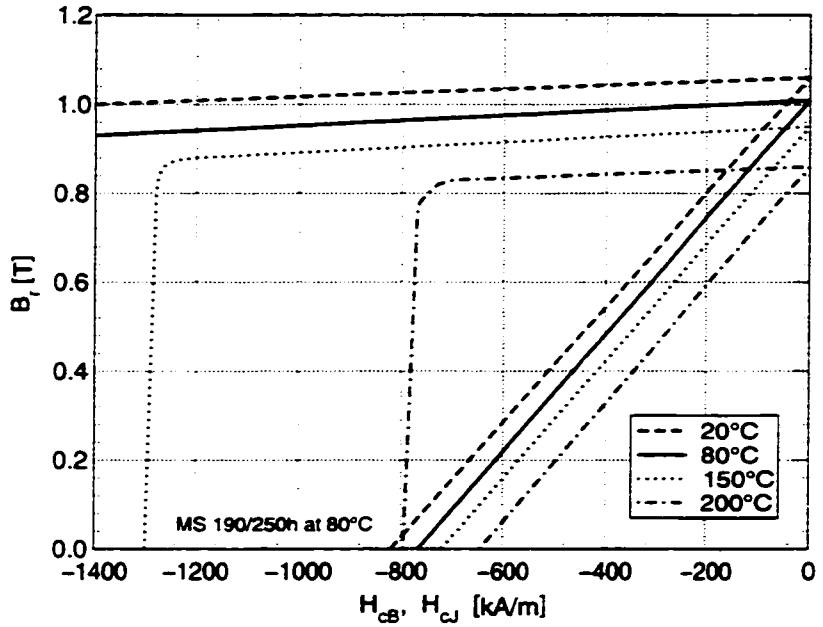

Figure 4.37: Coercive field strengths for $B = 0$ (H_{cB}) and $J = 0$ (H_{cJ}) for different temperatures for magnet material MS 190/250 h

density mark, $B = 0T$, which removes the magnets from the point of possible demagnetization by a safe margin. Also the surrounding iron is already exhibiting significant saturation, which prevents large further increases of the flux density caused by the ring winding m.m.f. Therefore, even under short circuit conditions a demagnetization of the permanent magnet is impossible.

Investigating the flux density at the iron pole (Figure 4.36), it shows that at the magnet's side the major part of the permanent magnet is not exposed to potentially damaging negative flux densities either. However, local demagnetization can occur at the bottom edge of the magnet where the flux density reaches its minimum at $B_{min} = -0.17T$. Since this flux density only occurs in a locally very confined area it does not pose a threat to the overall magnetization of the magnet. Striving for a 100% reliable operation there are several ways to avoid even local demagnetization:

1. NdFeB magnet's coercive field strength for the internal polarization H_{cJ} is significantly larger than that exhibited with respect to the external flux density H_{cB}. Therefore, even negative external fields do not demagnetize the magnet until the

curves cross each other. Extending the curves given in Figure 4.37 shows that the plots usually cross at a value of $H = 2\text{-}3\,H_{cB}$ and large negative external flux density values. However, the circumstances change dramatically at higher temperatures: For a temperature of $200°C$ demagnetization will occur already at small negative external B values. It is therefore mandatory to keep the operating temperature below the specified levels to avoid local demagnetization.

2. Instead of relying on the material properties, geometrical counter measures can be applied. Since potential demagnetization only occurs directly at the air gap, the stator poles can be constructed about $1\text{-}2\,mm$ higher than the permanent magnets. That way the magnet material is physically removed from the potentially damaging areas.

3. Another option is to adjust the magnetic circuit to facilitate an operating point of higher magnet flux density B_{pm}. That way the superposition of the fields would still lead to positive flux density values in the areas of possible demagnetization.

4.4 Design Recommendations for the Reduced Magnet Material Design

Summarized from the analyses given in this chapter, the following recommendations and insights for a successful *reduced magnet material* passive rotor design are given. Within the given value ranges of the different parameters the sensitivity towards the force density is small. Outside of the recommended ranges the sensitivity can be very high and must be judged by the characteristic curves they are derived from.

- The air gap δ is the primary influence factor on the dimensions of the magnetic circuit because it influences the air gap reluctance predominantly. The maximum energy transfer from the magnets to the air gap requires that the remaining reluctances are matched to the air gap reluctance. Therefore, the remaining geometries need to be adjusted to meet this condition (see the design tables in Appendix A).

- Useful pole pitches lie in the $8\text{-}20\,mm$ range and are tied to the air gap δ in a way that larger air gaps require larger pole pitches to facilitate an *optimum magnet use*

and magnet width (see the design tables in Appendix A).

- The most suitable magnet widths are found in the 0.4-0.5 τ_p range, which offers the best compromise between the magnet m.m.f. Θ_{pm} and the ring winding flux path.
- The force density exhibits a clear maximum for rotor pole width between 0.75 τ_p and 0.88 τ_p.
- The maximum pole depth is solely restricted by mechanical constraints because of the cylindrical shapes of rotor and stator. As a minimum pole depth for efficient magnet use, a depth of $d_s = 20\text{-}30\,\delta$ is recommended.
- The magnet's height to width ratio should be $\frac{h_s}{d_s} = 1.5\text{-}2.0$ to keep the leakage losses below 50%.
- The permanent magnet induction B_{pm} should be adjusted to the *optimum value* of $B_{pm} = \frac{1}{2}B_r$ or slightly higher, but never lower to curtail local demagnetization.
- The effective flux accumulation factor C_{eff} should lie in the 3.0-3.5 range to achieve a maximum force density with lowest possible external power input while still avoiding saturation.
- The maximum useful ring winding m.m.f. per air gap pair is $\Theta_{r,one\,side} = 3000$ A-turns to avoid high saturation losses.
- Three or four phase systems are preferred over two phase systems for their low torque ripple, but lead to a more complicated machine as well.
- High power and corrosion free NdFeB or SmCo magnets are the magnet materials of choice.
- The high operating frequencies require careful consideration of the iron materials used for the rotor and the stator to keep hysteresis losses low.

Chapter 5

Conclusions

It is shown in this dissertation that two-dimensional finite element analysis is useful for qualitative investigation of passive rotor transverse flux motors, but quantitative results can only be obtained if the solution is known in advance. For quantitative results three-dimensional analyses must be used to properly capture the full geometry of the magnetic circuit and to model leakages in all dimensions. It is also shown that linear reluctance models can be used successfully to calculate the flux densities in the air gap. A comparison of the analytical values with the three-dimensional finite element analysis results also ensures that there are no principal modeling errors in the finite element model defined and analyzed with the Vector Fields' Opera 3D simulation package. It is found that the slanted rotor design shows a significant deviation from the linear torque increase at a ring winding m.m.f. of $\Theta_r = 1500\,A$-turns, while the *reduced magnet material* design exhibits strong saturation only at a ring winding m.m.f. of $\Theta_r \geq 2500\,A$-turns. It is found that this is caused by the pointed edge of the slanted rotor that has limited flux carrying capability. It is therefore recommended that an alternate slanted rotor design be employed that does not have pointed edges. However, it would be premature to eliminate single track passive rotor designs completely from further research, because they still have the mechanical advantage of the short rotor cylinders.

An example of a single track machine that is worthwhile for further investigation is given in Figure 5.1. The design shown in the figure is a combined two phase design. The two rotor halves at the front and the rear have an offset of $0.5\,\tau_p$ and share common parts of the stator which reduces the required amount of permanent magnet material.

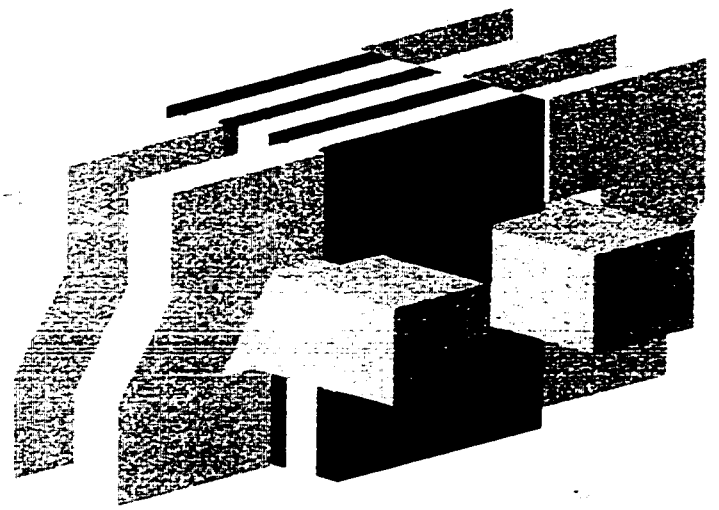

Figure 5.1: Combined two phase design

Also the winding partly reaches into the rotor area as a compromise to reduce the magnet material use, but to still ensure the mechanical stability of the winding mount. The width of the stator parts common for both phases can most likely be reduced as shown in the figure without adverse saturation effects because of the $0.5\,\tau_p$ offset of the rotors which leads to the same offsets in the fields as well. Finite element analysis can be used to verify this assumption.

In Chapter 4 the *reduced magnet material* design is analyzed. This design uses the same amounts of permanent magnets as active rotor designs do, but less core iron. An analytical approach based on a linear reluctance model is given for the *reduced magnet material* design that facilitates the nearly optimum use of the permanent magnet material for torque production by operating the magnets close to their energy maximum. It is further investigated which geometrical relations provide the highest force densities. The results are summarized as design recommendations in Section 4.4. The main insights are that the air gap length largely influences the choice of sensible pole pitches, that the best width for the permanent magnets lies between $0.4\,\tau_p$ and $0.5\,\tau_p$ and that the highest force densities are achieved for rotor pole widths between $0.75\,\tau_p$ and $0.88\,\tau_p$. By combining the design recommendations with the near optimum magnet use design procedure, it is

possible to find magnetic circuit layouts that meet both the criteria of minimum magnet use and high force density.

Comparing the results to active rotor designs [5] it is found that the passive rotor designs retain the high achievable force densities and are comparable in terms of induced no-load voltages, torque pulsations and saturation effects. This shows that the fixed location of the permanent magnets on the stator has no negative effects on the machine design, but offers the benefit of facilitated active fluid cooling of the permanent magnets in high performance machines and better mechanical protection of the magnets.

References

[1] Weh, H.: Entwicklung elektrischer Antriebe im Zeichen der Drehstromtechnik, etz., Bd. 110 (1989), H. 5, pp. 196-198

[2] Weh, H., Shalaby M.: Highly Effective Magnetic Circuits for Permanent Magnet Excited Synchronous Machines, *Proc. ICEM*, Cambridge (USA), 1990, pp. 143-148

[3] Weh, H.: Synchronous Machines with New Topologies, *SM100: International Conference on the Evolution and Modern Aspects of Synchronous Machines*, Zürich, 1991, Part 2, pp. C1-C9

[4] Harris, M.R., Pajooman, G.H., Abu-Sharkh, S.M.: Comparison of alternative topologies for VRPM (transverse flux) electrical machines, IEE Colloquium on New Topologies for Permanent Magnet Machines (Digest No. 1997/090), IEE, 1997, pp. 2/1-7

[5] Beyer, S.: Untersuchungen am magnetischen Kreis der permanenterregten Transversalflußmaschine in Sammler-Bauweise, Dissertation, Technical University of Braunschweig, 1997

[6] Degèle, B.: Optimierung des Betriebsverhaltens einer elektrisch erregten Transversalflußmaschine, Dissertation, Technical University of Braunschweig, 1997

[7] Balkan-S.N., Bulent, E.H.: A comparison of torque capabilities of axial flux and radial flux type of brushless DC (BLDC) drives for wide speed range applications, Proceedings of the IEEE 1999 International Conference on Power Electronics and Drive Systems, PEDS'99 (Cat. No. 99TH8475), IEEE, 1999, pp. 719-724 vol. 2

[8] D'Angelo, G., Di Stefano, R., Scarano, M.: A TF PM motor wheel drive: test and experimental results, ICEM96 Proceedings, International Conference on Electrical Machines, Spain, 1996, pp. 179-183 vol. 3

[9] Bork, M., Henneberger, G.: New transverse flux concept for an electric vehicle drive system, ICEM96 Proceedings, International Conference on Electrical Machines, Spain, 1996, pp. 308-313 vol. 2

[10] Mecrow, B.C., Jack, A.G., Maddison, C.P.: Permanent magnet machines for high torque, low speed applications, ICEM96 Proceedings, International Conference on Electrical Machines, 1996, pp461-466 vol. 3

[11] Wüst, B., Müller, R.: High-capacity drive system for road vehicles with electrical and hybrid drive, Symposium Proceedings EVS-11, 11th International Electric Vehicle Symposium, Electric Vehicles: The Environment-Friendly Mobility, Italy, 1992 pp. 8.05/1-10 vol. 1

[12] Mitcham, AJ: Transverse Flux motors for electric propulsion of ships, IEE Colloquium on New Topologies for Permanent Magnet Machines (Digest No. 1997/090), IEE, 1997, pp. 3/1-6

[13] Patterson, D., Spee, R.: The design and development of an axial flux permanent magnet brushless DC motor for wheel drive in a solar powered vehicle, IEEE Transactions on Industry Applications, vol. 31, no. 5, Sept.-Oct. 1995, pp. 1054-1061

[14] Harris, M.R., Pajooman, G.H., Abu-Sharkh, S.M.: The problem of power factor in VRPM (transverse flux) machines, Eighth International Conference on Electrical Machines and Drives (Conf. Publ. No. 444), IEE, 1997, pp. 386-390

[15] Vas, P.: Vector control of AC machines, Oxford University Press, 1990

[16] Zhang, Z., Profumo, F., Tenconi, A.: Analysis and Experimental Validation of the Performance of an Axial Flux Permanent Magnet Brushless DC Motor with Powder Iron Metallurgy Cores, *IEEE Transactions on Magnetics*, Vol. 33, No. 5, September 1997, pp. 4194-4196

[17] Vogt, K. : Berechnung elektrischer Maschinen, VCH, 1996

[18] Weh, H.: Drive Concepts with New Machines, *Speedam-Symposium* (Italy), May 1992, pp. 29-32

[19] Weh, H.: Direktantriebe für Schienenfahrzeuge der Zukunft, *ETG-Fachtagung*, Essen, Germany, October 1995

[20] Böhm, H., Schmidt, D., Lößel, W.: Elektrische Ausrüstung der ICE-Serientriebköpfe Baureihe 401, AEG/ABB/Siemens-Sonderdruck Verkehrstechnik, 1989

[21] Lange, A.: Transverse flux machine, *US Patent 5,773,910*, 1998

[22] Lange, A., Knoll, S.: Transverse flux motor with magnetic floor gap, *US Patent 5,777,418*, 1998

[23] Nolle, E., Multi-phase transverse magnetic flux machine, *US Patent 5,854,521*, 1998

[24] Weh, H.: Transversal flow machine in accumulator arrangement *US Patent 5,051,641*, 1991

[25] Weh, H.: Electric Drives with New Machine Configurations, *ISPE'92*, Seoul, Korea, 1992

[26] Weh, H.: Transverse Flux (TF) Machines in Drive and Generator Application, Stockholm Power Tech, 1995

[27] Weh, H.: Transversalflußmaschinen mit großer Kraftdichte und und hohem Wirkungsgrad, Hannover-Messe, 1995

[28] Weh, H: Electrical machine, *World Patent* W09504399A1 (or: *European Patent* EP711469A1), 1996

[29] Weh, H.: Machine with transverse flux, *US Patent 5,633,551*, 1997.

[30] Weh, H.: Electrical machine, *European Patent*, EP711469B1, 1998

[31] Cook, R.D., Malkus, D.S., Plesha, M.E.: Concepts and Application of finite Element Analysis, Wiley, 3rd edition, 1989

[32] Humphrey Jr., S.: Field Solutions on Computers, CRC Press, 1997

[33] Kardestunger, H., Norrie, D.: Finite Element Handbook, McGraw-Hill, 1987

[34] Binns, K.J., Lawrenson, P.J., Trowbridge, C. : The Analytical and Numerical Solution of Electric and Magnetic Fields, Wiley, 1992

[35] Brenner, S.C., Scott, L.R.: The Mathematical Theory of finite Element Methods, Springer, 1996

[36] Jiang, J.: Analytische und dreidimensionale numerische Berechnung von Transversalflußmaschinen, Dissertation, Technical University of Braunschweig, 1988

[37] Strassacker, G.: Analytische und numerische Methoden der Feldberechnung, Teubner, 1993

[38] N.N.: ANSYS User's Manual, Volume I Procedures, SAS IP, 1995

[39] N.N.: ANSYS User's Manual, Volume IV Theory, SAS IP, 1995

[40] Lehner, G.: Elekromagnetische Feldtheorie für Ingenieure und Physiker, Springer, 1990

[41] N.N.: Opera-3D Post-Processor Reference, Vector Fields Limited, 1998

[42] N.N.: Opera-3D User Guide, Vector Fields Limited, 1998

[43] Zienkiewicz, O.C., Lyness, J., Owen, D.R.J.: Three-Dimensional Magnetic Field Determination Using Scalar Potential - A Finite Element Solution, *IEEE Transactions on Magnetics*, Vol. Mag-13, No. 5, pp. 1649-1656, September 1977

[44] Simkin, J., Trowbridge, C.W.: On the Use of the Total Scalar Potential in the Numerical Solution of Field Problems in Electromagnetics, *International Journal for Numerical Methods in Engineering*, Vol. 14, pp. 423-440, 1979

[45] Chari, M., Silvester, P.: Finite Elements in Electrical an Magnetic Field Problems, Wiley, 1980

[46] Boll, R.: Weichmagnetische Werkstoffe, Technical Data Book, Vacuumschmelze Hanau, 1990

[47] Hasubek, B.: 2D Finite Element Analysis of Passive Rotor Transverse Flux Machines, Student Poster Presentation, *IEEE PES Winter Meeting*, January 31.- February 4, 1999

[48] Hasubek, B., Nowicki, E.P.: Two-Dimensional Finite Element Analysis of Passive Rotor Transverse Flux Motors with Slanted Rotor Design, *IEEE Canadian Conference on Electrical and Computer Engineering*, 1999, pp. 1199-1204

[49] N.N.: Product Information Catalog on Permanent Magnets, Magnetfabrik Schramberg, 04/97

[50] N.N.: Product Information on Permanent Magnets, The Magnet Source, 1997

[51] Parker, R. J. : Advances in permanent magnetism, Wiley, New York, 1989

[52] N.N.: Opera-3D Application Notes, Vector Fields Limited, 1998

[53] N.N.: Opera-3D Pre-Processor Reference, Vector Fields Limited, 1998

[54] N.N.: Elektro-Bauteile: Schnittbandkerne, Ringbandkerne, Zubehör, Gebrüder Waasner GmbH, Elektro-Technische Fabrik, 1998

[55] Moskowitz, L. R.: Permanent magnet design and application handbook, Cahners Books International, Boston , 1976

[56] Horstmann, C.S., Cornell G.: Core JavaTM 2 Volume 1: Fundamentals, Sun Microsystems Press, 4^{th} Edition, 1998

[57] Flanagan, D.: Java in a Nutshell, O'Reilly, 2^{nd} Edition, 1997

[58] Flanagan, D.: Java Examples in a Nutshell, O'Reilly, 1^{st} Edition, 1997

[59] Vollmer, R.: Einrichtung zur Bestimmung der Ummagnetisierungsverluste bei Dreh- und Wechselmagnetisierung, Dissertation, University of Hannover, 1983

[60] Wahlen, H.-J. : Konstruktionsmöglichkeiten und Entwurfsgrenzen von hochtourigen Scheibenläufer-Synchronmaschinen mit Permanenterregung, Dissertation, Technical University of Braunschweig, 1984

Appendix A

Design Tables

The design tables list the dimensions and the theoretical and finite element solutions for the air gap and the permanent magnet flux density and the force densities. The designs are derived from the *optimum magnet use* layout approach for the *reduced magnet material* passive rotor transverse flux motor design presented in Chapter 4. All values refer to the rotor position $x = 0.5\tau_p$. The parameter are varied as follows:

- Air gap $\delta = 0.5,\ 0.75,\ 1.0\,mm$
- Effective flux accumulation factors of $C_{eff} = 1.5,\ 2.0, \ldots,\ 3.5$
- Stator depth $d_s = 10,\ 20\,mm$
- Rotor pole width $w_p = 0.7,\ 0.85,\ 1.0\,\tau_p$

Air gap		Flux acc. factor	PM width	rel. PM width	Pole pitch	Rotor pole width	Stator depth	Flux acc. factor	Stator height	Th. air gap B	FEA air gap B	FEA PM B	Carter factor	Th. force dens.	FEA force dens.	PM leakage
δ		C_{eff}	w_{pm}	$\frac{w_{pm}}{\tau_p}$	τ_p	w_r	d_s	C_m	h_s	$B_{\delta_{pm_t}}$	$B_{\delta_{pm_F}}$	B_{pm}	k_c	F_{Ax_t}	F_{Ax_F}	σ_{pm}
$[mm]$			$[mm]$		$[mm]$	$[mm]$	$[mm]$	$[mm]$	$[mm]$	$[T]$	$[T]$	$[T]$		$\left[\frac{kN}{m^2}\right]$	$\left[\frac{kN}{m^2}\right]$	
0.50	1.5	1.57	1.57	0.22	7.14	5.00	10.0	3.25	8.13	0.76	0.73	0.523	1.09	96.9	79.5	0.63
0.50	2.0	2.10	2.10	0.29	7.14	5.00	10.0	4.00	10.01	1.01	0.96	0.530	1.15	122.4	89.2	0.61
0.50	2.5	2.62	2.62	0.37	7.14	5.00	10.0	4.75	11.89	1.26	1.22	0.528	1.23	143.4	111.7	0.59
0.50	3.0	3.14	3.14	0.44	7.14	5.00	10.0	5.50	13.76	1.51	1.47	0.525	1.32	159.9	142.2	0.56
0.50	3.5	3.67	3.67	0.51	7.14	5.00	10.0	6.26	15.64	1.77	1.73	0.515	1.44	171.7	187.3	0.54
0.50	1.5	1.57	1.57	0.15	10.71	7.50	10.0	4.34	16.28	0.76	0.81	0.477	1.06	66.6	65.6	0.55
0.50	2.0	2.10	2.10	0.20	10.71	7.50	10.0	5.34	20.03	1.01	1.04	0.495	1.10	85.8	66.5	0.54
0.50	2.5	2.62	2.62	0.24	10.71	7.50	10.0	6.34	23.79	1.26	1.27	0.505	1.14	103.0	90.4	0.51
0.50	3.0	3.14	3.14	0.29	10.71	7.50	10.0	7.34	27.54	1.51	1.51	0.511	1.20	118.2	93.6	0.49
0.50	3.5	3.67	3.67	0.34	10.71	7.50	10.0	8.35	31.30	1.77	1.77	0.513	1.26	131.3	121.4	0.45
0.50	1.5	1.57	1.57	0.11	14.29	10.00	10.0	6.52	32.60	0.76	0.89	0.426	1.04	50.7	62.7	0.44
0.50	2.0	2.10	2.10	0.15	14.29	10.00	10.0	8.02	40.12	1.01	1.13	0.450	1.07	65.9	65.4	0.42
0.50	2.5	2.62	2.62	0.18	14.29	10.00	10.0	9.53	47.64	1.26	1.36	0.468	1.10	80.0	63.1	0.40
0.50	3.0	3.14	3.14	0.22	14.29	10.00	10.0	11.03	55.16	1.51	1.61	0.481	1.14	93.0	85.6	0.37
0.50	3.5	3.67	3.67	0.26	14.29	10.00	10.0	12.54	62.68	1.77	1.83	0.491	1.18	104.7	85.5	0.36

Table A.1: Air gap $0.5\,mm$, Stator depth $10\,mm$, Rotor pole width $0.7\,\tau_p$

Air gap δ [mm]	Flux acc. factor C_{eff}	PM width w_{pm} [mm]	rel. PM width $\frac{w_{pm}}{\tau_p}$	Pole pitch τ_p [mm]	Rotor pole width w_r [mm]	Stator depth d_s [mm]	Flux acc. factor C_m [mm]	Stator height h_s [mm]	Th. air gap B $B_{\delta_{pm_t}}$ [T]	FEA air gap B $B_{\delta_{pm_F}}$ [T]	FEA PM B B_{pm} [T]	Carter factor k_c	Th. force dens. F_{Ax_t} [$\frac{kN}{m^2}$]	FEA force dens. F_{Ax_F} [$\frac{kN}{m^2}$]	PM leakage σ_{pm}
0.50	1.5	1.57	0.27	5.88	5.00	10.0	2.83	7.07	0.76	0.73	0.531	1.12	115.4	91.7	0.66
0.50	2.0	2.10	0.36	5.88	5.00	10.0	3.52	8.79	1.01	0.96	0.532	1.19	143.7	104.0	0.63
0.50	2.5	2.62	0.45	5.88	5.00	10.0	4.21	10.51	1.26	1.21	0.528	1.30	165.5	133.7	0.61
0.50	3.0	3.14	0.53	5.88	5.00	10.0	4.90	12.24	1.51	1.51	0.516	1.42	180.7	165.2	0.60
0.50	3.5	3.67	0.62	5.88	5.00	10.0	5.58	13.96	1.77	1.81	0.501	1.59	188.9	193.0	0.58
0.50	1.5	1.57	0.18	8.82	7.50	10.0	3.49	13.08	0.76	0.78	0.499	1.07	79.9	65.2	0.60
0.50	2.0	2.10	0.24	8.82	7.50	10.0	4.34	16.27	1.01	0.76	0.634	1.12	102.0	84.5	0.32
0.50	2.5	2.62	0.30	8.82	7.50	10.0	5.19	19.46	1.26	1.25	0.517	1.18	121.2	107.0	0.56
0.50	3.0	3.14	0.36	8.82	7.50	10.0	6.04	22.65	1.51	1.50	0.519	1.25	137.5	113.1	0.53
0.50	3.5	3.67	0.42	8.82	7.50	10.0	6.89	25.84	1.77	1.73	0.519	1.33	150.6	144.2	0.50
0.50	1.5	1.57	0.13	11.76	10.00	10.0	4.55	22.76	0.76	0.84	0.460	1.05	61.0	64.6	0.52
0.50	2.0	2.10	0.18	11.76	10.00	10.0	5.66	28.31	1.01	1.07	0.479	1.09	78.8	67.3	0.51
0.50	2.5	2.62	0.22	11.76	10.00	10.0	6.77	33.87	1.26	1.30	0.492	1.13	95.0	88.8	0.47
0.50	3.0	3.14	0.27	11.76	10.00	10.0	7.88	39.42	1.51	1.53	0.501	1.17	109.5	110.5	0.45
0.50	3.5	3.67	0.31	11.76	10.00	10.0	8.99	44.97	1.77	1.76	0.508	1.23	122.3	114.1	0.42

Table A.2: Air gap $0.5\,mm$, Stator depth $10\,mm$, Rotor pole width $0.85\,\tau_p$

Air gap δ [mm]	Flux acc. factor C_{eff}	PM width w_{pm} [mm]	rel. PM width $\frac{w_{pm}}{\tau_p}$	Pole pitch τ_p [mm]	Rotor pole width w_r [mm]	Stator depth d_s [mm]	Flux acc. factor C_m [mm]	Stator height h_s [mm]	Th. air gap B $B_{\delta_{pm_t}}$ [T]	FEA air gap B $B_{\delta_{pm_F}}$ [T]	FEA PM B B_{pm} [T]	Carter factor k_c	Th. force dens. F_{Ax_t} $\left[\frac{kN}{m^2}\right]$	FEA force dens. F_{Ax_F} $\left[\frac{kN}{m^2}\right]$	PM leakage σ_{pm}
0.50	1.5	1.57	0.31	5.00	5.00	10.0	2.57	6.42	0.76	0.72	0.533	1.14	133.0	87.4	0.66
0.50	2.0	2.10	0.42	5.00	5.00	10.0	3.22	8.05	1.01	0.72	0.653	1.24	163.2	109.7	0.35
0.50	2.5	2.62	0.52	5.00	5.00	10.0	3.87	9.68	1.26	1.25	0.517	1.37	184.6	132.9	0.63
0.50	3.0	3.14	0.63	5.00	5.00	10.0	4.52	11.31	1.51	1.54	0.501	1.54	196.7	165.7	0.61
0.50	3.5	3.67	0.73	5.00	5.00	10.0	5.18	12.94	1.77	1.87	0.478	1.77	199.1	160.5	0.59
0.50	1.5	1.57	0.21	7.50	7.50	10.0	3.03	11.36	0.76	0.76	0.511	1.09	92.7	81.5	0.62
0.50	2.0	2.10	0.28	7.50	7.50	10.0	3.80	14.24	1.01	0.99	0.519	1.15	117.4	93.5	0.61
0.50	2.5	2.62	0.35	7.50	7.50	10.0	4.57	17.13	1.26	1.24	0.521	1.22	138.1	103.5	0.58
0.50	3.0	3.14	0.42	7.50	7.50	10.0	5.34	20.02	1.51	1.48	0.520	1.30	154.7	142.7	0.56
0.50	3.5	3.67	0.49	7.50	7.50	10.0	6.11	22.90	1.77	1.74	0.516	1.41	167.0	156.4	0.54
0.50	1.5	1.57	0.16	10.00	10.00	10.0	3.69	18.46	0.76	0.80	0.482	1.06	71.1	61.7	0.57
0.50	2.0	2.10	0.21	10.00	10.00	10.0	4.63	23.16	1.01	1.04	0.498	1.11	91.3	85.9	0.55
0.50	2.5	2.62	0.26	10.00	10.00	10.0	5.57	27.85	1.26	1.27	0.507	1.15	109.2	94.0	0.52
0.50	3.0	3.14	0.31	10.00	10.00	10.0	6.51	32.54	1.51	1.51	0.512	1.21	124.8	102.6	0.50
0.50	3.5	3.67	0.37	10.00	10.00	10.0	7.45	37.24	1.77	1.75	0.515	1.28	138.1	107.1	0.48

Table A.3: Air gap $0.5\,mm$, Stator depth $10\,mm$, Rotor pole width $1.0\,\tau_p$

Air gap δ [mm]	Flux acc. factor C_{eff}	PM width w_{pm} [mm]	rel. PM width $\frac{w_{pm}}{\tau_p}$	Pole pitch τ_p [mm]	Rotor pole width w_r [mm]	Stator depth d_s [mm]	Flux acc. factor C_m [mm]	Stator height h_s [mm]	Th. air gap B $B_{\delta_{pm_t}}$ [T]	FEA air gap B $B_{\delta_{pm_F}}$ [T]	FEA PM B B_{pm} [T]	Carter factor k_c	Th. force dens. F_{Ax_t} $\left[\frac{kN}{m^2}\right]$	FEA force dens. F_{Ax_F} $\left[\frac{kN}{m^2}\right]$	PM leakage σ_{pm}
0.50	1.5	1.57	0.22	7.14	5.00	20.0	2.60	6.50	0.76	0.74	0.519	1.09	96.9	76.3	0.79
0.50	2.0	2.10	0.29	7.14	5.00	20.0	3.20	8.00	1.01	0.98	0.521	1.15	122.4	87.7	0.79
0.50	2.5	2.62	0.37	7.14	5.00	20.0	3.80	9.51	1.26	1.26	0.515	1.23	143.4	111.1	0.76
0.50	3.0	3.14	0.44	7.14	5.00	20.0	4.40	11.01	1.51	1.52	0.506	1.32	159.9	142.8	0.75
0.50	3.5	3.67	0.51	7.14	5.00	20.0	5.00	12.51	1.77	1.81	0.490	1.44	171.7	188.4	0.74
0.50	1.5	1.57	0.15	10.71	7.50	20.0	2.89	10.84	0.76	0.78	0.493	1.06	66.6	58.1	0.78
0.50	2.0	2.10	0.20	10.71	7.50	20.0	3.56	13.34	1.01	1.02	0.504	1.10	85.8	60.1	0.78
0.50	2.5	2.62	0.24	10.71	7.50	20.0	4.23	15.84	1.26	1.26	0.506	1.14	103.0	83.7	0.75
0.50	3.0	3.14	0.29	10.71	7.50	20.0	4.89	18.35	1.51	1.51	0.506	1.20	118.2	88.9	0.73
0.50	3.5	3.67	0.34	10.71	7.50	20.0	5.56	20.85	1.77	1.81	0.502	1.26	131.3	115.5	0.69
0.50	1.5	1.57	0.11	14.29	10.00	20.0	3.25	16.27	0.76	0.82	0.468	1.04	50.7	50.8	0.74
0.50	2.0	2.10	0.15	14.29	10.00	20.0	4.00	20.02	1.01	1.06	0.483	1.07	65.9	52.6	0.73
0.50	2.5	2.62	0.18	14.29	10.00	20.0	4.75	23.77	1.26	1.30	0.492	1.10	80.0	50.4	0.72
0.50	3.0	3.14	0.22	14.29	10.00	20.0	5.50	27.52	1.51	1.55	0.496	1.14	93.0	73.4	0.69
0.50	3.5	3.67	0.26	14.29	10.00	20.0	6.26	31.28	1.77	1.80	0.498	1.18	104.7	75.0	0.67

Table A.4: Air gap $0.5\,mm$, Stator depth $20\,mm$, Rotor pole width $0.7\,\tau_p$

Air gap δ [mm]	Flux acc. factor C_{eff}	PM width w_{pm} [mm]	rel. PM width $\frac{w_{pm}}{\tau_p}$	Pole pitch τ_p [mm]	Rotor pole width w_r [mm]	Stator depth d_s [mm]	Flux acc. factor C_m [mm]	Stator height h_s [mm]	Th. air gap B $B_{\delta_{pm_t}}$ [T]	FEA air gap B $B_{\delta_{pm_F}}$ [T]	FEA PM B B_{pm} [T]	Carter factor k_c	Th. force dens. F_{Ax_t} $\left[\frac{kN}{m^2}\right]$	FEA force dens. F_{Ax_F} $\left[\frac{kN}{m^2}\right]$	PM leakage σ_{pm}
0.50	1.5	1.57	0.27	5.88	5.00	20.0	2.38	5.94	0.76	0.73	0.525	1.12	115.4	90.2	0.80
0.50	2.0	2.10	0.36	5.88	5.00	20.0	2.96	7.39	1.01	0.99	0.518	1.19	143.7	104.9	0.79
0.50	2.5	2.62	0.45	5.88	5.00	20.0	3.54	8.84	1.26	1.26	0.509	1.30	165.5	135.9	0.78
0.50	3.0	3.14	0.53	5.88	5.00	20.0	4.12	10.29	1.51	1.58	0.492	1.42	180.7	169.2	0.77
0.50	3.5	3.67	0.62	5.88	5.00	20.0	4.69	11.74	1.77	1.91	0.472	1.59	188.9	199.7	0.76
0.50	1.5	1.57	0.18	8.82	7.50	20.0	2.58	9.68	0.76	0.77	0.503	1.07	79.9	60.4	0.80
0.50	2.0	2.10	0.24	8.82	7.50	20.0	3.21	12.04	1.01	1.00	0.508	1.12	102.0	82.0	0.78
0.50	2.5	2.62	0.30	8.82	7.50	20.0	3.84	14.41	1.26	1.26	0.510	1.18	121.2	101.6	0.77
0.50	3.0	3.14	0.36	8.82	7.50	20.0	4.47	16.77	1.51	1.52	0.506	1.25	137.5	110.0	0.74
0.50	3.5	3.67	0.42	8.82	7.50	20.0	5.10	19.13	1.77	1.79	0.501	1.33	150.6	142.1	0.72
0.50	1.5	1.57	0.13	11.76	10.00	20.0	2.83	14.13	0.76	0.79	0.483	1.05	61.0	55.6	0.76
0.50	2.0	2.10	0.18	11.76	10.00	20.0	3.52	17.58	1.01	1.05	0.494	1.09	78.8	58.2	0.77
0.50	2.5	2.62	0.22	11.76	10.00	20.0	4.21	21.03	1.26	1.28	0.499	1.13	95.0	79.2	0.73
0.50	3.0	3.14	0.27	11.76	10.00	20.0	4.90	24.48	1.51	1.53	0.502	1.17	109.5	98.5	0.72
0.50	3.5	3.67	0.31	11.76	10.00	20.0	5.58	27.92	1.77	1.81	0.500	1.23	122.3	103.9	0.70

Table A.5: Air gap $0.5\,mm$, Stator depth $20\,mm$, Rotor pole width $0.85\,\tau_p$

Air gap δ [mm]	Flux acc. factor C_{eff}	PM width w_{pm} [mm]	rel. PM width $\frac{w_{pm}}{\tau_p}$	Pole pitch τ_p [mm]	Rotor pole width w_r [mm]	Stator depth d_s [mm]	Flux acc. factor C_m [mm]	Stator height h_s [mm]	Th. air gap B $B_{\delta_{pm_t}}$ [T]	FEA air gap B $B_{\delta_{pm_F}}$ [T]	FEA PM B B_{pm} [T]	Carter factor k_c	Th. force dens. F_{Ax_t} $\left[\frac{kN}{m^2}\right]$	FEA force dens. F_{Ax_F} $\left[\frac{kN}{m^2}\right]$	PM leakage σ_{pm}
0.50	1.5	1.57	0.31	5.00	5.00	20.0	2.23	5.57	0.76	0.74	0.520	1.14	133.0	88.3	0.80
0.50	2.0	2.10	0.42	5.00	5.00	20.0	2.79	6.98	1.01	1.01	0.512	1.24	163.2	121.2	0.79
0.50	2.5	2.62	0.52	5.00	5.00	20.0	3.36	8.40	1.26	1.30	0.495	1.37	184.6	138.5	0.78
0.50	3.0	3.14	0.63	5.00	5.00	20.0	3.93	9.81	1.51	1.63	0.474	1.54	196.7	171.6	0.78
0.50	3.5	3.67	0.73	5.00	5.00	20.0	4.49	11.23	1.77	1.99	0.446	1.77	199.1	175.9	0.76
0.50	1.5	1.57	0.21	7.50	7.50	20.0	2.39	8.94	0.76	0.76	0.508	1.09	92.7	76.7	0.80
0.50	2.0	2.10	0.28	7.50	7.50	20.0	2.99	11.22	1.01	1.01	0.511	1.15	117.4	89.9	0.80
0.50	2.5	2.62	0.35	7.50	7.50	20.0	3.60	13.49	1.26	1.27	0.508	1.22	138.1	101.5	0.77
0.50	3.0	3.14	0.42	7.50	7.50	20.0	4.20	15.76	1.51	1.53	0.502	1.30	154.7	139.8	0.75
0.50	3.5	3.67	0.49	7.50	7.50	20.0	4.81	18.04	1.77	1.84	0.491	1.41	167.0	155.9	0.74
0.50	1.5	1.57	0.16	10.00	10.00	20.0	2.57	12.84	0.76	0.78	0.493	1.06	71.1	55.4	0.78
0.50	2.0	2.10	0.21	10.00	10.00	20.0	3.22	16.10	1.01	1.03	0.501	1.11	91.3	78.0	0.77
0.50	2.5	2.62	0.26	10.00	10.00	20.0	3.87	19.36	1.26	1.28	0.504	1.15	109.2	86.6	0.76
0.50	3.0	3.14	0.31	10.00	10.00	20.0	4.52	22.62	1.51	1.53	0.504	1.21	124.8	95.2	0.73
0.50	3.5	3.67	0.37	10.00	10.00	20.0	5.18	25.88	1.77	1.80	0.502	1.28	138.1	101.8	0.72

Table A.6: Air gap $0.5\,mm$, Stator depth $20\,mm$, Rotor pole width $1.0\,\tau_p$

Air gap δ [mm]	Flux acc. factor C_{eff}	PM width w_{pm} [mm]	rel. PM width $\frac{w_{pm}}{\tau_p}$	Pole pitch τ_p [mm]	Rotor pole width w_r [mm]	Stator depth d_s [mm]	Flux acc. factor C_m [mm]	Stator height h_s [mm]	Th. air gap B $B_{\delta_{pm_t}}$ [T]	FEA air gap B $B_{\delta_{pm_F}}$ [T]	FEA PM B B_{pm} [T]	Carter factor k_c	Th. force dens. F_{Ax_t} [$\frac{kN}{m^2}$]	FEA force dens. F_{Ax_F} [$\frac{kN}{m^2}$]	PM leakage σ_{pm}
0.75	1.5	2.36	0.22	10.71	7.50	10.0	4.34	16.28	0.76	0.76	0.506	1.09	64.6	61.5	0.50
0.75	2.0	3.14	0.29	10.71	7.50	10.0	5.34	20.03	1.01	0.99	0.520	1.15	81.6	69.1	0.48
0.75	2.5	3.93	0.37	10.71	7.50	10.0	6.34	23.79	1.26	1.24	0.526	1.23	95.6	86.9	0.44
0.75	3.0	4.72	0.44	10.71	7.50	10.0	7.34	27.54	1.51	1.46	0.528	1.32	106.6	106.1	0.42
0.75	3.5	5.50	0.51	10.71	7.50	10.0	8.35	31.30	1.77	1.74	0.523	1.44	114.5	138.5	0.38
0.75	1.5	2.36	0.17	14.29	10.00	10.0	6.52	32.60	0.76	0.83	0.463	1.07	49.6	48.3	0.39
0.75	2.0	3.14	0.22	14.29	10.00	10.0	8.02	40.12	1.01	1.06	0.486	1.11	63.5	62.2	0.37
0.75	2.5	3.93	0.28	14.29	10.00	10.0	9.53	47.64	1.26	1.28	0.502	1.16	75.9	65.5	0.34
0.75	3.0	4.72	0.33	14.29	10.00	10.0	11.03	55.16	1.51	1.51	0.514	1.23	86.5	84.2	0.31
0.75	3.5	5.50	0.39	14.29	10.00	10.0	12.54	62.68	1.77	1.73	0.523	1.30	95.3	83.5	0.29
0.75	1.5	2.36	0.13	17.86	12.50	10.0	13.09	81.82	0.76	0.77	0.503	1.05	40.2	54.2	0.14
0.75	2.0	3.14	0.18	17.86	12.50	10.0	16.11	100.69	1.01	0.95	0.536	1.09	52.0	61.5	0.13
0.75	2.5	3.93	0.22	17.86	12.50	10.0	19.13	119.57	1.26	1.13	0.564	1.13	62.7	72.8	0.12
0.75	3.0	4.72	0.26	17.86	12.50	10.0	22.15	138.44	1.51	1.30	0.582	1.17	72.3	78.0	0.11
0.75	3.5	5.50	0.31	17.86	12.50	10.0	25.17	157.31	1.77	1.49	0.590	1.22	80.8	101.2	0.10

Table A.7: Air gap $0.75\,mm$, Stator depth $10\,mm$, Rotor pole width $0.7\,\tau_p$

Air gap δ [mm]	Flux acc. factor C_{eff}	PM width w_{pm} [mm]	rel. PM width $\frac{w_{pm}}{\tau_p}$	Pole pitch τ_p [mm]	Rotor pole width w_r [mm]	Stator depth d_s [mm]	Flux acc. factor C_m [mm]	Stator height h_s [mm]	Th. air gap B $B_{\delta_{pm_t}}$ [T]	FEA air gap B $B_{\delta_{pm_F}}$ [T]	FEA PM B B_{pm} [T]	Carter factor k_c	Th. force dens. F_{Ax_t} $\left[\frac{kN}{m^2}\right]$	FEA force dens. F_{Ax_F} $\left[\frac{kN}{m^2}\right]$	PM leakage σ_{pm}
0.75	1.5	2.36	0.27	8.82	7.50	10.0	3.49	13.08	0.76	0.74	0.521	1.12	76.9	70.4	0.55
0.75	2.0	3.14	0.36	8.82	7.50	10.0	4.34	16.27	1.01	0.74	0.645	1.19	95.8	77.0	0.29
0.75	2.5	3.93	0.45	8.82	7.50	10.0	5.19	19.46	1.26	1.23	0.527	1.30	110.4	100.7	0.50
0.75	3.0	4.72	0.53	8.82	7.50	10.0	6.04	22.65	1.51	1.50	0.522	1.42	120.5	123.7	0.47
0.75	3.5	5.50	0.62	8.82	7.50	10.0	6.89	25.84	1.77	1.78	0.512	1.59	125.9	142.5	0.45
0.75	1.5	2.36	0.20	11.76	10.00	10.0	4.55	22.76	0.76	0.79	0.491	1.08	59.3	50.9	0.48
0.75	2.0	3.14	0.27	11.76	10.00	10.0	5.66	28.31	1.01	1.01	0.508	1.14	75.3	76.9	0.44
0.75	2.5	3.93	0.33	11.76	10.00	10.0	6.77	33.87	1.26	1.24	0.518	1.21	88.9	83.0	0.41
0.75	3.0	4.72	0.40	11.76	10.00	10.0	7.88	39.42	1.51	1.47	0.523	1.29	99.9	101.2	0.39
0.75	3.5	5.50	0.47	11.76	10.00	10.0	8.99	44.97	1.77	1.74	0.524	1.39	108.3	127.8	0.37
0.75	1.5	2.36	0.16	14.71	12.50	10.0	6.55	40.95	0.76	0.84	0.455	1.07	48.3	51.3	0.38
0.75	2.0	3.14	0.21	14.71	12.50	10.0	8.15	50.94	1.01	1.08	0.479	1.11	61.9	65.7	0.34
0.75	2.5	3.93	0.27	14.71	12.50	10.0	9.75	60.93	1.26	1.29	0.496	1.16	74.0	82.4	0.32
0.75	3.0	4.72	0.32	14.71	12.50	10.0	11.35	70.92	1.51	1.54	0.508	1.22	84.5	85.9	0.29
0.75	3.5	5.50	0.37	14.71	12.50	10.0	12.95	80.91	1.77	1.75	0.517	1.29	93.4	87.3	0.28

Table A.8: Air gap $0.75\,mm$, Stator depth $10\,mm$, Rotor pole width $0.85\,\tau_p$

Air gap δ [mm]	Flux acc. factor C_{eff}	PM width w_{pm} [mm]	rel. PM width $\frac{w_{pm}}{\tau_p}$	Pole pitch τ_p [mm]	Rotor pole width w_r [mm]	Stator depth d_s [mm]	Flux acc. factor C_m [mm]	Stator height h_s [mm]	Th. air gap B $B_{\delta_{pm_t}}$ [T]	FEA air gap B $B_{\delta_{pm_F}}$ [T]	FEA PM B B_{pm} [T]	Carter factor k_c	Th. force dens. F_{Ax_t} $\left[\frac{kN}{m^2}\right]$	FEA force dens. F_{Ax_F} $\left[\frac{kN}{m^2}\right]$	PM leakage σ_{pm}
0.75	1.5	2.36	0.31	7.50	7.50	10.0	3.03	11.36	0.76	0.74	0.527	1.14	77.4	68.0	0.57
0.75	2.0	3.14	0.42	7.50	7.50	10.0	3.80	14.24	1.01	0.98	0.527	1.24	113.3	91.6	0.54
0.75	2.5	3.93	0.52	7.50	7.50	10.0	4.57	17.13	1.26	1.25	0.520	1.37	143.6	105.1	0.51
0.75	3.0	4.72	0.63	7.50	7.50	10.0	5.34	20.02	1.51	1.52	0.509	1.54	198.2	128.8	0.50
0.75	3.5	5.50	0.73	7.50	7.50	10.0	6.11	22.90	1.77	1.84	0.491	1.77	240.5	135.6	0.46
0.75	1.5	2.36	0.24	10.00	10.00	10.0	3.69	18.46	0.76	0.77	0.507	1.10	68.6	62.4	0.52
0.75	2.0	3.14	0.31	10.00	10.00	10.0	4.63	23.16	1.01	1.00	0.518	1.17	85.3	73.1	0.49
0.75	2.5	3.93	0.39	10.00	10.00	10.0	5.57	27.85	1.26	1.24	0.523	1.25	101.8	81.3	0.46
0.75	3.0	4.72	0.47	10.00	10.00	10.0	6.51	32.54	1.51	1.50	0.522	1.36	147.2	108.5	0.43
0.75	3.5	5.50	0.55	10.00	10.00	10.0	7.45	37.24	1.77	1.77	0.518	1.49	178.5	120.1	0.41
0.75	1.5	2.36	0.19	12.50	12.50	10.0	4.73	29.56	0.76	0.81	0.480	1.08	52.9	49.0	0.45
0.75	2.0	3.14	0.25	12.50	12.50	10.0	5.93	37.08	1.01	1.03	0.499	1.13	76.5	67.7	0.42
0.75	2.5	3.93	0.31	12.50	12.50	10.0	7.13	44.59	1.26	1.26	0.511	1.19	90.0	75.5	0.39
0.75	3.0	4.72	0.38	12.50	12.50	10.0	8.34	52.10	1.51	1.49	0.519	1.27	102.9	81.2	0.37
0.75	3.5	5.50	0.44	12.50	12.50	10.0	9.54	59.62	1.77	1.74	0.522	1.35	146.0	107.8	0.34

Table A.9: Air gap $0.75\,mm$, Stator depth $10\,mm$, Rotor pole width $1.0\,\tau_p$

Air gap δ [mm]	Flux acc. factor C_{eff}	PM width w_{pm} [mm]	rel. PM width $\frac{w_{pm}}{\tau_p}$	Pole pitch τ_p [mm]	Rotor pole width w_r [mm]	Stator depth d_s [mm]	Flux acc. factor C_m [mm]	Stator height h_s [mm]	Th. air gap B $B_{\delta_{pm_t}}$ [T]	FEA air gap B $B_{\delta_{pm_F}}$ [T]	FEA PM B B_{pm} [T]	Carter factor k_c	Th. force dens. F_{Ax_t} $\left[\frac{kN}{m^2}\right]$	FEA force dens. F_{Ax_F} $\left[\frac{kN}{m^2}\right]$	PM leakage σ_{pm}
0.75	1.5	2.36	0.22	10.71	7.50	20.0	2.89	10.84	0.76	0.75	0.512	1.09	64.6	56.4	0.73
0.75	2.0	3.14	0.29	10.71	7.50	20.0	3.56	13.34	1.01	1.00	0.517	1.15	81.6	64.9	0.73
0.75	2.5	3.93	0.37	10.71	7.50	20.0	4.23	15.84	1.26	1.26	0.515	1.23	95.6	83.0	0.68
0.75	3.0	4.72	0.44	10.71	7.50	20.0	4.89	18.35	1.51	1.52	0.508	1.32	106.6	103.8	0.67
0.75	3.5	5.50	0.51	10.71	7.50	20.0	5.56	20.85	1.77	1.79	0.496	1.44	114.5	136.5	0.64
0.75	1.5	2.36	0.17	14.29	10.00	20.0	3.25	16.27	0.76	0.78	0.492	1.07	49.6	40.9	0.70
0.75	2.0	3.14	0.22	14.29	10.00	20.0	4.00	20.02	1.01	1.02	0.503	1.11	63.5	54.5	0.67
0.75	2.5	3.93	0.28	14.29	10.00	20.0	4.75	23.77	1.26	1.26	0.509	1.16	75.9	59.1	0.66
0.75	3.0	4.72	0.33	14.29	10.00	20.0	5.50	27.52	1.51	1.52	0.508	1.23	86.5	76.7	0.62
0.75	3.5	5.50	0.39	14.29	10.00	20.0	6.26	31.28	1.77	1.78	0.507	1.30	95.3	79.6	0.60
0.75	1.5	2.36	0.13	17.86	12.50	20.0	3.72	23.25	0.76	0.83	0.468	1.05	40.2	41.2	0.66
0.75	2.0	3.14	0.18	17.86	12.50	20.0	4.58	28.61	1.01	1.07	0.485	1.09	52.0	43.1	0.64
0.75	2.5	3.93	0.22	17.86	12.50	20.0	5.44	33.97	1.26	1.31	0.494	1.13	62.7	57.3	0.61
0.75	3.0	4.72	0.26	17.86	12.50	20.0	6.29	39.33	1.51	1.55	0.500	1.17	72.3	59.9	0.60
0.75	3.5	5.50	0.31	17.86	12.50	20.0	7.15	44.69	1.77	1.81	0.502	1.22	80.8	80.5	0.55

Table A.10: Air gap $0.75\,mm$, Stator depth $20\,mm$, Rotor pole width $0.7\,\tau_p$

Air gap δ [mm]	Flux acc. factor C_{eff}	PM width w_{pm} [mm]	rel. PM width $\frac{w_{pm}}{\tau_p}$	Pole pitch τ_p [mm]	Rotor pole width w_r [mm]	Stator depth d_s [mm]	Flux acc. factor C_m [mm]	Stator height h_s [mm]	Th. air gap B $B_{\delta_{pm_t}}$ [T]	FEA air gap B $B_{\delta_{pm_F}}$ [T]	FEA PM B B_{pm} [T]	Carter factor k_c	Th. force dens. F_{Ax_t} [$\frac{kN}{m^2}$]	FEA force dens. F_{Ax_F} [$\frac{kN}{m^2}$]	PM leakage σ_{pm}
0.75	1.5	2.36	0.27	8.82	7.50	20.0	2.58	9.68	0.76	0.74	0.517	1.12	76.9	66.1	0.75
0.75	2.0	3.14	0.36	8.82	7.50	20.0	3.21	12.04	1.01	0.99	0.517	1.19	95.8	77.4	0.72
0.75	2.5	3.93	0.45	8.82	7.50	20.0	3.84	14.41	1.26	1.28	0.507	1.30	110.4	99.1	0.72
0.75	3.0	4.72	0.53	8.82	7.50	20.0	4.47	16.77	1.51	1.57	0.496	1.42	120.5	122.9	0.69
0.75	3.5	5.50	0.62	8.82	7.50	20.0	5.10	19.13	1.77	1.89	0.478	1.59	125.9	143.9	0.68
0.75	1.5	2.36	0.20	11.76	10.00	20.0	2.83	14.13	0.76	0.77	0.502	1.08	59.3	45.4	0.74
0.75	2.0	3.14	0.27	11.76	10.00	20.0	3.52	17.58	1.01	1.01	0.509	1.14	75.3	69.4	0.71
0.75	2.5	3.93	0.33	11.76	10.00	20.0	4.21	21.03	1.26	1.26	0.511	1.21	88.9	76.6	0.67
0.75	3.0	4.72	0.40	11.76	10.00	20.0	4.90	24.48	1.51	1.52	0.508	1.29	99.9	96.8	0.65
0.75	3.5	5.50	0.47	11.76	10.00	20.0	5.58	27.92	1.77	1.80	0.502	1.39	108.3	122.8	0.64
0.75	1.5	2.36	0.16	14.71	12.50	20.0	3.12	19.52	0.76	0.80	0.485	1.07	48.3	42.5	0.70
0.75	2.0	3.14	0.21	14.71	12.50	20.0	3.88	24.28	1.01	1.05	0.497	1.11	61.9	56.1	0.68
0.75	2.5	3.93	0.27	14.71	12.50	20.0	4.65	29.04	1.26	1.29	0.503	1.16	74.0	70.7	0.66
0.75	3.0	4.72	0.32	14.71	12.50	20.0	5.41	33.80	1.51	1.54	0.506	1.22	84.5	75.8	0.63
0.75	3.5	5.50	0.37	14.71	12.50	20.0	6.17	38.56	1.77	1.80	0.505	1.29	93.4	78.8	0.61

Table A.11: Air gap $0.75\,mm$, Stator depth $20\,mm$, Rotor pole width $0.85\,\tau_p$

Air gap δ [mm]	Flux acc. factor C_{eff}	PM width w_{pm} [mm]	rel. PM width $\frac{w_{pm}}{\tau_p}$	Pole pitch τ_p [mm]	Rotor pole width w_r [mm]	Stator depth d_s [mm]	Flux acc. factor C_m [mm]	Stator height h_s [mm]	Th. air gap B $B_{\delta_{pm_t}}$ [T]	FEA air gap B $B_{\delta_{pm_F}}$ [T]	FEA PM B B_{pm} [T]	Carter factor k_c	Th. force dens. F_{Ax_t} $\left[\frac{kN}{m^2}\right]$	FEA force dens. F_{Ax_F} $\left[\frac{kN}{m^2}\right]$	PM leakage σ_{pm}
0.75	1.5	2.36	0.31	7.50	7.50	20.0	2.39	8.94	0.76	0.75	0.517	1.14	88.7	65.8	0.75
0.75	2.0	3.14	0.42	7.50	7.50	20.0	2.99	11.22	1.01	1.01	0.510	1.24	108.8	89.3	0.73
0.75	2.5	3.93	0.52	7.50	7.50	20.0	3.60	13.49	1.26	1.30	0.497	1.37	123.1	105.1	0.72
0.75	3.0	4.72	0.63	7.50	7.50	20.0	4.20	15.76	1.51	1.63	0.478	1.54	131.1	129.2	0.70
0.75	3.5	5.50	0.73	7.50	7.50	20.0	4.81	18.04	1.77	1.96	0.453	1.77	132.7	140.8	0.68
0.75	1.5	2.36	0.24	10.00	10.00	20.0	2.57	12.84	0.76	0.76	0.508	1.10	68.8	57.5	0.74
0.75	2.0	3.14	0.31	10.00	10.00	20.0	3.22	16.10	1.01	1.01	0.511	1.17	86.4	68.8	0.72
0.75	2.5	3.93	0.39	10.00	10.00	20.0	3.87	19.36	1.26	1.27	0.508	1.25	100.8	78.2	0.70
0.75	3.0	4.72	0.47	10.00	10.00	20.0	4.52	22.62	1.51	1.56	0.499	1.36	111.6	105.3	0.67
0.75	3.5	5.50	0.55	10.00	10.00	20.0	5.18	25.88	1.77	1.85	0.488	1.49	118.8	119.2	0.65
0.75	1.5	2.36	0.19	12.50	12.50	20.0	2.78	17.37	0.76	0.78	0.496	1.08	56.1	43.0	0.72
0.75	2.0	3.14	0.25	12.50	12.50	20.0	3.49	21.78	1.01	1.02	0.504	1.13	71.5	60.4	0.70
0.75	2.5	3.93	0.31	12.50	12.50	20.0	4.19	26.20	1.26	1.27	0.507	1.19	84.7	68.9	0.67
0.75	3.0	4.72	0.38	12.50	12.50	20.0	4.90	30.61	1.51	1.53	0.506	1.27	95.6	76.1	0.65
0.75	3.5	5.50	0.44	12.50	12.50	20.0	5.60	35.02	1.77	1.78	0.503	1.35	104.3	102.5	0.63

Table A.12: Air gap $0.75\,mm$, Stator depth $20\,mm$, Rotor pole width $01.0\,\tau_p$

Air gap δ [mm]	Flux acc. factor C_{eff}	PM width w_{pm} [mm]	rel. PM width $\frac{w_{pm}}{\tau_p}$	Pole pitch τ_p [mm]	Rotor pole width w_r [mm]	Stator depth d_s [mm]	Flux acc. factor C_m [mm]	Stator height h_s [mm]	Th. air gap B $B_{\delta_{pm_t}}$ [T]	FEA air gap B $B_{\delta_{pm_F}}$ [T]	FEA PM B B_{pm} [T]	Carter factor k_c	Th. force dens. F_{Ax_t} $\left[\frac{kN}{m^2}\right]$	FEA force dens. F_{Ax_F} $\left[\frac{kN}{m^2}\right]$	PM leakage σ_{pm}
1.00	1.5	3.14	0.29	10.71	7.50	10.0	4.34	16.28	0.76	0.74	0.527	1.13	62.6	53.2	0.47
1.00	2.0	4.19	0.39	10.71	7.50	10.0	5.34	20.03	1.01	0.97	0.535	1.22	77.4	67.1	0.43
1.00	2.5	5.24	0.49	10.71	7.50	10.0	6.34	23.79	1.26	1.23	0.534	1.33	88.3	83.4	0.41
1.00	3.0	6.29	0.59	10.71	7.50	10.0	7.34	27.54	1.51	1.49	0.527	1.49	95.1	100.9	0.36
1.00	3.5	7.34	0.68	10.71	7.50	10.0	8.35	31.30	1.77	1.76	0.515	1.69	97.7	123.0	0.34
1.00	1.5	3.14	0.22	14.29	10.00	10.0	6.52	32.60	0.76	0.79	0.490	1.09	48.5	47.9	0.36
1.00	2.0	4.19	0.29	14.29	10.00	10.0	8.02	40.12	1.01	1.01	0.511	1.15	61.2	53.0	0.33
1.00	2.5	5.24	0.37	14.29	10.00	10.0	9.53	47.64	1.26	1.24	0.526	1.23	71.7	65.5	0.30
1.00	3.0	6.29	0.44	14.29	10.00	10.0	11.03	55.16	1.51	1.46	0.531	1.32	80.0	78.2	0.28
1.00	3.5	7.34	0.51	14.29	10.00	10.0	12.54	62.68	1.77	1.67	0.535	1.44	85.9	101.7	0.26
1.00	1.5	3.14	0.18	17.86	12.50	10.0	13.09	81.82	0.76	0.71	0.538	1.07	39.5	45.5	0.13
1.00	2.0	4.19	0.23	17.86	12.50	10.0	16.11	100.69	1.01	1.11	0.474	1.12	50.5	56.5	0.19
1.00	2.5	5.24	0.29	17.86	12.50	10.0	19.13	119.57	1.26	1.31	0.497	1.18	60.0	59.7	0.17
1.00	3.0	6.29	0.35	17.86	12.50	10.0	22.15	138.44	1.51	1.51	0.514	1.24	68.1	74.9	0.16
1.00	3.5	7.34	0.41	17.86	12.50	10.0	25.17	157.31	1.77	1.73	0.526	1.32	74.7	85.2	0.15

Table A.13: Air gap $1.0\,mm$, Stator depth $10\,mm$, Rotor pole width $0.7\,\tau_p$

Air gap δ $[mm]$	Flux acc. factor C_{eff}	PM width w_{pm} $[mm]$	rel. PM width $\frac{w_{pm}}{\tau_p}$	Pole pitch τ_p $[mm]$	Rotor pole width w_r $[mm]$	Stator depth d_s $[mm]$	Flux acc. factor C_m $[mm]$	Stator height h_s $[mm]$	Th. air gap B $B_{\delta_{pm_t}}$ $[T]$	FEA air gap B $B_{\delta_{pm_F}}$ $[T]$	FEA PM B B_{pm} $[T]$	Carter factor k_c	Th. force dens. F_{Ax_t} $\left[\frac{kN}{m^2}\right]$	FEA force dens. F_{Ax_F} $\left[\frac{kN}{m^2}\right]$	PM leakage σ_{pm}
1.00	1.5	3.14	0.36	8.82	7.50	10.0	3.49	13.08	0.76	0.73	0.535	1.16	74.0	59.6	0.51
1.00	2.0	4.19	0.48	8.82	7.50	10.0	4.34	16.27	1.01	0.98	0.534	1.28	89.6	83.6	0.49
1.00	2.5	5.24	0.59	8.82	7.50	10.0	5.19	19.46	1.26	1.24	0.526	1.44	99.5	92.4	0.45
1.00	3.0	6.29	0.71	8.82	7.50	10.0	6.04	22.65	1.51	1.50	0.509	1.66	103.4	115.3	0.42
1.00	3.5	7.34	0.83	8.82	7.50	10.0	6.89	25.84	1.77	1.91	0.467	1.98	101.2	129.9	0.42
1.00	1.5	3.14	0.27	11.76	10.00	10.0	4.55	22.76	0.76	0.76	0.512	1.12	57.7	57.2	0.43
1.00	2.0	4.19	0.36	11.76	10.00	10.0	5.66	28.31	1.01	0.98	0.526	1.19	71.8	64.6	0.40
1.00	2.5	5.24	0.45	11.76	10.00	10.0	6.77	33.87	1.26	1.23	0.530	1.30	82.8	79.6	0.38
1.00	3.0	6.29	0.53	11.76	10.00	10.0	7.88	39.42	1.51	1.48	0.530	1.42	90.3	96.8	0.35
1.00	3.5	7.34	0.62	11.76	10.00	10.0	8.99	44.97	1.77	1.74	0.525	1.59	94.4	109.0	0.33
1.00	1.5	3.14	0.21	14.71	12.50	10.0	6.55	40.95	0.76	0.81	0.482	1.09	47.2	49.8	0.34
1.00	2.0	4.19	0.29	14.71	12.50	10.0	8.15	50.94	1.01	1.04	0.504	1.15	59.7	63.3	0.31
1.00	2.5	5.24	0.36	14.71	12.50	10.0	9.75	60.93	1.26	1.25	0.519	1.22	70.1	67.5	0.28
1.00	3.0	6.29	0.43	14.71	12.50	10.0	11.35	70.92	1.51	1.48	0.527	1.31	78.4	80.8	0.27
1.00	3.5	7.34	0.50	14.71	12.50	10.0	12.95	80.91	1.77	1.72	0.533	1.42	84.5	99.2	0.25

Table A.14: Air gap $1.0\,mm$, Stator depth $10\,mm$, Rotor pole width $0.85\,\tau_p$

Air gap δ $[mm]$	Flux acc. factor C_{eff}	PM width w_{pm} $[mm]$	rel. PM width $\frac{w_{pm}}{\tau_p}$	Pole pitch τ_p $[mm]$	Rotor pole width w_r $[mm]$	Stator depth d_s $[mm]$	Flux acc. factor C_m $[mm]$	Stator height h_s $[mm]$	Th. air gap B $B_{\delta_{pm_t}}$ $[T]$	FEA air gap B $B_{\delta_{pm_F}}$ $[T]$	FEA PM B B_{pm} $[T]$	Carter factor k_c	Th. force dens. F_{Ax_t} $\left[\frac{kN}{m^2}\right]$	FEA force dens. F_{Ax_F} $\left[\frac{kN}{m^2}\right]$	PM leakage σ_{pm}
1.00	1.5	3.14	0.42	7.50	7.50	10.0	3.03	11.36	0.76	0.73	0.534	1.19	84.6	64.0	0.52
1.00	2.0	4.19	0.56	7.50	7.50	10.0	3.80	14.24	1.01	0.99	0.524	1.34	100.2	75.6	0.50
1.00	2.5	5.24	0.70	7.50	7.50	10.0	4.57	17.13	1.26	1.31	0.504	1.56	108.0	90.1	0.47
1.00	3.0	6.29	0.84	7.50	7.50	10.0	5.34	20.02	1.51	1.60	0.473	1.88	107.6	94.9	0.44
1.00	3.5	7.34	0.98	7.50	7.50	10.0	6.11	22.90	1.77	1.96	0.421	2.39	98.5	45.1	0.39
1.00	1.5	3.14	0.31	10.00	10.00	10.0	3.69	18.46	0.76	0.74	0.523	1.14	66.5	54.8	0.47
1.00	2.0	4.19	0.42	10.00	10.00	10.0	4.63	23.16	1.01	0.98	0.528	1.24	81.6	72.5	0.44
1.00	2.5	5.24	0.52	10.00	10.00	10.0	5.57	27.85	1.26	1.24	0.526	1.37	92.3	84.3	0.41
1.00	3.0	6.29	0.63	10.00	10.00	10.0	6.51	32.54	1.51	1.52	0.519	1.54	98.3	101.3	0.38
1.00	3.5	7.34	0.73	10.00	10.00	10.0	7.45	37.24	1.77	1.80	0.507	1.77	99.5	109.5	0.36
1.00	1.5	3.14	0.25	12.50	12.50	10.0	4.73	29.56	0.76	0.77	0.502	1.11	54.7	51.1	0.41
1.00	2.0	4.19	0.34	12.50	12.50	10.0	5.93	37.08	1.01	0.99	0.518	1.18	68.4	60.1	0.38
1.00	2.5	5.24	0.42	12.50	12.50	10.0	7.13	44.59	1.26	1.24	0.526	1.27	79.3	77.5	0.35
1.00	3.0	6.29	0.50	12.50	12.50	10.0	8.34	52.10	1.51	1.48	0.528	1.39	87.2	87.2	0.32
1.00	3.5	7.34	0.59	12.50	12.50	10.0	9.54	59.62	1.77	1.74	0.527	1.54	92.0	95.7	0.30

Table A.15: Air gap $1.0\,mm$, Stator depth $10\,mm$, Rotor pole width $1.0\,\tau_p$

Air gap δ [mm]	Flux acc. factor C_{eff}	PM width w_{pm} [mm]	rel. PM width $\frac{w_{pm}}{\tau_p}$	Pole pitch τ_p [mm]	Rotor pole width w_r [mm]	Stator depth d_s [mm]	Flux acc. factor C_m [mm]	Stator height h_s [mm]	Th. air gap B $B_{\delta_{pm_t}}$ [T]	FEA air gap B $B_{\delta_{pm_F}}$ [T]	FEA PM B B_{pm} [T]	Carter factor k_c	Th. force dens. F_{Ax_t} $\left[\frac{kN}{m^2}\right]$	FEA force dens. F_{Ax_F} $\left[\frac{kN}{m^2}\right]$	PM leakage σ_{pm}
1.00	1.5	3.14	0.29	10.71	7.50	20.0	2.89	10.84	0.76	0.74	0.526	1.13	62.6	49.7	0.71
1.00	2.0	4.19	0.39	10.71	7.50	20.0	3.56	13.34	1.01	0.99	0.525	1.22	77.4	64.3	0.66
1.00	2.5	5.24	0.49	10.71	7.50	20.0	4.23	15.84	1.26	1.26	0.516	1.33	88.3	81.9	0.65
1.00	3.0	6.29	0.59	10.71	7.50	20.0	4.89	18.35	1.51	1.52	0.497	1.49	95.1	101.6	0.62
1.00	3.5	7.34	0.68	10.71	7.50	20.0	5.56	20.85	1.77	1.90	0.472	1.69	97.7	125.3	0.58
1.00	1.5	3.14	0.22	14.29	10.00	20.0	3.25	16.27	0.76	0.76	0.509	1.09	48.5	42.2	0.66
1.00	2.0	4.19	0.29	14.29	10.00	20.0	4.00	20.02	1.01	1.00	0.518	1.15	61.2	48.3	0.64
1.00	2.5	5.24	0.37	14.29	10.00	20.0	4.75	23.77	1.26	1.25	0.516	1.23	71.7	61.1	0.61
1.00	3.0	6.29	0.44	14.29	10.00	20.0	5.50	27.52	1.51	1.51	0.514	1.32	80.0	75.8	0.58
1.00	3.5	7.34	0.51	14.29	10.00	20.0	6.26	31.28	1.77	1.77	0.504	1.44	85.9	99.8	0.56
1.00	1.5	3.14	0.18	17.86	12.50	20.0	3.72	23.25	0.76	0.79	0.489	1.07	39.5	34.9	0.63
1.00	2.0	4.19	0.23	17.86	12.50	20.0	4.58	28.61	1.01	1.03	0.502	1.12	50.5	45.8	0.60
1.00	2.5	5.24	0.29	17.86	12.50	20.0	5.44	33.97	1.26	1.27	0.510	1.18	60.0	49.7	0.58
1.00	3.0	6.29	0.35	17.86	12.50	20.0	6.29	39.33	1.51	1.53	0.512	1.24	68.1	63.8	0.53
1.00	3.5	7.34	0.41	17.86	12.50	20.0	7.15	44.69	1.77	1.79	0.510	1.32	74.7	77.6	0.52

Table A.16: Air gap $1.0\,mm$, Stator depth $20\,mm$, Rotor pole width $0.7\,\tau_p$

Air gap δ [mm]	Flux acc. factor C_{eff}	PM width w_{pm} [mm]	rel. PM width $\frac{w_{pm}}{\tau_p}$	Pole pitch τ_p [mm]	Rotor pole width w_r [mm]	Stator depth d_s [mm]	Flux acc. factor C_m [mm]	Stator height h_s [mm]	Th. air gap B $B_{\delta_{pm_t}}$ [T]	FEA air gap B $B_{\delta_{pm_F}}$ [T]	FEA PM B B_{pm} [T]	Carter factor k_c	Th. force dens. F_{Ax_t} $\left[\frac{kN}{m^2}\right]$	FEA force dens. F_{Ax_F} $\left[\frac{kN}{m^2}\right]$	PM leakage σ_{pm}
1.00	1.5	3.14	0.36	8.82	7.50	20.0	2.58	9.68	0.76	0.74	0.525	1.16	74.0	57.2	0.71
1.00	2.0	4.19	0.48	8.82	7.50	20.0	3.21	12.04	1.01	0.74	0.525	1.28	89.6	81.5	0.79
1.00	2.5	5.24	0.59	8.82	7.50	20.0	3.84	14.41	1.26	1.31	0.498	1.44	99.5	92.5	0.67
1.00	3.0	6.29	0.71	8.82	7.50	20.0	4.47	16.77	1.51	1.60	0.472	1.66	103.4	117.7	0.65
1.00	3.5	7.34	0.83	8.82	7.50	20.0	5.10	19.13	1.77	2.07	0.417	1.98	101.2	133.3	0.68
1.00	1.5	3.14	0.27	11.76	10.00	20.0	2.83	14.13	0.76	0.75	0.515	1.12	57.7	51.9	0.69
1.00	2.0	4.19	0.36	11.76	10.00	20.0	3.52	17.58	1.01	1.01	0.517	1.19	71.8	60.6	0.67
1.00	2.5	5.24	0.45	11.76	10.00	20.0	4.21	21.03	1.26	1.28	0.511	1.30	82.8	76.6	0.65
1.00	3.0	6.29	0.53	11.76	10.00	20.0	4.90	24.48	1.51	1.56	0.502	1.42	90.3	94.8	0.62
1.00	3.5	7.34	0.62	11.76	10.00	20.0	5.58	27.92	1.77	1.87	0.487	1.59	94.4	109.9	0.60
1.00	1.5	3.14	0.21	14.71	12.50	20.0	3.12	19.52	0.76	0.78	0.501	1.09	47.2	43.2	0.66
1.00	2.0	4.19	0.29	14.71	12.50	20.0	3.88	24.28	1.01	1.02	0.511	1.15	59.7	55.5	0.64
1.00	2.5	5.24	0.36	14.71	12.50	20.0	4.65	29.04	1.26	1.27	0.513	1.22	70.1	61.1	0.61
1.00	3.0	6.29	0.43	14.71	12.50	20.0	5.41	33.80	1.51	1.54	0.509	1.31	78.4	76.8	0.59
1.00	3.5	7.34	0.50	14.71	12.50	20.0	6.17	38.56	1.77	1.79	0.507	1.42	84.5	95.6	0.55

Table A.17: Air gap $1.0\,mm$, Stator depth $20\,mm$, Rotor pole width $0.85\,\tau_p$

Air gap δ [mm]	Flux acc. factor C_{eff}	PM width w_{pm} [mm]	rel. PM width $\frac{w_{pm}}{\tau_p}$	Pole pitch τ_p [mm]	Rotor pole width w_r [mm]	Stator depth d_s [mm]	Flux acc. factor C_m [mm]	Stator height h_s [mm]	Th. air gap B $B_{\delta_{pm_t}}$ [T]	FEA air gap B $B_{\delta_{pm_F}}$ [T]	FEA PM B B_{pm} [T]	Carter factor k_c	Th. force dens. F_{Ax_t} $\left[\frac{kN}{m^2}\right]$	FEA force dens. F_{Ax_F} $\left[\frac{kN}{m^2}\right]$	PM leakage σ_{pm}
1.00	1.5	3.14	0.42	7.50	7.50	20.0	2.39	8.94	0.76	0.75	0.518	1.19	84.6	62.3	0.71
1.00	2.0	4.19	0.56	7.50	7.50	20.0	2.99	11.22	1.01	1.04	0.504	1.34	100.2	76.1	0.67
1.00	2.5	5.24	0.70	7.50	7.50	20.0	3.60	13.49	1.26	1.37	0.472	1.56	108.0	91.8	0.68
1.00	3.0	6.29	0.84	7.50	7.50	20.0	4.20	15.76	1.51	1.72	0.431	1.88	107.6	97.4	0.65
1.00	3.5	7.34	0.98	7.50	7.50	20.0	4.81	18.04	1.77	2.11	0.365	2.39	98.5	57.3	0.61
1.00	1.5	3.14	0.31	10.00	10.00	20.0	2.57	12.84	0.76	0.75	0.516	1.14	66.5	51.6	0.69
1.00	2.0	4.19	0.42	10.00	10.00	20.0	3.22	16.10	1.01	1.02	0.512	1.24	81.6	69.4	0.67
1.00	2.5	5.24	0.52	10.00	10.00	20.0	3.87	19.36	1.26	1.30	0.501	1.37	92.3	82.5	0.65
1.00	3.0	6.29	0.63	10.00	10.00	20.0	4.52	22.62	1.51	1.62	0.484	1.54	98.3	100.6	0.63
1.00	3.5	7.34	0.73	10.00	10.00	20.0	5.18	25.88	1.77	1.94	0.462	1.77	99.5	111.5	0.60
1.00	1.5	3.14	0.25	12.50	12.50	20.0	2.78	17.37	0.76	0.76	0.507	1.11	54.7	46.0	0.68
1.00	2.0	4.19	0.34	12.50	12.50	20.0	3.49	21.78	1.01	1.01	0.512	1.18	68.4	55.4	0.65
1.00	2.5	5.24	0.42	12.50	12.50	20.0	4.19	26.20	1.26	1.28	0.509	1.27	79.3	72.9	0.62
1.00	3.0	6.29	0.50	12.50	12.50	20.0	4.90	30.61	1.51	1.56	0.501	1.39	87.2	84.4	0.60
1.00	3.5	7.34	0.59	12.50	12.50	20.0	5.60	35.02	1.77	1.85	0.491	1.54	92.0	95.2	0.58

Table A.18: Air gap $1.0\,mm$, Stator depth $20\,mm$, Rotor pole width $1.0\,\tau_p$

Appendix B

Post-processing Command Files

B.1 Air Gap and PM Flux

```
/ Opera 3D command file for post processing the RMM TFMs
/ (c) 2000 Bodo E. Hasubek

$open 1 'FileList.inp' READ
$open 2 'FluxData.oup' OVER
$format 1 fixed 0 2
$format 2 string 1 string=','

/ Number of lines to process
$read 1 #nl

/ Run loop for all lines
$do #cnt 1 #nl

/ Read the parameters:
/ #lin  Linear or saturated simulation: lin = 1 for linear case
/ #del  Air gap
/ #pp           Pol pitch
/ #stw  Stator width
/ #sth  Stator height
/ #rwf  Rotor width as a fraction of the pole pitch
/ #rpf  Rotor position as a fraction of the pole pitch
/ #agy  Air gap y coordinate (middle)
```

```
/ #sty  Stator y coordinate (lower end)
/ #std  Stator depth
/ #wid  Winding depth
/ All data in mm unless it's a fraction of the pole pitch
$read 1 #lin #del #pp #stw #sth #rwf #rpf #agy #sty #std #wid

// Adjust the parameters for the file name
$const #ag      #del*100
$const #rw      #rwf*#pp
$const #stw     #stw*10
$const #rw      #rwf*#pp
$const #rwf     #rwf*10
$const #rpf     #rpf*10

/ Assemble the file name
$if #ag LT 100.0
$string file 'RMM_d0%int(#ag)'
$else
$string file 'RMM_d%int(#ag)'
$end if

$if #pp LT 10.0
$string file '&file&_t0%int(#pp)'
$else
$string file '&file&_t%int(#pp)'
$end if

$if #stw LT 100.0
$string file '&file&_sw0%int(#stw)'
$else
$string file '&file&_sw%int(#stw)'
$end if

$if #sth LT 10.0
$string file '&file&_sh0%int(#sth)'
$else
$string file '&file&_sh%int(#sth)'
$end if

$if #rwf LT 10.0
```

```
$string file '&file&_r0%int(#rwf)'
$else
$string file '&file&_r%int(#rwf)'
$end if

$if #rpf LT 10.0
$string file '&file&_p0%int(#rpf)'
$else
$string file '&file&_p%int(#rpf)'
$end if

$if #lin EQ 1.0
$string file '&file&_lin'
$else
$string file '&file&_sat'
$end if

/ Open database
ACTI FILE='&file&.op3'
LOAD

/ Calculate integral and average over pole pitch
CART CORN=4,
CART N1=40,N2=40,
CART X1=0,Y1=#agy,Z1=#std+#wid,
CART X2=#pp,Y2=#agy,Z2=#std+#wid,
CART X3=#pp,Y3=#agy,Z3=2*#std+#wid,
CART X4=0,Y4=#agy,Z4=2*#std+#wid,
CART

HIST COMP=BY,
HIST FILL=YES

/ Save values for output
$const #pint INTEGRAL
$const #pavg INTEGRAL/(#std*#pp)

/ Calculate integral and average under pole
CART CORN=4,
CART N1=40,N2=40,
```

```
CART X1=#pp-#rw/2,Y1=#agy,Z1=#std+#wid,
CART X2=#pp,Y2=#agy,Z2=#std+#wid,
CART X3=#pp,Y3=#agy,Z3=2*#std+#wid,
CART X4=#pp-#rw/2,Y4=#agy,Z4=2*#std+#wid,
CART

HIST COMP=BY,
HIST FILL=YES

/ Save values for output
$const #rint INTEGRAL
$const #ravg INTEGRAL/(#std*#rw/2)
$if abs(MINIMUM) GT MAXIMUM
$const #rmax abs(MINIMUM)
$else
$const #rmax MAXIMUM
$end if

/ Calculate integral, average and point for the permanent magnet
CART CORN=4,
CART N1=40,N2=40,
CART X1=#pp,Y1=#sty,Z1=#std+#wid,
CART X2=#pp,Y2=#sty,Z2=2.0*#std+#wid,
CART X3=#pp,Y3=#sty+#sth,Z3=2.0*#std+#wid,
CART X4=#pp,Y4=#sty+#sth,Z4=#std+#wid,
CART

HIST COMP=BX,
HIST FILL=YES

/ Save values for output
$const #pmin INTEGRAL
$const #pmav INTEGRAL/(#std*#sth)

/ BX at a point in the middle
POINT #pp,#sty+0.5*#sth,1.5*#std+#wid,BX
$const #pmpt BX

$format 3 string 0 string='&file&'
$assign 3 2 1 2 1 2 1 2 1 2 1 2 1 2 1 2 1
```

```
/ Write one line for each database delimited with commas
$WRITE 2 #pint #pavg #rint #rmax #ravg #pmin #pmav #pmpt

$end do

$CLOSE 1
$close 2

end
yes
```

B.2 Forces

```
/ FPost.comi
/ Opera 3D command file for post processing the forces of RMM TFMs
/ (c) 2000 Bodo E. Hasubek
/
/ Two values are printed:
/ The force in x direction calculated directly along the iron surface
/ The force in x direction calculated along an air surface surrounding
/ the iron surface
/ Usually the second value is more reliable, because it excludes field
/ singularities that occur at sharp iron edges
/
$open 1 'FileList.inp' READ
$open 2 'ForceData.oup' OVER
$format 1 fixed 0 2
$format 3 string 1 string=';'

/ Text for the field names
/ (A zero string length forces the program to use the actual length)
$format 5 string 0 string='DB name'
$format 6 string 0 string='Force on surface'
$format 7 string 0 string='Force with air layer'

/ Number of lines to process
$read 1 #nl
```

```
/ Produce the table header
$assign 5 3 6 3 7 3
$write 2

/ Run loop for all lines
$do #cnt 1 #nl

/ Read the parameters:
/ #lin  Linear or saturated simulation: lin = 1 for linear case
/ #del  Air gap
/ #pp           Pol pitch
/ #stw  Stator width
/ #sth  Stator height
/ #rwf  Rotor width as a fraction of the pole pitch
/ #rpf  Rotor position as a fraction of the pole pitch
/ #agy  Air gap y coordinate (middle)
/ #sty  Stator y coordinate (lower end)
/ #std  Stator depth
/ #wid  Winding depth
/ All data in mm unless it's a fraction of the pole pitch
$read 1 #lin #del #pp #stw #sth #rwf #rpf #agy #sty #std #wid

// Adjust the parameters for the file name
$const #ag      #del*100
$const #rw      #rwf*#pp
$const #stw     #stw*10
$const #rw      #rwf*#pp
$const #rwf     #rwf*10
$const #rpf1    #rpf*10

/ Assemble the file name
$if #ag LT 100.0
$string file 'RMM_d0%int(#ag)'
$else
$string file 'RMM_d%int(#ag)'
$end if

$if #pp LT 10.0
$string file '&file&_t0%int(#pp)'
$else
```

```
$string file '&file&_t%int(#pp)'
$end if

$if #stw LT 100.0
$string file '&file&_sw0%int(#stw)'
$else
$string file '&file&_sw%int(#stw)'
$end if

$if #sth LT 10.0
$string file '&file&_sh0%int(#sth)'
$else
$string file '&file&_sh%int(#sth)'
$end if

$if #rwf LT 10.0
$string file '&file&_r0%int(#rwf)'
$else
$string file '&file&_r%int(#rwf)'
$end if

$if #rpf1 LT 10.0
$string file '&file&_p0%int(#rpf1)'
$else
$string file '&file&_p%int(#rpf1)'
$end if

$if #lin EQ 1.0
$string file '&file&_lin'
$else
$string file '&file&_sat'
$end if

/ Open database
ACTI FILE='&file&.op3'
LOAD

/ Select all surfaces that belong to the rotor
SELE LABEL=+ROTOR,
SELE TYPE=SURF,
```

```
SELE ADD=NO,REMOVE=NO,
SELE COIL=NO,
SELE

/ Integrate the Maxwell Stresses
INTE TAVE=YES

/ Save value for output
$const #onsf FX

/ Add air layer around the iron surface
SELE ADD=YES,REMOVE=NO

/ Integrate the Maxwell Stresses again
INTE TAVE=YES

/ Save value for output
$const #onar FX

$format 4 string 0 string='&file&'
$assign 4 3 1 3 1 3

/ Write one line for each database delimited with commas
$WRITE 2 #onsf #onar

$end do

$CLOSE 1
$close 2

end
yes
```

Appendix C

Input file formats

C.1 RMMi and RMMiPost

General rules:

- Each case definition starts with the key character '@'.
- You can define any number of cases in one file.
- Separator characters are space, tab and '\\n'. Do NOT use ',', ';' or ':' as separators!
- Strings such as filenames etc. must be quoted with single or double quotes.
- C++ style ('//')comments allowed.
- Empty lines allowed.
- Numbers can only contain [0-9] and [.-], i.e. no scientific notation!
- Parameters can be given on the same line or spread over multiple lines.

Example:

```
// Case 23
@                   // Start marker
"quit"              // Quit Opera 3D after processing
"sat"               // linear or non-linear analysis
2000.0              // M.M.F. in A-turns
765880.0            // PM coercive force in A/m
1.048               // Relative permeability of the PM
```

```
0.75              // Air gap
11.76             // Pole pitch
30                // Air padding
 5                // Extra air in z-direction
20                // Rotor height
 2                // Rotor edge height
21.03             // Stator height/PM height
7.83              // Stator Iron width
0.85              // Rotor width as fraction of the pole pitch
20                // Stator depth
20                // Winding depth
0.0               // Rotor position (as fraction of the pole pitch)
// END
```

C.2 Post-processing

General rules:

- The first line contains the number of data lines in the file.
- No comments or empty lines are allowed.
- Each following line contains a space separated list containing the following values:
  - Linear or saturated simulation indicator: 1 = linear, 0 = non-linear
  - Air gap
  - Pole pitch
  - Stator width
  - Stator height
  - Rotor width as a fraction of the pole pitch
  - Rotor position as a fraction of the pole pitch
  - Air gap y coordinate (middle)
  - Stator y coordinate (lower end)
  - Stator depth
  - Winding depth

Example:

```
2
0 0.75 11.76 7.9 21.03 0.85 0.0 22.375 22.75 20.0 20.0 2.0
0 0.75 11.76 6.3 27.92 0.85 0.0 22.375 22.75 20.0 20.0 2.0
```